Formation and Characterization of Reduced Metal Complexes in the Gas Phase

Madanakrishna Katari

NNT : 2016SACLX091

THÈSE DE DOCTORAT
DE
L'UNIVERSITÉ PARIS-SACLAY
PRÉPARÉE À
" ÉCOLE POLYTECHNIQUE "

ECOLE DOCTORALE N° **571 2MIB**
Sciences Chimiques : Molécules, Matériaux, Instrumentation et Biosystèmes

Spécialité de doctorat **Chimie**

Par

Madanakrishna KATARI

Formation and Characterization of Reduced Metal Complexes in the Gas Phase

Thèse présentée et soutenue à l'Ecole Polytechnique , le 24 Novembre 2016 :

Composition du Jury :

Dr. Gilles Grégoire	DR CNRS, Orsay	Président
Dr. Dorothée Berthomieu	DR CNRS, Montpellier	Rapporteur
Prof. Carlos Afonso	Université de Rouen	Rapporteur
Dr. Ilaria Ciofini	DR CNRS, Paris	Examinateur
Dr. Gilles Frison	CR CNRS, Palaiseau	Directeur de thèse

This thesis is dedicated to my parents
for their love, and endless support

Acknowledgement

It is a great pleasure for me to thank all the people who supported and helped me during the whole period of my doctoral programme. My first and deepest appreciation goes to my supervisor, Dr. Gilles FRISON, for his continuous guidance and support in all stages of my thesis. I would like to thank all his contributions of time, ideas and funding that made my Ph.D. His enthusiasm, passion and vast knowledge have inspired me to overcome all the abstacles and challenges all along my Ph.D. pursuit.

I am sincerely grateful to the jury members of my thesis including reviewers: Dr. Dorothée Berthonieu and Dr Carlos Afonso who spent their valuable time for serving on committee and giving me many invaluable comments and constructive advices to the thesis. I also thank to examiners of my thesis commitee Dr. Gilles Grégoire and Dr. Ilaria Ciofini.

I am thankful to the past director of laboratory Dr. Gilles Ohanessian for his acceptance for me to work as PhD studend and also present director Dr. Corinne Gosmini for her support along my thesis period.

I would like to thank Dr. Duncan Carmichael, Dr. Guillaume van der Rest and Edith Nicol, Vincent Steinmetz, Dr. Eleonore Payen de la Garanderie for their help during my experiments. I am really grateful to them for their constant and enthusiastic help in these three years.

I also acknowledge all my past and present colleagues and friends at Ecole Polytechnique. I thank them all name by name for providing the cheerful working environment.

Finally, I wish to thank my parents whose unconditional love provided me inspiration and was my driving force, and my wife for her endless love and continuous support through all the thesis time. I would not have made this far without them. I also express my gratitude to all my other family members and friends in India.

Table of Content

Chapter I

General Introduction

Introduction Générale (in French)

Développer un nouvel outil analytique pour l'aide à la conception de catalyseurs organométalliques plus efficaces représente un défi majeur aux applications très nombreuses. Pendant longtemps, les procédés en catalyse organométallique homogène étaient essentiellement basés sur les coûteux métaux dits « nobles » tels que le platine, le palladium et le rhodium. Ces métaux sont non seulement difficiles à obtenir en raison de leur faible abondance, mais leur approvisionnement ne peut être garanti à moyen terme. Leur production à partir de minerais pose de graves problèmes écologiques et leur prix varie énormément. Il est donc très important pour l'industrie chimique de pouvoir remplacer ces métaux par des métaux « communs » plus abondants et plus facilement accessibles tels que le zinc, le fer ou le cobalt. D'une manière plus générale, le développement d'approches plus « vertes » pour la catalyse, comme l'utilisation de la lumière visible en photocatalyse, est fortement recommandé.[1]

Les exceptionnelles performances obtenues en catalyse avec les métaux nobles résultent de la nature de leur états d'oxydation préférentiels, qui sont séparés de deux unités (Pd (0) / Pd (II) ; Rh (I) / Rh (III) ; etc…). Les processus chimiques de formation ou de rupture d'une liaison impliquant deux électrons, ces métaux sont donc particulièrement bien adaptés pour catalyser la formation et la rupture des liaisons. Les métaux communs, appartenant à la première ligne des métaux de transition dans le tableau périodique, ont à l'inverse des degrés d'oxydation préférentiels qui diffèrent d'une seule unité (Fe(II) / Fe (III) ; Co (II) / Co (III)). Contrairement aux métaux nobles, ces métaux de transition ne peuvent pas faciliter des processus classiques à deux électrons, à moins qu'un deuxième site ne soit prévu pour stocker ou donner un second électron. Des recherches récentes ont montré que des ligands « non innocents », tels que les ligands bis(imino)pyridines[2] et terpyridines,[3] peuvent accepter ce

second électron, et ces ligands ont été utilisés dans diverses réactions catalysées par des complexes à base de fer ou de cobalt.[4] Ces systèmes moléculaires ont été étudiés en détails par un large éventail de techniques, mais leur instabilité en solution et leur très faible concentration, de surcroit au sein d'un mélange complexe dans lequel de nombreux radicaux sont potentiellement présents, rend extrèmement difficile leur étude et leur caractérisation à l'aide de nombreuses techniques expérimentales telles que la résonance magnétique nucléaire (RMN), la résonance paramagnétique électronique (RPE) ou la diffraction des rayons X. Cela signifie que la nature précise d'une grande partie de ces intermédiaires reste encore mal connue. Par exemple, l'implication d'états électroniques quasi-dégénérés dans l'un des systèmes les plus importants en catalyse au fer, le complexe [Fe(bis(imino)pyridine)], rend difficile la détermination de sa structure électronique[5].

Les techniques de dissociation par capture d'électrons (ECD) et par transfert d'électrons (ETD) sont les méthodes les plus utilisées parmi l'ensemble des techniques utilisées en spectrométrie de masse et regroupées sous le terme générique de méthodes de dissociation activée par des électrons (ExD). Ce sont des techniques de fragmentation récentes qui ont montré un très fort potentiel pour l'analyse de peptides ou de protéines.[6] En ECD et ETD, un polycation est partiellement réduit par un électron, c'est à dire qu'une espèce chimique dont l'état électronique est à couche fermée est transformée en un intermédiaire cationique à couche ouverte, ce dernier subissant une fragmentation.[7]

$$ML_n^{m+} + e^- \longrightarrow [ML_n^{(m-1)+\bullet}] \longrightarrow \text{Fragments}$$

Le (ou les) mécanisme(s) exact(s) impliqué(s) dans un tel processus est(sont) encore source de nombreuses questions et discussions dans la littérature, et une meilleure compréhension de ces mécanismes s'avère nécessaire pour utiliser au mieux ces techniques dans de nombreuses applications.[8] Une des principales questions non encore résolue est de connaître le site

d’attachement de l'électron ajouté, ce qui permettrait de mieux comprendre la nature des fragments observés. Une autre question est liée à la question précédente: est-il possible d’obtenir une description appropriée, et en un temps raisonnable, de la structure électronique de ces cations radicaux à partir des méthodes actuelles de chimie théorique ?[9]

La question fondamentale du site de résidence de l’électron ajouté dans un processus de réduction électronique se pose non seulement pour les protéines et les peptides (les molécules étudiées le plus fréquemment par les techniques ExD), mais aussi pour les complexes organométalliques. Pour ces composés, l'électron ajouté peut être sur le centre métallique, sur un ligand ou un groupe chimique spécifique d'un ligand, ou bien il peut également être partagé entre ces différents sites. Cette question fondamentale peut avoir des implications importantes dans le sens où la connaissance et la compréhension précise de la structure électronique des espèces chimiques le long d'un processus catalytique facilitent son amélioration, permettant ainsi une conception rationnelle de nouveaux ligands et de nouveaux composés organométalliques possédant les propriétés structurales et électroniques adaptées. Ceci est tout particulièrement approprié pour les complexes organométalliques possédant des ligands non-innocents. En effet, la capacité des ligands non-innocents (ou ligands redox) à piéger et/ou à fournir un ou des électrons au centre métallique des complexes organométalliques leur confère un intérêt chimique incontestable, et ce type de complexes a démontré sa pertinence dans le développement de nouvelles méthodologies de synthèse. Ceci est parfaitement illustré par les complexes de métaux de base tels que Fe ou Cu, complexes qui sont alors bien adaptés pour participer à des procédés catalytiques pour lesquels deux électrons sont nécessaires, ceci étant rendu possible par la participation rédox de leurs ligands.[10] Pour de tels procédés, il est donc fondamental de comprendre la structure électronique du complexe métal-ligand pour donner un aperçu de leur activité catalytique.[11]

Dans ce contexte, notre travail a consisté à développer une nouvelle méthode analytique pour les complexes organométalliques permettant de (*i*) produire des complexes organométalliques réduits en phase gazeuse, et (*ii*) caractériser leur structure électronique en combinant approches expérimentales et théoriques. L'objectif était de mettre en place une nouvelle méthode notamment pour distinguer entre la réduction du métal et la réduction des ligands pendant le processus catalytique.

Après cette introduction générale (chapitre I), le chapitre II décrit le fond méthodologique et théorique utilisé dans le cadre de cette thèse. Cela concerne les instruments expérimentaux ainsi que les méthodes de calcul.

Le chapitre III traite de la formation d'ions à charges multiples en phase gazeuse et de leur réduction électronique avec les méthodes d'activation par des électrons telles que la dissociation par capture d'électrons et la dissociation par transfert d'électrons.

Le quatrième chapitre explore l'aptitude des méthodes de calcul, et en particulier de nombreuses fonctionnelles développées dans le cadre de la théorie de la fonctionnelle de la densité (DFT), à déterminer la structure électronique de composés organométalliques réduites formés dans le chapitre précédent.

Dans le chapitre V, nous avons évalué la précision des fonctionnelles de la DFT, et en particulier les fonctionnelles hybrides à séparation de portée qui se sont révélées très pertinentes pour décrire la structure électronique au chapitre IV, pour reproduire les spectres infrarouges. Nous avons de plus déterminé et quantifié leur marge d'erreur.

Dans le dernier chapitre (chapitre VI), à l'aide des connaissances accumulées dans les chapitres précédents, nous avons détaillé la caractérisation de onze complexes radicalaires de zinc et de ruthénium en combinant les approches expérimentales et théoriques.

References

[1]. T. P. Yoon, M. A. Ischay, J. Du, *Nat. Chem.* **2010**, *2*, 527–532.

[2]. D. Enright, S. Gambarotta, G. P. A. Yap, P. H. M. Budzelaar, *Angew. Chem. Int. Ed.* **2002**, *41*, 3873–3876.

[3]. A. M. Tondreau, C. C. H. Atienza, J. M. Darmon, C. Milsmann, H. M. Hoyt, K. J. Weller, S. A. Nye, K. M. Lewis, J. Boyer, J. G. P. Delis, E. Lobovsky, P. J. Chirik *Organometallics* **2012**, *31*, 4886–4893.

[4]. (a) K. T. Sylvester, P. J. Chirik *J. Am. Chem. Soc.* **2009**, *131*, 8772–8774; (b) A. M. Tondreau, C. Milsmann, A. D. Patrick, H. M. Hoyt, E. Lobkovsky, K. Wieghardt, P. J. Chirik *J. Am. Chem. Soc.* **2010**, *132*, 15046–15059.

[5]. (a) A. M. Tondreau, S. C. E. Stieber, C. Milsmann, E. Lobkovsky, T. Weyhermüller, S. P. Semproni, P. J. Chirik, *Inorg. Chem.* **2013**, *52*, 635–646; (b) J. M. Darmon, Z. R. Turner, E. Lobovsky, P. J. Chirik, *Inorg. Chem.* **2012**, *31*, 2275–2285.

[6]. (a) L. M. Mikesh, B. Ueberheide, A. Chi, J. C. Coon, J. E. P. Syka, J. Shabanowitz, D. F. Hunt, *Biochim. Biophys. Acta*, **2006**, *1764*, 1811–1822; (b) H. J. Cooper, K. Hakansson, A. G. Marshall *Mass Spectrom. Rev.* **2005**, *24*, 201–222.

[7]. (a) J. Simons *Chem. Phys. Lett.* **2010**, *484*, 81–95; (b) F. Turecek, R. R. Julian *Chem. Rev.* **2013**, *113*, 6691–6733.

[8]. (a) I. Swierszcz, P. Skurski, J. Simons *J. Phys. Chem. A*, **2012**, *116*, 1828–1837; (b) S. Maclot, J. Rangama, S. B. Nielsen, J. C. Poully *Int. J. Mass Spectrom.* **2013**, *337*, 1–11; (c) M. D. Wodrich, K. O. Zhurov, A. Vorobyev, H. Ben Hamidane, C. Corminboeuf, Y. O. Tsybin *J. Phys. Chem. B*, **2012**, *116*, 10807–10815 ; (d) F. Turecek, T. W. Chung, C. L. Moss, J. A. Wyer, A. Ehlerding, A. I. S. Holm, H. Zettergren, S. B. Nielsen, P. Hvelplund, J. Chamot-Rooke, B. Bythell, B. Paizs *J. Am. Chem. Soc.*, **2010**, *132*, 10728–10740.

[9]. A. I. Gilson, G. van der Rest, J. Chamot-Rooke, W. Kurlancheek, M.Head-Gordon, D. Jacquemin, G. Frison *J. Phys. Chem. Lett.* **2011**, *2*, 1426–1431.

[10]. (a) S. Blanchard, E. Derat, M. Desage-El Murr, L. Fensterbank, M. Malacria, V. Mouriès-Mansuy *Eur. J. Inorg. Chem.* **2012**, 376–389 ; (b) O. R. Luca, R. H. Crabtree *Chem. Soc. Rev.* **2013**, *42*, 1440–1459.

[11]. P. J. Chirik, K. Wieghardt *Science*, **2010**, *327*, 794–795.

General Introduction (in English)

Developing a new analytical tool for building efficient catalysts with transition metals that has immense potential of applications throughout the homogeneous catalysis is a relevant but challenging task. For a long time, reported processes in homogeneous organometallic catalysis were exclusively based on using the expensive precious metals such as platinum, palladium and rhodium. These metals are not only difficult to obtain due to their low abundance, but also their supplies will probably be exhausted in the medium term. Their production from ores is environmentally catastrophic and their price varies wildly. Therefore, it is very important for the chemical industry to replace these expensive metals with more abundant and easily obtained "base" metals such as zinc, iron or cobalt. In a more general way, developing greener approaches for catalysis, such as the use of visible light in photocatalysis, is highly recommended.[1]

The exceptional catalytic competence of the precious metals arises from the nature of their preferred oxidation states, which generally are separated by two electrons (Pd(0)/Pd(II); Rh(I)/Rh(III); etc). As the bond-making and breaking processes involved two electrons, these metals are uniquely well adapted to catalyze bonds formation and cleavage. The base metals, from the first row elements, which should ideally replace the precious metals, have preferred oxidation levels that are separated by only one electron such as (Fe(II)/Fe(III) and Co(II)/Co(III)). Unlike noble metals, these transition metals cannot easily support classical two-electron processes unless a second site is provided for storing or delivering an electron. Recent research has shown that 'non-innocent' ligands such as bis(imino)pyridines[2] and terpyridines,[3] can accept this second electron and these ligands have been used to assist iron and cobalt centers in various catalytic reactions.[4] These systems have been studied extensively by a wide range of techniques, but their instabilities in solution, their often low concentration in mixture, their complexities and the electron-separated nature of their

intermediates rule out analysis not only by diamagnetic-friendly techniques such as NMR, but also by other techniques such as X-ray analysis and EPR. It means that the precise nature of many of the catalytic species or intermediate remains in doubt. For instance, the involvement of near-degenerate electronic states in one of the most important [Fe(bis(imino)pyridine)] systems make the determination of the electronics of the system particularly difficult to delineate.[5]

The Electron Capture and Electron Transfer Dissociation (ECD/ETD) techniques are the most used methods among the Electron activated Dissociation (ExD) techniques in mass spectrometry. They provide new fragmentation techniques that have shown a profound potential for the analysis of peptides or proteins.[6] In ECD and ETD, a multiply charged cation is partially reduced by receiving an electron, thereby going from a closed-shell species to an intermediate cation-radical that undergoes fragmentation.[7]

$$ML_n^{m+} + e^- \longrightarrow [ML_n^{(m-1)+\bullet}] \longrightarrow \text{Fragments}$$

The exact mechanism(s) implicated in such a process are still a matter of active discussion and a better understanding of them is required to expertise their applications.[8] One main issue is to know the location of the added electron in order to be able to answer the question of the nature of the observed fragments. Another issue is related to this former question: how can a proper and time-efficient description of the electronic structure of such radical cations be obtained from theoretical chemistry methods ?[9]

The fundamental question of the residence site of an added electron in an electronic reduction process arises not only for proteins and peptides (the molecules most frequently studied by ExD techniques), but also for organometallic complexes. For these compounds, the added electron can be on metal, on a ligand or a specific chemical group of a ligand or it can also be

shared by multiple ligands or between ligands and metal. This fundamental question may have important implications in the sense that the knowledge and understanding of the electronic structure of the species along a catalytic process facilitate its improvement by a rational design of new ligands and organometallic compounds able to tune the reactive properties. This is particularly true for organometallic complexes with non-innocent ligands. The ability of non-innocent (or redox) ligands to delocalize and/or provide electrons to the metal center of organometallic complexes confers them an undisputable chemical interest, and they have proved their valuables in the development of novel synthetic methodologies. This is especially well exemplified in the way that typical base metals, like Fe or Cu, can be adapted to participate in catalytic processes for which two electrons are required by means of a redox participation from their ligands.[10] For such processes, it is thus fundamental to understand the electronic structure of the metal-ligand complex to provide insights into their catalytic activity.[11]

From this background, we worked to develop a new analytical method for organometallic complexes, that is (i) to produce electron reduced organometallic complexes in the gas phase, and (ii) to characterize their electronic structure with combined experimental and theoretical techniques. This will allow setting up a novel method to distinguish between metal reduction and ligand reduction during catalytic process.

After this introduction (Chapter I), Chapter II is used to describe the methodological and theoretical background used along this thesis. This concerns experimental instruments as well as computational methods.

Chapter III deals with formation of multiply-charged ions in the gas phase and their electronic reduction with electron activated methods such as electron capture dissociation and electron transfer dissociation.

The fourth chapter explores the ability of calculations, using various density functional theory methods, to determine electronic structure of typical reduced organometallic metal species formed in the previous chapter.

In chapter V, we assessed the ability of DFT functionals, in particular range-separated hybrid functionals which seems to perform well for the electronic structure as observed in chapter IV, to properly reproduce the infrared spectra, and we have established and quantified their error margin.

In the final chapter VI, using knowledge accumulated in previous chapters, we detailed the characterization of open-shell radical species with eleven specific examples of zinc and ruthenium complexes.

I.1. References

[1]. T. P. Yoon, M. A. Ischay, J. Du, *Nat. Chem.* **2010**, *2*, 527–532.

[2]. D. Enright, S. Gambarotta, G. P. A. Yap, P. H. M. Budzelaar, *Angew. Chem. Int. Ed.* **2002**, *41*, 3873–3876.

[3]. A. M. Tondreau, C. C. H. Atienza, J. M. Darmon, C. Milsmann, H. M. Hoyt, K. J. Weller, S. A. Nye, K. M. Lewis, J. Boyer, J. G. P. Delis, E. Lobovsky, P. J. Chirik *Organometallics* **2012**, *31*, 4886–4893.

[4]. (a) K. T. Sylvester, P. J. Chirik *J. Am. Chem. Soc.* **2009**, *131*, 8772–8774; (b) A. M. Tondreau, C. Milsmann, A. D. Patrick, H. M. Hoyt, E. Lobkovsky, K. Wieghardt, P. J. Chirik *J. Am. Chem. Soc.* **2010**, *132*, 15046–15059.

[5]. (a) A. M. Tondreau, S. C. E. Stieber, C. Milsmann, E. Lobkovsky, T. Weyhermüller, S. P. Semproni, P. J. Chirik, *Inorg. Chem.* **2013**, *52*, 635–646; (b) J. M. Darmon, Z. R. Turner, E. Lobovsky, P. J. Chirik, *Inorg. Chem.* **2012**, *31*, 2275–2285.

[6]. (a) L. M. Mikesh, B. Ueberheide, A. Chi, J. C. Coon, J. E. P. Syka, J. Shabanowitz, D. F. Hunt, *Biochim. Biophys. Acta*, **2006**, *1764*, 1811–1822; (b) H. J. Cooper, K. Hakansson, A. G. Marshall *Mass Spectrom. Rev.* **2005**, *24*, 201–222.

[7]. (a) J. Simons *Chem. Phys. Lett.* **2010**, *484*, 81–95; (b) F. Turecek, R. R. Julian *Chem. Rev.* **2013**, *113*, 6691–6733.

[8]. (a) I. Swierszcz, P. Skurski, J. Simons *J. Phys. Chem. A*, **2012**, *116*, 1828–1837; (b) S. Maclot, J. Rangama, S. B. Nielsen, J. C. Poully *Int. J. Mass Spectrom.* **2013**, *337*, 1–11; (c) M. D. Wodrich, K. O. Zhurov, A. Vorobyev, H. Ben Hamidane, C. Corminboeuf, Y. O. Tsybin *J. Phys. Chem. B*, **2012**, *116*, 10807–10815 ; (d) F. Turecek, T. W. Chung, C. L. Moss, J. A. Wyer, A. Ehlerding, A. I. S. Holm, H. Zettergren, S. B. Nielsen, P. Hvelplund, J. Chamot-Rooke, B. Bythell, B. Paizs *J. Am. Chem. Soc.*, **2010**, *132*, 10728–10740.

[9]. A. I. Gilson, G. van der Rest, J. Chamot-Rooke, W. Kurlancheek, M.Head-Gordon, D. Jacquemin, G. Frison *J. Phys. Chem. Lett.* **2011**, *2*, 1426–1431.

[10]. (a) S. Blanchard, E. Derat, M. Desage-El Murr, L. Fensterbank, M. Malacria, V. Mouriès-Mansuy *Eur. J. Inorg. Chem.* **2012**, 376–389 ; (b) O. R. Luca, R. H. Crabtree *Chem. Soc. Rev.* **2013**, *42*, 1440–1459.

[11]. P. J. Chirik, K. Wieghardt *Science*, **2010**, *327*, 794–795.

Chapter II

Methodology

Part A: Experimental Methodology

IIA.1. Introduction

In this chapter, we described the theoretical background of computational calculations, methodology and instruments used for performing the IR spectroscopy of mass-selected ions. The aim of the thesis is to provide an analytical tool for characterizing the electronic structure of reduced metal ions in the gas phase via combination of mass spectrometry, infrared spectroscopy and DFT calculations.

In general, the organometallic complexes have been studied extensively for the purpose of homogeneous catalysis by utilizing the expensive noble metals such as platinum, palladium and rhodium. These metals are not only difficult to obtain with their abundance, but also their supplies will probably be exhausted in the medium term. Their production from ores is environmentally catastrophic. Therefore, for past few years, it has been a keen interest to replace these expensive metals with more abundant and easily obtained “base” metals such as zinc, iron or cobalt.

However, the utilization of these "base" metals in catalysis requires high redox properties of the ligands. Nevertheless, the experimental methods such as NMR, EPR, cyclic voltammetry and UV/Vis spectroscopy could not provide sufficient information in the solution phase at the molecular level. However, it is also very difficult to analyze when a species presents in the mixture of ions, having low concentrated solution and/or ion is unstable. Focused on this prospect, we aimed to develop an analytical tool to study transition organometallic complexes containing non-innocent ligands in the gas phase with the combination of spectroscopic techniques and computational calculations.

Experimentally, the idea is to selectively isolate the ions of interest using mass spectrometry, then to reduce these ions with the available fragmentations techniques, and further to irradiate them with infrared light. Different instrumental approaches have been developed and works have been reported on photodissociation of trapped ions in mass spectrometer.[1,2] Methods such as Linear or quadrupolar radio-frequency ion-traps as well as Penning ion traps have been used, and many recent developments have been aimed at trapping ions at low temperature.

Particularly, the tandem mass spectrometer, installed at Centre Laser Infrarouge d'Orsay (CLIO) is coupled with two tunable infrared lasers and an auxiliary CO_2 laser. The first laser is the Free Electron Laser of the CLIO and is tunable in the mid-infrared from ~100 to ~2000 cm^{-1}. It is routinely used to derive IR spectra of gas-phase ions in the 800-2000 cm^{-1} range. The second tunable infrared laser is a tabletop Optical Parametric Oscillator/Amplifier (OPO/OPA) laser. It is efficiently tunable in the 2500-4000 cm^{-1} near-infrared spectral range, which is useful for characterizing the NH and OH stretching modes, and in particular their spectral shifts which are characteristic of hydrogen bonding motifs.

An important factor to convince people of using IR activation for analytical purpose is the irradiation time. When using the IR Free Electron Laser, the irradiation time is typically of the order of few 100 ms. Tabletop laser is less powerful in comparison with the Free Electron Lasers and the irradiation time may have to be increased up to 1s depending on the dissociation energy threshold of the molecular ion. In this case, an auxiliary CO_2 laser can be used for enhancing the fragmentation yield.

IIA.2. Tandem Mass Spectrometry

IIA.2.1. General View

Tandem mass spectrometry (MS/MS) is a powerful analytical technique used to quantify known materials and to identify unknown compounds within a sample. The complete process involves the conversion of the sample into gaseous ions, with or without fragmentation, which are then characterized by their mass to charge ratios (m/z) and relative abundances.

Our experimental set-ups are based on two commercial tandem mass spectrometers; both of them are equipped with an Electrospray Source Ionization (ESI). One instrument, a Bruker SolariX is based on 9.4 Tesla at our laboratory, *Laboratoire de Chimie Moléculaire* (LCM), Ecole Polytechnique, which we used for our preliminary studies as this instrument facilitated with electron capture dissociation (ECD) and electron transfer dissociation (ETD), collision induced dissociation (CID) fragmentation techniques. The second instrument is from *Laboratoire de Chimie Physique* (LCP), Orsay, is a Bruker Apex Qe, and is based on a 7 tesla Fourier Transform Ion Cyclotron Resonance (FT-ICR) mass spectrometer. This instrument facilitated with CID and ECD techniques, and coupled with Infrared multi photon dissociation spectroscopy (IRMPD). CLIO has practical advantages for using commercial instruments. In the context of our work, the most important advantage is that CLIO provides a conventional way to perform the Electron capture dissociation (ECD) of mass-selected ions. This is particularly important for probing the structures of fragments for example, reactive intermediates involved in the peptide sequencing process. The following sections have been covered the detailed intrinsic technical aspects of the instruments that have been used for our research work.

IIA.2.2. FT–ICR mass spectrometer set-up

One of the mass spectrometers used during the thesis work is a hybrid 7 Tesla FT-ICR tandem mass spectrometer (Bruker, APEX Qe). It is called "hybrid" because there is a Quadrupole and hexapole (Qh) interface between the high pressure ion source region and the high vacuum region containing the ICR cell. The instrument is equipped with a conventional external electrospray ionization source (ESI). A scheme of the mass spectrometer which integrates the ICR is shown in Figure 1.1.

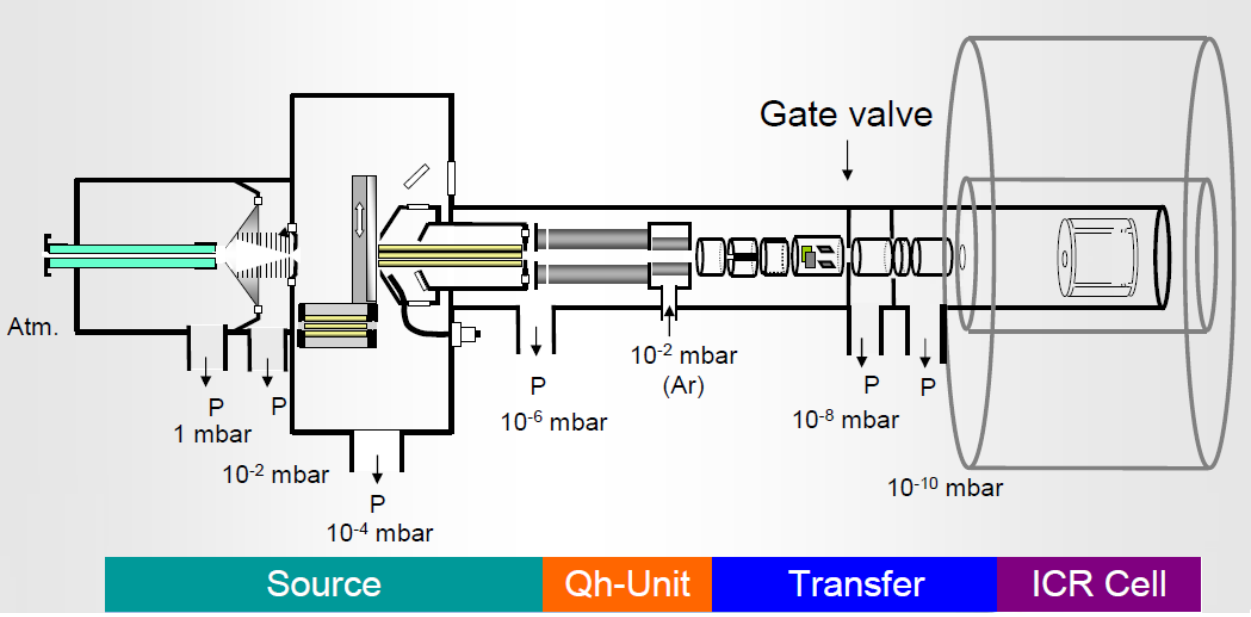

Figure 1.1: Schematic view of FT-ICR mass spectrometer (Bruker APEX Qe). The source, the Qh-unit (Quadrupole and hexapole), the transfer optics and the ICR cell are shown. The typical pressure of each region is specified in mbar.

The ESI source is the standard atmospheric pressure ion source for the measurement of singly charged samples such as benzodiazepines, and multiple charged samples such as proteins, peptides, and nucleic acids. The sample solution is introduced through the nebulizer assembly into the spray chamber, where it is subjected to the ESI process by means of an electrical field between the inner chamber wall and the spray shield, and with the aid of a nebulizer gas (N_2).

The heated drying gas (N_2) which flows in the opposite direction of the stream of droplets enters in the spray chamber. Here, it's used to aid volatilization, then for the ionization, and later to carry away any uncharged material.

The continuous flows of electrosprayed ions is guided through Qh towards the ICR where ion manipulation takes place, and then before ions are sequentially ejected towards a conventional electron multiplier detector. This Qh interface consists of a linear quadrupole for mass selection and a linear hexapole ion trap. The latter is fitted in a pressurized (~10-3 mbar of Argon) cell and its purpose is fourfold. Hence, a weak abundant species from a complex mixture can be mass-selected using the quadrupole, and then accumulated in the hexapole ion trap. Secondly, the thermalization of the ions is ensured through multiple collisions of the ions with the argon buffer gas. As a result, thermalized ions are injected in the high vacuum region of the ICR cell.[3] This is important since only radioactive cooling could occur in this low pressure region. Eventually, ion-molecule reactions can also be performed between the trapped ions and neutral seeded in the Argon line.

The third component of the mass spectrometer is the Ion Cyclotron Resonance (ICR) cell which is located in the ultra-high vacuum part of the instrument. The pressure in this part is routinely of the order of ~5.10-10 mbar in the instrument used. These low pressure conditions have to be maintained in order to minimize ion-molecule collisions which would perturb the trajectory of the ions and in turn the ion detection.

The first FT-ICR experiment was performed by Comisarow and Marshall in the 70's, based on earlier developments in the 1930's.[4] Since then, significant improvements have been made, especially in terms of resolution and mass range.[5]

The basis of ion cyclotron motion is derived from the interaction of an ion with a spatially uniform magnetic field. An ion of charge *q*, and mass *m*, moving in a magnetic field **B**, will

experience a magnetic Lorentz force F that is perpendicular to both the direction of the ion velocity ***v***, and the magnetic field (Equation 1.1).

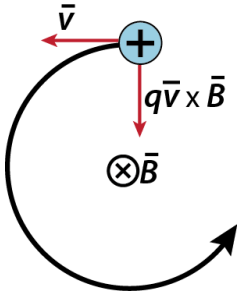

Figure 1.2. The path of a positive ion moving at a constant velocity in a magnetic field is bent into a circle by the Lorentz magnetic force. The z-direction is defined as the vector pointing into the plane of the page.

$$F = \text{mass acceleration} = m\frac{dv}{dt} = q\boldsymbol{v} \times \boldsymbol{B} \tag{1.1}$$

As a consequence of this force, the ion path will bend into a circle of radius r in the plane perpendicular to the magnetic field (Figure 1.2). The Lorentz magnetic force is equal to the product of the ion mass and the angular acceleration in the xy plane, $|dv/dt| = v^2 r$, resulting in Equation 1.2.

$$\frac{mv_{xy}^2}{r} = q\boldsymbol{v}_{xy}\mathrm{B} \tag{1.2}$$

By substitution of the angular velocity about the z-axis, $\omega = v_{xy}/r$, Equation 1.2 becomes Equation 1.3, which can be rearranged to give the equation for ion cyclotron motion (Equation 1.4), where ωc is the cyclotron frequency.

$$m\omega^2 r = q\omega r B \tag{1.3}$$

$$\omega_c = \frac{qB}{m} \tag{1.4}$$

Thus, the motion of the ion within an ICR is dependent only on an ions *m/z* and the strength of the magnetic field, which is kept constant for FT-ICR. It is independent of the initial kinetic energy from ion formation or transfer, which means that translational focusing is not required for precise determination of *m/z*.[6] The magnetic field of FT-ICR mass spectrometer used is 7.4 Tesla, It allows for a high mass resolution which is proportional to magnetic field strength.

Ion manipulation, including trapping, mass-selection, ejection, and mass-analysis, is essentially based on the cyclotron motion. The working principle of ion detection is illustrated in Figure 1.3. Different configurations have been proposed for the ICR cell, and the Bruker infinity cell has a cylindrical shape, made of two sets of electrodes or plates: two "detection plates" and two "excitation plates". Due to the cyclotron motion of the charged particles, an alternative image current can be detected on the two detection plates (Figure 1.3). For this purpose, ions are excited to a large cyclotron orbit radius using a resonant RF excitation voltage applied to "excitation electrodes". In practice, a broadband frequency radio frequency (RF) signal is used for the excitation over a large frequency range (*i.e. m/z* range), and a transient image current is detected, which is a combination of the image current of all individual ions. Hence, the mass spectrum can be derived by Fourier transform of the image current, as proposed by Comisarow and Marshall in 1974.[4] Mass selection in the ICR cell can be achieved using a dedicated broadband excitation signal in order to increase the orbital radius of all ions except for those with a given frequency (*m/z*) range. As a result all the non-desired ions are neutralized on the electrodes.

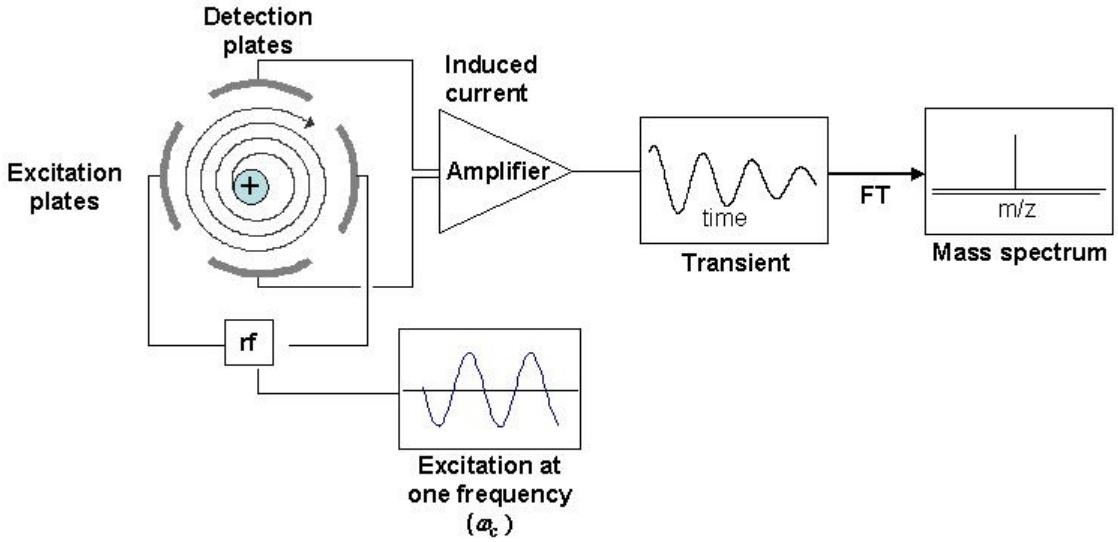

Figure 1.3: Detection and analysis of the ions in the ICR cell. The cyclotron orbit radius of the ions can be increased by applying an RF excitation on the "excitation plates". An induced time-dependent image current can be detected on the "detection plates". Mass spectrum can be derived using Fourier transform methods applied on transient image current

For performing IRMPD spectroscopy, the laser beam is mildly focused and aligned along the magnetic field axis. A detailed discussion of the ion-laser overlap issue is also provided, and the beam waist is of the order of one millimeter.[7]

The consequence on development of commercial analytical instrumentation demonstrated that ion-molecule reactions were not limited to FT-ICR-MS, but were also compatible with most modern mass analyzers; such as, ion trap,[8] triple–quadrupole,[9] quadrupole-TOF[10] and orbitrap instruments.[11]

IIA.3. Fragmentation Techniques:

A typical MS/MS experiment, as illustrated in Figure 1.4, involves isolation of the desired precursor ion, characterized by a specific *m/z*, followed by activation and dissociation into product ions. The resulting product ions are then mass analyzed in the ICR cell. There are many different MS/MS techniques that have been developed over the years and each method

distinguished by the different modes of activation of the precursor ions and by the types of products that are formed.

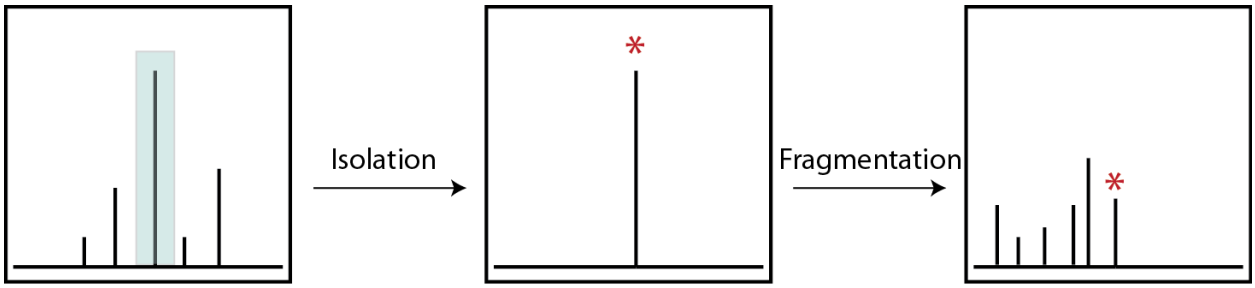

Figure 1.4: A typical MS/MS experiment involves isolation of precursor ions, followed by fragmentation, and detection of fragment ions.

Searching for the most informative fragmentation patterns has led to the development of a vast array of activation modes that offer complementary ion reactivity and dissociation pathways. Collisional activation of ions using atoms, molecules or surface which results in unimolecular dissociation of activated ions, still plays a key role in tandem mass spectrometry. The discovery of electron activated dissociation methods, such as electron capture dissociation (ECD), electron transfer dissociation (ETD) and electron photo detachment dissociation (EPD) showed a significant impact, especially for structural analysis of large biomolecules. Similarly, photon activation opened promising new frontiers in the fragmentation of ion, owing to the ability of tightly controlled internal energy deposition and easy implementation on commercial instruments. Ion activation by photons includes slow heating methods such as infrared multiple photon dissociation (IRMPD) and black-body infrared radiative dissociation (BIRD) and methods like with high-energy photos ultra-violet photodissociation (UVPD).

IIA.3.1 Electron Capture Dissociation (ECD)

Electron capture dissociation (ECD) has been developed as an efficient ion fragmentation technique in tandem mass spectrometry (MS/MS). This was first described by Zubarev *et al*. in 1998[12] and has proved as a valuable MS/MS fragmentation technique for biomolecular analysis.[13]

In the instrumentation process of ECD, the ESI-produced multiply protonated ions for example peptides and proteins $[M+nH]^{n+}$ capture a low-energy (<0.2eV) electron to produce the odd-electron ion $[M+nH]^{(n-1)+\bullet}$ which is not observable. However, it has been illustrated from literature that as odd-electron ion is accompanied by hydrogen loss, and forms $[M+(n-1)H]^{(n-1)+\bullet}$.[14] The mass of the reduced ion is essentially equal to that of the parent ion (differing by the mass of an electron), with a charge that has decreased by one. Consequently, it is essential that the precursor ions must be at least doubly charged, otherwise electron capture leads to neutral radical species which are undetectable via MS. Thus, the multi-charging capability of ESI makes the combination of ECD and ESI-FTICR-MS very desirable. ECD is a fragmentation technique and is more often used for analysis of post-translational modifications of proteins. It is also preferentially used for top-down analysis of proteins with size no larger than 35kDa. The principal of operation is shown in Figure 1.5 below. The electrons produced by the hollow cathode channel are pulsed into the ICR cell, which causes fragmentation of the ions (already trapped in the ICR cell). We performed ECD experiment on organometallic species with the mass spectrometers at our laboratory and at CLIO. Both of these instruments have been facilitated with the ECD fragmentation technique. The typical parameters of ECD in mass spectrometry at CLIO are as follows: The ECD pulse length of the electron beam can vary from 0.2 s to 0.001s with ECD bias (ionization energy of electrons) of

~1.0-3.0V. ECD lens parameter allows focusing of the electron beam and has a standard setting of ~15.0V, and ECD heater value of 1.6-1.8A.

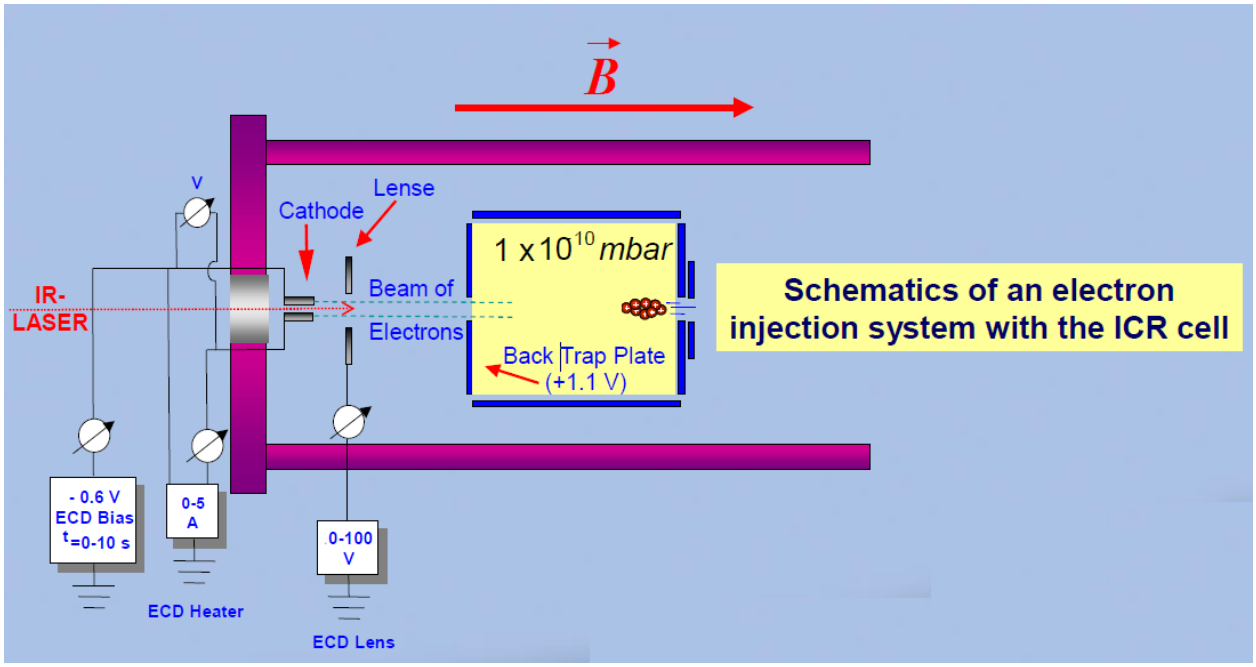

Figure 1.5: Schematic representation of an electron injection system into an ICR cel for electron capture dissociation experiment.

Because of the concomitant charge reduction, the sensitivity of ECD-based MS/MS is lower than in traditional MS/MS. Furthermore, not all precursor ions should be allowed to capture electrons to avoid excessive neutralization of the fragments.[15] The average ECD efficiency for peptides may vary about 20 to 50%, but can be higher for proteins.[16]

IIA.3.2. Electron Transfer Dissociation (ETD)

Electron-transfer dissociation (ETD) is also a method of fragmenting multiply-charged gaseous macromolecules in a mass spectrometer and introduced few years later than ECD.[17] Similar to electron-capture dissociation, ETD induces fragmentation of large, multiply-

charged cations by transferring electrons to them.[18] In particular, ETD is more often employed than ECD for peptide and protein structure analysis. The main reason is the implementation of efficient ETD MS/MS on relatively affordable, robust and widespread ion trap mass spectrometers, which deliver proteomics-grade performance, especially when coupled with high resolution mass analyzers, such as Orbitrap FTMS or time-of-flight TOF-MS.[19] In contrast, ETD has received broad commercial implementation more on Fourier transform ion cyclotron resonance mass spectrometers (FT-ICR MS), which are powerful instruments, but are more complex to use and maintain.[20]

We were access to perform ETD experiments only in mass spectrometer at our laboratory and unfortunately, there is no availability of ETD technique in the mass spectrometry at CLIO, consequently, to study them further by IR spectroscopy. In principle, The ETD ion/ion reactions in the ESI-ETD instrument use a single reagent species and odd-electron anions are generated within a chemical ionization (CI) source mounted on the source octopole and transferred into the collision cell. These anions interact with multiply charged cations isolated in quadrupole, and after ETD fragmentation, the resulting multiply charged fragments and any remaining parent ions are transferred to the Ion Cyclotron Resonance (ICR) cell for detection. As shown in Figure 1.4, both the API and CI ion sources operate simultaneously. However, analyte and reagent ions are transferred consecutively. First, the multiply charged analyte cations are isolated and accumulated. During this period, the reagent anions from the CI source are blocked via the gate lens. For accumulation of reagent anions in the collision cell, the ion optics operate only partially in negative- ion mode. The API source is maintained in positive mode to ensure an undisturbed spraying process. Once reagent anions and multiply charged cations are trapped together in a combination of RF fields, the ion-ion reaction occurs as long as the reagent accumulation continues and for a defined reaction time. The resulting

multiply charged fragments and any remaining parent ions are then transferred to the ICR cell for detection.

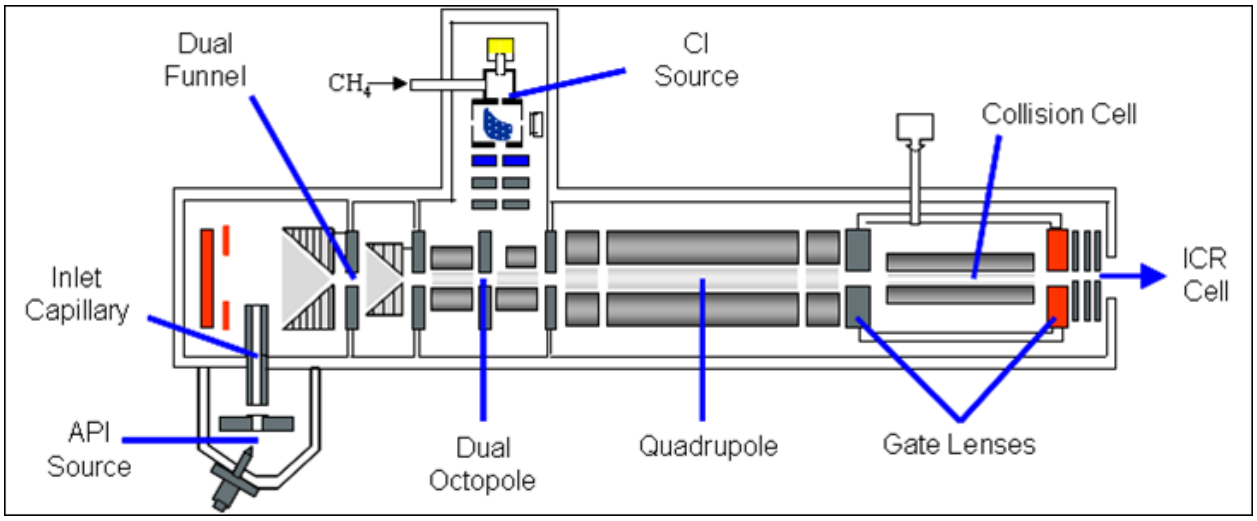

Figure 1.6: A Schematic representation of an electron injection system into an ICR cel for electron capture dissociation experiment.

Overall, the major applications of electron activated dissociation methods such as ECD and ETD have been widely explored in the field of peptide and protein analysis such as the analysis of post-translational modifications including g-carboxyglutamic acid,[21] N- and O-glycosylation,[22,23] phosphorylation,[24,25] and top-down sequencing. ECD has also been applied to protein folding analysis. Few studies have shown their use for cationized oligosaccharide[26] and phosphocholine[27] fragmentation, as well as for the generation of reduced cation species in water clusters[28]. Specifically, the utility of these fragmentation techniques have not explored of their necessity in the organometallic chemistry, Recently, Asakawa and coworkers have promptly used these electron dissociation methods for the description of Ni^{+2}-, Cu^{+2}- and Zn^{+2}-polyhistidine oligomer complexes in the absence of remote protons.[29] In this view, we motivated to use these techniques to study of electronic structure of our metal species presented in this thesis. Indeed, these electron activated methods have worked very efficiently to generate radical cationic complexes from dicationic complexes.

IIA.4. Infrared Multi-Photon Dissociation (IRMPD)

IIA.4.1. General View

The vibrational spectrum provides a wealth of structural information about an ion or a compound, such as on the location of charge (e.g. proton), the presence or absence of chemical moieties, its symmetry, and its hydrogen bonding interactions.

The first use of tunable lasers in combination with ion trapping approaches in mass spectrometry was in 1970's, when Beauchamp and co-workers irradiated ions in the Penning trap of a Fourier transform ion cyclotron resonance (FT-ICR) mass spectrometer with the output from a line-tunable CO_2 laser (925–1085 cm^{-1}).[30] Among gas discharge lasers in the infrared, CO lasers are also useful, as they cover the 1600–1900 cm^{-1} range.[31]. These lasers were employed later in elegant laser spectroscopy studies on ions by Lee and co-workers. In their ''messenger'' technique, an inert atom (e.g. argon) or molecule (e.g. H_2) is tagged to a cold complex formed in a supersonic expansion, and is detached due to the absorption of a single infrared photon.[32] The loss of the tag also results in a change in mass, which is detected by the mass analyzer. It took until the emergence of powerful and widely tunable free electron lasers (FELs) in 2000 to see a renaissance in IRMPD spectroscopy.

IIA.4.2. Principles

Since the beginning of mass spectrometry, gas-phase physical chemists have continuously showed a particular interest for the structures, energetics, and chemistry of gas phase ions. Infrared spectroscopy has long been considered a method of choice for structural characterization. IR absorption spectra are derived by monitoring the ratio between the transmitted infrared light (I_T) and incident infrared light (I_0). Such direct absorption

spectroscopy usually requires 10^{10} ion/cm^3 or higher density number.[33] Direct absorption spectroscopy is thus impossible in a Paul or in a Penning ion trap where the maximum number of ions is 106 ions, within a small volume (few mm^3). Alternatively photon absorption can be probed by monitoring the IR induced fragmentation of the trapped ions. It is worth to say that dissociation threshold for typical molecular ions is of the order of 1 eV, *i.e.* an order of magnitude larger than that of an infrared photon. One immediately sees that multiple photons have to be absorbed in order to induce ion dissociation. This photon absorption is considered to proceed stepwise, and it is named "InfraRed Multi Photon Dissociation" (IRMPD).

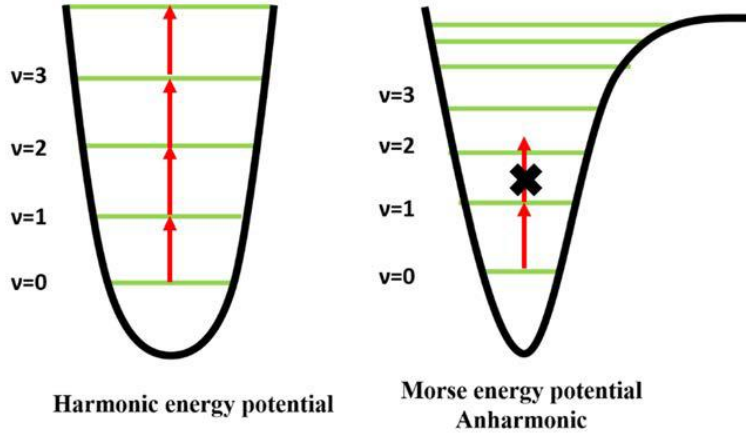

Figure 1.3: Multiple Photon Absorption through a single IR active vibrational mode assuming that the potential is harmonic (left) or anharmonic (right).

The energy potential associated with the vibrational pumping mode is shown in Figure 1.7. This vibrational mode is called "resonant mode" or "pumping mode", because the energy is pumped into the molecular ion through this vibrational mode. If the energy potential associated with this mode is assumed to be harmonic, multiple IR photons could be absorbed consecutively. Nevertheless, due to the anharmonicity of the potential, only few photons can be sequentially absorbed depending on the laser spectral width relative to the anharmonicity. This is often referred to the "anharmonic bottleneck".

Figure 1.8 illustrates the general understanding of the non-coherent multiple photon absorption process. Assuming that the anharmonicity associated with the pumping mode is large compared to the width of the laser, only one photon could be resonantly absorbed by the pumping mode. Prior to the subsequent photon absorption, it is assumed that there is de-excitation (v=1→0) of the pumping mode and redistribution of the internal energy into the other vibrational modes of the molecular ion. This diffusion of the energy is known as Intramolecular Vibrational Redistribution (IVR),[34] and it is crucial for allowing subsequent photon absorptions. After partial or complete (*i.e.* statistical redistribution of the energy) IVR, the resonant mode can absorb another photon through the first vibrational transition (v=0→1). The multiple photon absorption process can be seen as successive cycles involving IR absorption in the pumping mode followed by IVR. As a result, there is a stepwise increase of the internal energy of the ion as shown in the bottom panel of Figure 1.8.

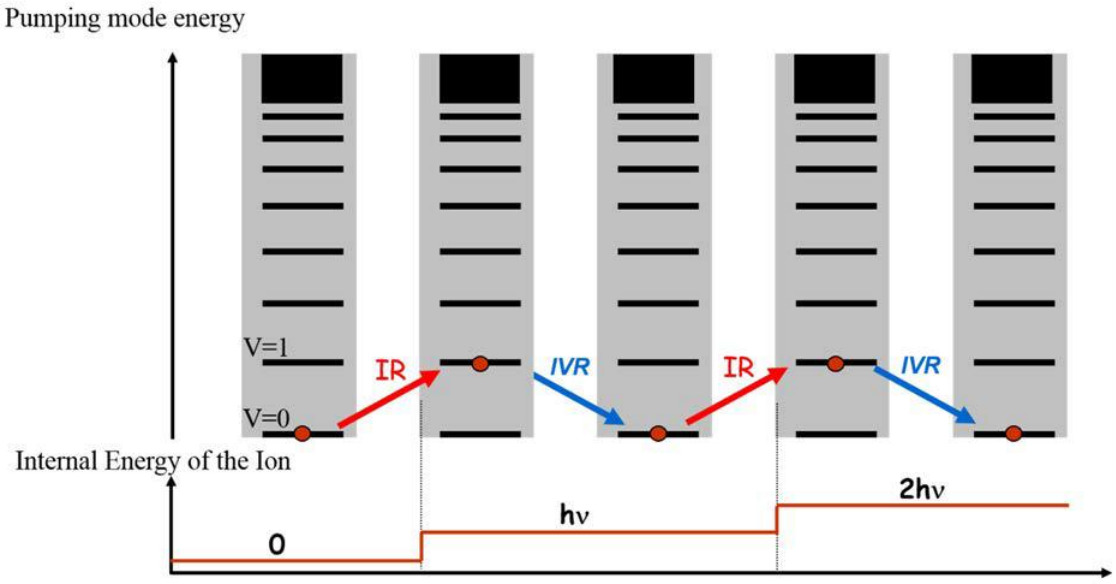

Figure 1.8: Schematic representation of the multiple photon absorption process. It is assumed that as energy raise can be understood as successive cycles involving resonant one photon absorption (red arrows) and intramolecular vibrational energy redistribution (IVR, represented as arrows in blue). This can be represented using the vibrational energy levels of the "pumping mode" as a function of time as in the top panel. The evolution of total energy of the ion as a function of time is given in the bottom panel.

The nature of the absorption of multiple IR photons has been intensively discussed in the literature in the seventies.[35] Highly intense lasers were used to investigate whether the fragmentation of neutral molecule could be isotopically selective or not. It was suggested that the multiple photon absorption mechanism proceeds through three steps, evolving with the density of vibrational states. The earlier steps of the process were supposed to follow a coherent multiphoton absorption process, and the laser peak power was shown to be critical.[36] This coherent multiple absorption process was named "IR MultiPhoton Dissociation" (IRMPD).[33] In order to make the distinction with this coherent IRMPD process, the incoherent IRMPD process at play in our case is thus named "IR multiple photon dissociation".

The first attempt of modeling the multiple photon absorption process by a molecular system irradiated by an IR FEL was proposed by von Helden and coworkers.[37] Gas phase neutral C60 was irradiated with the FELIX IR FEL and thermal emission of electrons was monitored. It was observed that the excitation was much more efficient when the IR radiation was chirped to lower frequencies during the macropulse. A model was used to understand these phenomena. More recently, Parneix and coworkers proposed a kinetic model of the energy absorption and distribution (IVR) during the macropulse of an IR FEL.[38] All the steps including absorption, stimulated emission, spontaneous emission, and dissociation were taken into account. Monte Carlo simulations of the IRMPD process relied on anharmonic potential energy surfaces calculated using quantum chemical calculations.

IIA.4.3. IR-Free Electron Laser (FEL)

In 1976, the first paper was published that related to IR Free Electron Lasers (FEL) by the group of Smith at Stanford.[39] They showed that amplification of infrared radiation of a CO_2 laser could be achieved with relativistic free electrons passing through a spatially periodic

transverse magnetic field called undulator. A year later, the same group showed that IR photons can be generated and amplified using free electrons passing through the undulator which was placed within an optical cavity.[40] Indeed, photon emission relies on the deviation of the trajectory of quasi-relativistic electrons. The electrons beam was tuned at 24 MeV and an IR beam centered at 3.417 μm with a width of 0.008 μm and an average power of 360 mW was obtained. As stressed in the introduction, the electron medium is unique in the sense that it allows a wide tunability and constitutes at the same time the amplification medium.[40] Nowadays, the FELs under operation produce Ultra Violet and Infrared up to far IR light. X-ray production is currently being developed.[41]

A schematic view of the Infrared FEL is provided in Figure 1.9. The trajectory of the electron beam is modified when it passes through the magnetic cavity or undulator, where the photon emission occurs. The IR FEL beam is then extracted through a hole in one of the cavity mirrors. The amplification and the coherence of the IR FEL beam is the subtle result of the interaction or the electrons and emitted light stored in the optical cavity. The wavelength of the IR FEL beam depends on the energy of the electrons and of the period and strength of the magnetic field.

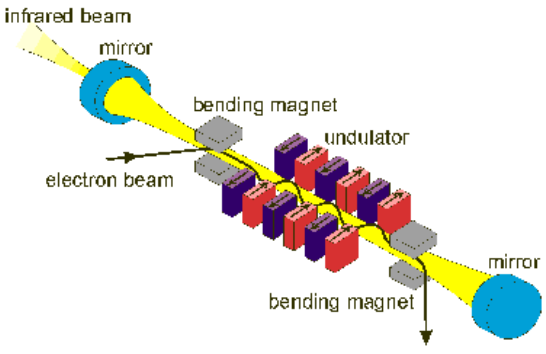

Figure 1.9: Magnetic cavity of the CLIO IR FEL. Two magnetic benders (or electrostatic dipoles) are used to direct the electron beam (in black) into the undulator and extract it towards a beam dump at the exit of the undulator (north and south poles in violet and red, respectively). Under the influence of the alternative magnetic field, the quasi relativistic electrons bundle onto a snacking path which is at the origin of the photon emission. The interaction between the electrons and IR photons (yellow) beams is at the origin of the IR beam amplification.

The temporal structure of the IR FEL shown in Figure 1.10 is induced by that of the electron beam. The CLIO laser produces trains of IR pulses, called macropulses, at 25 Hz. These macropulses are composed of picosecond long pulses at 62.5 MHz. It should be noted that two consecutive picopulses are separated by 16 nanoseconds, which is the order of magnitude of the lifetime of excited vibrational state, typically ranges from picosecond to nanosecond.[42] It is thus conceivable that there is enough time for IVR to proceed between two consecutive pico-pulses. The efficient noncoherent multiple photon absorption process observed with IR FEL may thus not only due to its high intensity, but also to its pulsed structure.[43]

For a given electron energy, continuous tunability can be obtained from λ to 2λ with a relatively constant laser power. The laser mean power is routinely higher than 1 W which corresponds to macropulse (picopulse) energy of 40 mJ (80 μJ). The bandwidth of the IR FEL strongly depends on the laser cavity length. Bandwidth of 10-20 cm^{-1} in the 800-2000 cm^{-1} range is generally used.

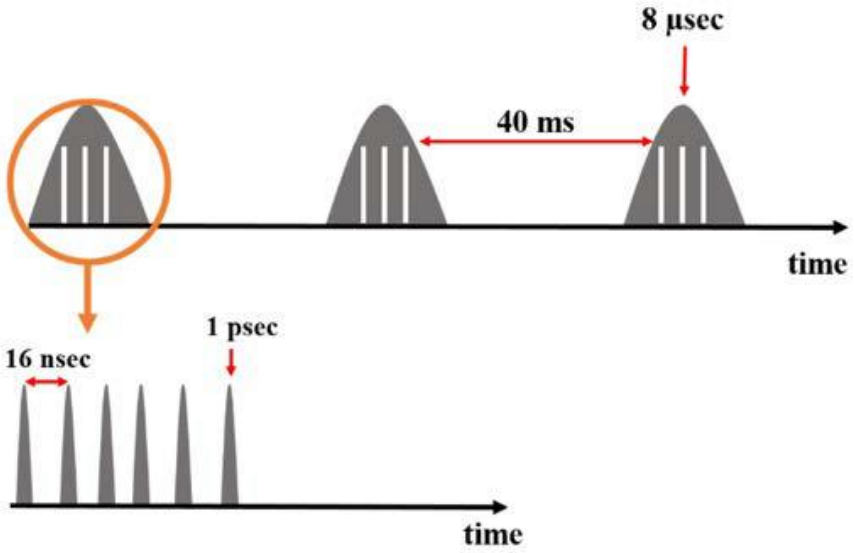

Figure 1.10: Temporal structure of the CLIO IR FEL at Orsay. Trains of pulses (called macropulses) are delivered at 25 Hz as illustrated in the top of the Figure. Each individual macropulse is composed of ~1 pico-second pulses separated by 16 nanoseconds as illustrated in the bottom of the Figure

The operation of the FEL at CLIO started in 1991, and currently, J.-M. Ortega is the in charge of CLIO. Presently, the CLIO FEL is mainly used for IRMPD spectroscopy. The development towards long-wavelength is an important research topic. CLIO has an important characteristic, which could be used for two-photon IRMPD experiments: there are two independent undulators which allow for lasing simultaneously at two different wavelengths.[44] Beside the IRMPD set-ups, there are two others: one uses the IR FEL for Second Harmonic Generation (SHG) experiments for probing adsorption phenomena on surfaces[45] with applications in Electrochemistry.[46] The second experimental set-up couples Atomic Force Microscopy (AFM) with IR CLIO FEL which provides another dimension to AFM. These methods have wide range of applications mainly forthe biological systems such as bacteria[47] and phenomena at the sub-cellular level.[48]

In particular, free electron lasers (FELs) are uniquely placed to carry out IRMPD experiments, given their continuous and wide tunability, as well as high spectral brightness (i.e., peak power > 10 MW). Currently, there are three free electron lasers in the world where IRMPD experiments are routinely carried out: the Free Electron Laser for Infrared eXperiments (FELIX) near Utrecht in the Netherlands,[49] the Centre Infrarouge Laser Orsay (CLIO)[50] near Paris in France and FEL-SUT (Tokyo, Japan). Construction of a similar FEL is under way at the Fritz–Haber Institute (Berlin, Germany). FELIX and CLIO operate as user facilities.

IIA.5. Non-innocent ligands

IIA.5.1. General view

In catalytic system, ligand plays an important role by allowing fine-tuning of reactivity and selectivity through steric or electronic interactions all along the catalytic cycle. However, the optimization of a catalytic system often needs deeper and extensive structural modifications. To date, a ligand mostly known as well characterized closed-shell molecule that shows well defined tasks, and in this prospect, the less defined and intriguing electronic structure of non-innocent ligands (NILs) holds promises as to their use in innovative organometallic catalysis.[51] Numerous non-innocent ligands are known at present and their numbers are increasing each year: new types of ligands are being synthesized and already known ligands are shown to be non-innocent.[52] The word "non-innocent" was initially coined in 1966 in a seminal work done by Jorgensen[53] stating that "ligands are innocent when they allow oxidation states of the central atom to be defined", though the closer definition of what a NIL is not. This statement clearly indicates that NILs are essential molecular scaffolds that are capable to delocalize part of the electron density of the complexes to which they belong. The reasons for this are the higher energy HOMO or low-lying LUMO levels (excluding the lone pair that coordinates to the metal center) of these ligands as compared to those of typical ligands, and NILs will therefore participate in electronic transfer through bonding process.[54] This specificity can enhance the scope of redox events that a metal can perform by overcoming the limitations imparted by its original electronic structure. Since their introduction in the field of organometallic chemistry, NILs and complexes thereof have attracted much attention, mainly devoted to the identification, extensive studies, and rationalization of their unusual electronic properties.[55] However, NILs are now emerging as

synthetically useful and attractive scaffolds with broad and exciting perspectives as their uses could open up the field of reactivity of easily accessible base metals.

IIA.5.2. Structural evolution

Before we start to discuss the term "non-innocent ligand", it is necessary to introduce two terms: *formal oxidation state* and *physical* or *spectroscopic oxidation state*. These two terms are, at first sight, very similar but not identical. The *formal oxidation state* of a given metal ion in a mononuclear coordination compound is commonly defined by "the charge remaining on the metal after all ligands have been removed in their normal, closed-shell configuration – that is with their electron pair".[56] For example, the *formal oxidation state* of the iron in a neutral [Fe(acac)$_3$] (acac = acetylacetonato) is +3, because when calculating the *formal oxidation state*, one removes three acac ligands as usual in their closed-shell anionic form leaving the charge +3 on the metal.

On the other hand, it is sometimes possible to determine the electronic configuration of the metal in the complex directly by various spectroscopic methods. To determine the oxidation state of the metal in iron complexes, for example, it is usual practice to apply ^{57}Fe Mössbauer spectroscopy. By knowing the electronic configuration of the metal in the complex, one can immediately calculate the oxidation state of the metal ion. In 1969 Jörgensen suggested that the oxidation state of the metal ion, which is determined from its known electronic configuration, should be specified as the physical or the spectroscopic oxidation state.[57] A Mössbauer spectrum recorded on [Fe(acac)$_3$] confirms the physical oxidation state of iron to be +3.[58]

Although both, the formal and the physical oxidation state of the iron in our example [Fe(acac)$_3$] were shown to be the same, it is not always the case. In 1966 Balch and Holm reported the reaction of nickel chloride with o-phenylenediamine in aqueous ammonia resulting in the formation of a neutral complex with the "brutto" formula [Ni($C_6H_4(NH)_2)_2$].[59] Which structure corresponds to the given "brutto" formula and which oxidation state has the metal in this complex ?

Let us first apply the rules for determining the formal oxidation state of the nickel. Two "classical" structures can be drawn for this complex,

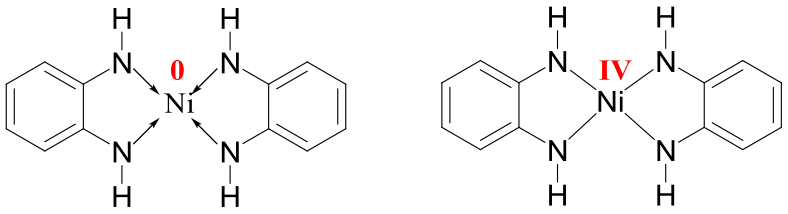

A **B**

Structure **A** comprises two o-benzoquinonediimine neutral ligands, while structure **B** consists of two o-phenylenediamido(2–) dianions. Both ligands are "normal" closed-shell ligands. After removing the ligands in their closed-shell form, we obtain the formal oxidation state of the nickel. For structure **A,** the *formal oxidation state* of the nickel is zero, while for structure **B** we obtain the unusually high *formal oxidation state* +4 (?). Certainly we can speculate that the complex contains two types of the ligand: one o-benzoquinonediimine and one o-phenylenediamido(2–), but several methods, including single crystal X-ray analysis,[60] confirm that the two ligands are identical.

On the other hand, it was shown by various spectroscopic methods and DFT calculations that the electronic configuration of nickel in [Ni($C_6H_4(NH)_2)_2$] and related complexes is d^8 and consequently, the *physical oxidation state* is +2.[61] It is important to note that the *formal oxidation state* of the nickel determined to be 0 or +4, depending on the proposed structure,

does not agree with the *physical oxidation state* being +2. In the example $[Ni(C_6H_4(NH)_s)_2]$ discussed above. If the oxidation state of the nickel is +2 and two coordinated ligands are identical, then both o-phenylenediamine-derived ligands should possess the charge –1. Both ligands in electronic structures **A** and **B** shown above are in their closed-shell forms, while the +2 oxidation state of the nickel forces the two ligands to be open-shell radical monoanions (electronic structure **C**).

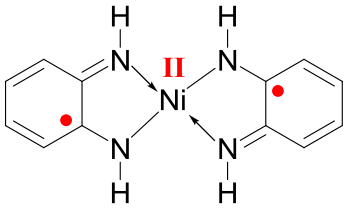

C

Such an electronic structure of $[Ni(C_6H_4(NH)_2)_2]$ was proposed by Balch and Holm in 1966.[59] Ligands that have several, at least two, different oxidation states available at common redox potentials are called non-innocent. Since two redox forms of such ligands are associated through one electron oxidation-reduction process, one redox form of the ligands is "normal" closed-shell, and the other one is therefore open-shell radical. Three redox forms of an o-phenylenediamine derived ligand and their relationship are shown in scheme 1.

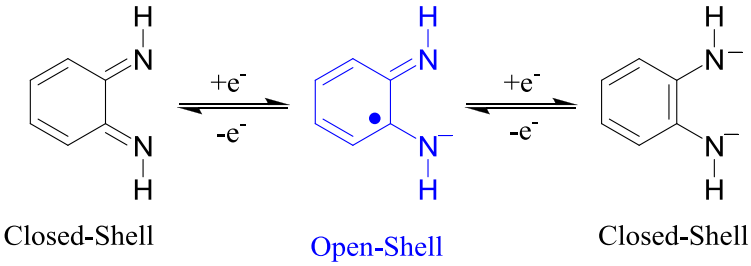

***Scheme 1**: Different redox states of the o-phenylenediamine derived ligand*

Instead, many coordination chemists still prefer to operate with closed-shell ligands and π-back donation schemes, even when the closed-shell terminology is not appropriate any more.

Despite of it the number of articles are increasing every year containing the term "non-innocent". Complexes of transition metals with non-innocent ligands are of particular interest with regard to their electronic structures. Since late transition metals commonly have several oxidation states available, ambiguity of oxidation state determination may arise with transition metal coordinated to the non-innocent ligand. In this Context, It is always been a question on what would be the electronic structure of metal complexes with non-innocent ligands and how the oxidation state of metal atom plays during the catalysis ?.

IIA.5.3. Role of non-innocent ligands in organometallic complexes

Multidentate ligands have the advantage that they can simultaneously increase the electronic density and stabilize the coordination sphere of transition metals. In particular, the pincer-type species, referring a tridentate coordinating ligand framework offers a significant opportunities to play the steric and electronic properties of transition metal complexes.[62] Generally, the side arms of a pincer ligand contain neutral, two-electron Lewis donor moieties (e.g.:PR_2, NR_2, or SR), which are connected through a linker group (mostly CH_2 or O) to a neutral or monoanionic anchoring site (e.g: pyridyl or phenyl group). In the past decade, various research groups have employed such kind of ligands for stabilizing low valent transition metal complexes. For example, Aryl-substituted bis(imino)pyridines,[63] have emerged as a prominent class of ligands due to their ease of synthesis, steric and electronic modularity, and ability to stabilize a range of transition metal and alkali metal ions.[64]

One of major challenges in organomettalic chemistry is to replace noble metals with more common transition metals from the differences in electronic structure on their prominent role in the industrial preparation of many chemicals. A noble metal like platinum often favors two electron redox changes to promote bond making and breaking events. For the base metals, one-electron redox changes occur more frequently and present challenges for controlling

reactivity and stabilizing or maintaining the function of the catalyst. From recent work done by Chirik and co-workers[65], it has been known that the donation of an electron from ligand changes the oxidation state of the metal through and leads in changes in electronic structure occur at the metal. Chelating "non-innocent" ligands[66] in transition metal complexes have more energetically accessible levels that allow redox reactions to change their charge state during catalysis. For example Iron-based bis(imino)pyridine ligamds,[67] [(Ar-PDI)Fe] (Ar-PDI = 2,6-(2,6-$^{i}Pr_2C_6H_3N{=}CMe)_2C_5H_3N$), Sodium amalgam reduction of the ferrous dihalide complexes, (Ar-PDI)FeX_2 furnishes an unusual iron bis(dinitrogen) complex, (Ar-PDI)Fe$(N_2)_2$ (Scheme 2).[65] During the course of the reduction reaction, intermediate four-coordinate iron monohalide compounds, (Ar-PDI)FeX, found to be with quartet (S = 3/2) ground states.[68] Particularly, (Ar-PDI)Fe$(N_2)_2$ is an effective precatalyst for the hydrogenation and hydrosilation of olefins with synthetically useful turnover frequencies at parts per million catalyst loadings in nonpolar media.[65]

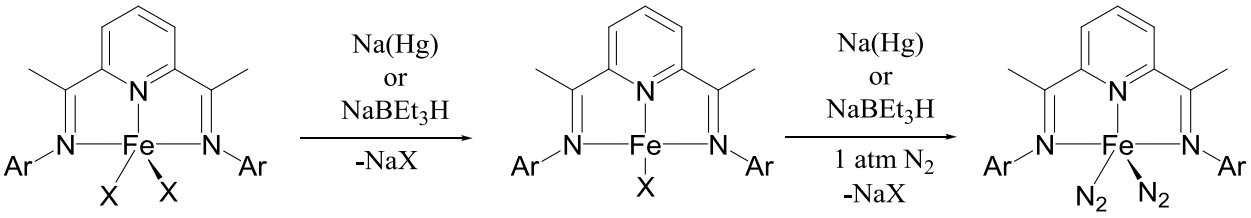

***Scheme 2**: Formation of four (Ar-PDI)FeX coordinated by the reduction of (Ar-PDI)FeX_2*

One interesting feature of (Ar-PDI)Fe$(N_2)_2$ is its NMR spectrum, where resonances are observed over a 15 ppm chemical shift range.[69] Salient features include observation of an imine methyl group centered at 13.61 ppm and a *p*-pyridine resonance at 2.58 ppm (benzene-d_6, 23 °C, 1 atm N_2). These observations suggest energetically accessible S =1 states, an unexpected electronic configuration for an iron(0) center. These observations explained that the bis(imino)pyridine ligand is responsible for the unusual properties in catalysis. It is now well-established that chelates of this type are both chemically,[70] and redox active,[71] potentially

accepting up to three electrons in the conjugated π-system.[72] The ability of bis-(imino)pyridines to serve as electron reservoirs may ultimately prove useful in designing new catalysts or reagents for small molecule activation.[73] The reduction of the terdentate chelate populates molecular orbitals of the bis(imino)pyridine fragment that are anti-bonding with respect to the imine but bonding with respect to the carbon backbone. As a consequence, the N_{imine}–C_{imine} bonds elongate while the C_{imine}–C_{ipso} distances contract.[51] (Scheme 3)

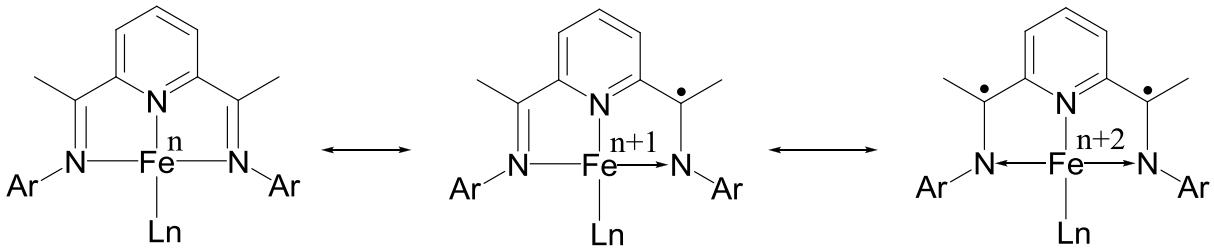

***Scheme 3**: General mesomeric electronic configurations of bis(imino)pyridine in Iron coordinated complexes.*

Along with the Chirik.'s bis(imino)pyridine [NNN]Fe(N_2)$_2$ complex (**I** in Figure 1.11), other research groups have applied different types of ligand systems to stabilize other low valent iron complexes. Danopoulos and co-workers reported a bis(carbene)pyridine ligand stabilizing the bis(dinitrogen)iron [CNC]Fe(N_2)$_2$ complex **II**.[74] (Figure 1.11) (Dipp = 2,6-Diisopropylphenyl in **I** and **II**) It has also been shown that pincer-stabilized iron(0) complexes are the active species in catalytic reactions such as alkene hydrosilylation and asymmetric hydrogenation of ketones and imines by isolating their bis-carbonyl complexes.[75] Recently, Milstein and co-workers demonstrated the non-innocent behavior of bipyridine-based PNN pincer ligands with iron biscarbonyl complexes **III**.[76]

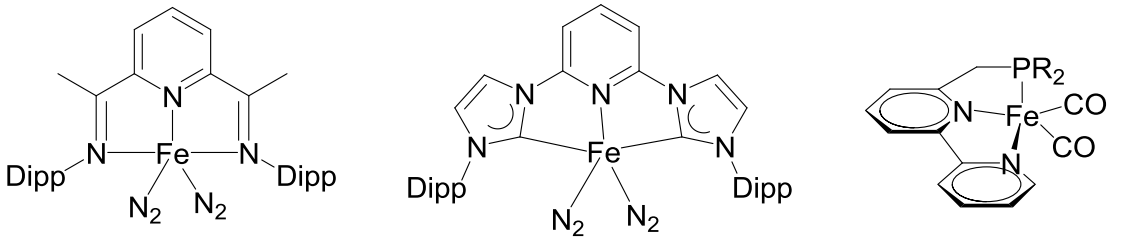

Chirik **2004** (**I**) Danopoulus **2004** (**II**) Milstein **2014** (**III**)

Figure 1.11*: Examples of iron(0) complexes for catalytic applications.*

In addition to their interesting structural features, bis(imino)pyridines based iron complexes emerging high catalytic activity for different reactions such as hydrogenation,[77,78] hydrosilylation,[65,79] and hydroboration,[80] dehydrogenative CH activation,[81] and also proton reduction with a Ni-bis(imino)pyridine complex, alcohol oxidation by Zn- and Cu-salen compounds,[82] and water oxidation by Ru-bipyridine complexes,[83]. Another interesting applications of Ru-bipyridine complexes as photoredox catalyst in crossed [2+2] cycloadditions of acyclic enones,[84,85] and asymmetric alkylation of aldehydes.[86] Stephenson has shown that radical species generated by photoredox catalysis can be intermediates in highly efficient in tin-free radical dehalogenation reactions.[87]

As mentioned, apart from their emerging catalytic applications, it has always been a question on the electronic structure of such metal complexes. In this regards, we have chosen few non-innocent bidentate ligands namely, 2,2'-bipyridine, amide or ester functional group substituted bipyridines, 4,5-diazafluoren-9-one, 1,10-phenanthroline, and bis(imino)pyridine type tridentate ligands to investigate the electronic structure of reduced metal-ligand complex to provide more insights into their catalytic activity.

Part B: Computational Methodology

IIB.1. General View

Many quantum mechanical (QM) methods have been developed over the years. For optimizing the geometry of a molecule and calculating its properties, such as its vibrational spectrum, each method and basis set combination has its own figures of merit. It is thus of interest to recall the main features of the density functional method that used for our study. More detailed descriptions are available in number of books.[88,89]

As an example, a standard method in computational chemistry is "Coupled Cluster including Single and Double excitations, plus a perturbative treatment of connected Triples [CCSD(T)]. It is often used as a reference for quantitative energetics, however it suffers from being computationally very expensive for systems larger than about ten atoms. Density Functional Theory (DFT) is often the choice for calculations on larger systems however it has limitations, e.g. most early functionals fail to describe weakly interacting systems. DFT is still developing at high pace, are the Minnesota series of functional[90] and Grimme's empirical corrections for dispersion.[91] A less intensive alternative is the Hartree-Fock (HF) formalism which provides molecular orbitals, and is a starting point for CCSD(T) (Figure 1.12). Intermediate in complexity is Møller–Plesset perturbation (MP) theory in which second order perturbation theory is used to add to the single HF configuration, the effect of excited configurations in an approximate manner. Understanding the basic theory in each case helps to identify the reasons for successes and drawbacks of each approach. However, there remains the need of calibration on every new system to be studied, i.e. running calculations and then using the end result to determine whether a method and basis set combination is suitable or not.

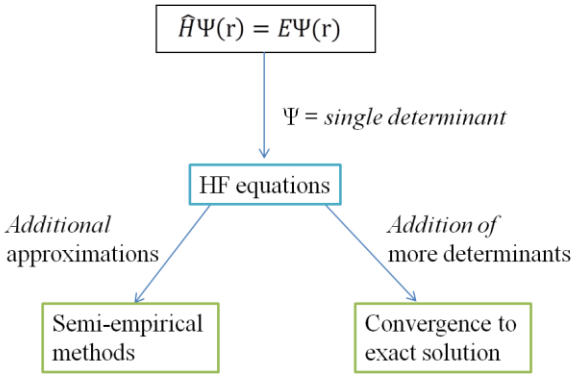

Figure 1.12: The HF model as a starting point for more approximate or more accurate treatments

The following theoretical background was adapted by various books of quantum chemistry and molecular mechanics,[92,93,94] and also scientific articles that will be mentioned in the text. We present the methods and tools used during the thesis work. Unlike classical mechanics, quantum mechanics is probabilistic. Indeed, according to the Heisenberg uncertainty principle, it is impossible to determine the position and velocity of the particle at a given time t simultaneously. However, it is possible to calculate the probability P(r, t) of a particle is in a position r and at given time t. It corresponds to Ψ^2 (r, t), where Ψ (r, t) is the wave function obtained by solving the time dependent Schrödinger equation for a non-relativistic particle:

$$\hat{H}(r,t)\Psi(\mathrm{r},\mathrm{t}) = \mathrm{i}\frac{\partial\,\Psi(r,t)}{\partial t} \tag{1.5}$$

where H(r, t) is the Hamiltonian operator for time dependent system.

In steady state, the Schrödinger equation is

$$\hat{H}\Psi(\mathrm{r}) = E\Psi(\mathrm{r}) \tag{1.6}$$

where E is the energy of the system at a stationary state.

The Hamiltonian operator for poly-electron is written as the sum of kinetic energy (T) and potential energy operators (V):

$$\hat{H} = \hat{T} + \hat{V} \tag{1.7}$$

with

$$\hat{T} = -\sum_{k=1}^{M} \frac{\nabla_k^2}{2M_k} - \sum_{i=1}^{n} \frac{\nabla_i^2}{2} \quad (1.8)$$

where M_k represents the sum of the kinetic energy of nuclei mass *M*, n is number of electrons, and

$$\hat{V} = -\sum_{i=1}^{n}\sum_{k=1}^{M} \frac{Z_k}{R_{i,k}} + \sum_{i=1}^{n}\sum_{j<i} \frac{1}{r_{ij}} + \sum_{k=1}^{M}\sum_{l<k} \frac{Z_k Z_l}{R_{k,l}} \quad (1.9)$$

where representing terms Coulomb electron-nucleus attractions, Coulomb electron-electron and nucleus-nucleus repulsion respectively.

Except for the hydrogen atom and hydrogen-like ions, the exact resolution of the Schrödinger equation is currently impossible because of two electron term. A set of approximation was used to allow closer to exact resolutions of equation (1.6). Few of those and which we have used in this thesis from quantum chemistry are presented below.

IIB.2. Density Functional Theory (DFT)

Density functional theory has become the most popular quantum chemical method over the last two decades.[88,89] The premise behind DFT is that the energy of molecule can be determined from the electron density instead of wave function, hence the name density functional theory comes from the use of functionals of the electron density. DFT has been very popular for calculations in various branches since the 1970's. However, DFT was not considered accurate enough for calculations in quantum chemistry until the 1990's, when the approximations used in the theory were greatly refined to better model the exchange and correlation interactions and computational costs are also relatively low when compared to traditional methods. It solves for the one-electron density of a molecular system, which is

known to contain all information about the electrons of the system. While the electron-nucleus attraction and the Coulombic electron-electron repulsion operators can be readily expressed in terms of the one-electron density, this is true neither for kinetic energy nor for electron-electron exchange interaction energy. Thus the very simple and appealing formal basis of DFT has led to rather complicated developments in order to bring to its present status. Those terms for which there is no simple expression known are globally named the exchange correlation energy, include the effects of quantum mechanical exchange correlation, self-interaction corrections, and the difference of the kinetic energy between a fictitious non-interacting system and the real one. There have been several general levels of increasing complexity to approximately describe the exchange correlation correction. In the local density approximation (LDA), exchange correlation functional is determined solely from the density at concern location, while in the generalized gradient approximation (GGA), the gradient of the density is included in addition to the local density. In hybrid functionals also include some fraction of Hartree-Fock exchange,[95] while the meta-GGA approximation amounts to including terms that depend the kinetic energy in addition to the density and the magnitude of the gradient of the density.

The DFT was developed from the two seminal work by Hohenberg and Kohn, the electronic energy will be completely determined by the density ρ(e). Indeed, Hohenberg and Kohn, inspired by the Thomas-Fermi model showed that the external potential, wherein move of interacting particles are determined by the electron density. Thereby, energy is a density functional

$$E[\rho] = T[\rho] + V_{ee}[\rho] + V_{Ne}[\rho] \tag{1.10}$$

where $T[\rho]$ is the kinetic energy of electrons, $V_{ee}[\rho]$ is Coulomb electron-electron repulsion energy and $V_{Ne}[\rho]$ is Coulomb electron-nucleus attraction energy.

$$V_{Ne}[\rho] = -\sum_a^N \int \frac{Z_a(R_a)\rho(r)}{|R_a - r|} dr \quad (1.11)$$

T[ρ] + V_{ee}[ρ] is an unknown function that is called the Hohenberg-Kohn function (F_{HK}[ρ]). The electron-electron Coulomb repulsion is separated into two terms:

$$V_{ee}[\rho] = J[\rho] + E_{ncl}[\rho] \quad (1.12)$$

where J[ρ] is the Coulomb term with the expression,

$$J[\rho] = \frac{1}{2} \int \int \frac{\rho(r_1)\rho(r_2)}{r_{12}} dr_1 dr_2 \quad (1.13)$$

and E_{ncl}[ρ] is an unconventional contribution including self-interaction correction exchange and electron correlation but has no known analytical writing.

Unlike the Hartree-Fock method, the Coulomb interaction of an electron with itself can not compensate exactly with the exchange interaction. The conventional DFT therefore has an error of self interaction. This is usually negligible, but it can become substantial for specific molecular systems.

The functional of Hohenberg and Kohn $F_{HK}[\rho]$ then as an expression:

$$F_{HK}[\rho] = T[\rho] + J[\rho] + E_{ncl}[\rho] \quad (1.14)$$

The second theorem of Hohenberg and Kohn states that the functional E[ρ] gives the lowest energy only if the density ρ is the same as that of the ground state. Thus, this density can be determined using the variational principle:

$$E[\rho] \geq E_0[\rho_0] \quad (1.15)$$

The limit of Hohenberg and Kohn model is that the specific form of F_{HK}[ρ] is not known. However, Kohn and Sham proposed a new expression of F_{HK}[ρ], denoted by F[ρ],

$$F[\rho] = T_s[\rho] + J[\rho] + E_{XC}[\rho] \quad (1.16)$$

where $T_s[\rho]$ is the kinetic energy of the fictional system consists of particles without interaction and $E_{XC}[\rho]$ is the exchange-correlation energy which is expressed as

$$E_{XC}[\rho] = (T[\rho] - T_s[\rho]) + (V_{ee}[\rho] - J[\rho]) \quad (1.17)$$

The functional $E_{XC}[\rho]$, the exact analytic expression is unknown, is generally split into two separate terms, one is functional exchange which is associated with the electron-electron interaction energy of same spin $E_X[\rho]$ and the other is the correlation function $E_C[\rho]$ which is associated with the opposite spin electron-electron interaction:

$$E_{XC}[\rho] = E_X[\rho] + E_C[\rho] \quad (1.18)$$

Approximate writings $E_X[\rho]$ and $E_C[\rho]$ should be introduced to calculate these terms. These approximations to estimate $E_{XC}[\rho]$, which thus introduce errors in this exact theory, depend on the class of functional considered, and will also be directly related to the accuracy of functional. Articles and reviews testing the functional quality have been published.[96] Minimizing energy amounts to solving the Kohn-Sham equations to determine $\Psi_i(r)$ called Kohn-Sham orbital and ε_i is the energy associated Kohn-Sham orbital. The iterative process allows the resolution of this set of equations from test functions. The density $\rho(r)$ of the fictitious system imposed equal to that of the real system, is expressed by definition from $\Psi_i(r)$ orbital

$$\rho(r) = \sum_{i=1}^{n} |\Psi_i(r)|^2 \quad (1.19)$$

In the work presented in this thesis, all theoretical results were obtained using calculations by DFT methods. In general, DFT methods are used to find low energy structures and their energies from optimized geometries and to perform single point energy calculations if necessary with higher basis sets. Vibrational frequencies are also obtained at the optimized geometries.

IIB.2.1. Local Density Approximation (LDA)

This approach introduces the model system on which virtually all approximate exchange correlation functionals are based. At the center of this model is the idea of a hypothetical *uniform electron gas*. This approximation is a good physical model when studying an atom or molecule in which the electron density varies slowly as simple metals such as sodium. The shape of the functional exchange-correlation energy is known exactly

$$E_{XC}^{LDA}[\rho] = \int \rho(\vec{r})\varepsilon_{XC}\big(\rho(\vec{r})\big)d\vec{r} \tag{1.20}$$

The exchange part ε_X derived by the relationship of Bloch and Dirac

$$\varepsilon_X(\rho(\vec{r}))= -\frac{3}{4}\sqrt[3]{\frac{3\rho(\vec{r})}{\pi}} \tag{1.21}$$

The analytical expression of the correlation energy is not known. However, highly accurate numerical quantum Monte-Carlo simulations of the homogeneous electron gas are available from the work of Ceperly and Alder, 1980. Several expressions of $\varepsilon_C(\rho(\vec{r}))$ have been proposed in the literature.[97] Taking into account of spin polarization, the electronic density expression as

$$\rho(\vec{r}) = \rho_\alpha(\vec{r}) + \rho_\beta(\vec{r}) \tag{1.22}$$

In the simple case, i.e. when $\rho_\alpha(\vec{r})$ equals to $\rho_\beta(\vec{r})$, there are spin-off. But in cases where $\rho_\alpha(\vec{r})$ is different from $\rho_\beta(\vec{r})$, then there is spin polarization. This effect is included in the correlation energy is estimated by a spin polarization parameter:

$$\xi = \frac{\rho_\alpha(\vec{r}) - \rho_\beta(\vec{r})}{\rho(\vec{r})} \tag{1.23}$$

Then, there is the Local Spin density approximation (LSDA). The equation (1.20) becomes

$$E_{XC}^{LSDA}\big[\rho_\alpha, \rho_\beta\big] = \int \rho(\vec{r})\varepsilon_{XC}\left(\rho_\alpha(\vec{r}) + \rho_\beta(\vec{r})\right)d\vec{r} \tag{1.24}$$

The functional LDA does not deal with non-local correlation and actually the electron gas is not homogeneous. Therefore, other functional have been constructed to take account of these two effects.

IIB.2.2. The Generalized Gradient Approximation (GGA)

In this generation of functional, there is not only to consider the electron density $\rho(\vec{r})$ at a particular point in space $\vec{r}$ but also its gradient ($\nabla\rho(\vec{r})$) to consider the inhomogeneity of the electron density. Equation (1.24) then becomes:

$$E_{XC}^{GGA}[\rho_\alpha, \rho_\beta] = \int f(\rho_\alpha, \rho_\beta, \nabla\rho_\alpha, \nabla\rho_\beta) d\vec{r} \quad (1.25)$$

However, the GGA functional are non-local approximation methods because they depend on the density and its first derivatives at a given point only.

The exchange functional of GGA usually has to first term exchange functional of LDA plus a corrective term:

$$E_X^{GGA} = E_X^{LDA} - \sum_\sigma \int F(s_\sigma) \rho_\sigma^{\frac{4}{3}}(\vec{r}) d\vec{r} \quad (1.26)$$

the function F is the *reduced density gradient* for spin σ

$$s_\sigma = \frac{|\nabla\rho_\sigma(\vec{r})|}{\rho_\sigma^{\frac{4}{3}}(\vec{r})} \quad (1.27)$$

s_σ is to be understood as a local inhomogeneity parameter.

The exchange functionals of GGA are coupled with the correlation functional, knowing that only a few combinations are used. Possible corrections for exchange functional, that we find the most used Becke[98] and the Perdew, Burke and Ernzerhof.[99] Regarding the correlation functional, Lee, Yang and Parr[100] and Perdew[101] are most commonly used to my knowledge.

IIB.2.3. Meta-GGA functional

Meta-GGA functional, which are an extension of GGA functional depend more explicitly the Laplacian of the spin density $\nabla^2\rho_\sigma(\vec{r})$ or the density of kinetic energy $\tau_\sigma(\vec{r})$.[102] There are several possible definitions of kinetic energy density including:

$$\tau_\sigma(r) = \frac{1}{2}\sum_i |\nabla\Psi_i(r)|^2 \quad (1.28)$$

Compared to GGA, meta-GGA have a semi-local density dependence, its first derivatives and orbital Kohn-Sham and at a given point in an interval around this point.

IIB.2.4. Hybrid functional

Hybrid functional were built to correct the mistake of self-interaction and to better address the non-local correlation phenomena due to the approximations made in classical functionals, LDA and GGA. Indeed, by the construction, these two classical functionals, non-local correlations cannot take into account such as van der Waals interactions, and they lead to an electronic on-shoring. To consider these non-local correlations explicitly, Becke introduced hybrid functional; part of the energy exchange of exact Hartree-Fock model is introduced in the energy exchange and correlation of the DFT.[103] The expression of exchange correlation of energy as

$$E_{XC} = E_{XC}^{DFT} + a_0(E_X^{exact} - E_X^{DFT}) \quad (1.29)$$

The parameter a_0 can be set by theoretically or using experimental data such as atomization energies, ionization potentials or proton affinities. The most popular hybrid functional is known as B3LYP which stands for Becke three parameter Lee-Yang-Parr and owns ~20% of HF exchange.[100,103]

The density functional used in the thesis to obtain results presented are B3LYP, CAM-B3LYP, LC-BLYP (hybrid GGA) functional, M062X (hybrid meta-GGA) functional and ωB97X-D.

IIB.2.5. Long-range Corrected functional

In DFT, electronic states are usually determined by solving the nonlinear Kohn-Sham equation with an exchange-correlation density functional. The most remarkable characteristic of DFT is the exchange-correlation energy part that is approximated by a one-electron potential functional. Hence, calculated DFT results depend on the form of this exchange-correlation functional. The uniform addition of a part of the exact Hartree-Fock exchange model can reduce only partial self-interaction error. Thus, another functional category was developed, it is long range corrected functional (Range-Separated Hybrid. RSH).[104] Unlike in conventional hybrid functional, the percentage of Hartree-Fock exchange will increase along with the inter-electronic distance. This growth will be governed by the attenuation parameter, as shown by the expression of the electronic repulsion operator

$$\frac{1}{r_{12}} = \frac{\mathrm{erf}\,(\omega r_{12})}{r_{12}} + \frac{1-\mathrm{erf}\,(\omega r_{12})}{r_{12}} \qquad (1.30)$$

where erf is the Gaussian function error and $r_{12} = |r_1 - r_2|$. The ω parameter defines the velocity at which the value of 1 is reached by this error function, so more ω parameter will be the more the transition from the Kohn-Sham exchange to the exact Hartree-Fock exchange. The equation (1.30) was generalized by Yanai et al. introducing two new α and β parameters[105]

$$\frac{1}{r_{12}} = \frac{\alpha+\beta\,\mathrm{erf}\,(\omega r_{12})}{r_{12}} + \frac{1-[\alpha+\beta\,\mathrm{erf}(\omega r_{12})]}{r_{12}} \qquad (1.31)$$

such that $0\leq\alpha+\beta\leq1$, $0\leq\alpha\leq1$ and $0\leq\beta\leq1$

There are different approaches to account dispersion effects that are missing in the DFT. Among them, (i) certain functional explicitly include a term of nonlocal dispersion, (ii) other are set as the functional Minnesota, and (iii) Another approach is to add a term empirical dispersion patch. The discussion in this section is centered on the point (iii). The functional that we used this correction is ωB97X-D.

Grimme has proposed a form of correction for the treatment of missing dispersion effects in the DFT and is currently the most used. This correction is made by adding empirical corrective terms depending on the number of atoms N, the dispersion coefficient for the pair of atoms i and j is C_6^{ij}, the inter-atomic distance R_{ij}, a factor s_6 scale and a damping function $f_{dmp}(R_{ij})$

Such that

$$E_{DFT-D} = E_{KS-DFT} + E_D \tag{1.32}$$

Where E_D is the dispersion energy and:

$$E_D = -s_6 \sum_{i=1}^{N-1} \sum_{j=i+1}^{N} \frac{C_6^{ij}}{R_{ij}^6} f_{dmp}(R_{ij}) \tag{1.33}$$

With

$$f_{dmp}(R) = \frac{1}{1+ e^{-\alpha(\frac{R}{R_0}-1)}} \tag{1.34}$$

α is a parameter, and R_0 is the sum of the atomic radii Van der Waals.[106]

1B.3 Basis Sets

All of the methods described above rely on a representation of the one-electron wave functions (molecular orbitals) or density. Development as a linear combination of predefined basis functions is used nearly universally, and Gaussian basis functions are by far the most

common. A molecular orbital is thus described as a linear combination of Gaussian basis functions whose coefficients are determined using the iterative self-consistent field method (SCF)[88,89]. Since individual Gaussians are not good models of atomic orbitals, linear combination of Gaussians are used instead, often with predefined coefficients for part of them (called contracted Gaussians). Several series of basis sets of varying sophistication have been developed. For light main group elements, the most prominent series are those of Pople *et al*.[107] and of Dunning *et al*.[108]

1B.3.1. Atom-Centered Basis Sets

Basis functions are used to create the atomic orbitals (AO) or molecular orbitals and are usually expanded as a linear combination of such functions with the coefficients to be determined. These basis functions can be classified into two main types:

- Slater-type orbitals, also called STOs, have the exponential dependence: $e^{-\zeta r}$ and are very close in their mathematical expression to the real AO:

$$\eta^{STO} = Nr^{n-1}e^{-\zeta r}Y_{lm}(\Theta,\Phi) \qquad ()$$

  where N is a factor of normalization, ζ is the exponent. r, Θ and Φ are spherical coordinates and Y_{lm} is the angular momentum part (function describing the shape). Finally n, l and m are the classical quantum numbers: principal, angular momentum and magnetic, respectively.

- Gaussian-type orbitals, also known as GTOs, which have the exponential dependence:$e^{-\alpha r2}$:

$$\eta^{GTO} = Nx^l y^m z^n e^{-\alpha r2} \qquad ()$$

  where N is, as previously, a normalization factor, x, y and z are Cartesian coordinates.

Linear representations of one-electron functions are usually adopted, and these combinations are often called *contracted Gaussians*:

$$f(r) = \sum_{\mu=1}^{p} c_\mu \varphi_\mu(r)$$

Despite the fact that, STOs reproduce much better the wave function in the proximity of the nuclei, their use has become less and less frequent in favor of GTOs, for which the calculation of multi-center two electron integrals is essentially simpler.

Some of the terms used to describe localized atom-centered basis sets:

1B.3.1.1. Minimal Basis Set

The minimal (or minimum) basis[109] set is one in which, a single basis function is used for each orbital on each free atom. However, each atom in the second period of the periodic table would have basis functions of p type which are added to the basis functions corresponding to the 1s and 2s orbitals of the free atom. So, a minimal set consists of a 1s function for hydrogen and 1s, 2s, and 2p (five functions: two s functions and three p functions) for Li. . . Ne atoms. Minimal basis sets are known to give surprisingly good results for geometry searches but are large contaminated in energy calculations, however they are much cheaper than their larger counterparts.

1B.3.1.2. Double-Zeta (DZ) and Triple-Zeta (TZ) Basis Set

The double-zeta basis set is obtained by considering two basis functions for each atomic orbital of the occupied shells.[109] So, replacing each STO of a minimal basis set by two basis functions differ in their orbital exponents ζ (zeta). For instance, 2 functions for H or He, 10 functions for Li. . . Ne, and 18 functions for Na. . . Ar. The triple-zeta is the same as double-zeta but three basis functions differ in their orbital exponents are here applied.

1B.3.1.3. Split-Valence (SV) Basis Set

Since the valence electrons take principally part in the bonding, it is also common to represent valence orbitals by more than one basis function (each of which can in turn be composed of a fixed linear combination of primitive Gaussian functions). This basis sets are called split-valence basis and it uses generally two STOs for each valence atomic orbital and only one STO for each inner-shell atomic orbital.[110] Since the different orbitals of the split have different spatial extents, the combination allows the electron density to adjust its spatial extent appropriate to the particular molecular environment.

1B.3.1.4. Polarization (P) Basis Functions

To give additional flexibility to the description of molecular orbitals (MOs), polarization functions[111] can be added where for example a p-function is added to light atoms (hydrogen and helium). Similarly, d-type functions can be added to a basis set with valence p orbitals, and f-type functions to a basis set with d-type orbitals, and so on. These are auxiliary functions with one additional node, and are denoted by an asterisk,∗. Two asterisks, **, indicate that polarization functions are also added to light atoms (hydrogen and helium).

1B.3.1.5. Diffuse Basis Functions

Another common addition to basis sets is the addition of diffuse functions,(32; 33) denoted by a plus sign,'+'. They are formed by the addition of four highly diffuse functions (s,p_x,p_y,p_z) on each non-hydrogen atom. Two plus signs, ++, indicate that a highly diffuse s functions are also added to light atoms (hydrogen and helium). A highly diffuse function is one with a very small orbital exponent. This type of addition is so applicable for anions and compounds with lone pairs of electrons in order to have significant electron density at large distances from the nuclei and improve the accuracy of the basis.

We have used both series, at the valence double ζ level with various types of polarization functionals and also diffuse functionals in the case of anions. In particular, the polarized basis set 6-31G (d) and a basis set polarization and diffusion 6-31+G (d,p), split valency basis set Def2-SVP and LANL2DZ which includes the effective core potential term.

All computational results present in this thesis are obtained using the Gaussian09 software Package.[112] Structure display and manipulation were made using the Chemcraft software.

II. References

[1]. R. C. Dunbar, *Int. J. Mass spectrom.* **2000**, *200*, 571–589.

[2]. M. A. Duncan, *Int. J. Mass spectrom.* **2000**, *200*, 545–569.

[3]. P. A. Remes, G. L. Glish, *Int. J. Mass spectrom.* **2007**, *265*, 176–181.

[4]. M. B. Comisarow, A. G. Marshall, *J. Mass Spectrom.* **1996**, *31*, 586–587.

[5]. (a) A. G. Marshall, *Int. J. Mass spectrom.* **2000**, *200*, 331–356; (b) A. G. Marshall, C. L. Hendrickson, G. S. Jackson, *Mass Spectrom. Rev.* **1998**, *17*, 1–35; (c) I. J. Amster, *J. Mass Spectrom.* **1996**, *31*, 1325–1337.

[6]. A. Marshall, C. Hendrickson, G. S. Jackson, *Mass Spectrom. Rev.* **1998**, *17*, 1–35.

[7]. J. M. Bakker, T. Besson, J. Lemaire, D. Scuderi, P. Maitre, *J. Phys. Chem. A* **2007**, *111*, 13415–13424

[8]. J. E. P. Syka, J. J. Coon, M. J. Schroeder, J. Shabanowitz, D. F. Hunt, *Proc. Natl. Acad. Sci*. U. S. A., **2004**, *101*, 9528–9533.

[9]. V. G. Voinov, M. L. Deinzer, D. F. Barofsky, *Anal. Chem*., **2009**, *81*, 1238–1243.

[10]. T. Baba, J. L. Campbell, J. C. Y. Le Blanc, J. W. Hager, B. A. Thomson, *Anal. Chem*., **2015**, *87*, 785–792.

[11]. G. C. McAlister, D. Phanstiel, D. M. Good, W. T. Berggren, J. J. Coon, *Anal. Chem*., **2007**, *79*, 3525–3534.

[12]. R. A. Zubarev, N. L. Kelleher, F. W. McLafferty, *J. Am. Chem. Soc*., **1998**, *120*, 3265–3266.

[13]. H. J. Cooper, K. Hakansson, A. G. Marshall, *Mass Spectrom. Rev*., **2005**, *24*, 201–222.

[14]. K. Breuker, H. B. Oh, B. A. Cerda, D. M. Horn, F. W. McLafferty, *Eur. J. Mass Spectrom*., **2002**, *8*, 177–180.

[15]. R. A. Zubarev, K. F. Haselmann, B. A. Budnik, F. Kjeldsen, F. Jensen, *Eur J Mass Spectrom.* **2002**, *8*, 337-349.

[16]. K. Hakansson, M. R. Emmett, C. L. Hendrickson, A. G. Marshall, *Anal Chem*, **2001**, *73*, 3605-3610.

[17]. J. E. P. Syka, J. J. Coon, M. J. Schroeder, J. Shabanowitz, D. F. Hunt, *Proc. Natl. Acad. Sci*. U. S. A., **2004**, *101*, 9528–9533.

[18]. G. Hart-Smith, *Analytica Chimica Acta*, **2014**, *808*, 44–55

[19]. (a) G. C. McAlister, W. T. Berggren, J. Griep-Raming, S. Horning, A. Makarov, D. Phanstiel, G. Stafford, D. L. Swaney, J. E. P. Syka, V. Zabrouskov, J. J. Coon, *J. Proteome*

Res., **2008**, *7*, 3127–3136. (b) Y. O. Tsybin, L. Fornelli, C. Stoermer, M. Luebeck, J. Parra, S. Nallet, F. M. Wurm, R. Hartmer, *Anal. Chem*., **2011**, *83*, 8919–8927.

[20]. H. J. Cooper, K. Hakansson, A. G. Marshall, *Mass Spectrom. Rev*., **2005**, *24*, 201–222.

[21]. R. L. Kelleher, R. A. Zubarev, K. Bush, B. Furie, B. C. Furie, F. W.McLafferty, C. T. Walsh, *Anal. Chem*., **1999**, *71*, 4250–4253.

[22]. K. Hakansson, H. J. Cooper, M. R. Emmett, C. E. Costello, A. G. Marshall, C. L. Nilsson, *Anal. Chem*., **2001**, *73*, 4530–4536.

[23]. E. Mirgorodskaya, P. Roepstorff, R. A. Zubarev, *Anal. Chem*., **1999**, *71*, 4431–4436.

[24]. S. D. H. Shi, M. E. Hemling, S. A. Carr, D. M. Horn, I. Lindh, F. W. McLafferty, *Anal. Chem*., **2001**, *73*, 19–22.

[25]. A. Stensballe, O. N. Jensen, J. V. Olsen, K. F. Haselmann, R. A. Zubarev, *Rapid Commun. Mass Spectrom*., **2000**, *14*, 1793–1800.

[26]. (a) J. T. Adamson, K. Hakansson, *Anal. Chem*., **2007**, *79*, 2901–2910; (b) L. Han, C. E. Costello, *J. Am. Soc. Mass Spectrom*., **2011**, *22*, 997–1013.

[27]. P. F. James, M. A. Perugini, R. A. J. O'Hair, *J. Am. Soc. Mass Spectrom*., **2008**, *19*, 978–986.

[28]. (a) W. A. Donald, R. D. Leib, J. T. O'Brien, A. I. S. Holm, E. R. Williams, *Proc. Natl. Acad. Sci*. U. S. A., **2008**, *105*, 18102–18107. (b) W. A. Donald, R. D. Leib, J. T. O'Brien, E. R. Williams, *Chem.–Eur. J*., **2009**, *15*, 5926–5934 (c) W. A. Donald, M. Demireva, R. D. Leib, M. J. Aiken, E. R. Williams, *J. Am. Chem. Soc*., **2010**, *132*, 4633–4640.

[29]. D. Asakawa, E. D. Pauw, *J. Am. Soc. Mass Spectrum*., **2016**, *27*, 1165-1175.

[30]. R. L. Woodin, D. S. Bomse, J. L. Beauchamp, *J. Am. Chem. Soc*., **1978**, *100*, 3248–3250.

[31]. M. A. Odeneye, A. Stace, *Phys. Chem. Chem. Phys*., **2005**, *7*, 998–1004.

[32]. L. Yeh, M. Okumura, J. D. Myers, J. M. Price, Y. T. Lee, *J. Chem. Phys*., **1989**, *91*, 7319–7330.

[33]. J. Oomens, B. G. Sartakov, G. Meijer, G. Von Helden, *Int. J. Mass spectrom.* **2006**, *254*, 1–19.

[34]. R. L. Woodin, D. S. Bomse, J. L. Beauchamp, *J. Am. Chem. Soc.* **1978**, *100*, 3248–3250.

[35] E. R. Grant, M. J. Coggiola, Y. T. Lee, P. A. Schulz, S. Sudbo Aa, Y. R. Shen, *In State-to-State Chemistry, Am. Chem. Soc*, **1977**, *56*, 72–86.

[36]. J. G. Black, E. Yablonovitch, N. Bloembergen, S. Mukamel, *Phys. Rev. Lett.* **1977**, *38*, 1131–1134.

[37]. G. von Helden, I. Holleman, G. Meijer, B. Sartakov, *Opt. Express* **1999**, *4*, 46–52.

[38]. (a) P. Parneix, M. Basire, F. Calvo, *J. Phys. Chem. A*, **2013**, *117*, 3954; (b) F. Calvo, C. Falvo, P. Parneix, *J. Phys. Chem. A*, **2014**, *118*, 5427–5436.

[39]. L. R. Elias, W. M. Fairbank, J. M. J. Madey, H. A. Schwettman, T. I. Smith, *Phys. Rev. Lett.* **1976**, *36*, 717–720.

[40]. D. A. G. Deacon, L. R. Elias, J. M. J. Madey, G. J. Ramian, H. A. Schwettman, T. I. Smith, *Phys. Rev. Lett.* **1977**, *38*, 892–898.

[41]. J. M. Ortega, F. Glotin, R. Prazeres, J. P. Berthet, A. Dazzi, *Appl. Phys. Lett.* **2012**, *101*. 141117.

[42]. (a) A. Callegari, U. Merker, P. Engels, H. K. Srivastava, K. K. Lehmann, G. Scoles, *J. Chem. Phys.* **2000**, *113*, 10583; (b) P. M. Felker, A. H. Zewail, *J. Chem. Phys.* **1985**, *82*, 2961.

[43]. K. K. Lehmann, G. Scoles, B. H. Pate, *Annu. Rev. Phys. Chem.* **1994**, *45*, 241–274.

[44]. R. Prazeres, F. Glotin, C. Insa, D. A. Jaroszynski, J. M. Ortega, *Eur. Phys. Journal D* **1998**, *3*, 87–93.

[45]. O. Pluchery, C. Humbert, M. Valamanesh, E. Lacaze, B. Busson, *Phys.Chem.Chem.Phys.* **2009**, *11*, 7729–7737.

[46]. F. Vidal, A. Tadjeddine, C. Humbert, L. Dreesen, A. Peremans, P. A. Thiry, B. Busson, *J. Electroanal. Chem.* **2012**, *672*, 1–6.

[47]. A. Dazzi, R. Prazeres, E. Glotin, J. M. Ortega, *Opt. Lett.* **2005**, *30*, 2388–2390.

[48]. C. Policar, J. B. Waern, M. A. Plamont, S. Clede, C. Mayet, R. Prazeres, J. M. Ortega, A. Vessieres, A. Dazzi, *Angew. Chem.-Int. Ed.* **2011**, *50*, 860–864.

[49]. D. Oepts, A. F. G. van der Meer, P. W. van Amersfoort, *Infrared Phys. Technol.*, **1995**, *36*, 297–308.

[50]. J. Lemaire, P. Boissel, M. Heninger, G. Mauclaire, G. Bellec, H. Mestdagh, A. Simon, S. L. Caer, J. M. Ortega, F. Glotin, P. Maitre, *Phys. Rev. Lett.*, **2002**, *89*, 273002.

[51]. S. C. Bart, K. Chlopek, E. Bill, M. W. Bouwkamp, E. Lobkovsky, Frank Neese, K. Wieghardt, P. J. Chirik, *J. Am. Chem. Soc.* **2006**, *128*, 13901–13912.

[52]. (a) M. D. Ward, J. A. McCleverty, *J. Chem. Soc., Dalton Trans.* **2002**, 275–288; (b) A. Vlcek Jr., *Coord. Chem. Rev.* **2002**, *230*, 225–242; (c) P. Chaudhuri, K. Wieghardt, *Prog.*

Inorg. Chem. **2001**, *50*, 151–216. (d) C. G. Pierpont, *Coord. Chem. Rev.* **2001**, *216–217*, 99–125. (e) M. M. Conradie, J. Conradie, A. Ghosh, *J. Inorg. Biochem.* **2006**, *100*, 620–626.

[53]. K. Jorgensen, *Coord. Chem. Rev.* **1966**, *1*, 164–178.

[54]. S. K. Szilagyi, B. S. Lim, T. Glaser, R. H. Holm, B. Hedman, K. O. Hodgson, E. I. Solomon, *J. Am. Chem. Soc.* **2003**, *125*, 9158–9169.

[55]. (a) W. Kaim, *Inorg. Chem.* **2011**, *50*, 9752–9765.; (b) M. D. Ward, J. A. McCleverty, *J. Chem. Soc., Dalton Trans.* **2002**, 275–288; (c) P. Chaudhuri, C. N. Verdani, E. Bill, E. Bothe, T. Weyhermüller, K. Wieghardt, *J. Am. Chem. Soc.* **2001**, *123*, 2213–2223; (d) C. G. Pierpont, *Coord. Chem. Rev.* **2001**, *216–217*, 99–125.

[56]. L. S. Hegedus, *Transition Metals in the Synthesis of Complex Organic Molecules*; University Science Books: Mill Valley, CA, **1994**, p. 3.

[57]. C. K. Jörgensen, *Oxidation Numbers and Oxidation States*, Springer: Heidelberg, Germany, **1969**.

]58]. L. M. Epstein, *J. Chem. Phys.* **1962**, *36*, 2731–2737.

]59]. A. L. Balch, R. H. Holm, *J. Am. Chem. Soc.* **1966**, 5201–5209.

]60]. G. S. Hall, R. H. Soderberg, *Inorg. Chem.* **1968**, *7*, 2300–2303.

]61] (a) D. Herebian, E. Bothe, F. Neese, T. Weyhermüller, K. Wieghardt, *J. Am. Chem. Soc.* **2003**, *125*, 9116–9128. (b) V. Bachler, G. Olbrich, F. Neese, K. Wieghardt, *Inorg. Chem.* **2002**, *41*, 4179–4193. (c) D. Herebian, K. E. Wieghardt, F. Neese *J. Am. Chem. Soc.* **2003**, *125*, 10997–11005.

[62]. (a) D. Morales-Morales, C. M. Jensen, *The Chemistry of Pincer Compounds; Elsevier*: Amsterdam, **2007**. (b) G. van Koten, D. Milstein, *Organometallic Pincer Chemistry; Springer*: Berlin, **2013**. (c) K. J. Szabo, O. F. Wendt, *Pincer and Pincer-Type Complexes: Applications in Organic Synthesis and Catalysis*; Wiley-VCH Verlag & Co.: Weinheim, Germany, **2014.**

[63]. S. D. Ittel, L. K. Johnson, M. Brookhart, *Chem. Rev*. **2000**, *100*, 1169−1203

[64]. I. J. Blackmore, V. C. Gibson, P. B. Hitchcock, C. W. Rees, D. J. Williams, A. J. P. White, *J. Am. Chem. Soc*. **2005**, *127*, 6012−6020.

[65]. S. C. Bart, E. Lobkovsky, P. J. Chirik, *J. Am. Chem. Soc*. **2004**, *126*, 13794−13807.

[66]. C. Bolm, *Nat. Chem*,.**2009** *1*, 420.

[67]. (a) S. C. Bart, K. Chłopek, E. Bill, M. W. Bouwkamp, E. Lobkovsky, F. Neese, K. Wieghardt, P. J. Chirik, *J. Am. Chem. Soc*. **2006**, *128*, 13901−13912; (b) Q. Knijnenburg, S. Gambarotta, P. H. M. Budzelaar, *Dalton Trans*. **2006**, 5442−5448.

[68]. M. W. Bouwkamp, S. C. Bart, E. J. Hawrelak, R. J. Trovitch, E. Lobkovsky, P. J. Chirik, *Chem. Commun.* **2005**, 3406−3408.

[69]. S. C. Bart, K. Chłopek, E. Bill, M. W. Bouwkamp, E. Lobkovsky, F. Neese, K. Wieghardt, P. J. Chirik, *J. Am. Chem. Soc*. **2006**, *128*, 13901−13912.

[70]. (a) M. W. Bouwkamp, E. Lobkovsky, P. J. Chirik, *Inorg. Chem.* **2006**, *45*, 2−5; (b) I. Sugiyama, S. Korobkov, S. Gambarotta, A. Mueller, P. H. M. Budzelaar, *Inorg. Chem.* **2004**, *43*, 5771−5779; (c) J. Scott, S. Gambarotta, I. Korobkov, P. H. M. Budzelaar, *J. Am. Chem. Soc.* **2005**, *127*, 13019−13029; (d) T. K. Kooistra, D. G. H. Hetterscheid, E. Schwartz, Q. Knijnenburg, P. H. M. Budzelaar, A. W. Gal, *Inorg. Chim. Acta* **2004**, *357*, 2945−2952; (e) H. Sugiyama, G. Aharonian, S. Gambarotta, G. P. A. Yap, P. H. M. Budzelaar, *J. Am. Chem. Soc*. **2002**, *124*, 12268−12274; (f) D. Reardon, F. Conan, S. Gambarotta, G. Yap, Q. Y. Wang, *J. Am. Chem. Soc.* **1999**, *121*, 9318−9325; (g) M. Bruce, V. C. Gibson, C. Redshaw, G. A. Solan, A. J. P. White, D. J. Williams, *Chem. Commun.* **1998**, 2523−2524.

[71]. (a) P. H. M. Budzelaar, B. de Bruin, A. W. Gal, K. Wieghardt, J. H. van Lenthe, *Inorg. Chem.* **2001**, *40*, 4649−4655; (b) J. Scott, S. Gambarotta, I. Korobkov, Q. Knijnenburg, B. de Bruin, P. H. M. Budzelaar, *J. Am. Chem. Soc.* **2005**, *127*, 17204−17206. (c) J. Scott, S. Gambarotta, I. Korobkov, P. H. M. Budzelaar, *Organometallics* **2005**, *24*, 6298−6300.

[72]. D. Enright, S. Gambarotta, G. P. A. Yap, P. H. M. Budzelaar, *Angew. Chem., Int. Ed.* **2002**, *41*, 3873−3876.

[73]. J. Scott, S. Gambarotta, I. Korobkov, *Can. J. Chem.* **2005**, *83*, 279−285.

[74]. A. A. Danopoulos, J. A. Wright, W. B. Motherwell, *Chem. Commun*. **2005**, 784−786.

[75]. (a) D. Peng, Y. Zhang, X. Du, L. Zhang, X. Leng, M. D. Walter, Z. Huang, *J. Am. Chem. Soc*. **2013**, *135*, 19154−19166; (b) P. O. Lagaditis, P. E. Sues, J. F. Sonnenberg, K. Y. Wan, A. J. Lough, R. H. Morris, *J. Am. Chem. Soc*. **2014**, *136*, 1367−1380.

[76]. T. Zell, P. Milko, K. L. Fillman, Y. Diskin-Posner, T. Bendikov, M. A. Iron, G. Leitus, Y. Ben-David, M. L. Neidig, D. Milstein, *Chem. Eur. J*. **2014**, *20*, 4403−4413.

[77]. (a) R. Langer, G. Leitus, Y. Ben-David, D. Milstein, *Angew. Chem., Int. Ed*. **2011**, *50*, 2120−2124; (b) R. P. Yu, J. M. Darmon, J. M. Hoyt, G. W. Margulieux, Z. R. Turner, P. J. Chirik, *ACS Catal*. **2012**, *2*, 1760−1764.

[78]. S. C. Bart, E. Lobkovsky, E. Bill, P. J. Chirik, *J. Am. Chem. Soc*., **2006**, 128, 5302−5303.

[79] A. M. Tondreau, C. C. H. Atienza, K. J. Weller, S. A. Nye, K. M. Lewis, J. G. P. Delis, P. J. Chirik, *Science* **2012**, *335*, 567−570.

[80]. Obligacion, J. V.; Chirik, P. *J. Org. Lett*. **2013**, *15*, 2680−2683.

[81]. S. C. Bart, A. C. Bowman, E. Lobkovsky, P. J. Chirik, *J. Am. Chem. Soc*., **2007**, *129*, 7212−7213.

[82]. P. Chaudhuri, M. Hess, J. Muller, K. Hildenbrand, E. Bill, T. Weyhermuller, K. Wieghardt, *J. Am. Chem. Soc*., **1999**, *121*, 9599−9610.

[83]. (a) J. L. Cape, S. V. Lymar, T. Lightbody, J. K. Hurst, *Inorg. Chem*., **2009**, *48*, 4400−4410. (b) J. K. Hurst, J. L. Cape, A. E. Clark, S. Das, C. Qin, *Inorg. Chem*., **2008**, *47*, 1753−1764. (c) H. Yamada, W. F. Siems, T. Koike, J. K. Hurst, *J. Am. Chem. Soc*., **2004**, *126*, 9786−9795.

[84]. T. P. Yoon, .A. Ischay, J. Du, *Nat. Chem*., **2010**, *2*, 527−532.

[85]. (a) T. P. Yoon, J. Du, *J. Am. Chem. Soc*. **2009**, *131*, 14604–14605; (b) M. A. Ischay, M. E. Anzovino, J. Du, T. P. Yoon, *J. Am. Chem. Soc*. **2008**, *130*, 12886–12887.

[86]. D. A. Nicewicz, D. W. C. MacMillan, *Science*, **2008**, *322*, 77-80.

[87]. J. M. R. Narayanam, J. W. Tucker, C. R. J. Stephenson, *J. Am. Chem. Soc*., **2009**, *131***,** 8756–8757.

[88]. N. S. Ostlund, A. Szabo, *Modern Quantum Chemistry: Introduction to Advanced Electronic Structure and Theory*; Dover Publications: Mineola NY, **1996**.

[89]. C. J. Cramer, *Essentials of Computational Chemistry: Theories and Models, 2nd ed.*; John Wiley & Sons: Chichester, **2008**.

[90]. Y. Zhao, D. G. Truhlar, *Acc. Chem. Res.* **2008**, *41*, 157–167.

[91]. S. Grimme, *WIREs Comput. Mol. Sci.* **2011**, *1*, 211–228.

[92]. F. Jensen, *Introduction to Computational Chemistry*, 2nd Edition, Chichester, *John Wiley& Sons Ltd*, **2007**, 620 pages.

[93]. P. Atkins, R. Friedman, *Molecular Quantum Mechanics*, 4th Edition, Oxford, *Oxford University Press*, **2005**, 588 pages.

[94]. W. Koch, M. C. Holthausen, *A Chemist's Guide to density Functional Theory*, 2nd Edition, Weinheim, *Wiley-VCH*, **2002**, 313 pages.

[95]. A. D. Becke, *J. Chem. Phys.* **1993**, *98*, 5648–5652.

[96]. (a) E. R. Johnson, I. D. Mackie, G. A. Dilabio, *J. Phys. Org. Chem.* **2009**, *22*, 1127–1135. (b) S. F. Sousa, P. A. Fernandes, M. J. Ramos, *J. Phys. Chem. A* **2007**, *111*, 10439–10452. (c) A. Karton, D. Gruzman, J. M. L. Martin, *J. Phys. Chem. A* **2009**, *113*, 8434–8447. (d) E. A. Amin, D. G. Truhlar, *J. Chem. Theory Comput.* **2008**, *4*, 75–85. (d) B. Santra, A. Michaelides, M. Fuchs, A. Tkatchenko, C. Filippi, M. Scheffler, *J. Chem. Phys.* **2008**, *129*,

194111. (e) A. J. Thakkar, S. P. McCarthy, *J. Chem. Phys.* **2009**, *131*, 134109. (f) K. E. Riley, B. T. Op't Holt, K. M. Merz Jr, *J. Chem. Theory Comput.* **2007**, *3*, 407–433. (g) Y. Zhao, D. G. Truhlar, *J. Phys. Chem. A* **2005**, *109*, 5656–5667. (h) Y. Zhao, D. G. Truhlar, *J. Chem. Theory Comput.* **2005**, *1*, 415–432. (i) Y. Zhao, D. G. Truhlar, *J. Phys. Chem. A* **2006**, *110*, 5121–5129. (j) Y. Zhao, D. G. Truhlar, *J. Chem. Theory Comput.* **2007**, *3*, 289–300. (k) V. Riffet, G. Frison, G. Bouchoux, *Phys. Chem. Chem. Phys.* **2011**, *13*, 18561–18580.

[97]. (a) L. Hedin, B. I. Lundqvist, *J. Phys. C: Solid St. Phys.* **1971**, *4*, 2064-2083. (b) S. J. Vosko, L. Wilk, M. Nusair, *Can. J. Phys.* **1980**, *58*, 1200–1211. (c) J. P. Perdew, A. Zunger, *Phys. Rev. B* **1981**, *23*, 5048–5079. (d) J. P. Perdew, Y. Wang, *Phys. Rev. B* **1992**, *45*, 13244–13249.

[98]. A. D. Becke, *Phys. Rev. A* **1988**, *38*, 3098–3100.

[99]. J. P. Perdew, K. Burke, M. Ernzerhof, *Phys. Rev. Lett.* **1996**, *77*, 3865–3868.

[100]. C. Lee, W. Yang, R. G. Parr, *Phys. Rev. B* **1988**, *37*, 785–789.

[101]. (a) J. P. Perdew, *Phys. Rev. B* **1986**, *33*, 8822–8824. (b) J. P. Perdew, *Electronic Structure of Solids '91*, Berlin, Akademie Verlag, **1991**,249 pages.

[102]. (a) T. V. Voorhis, G. E. Scuseria, *J. Chem. Phys.* **1998**, *109*, 400–410; (b) J. P. Perdew, S. Kurth, A. Zupan, P. Blaha, *Phys. Rev. Lett.* **1999**, *82*, 2544–2547; (c) J. Tao, J. P. Perdew, V. N. Staroverov, G. E. Scuseria, *Phys. Rev. Lett.* **2003**, *91*, 146401–146401.

[103]. A. D. Becke, *J. Chem. Phys.* **1993**, *98*, 1372–1377.

[104]. (a) T. Leininger, H. Stoll, H. Werner, A. Savin, *Chem. Phys. Lett.* **1997**, *275*, 151–160. (b) I. C. Gerber, J. G. Angyan, *Chem. Phys. Lett.* **2005**, *415*, 100–105. (c) I. C. Gerber, J. G. Angyan, *J. Chem. Phys.* **2007**, *127*, 054101. (d) T. Tsuneda1, K. Hirao, *WIREs Comput Mol Sci* **2014**, *4*:375–390.

[105]. T. Yanai, D. P. Tew, N. C. Handy, *Chem. Phys. Lett.* **2004**, *393*, 51–57.

[106]. Grimme, S. *J. Comput. Chem.* **2004**, *25*, 1463–1473.

[107]. M. J. Frisch, J. A. Pople, J. S. Binkley, *J. Chem. Phys.* **1984**, *80*, 3265-3269.

]108]. T. H. Dunning, *J. Chem. Phys.* **1989**, *90*, 1007-1023.

[109]. S. Wilson. *Adv. Chem. Phys.*, **1987**, *67*:439–500.

[110]. E. R. Davidson and D. Feller. *Chem. Rev.* **1986**, *86*, 681–696.

[111]. (a) M. M. Francl, W. J. Pietro, W. J. Hehre, J. S. Binkley, M. S. Gordon, D. J. Defrees, and J. A. Pople. *J. Chem. Phys.* **1982**, *77*, 3654–3665. (b) W. J. Hehre, R. Ditchfield, and J. A. Pople. *J. Chem. Phys.* **1972**, *56*, 2257–2261.

[112].Gaussian 09, Revision **E.01**, M. J. Frisch, G. W. Trucks, H. B. Schlegel, G. E. Scuseria, M. A. Robb, J. R. Cheeseman, G. Scalmani, V. Barone, B. Mennucci, G. A. Petersson, H. Nakatsuji, M. Caricato, X. Li, H. P. Hratchian, A. F. Izmaylov, J. Bloino, G. Zheng, J. L. Sonnenberg, M. Hada, M. Ehara, K. Toyota, R. Fukuda, J. Hasegawa, M. Ishida, T. Nakajima, Y. Honda, O. Kitao, H. Nakai, T. Vreven, J. A. Montgomery, Jr., J. E. Peralta, F. Ogliaro, M. Bearpark, J. J. Heyd, E. Brothers, K. N. Kudin, V. N. Staroverov, R. Kobayashi, J. Normand, K. Raghavachari, A. Rendell, J. C. Burant, S. S. Iyengar, J. Tomasi, M. Cossi, N. Rega, J. M. Millam, M. Klene, J. E. Knox, J. B. Cross, V. Bakken, C. Adamo, J. Jaramillo, R. Gomperts, R. E. Stratmann, O. Yazyev, A. J. Austin, R. Cammi, C. Pomelli, J. W. Ochterski, R. L. Martin, K. Morokuma, V. G. Zakrzewski, G. A. Voth, P. Salvador, J. J. Dannenberg, S. Dapprich, A. D. Daniels, Ö. Farkas, J. B. Foresman, J. V. Ortiz, J. Cioslowski, D. J. Fox, Gaussian, Inc., Wallingford CT, **2009**.

Chapter III

Formation of reduced metal complexes

III.1. Introduction

Mass spectrometry (MS) has developed rapidly in the last two decades.[1] This makes it a modern analytical methods, which plays a crucial role not only for qualitative and quantitative analyses but also for structural characterization.[2,3] A large variety of different mass spectrometer designs are commercially available today, aimed at different research applications. For example, tandem quadrupole and ion trap mass spectrometers often serve as highly specific and sensitive detectors for chromatography, mostly for identification and quantification of known compounds. Orbitrap and Fourier transform ion cyclotron resonance instruments (FT-ICR)[4,5] provide high resolving power and high mass accuracy at sub parts-per-million (ppm) levels; they can be readily combined with a wide range of ion activation and fragmentation techniques,[6] such as infrared multiphoton dissociation (IRMPD),[7] and electron-based ion fragmentation techniques (ExD). The latter includes electron capture dissociation (ECD) and electron transfer dissociation (ETD) methods, which have been vastly used in proteomic research.[8,9] ECD and ETD methods, which require multiply charged molecules, have been mostly applied to peptides and proteins,[10,11,12] which are easily obtained as multiply protonated cations through electrospray ionization (ESI). On the opposite, the use of these fragmentation techniques for other chemical compounds, such as organometallic complexes, remain scarce. Many small molecules generate singly-charged species after ESI in positive ion mode, which of course would result in charge neutralization after electron capture and no possibility for mass spectral analysis. Negative ions formed by ESI can also be studied through electron activated dissociation techniques, such as negative electron transfer dissociation (NETD)[13] or electron-detachment dissociation (EDD)[14] methods, but their use is less frequent. In many cases however, it seems possible to form multiply-charged organometallic species in the gas phase. Therefore, ECD and ETD techniques would be well

adapted methods to be applied on organometallic complexes and to possibly generate reduced radical species.

An important aspect of electron activated methods is the internal energy imparted into a molecule by the incoming electron. It is clear that ECD bring significantly more internal energy than ETD process. As a result, using these methods with organometallic complexes should lead to various mass spectra. In particular, the ECD mass spectrum may show additional peaks via the opening of new competitive fragmentation channels. In the most common implementation of ECD on FT-ICR MS, it is possible to define the average electron energy by varying the potential difference between the electron emitting surface (cathode) and the ion–electron interaction in the ICR cell,[15] Nevertheless, to produce sufficient flux of electrons for efficient ECD MS/MS it is practically very challenging to reduce electron energy below 1 eV.[16,17] The influence of the use of ECD versus ETD methods on the formation of reduced radical organometallic complexes will be discussed with examples in the following parts of this chapter.

In the course of our work, we have been especially interested to study organometallic species containing non-innocent ligands. Series of ligands, including bipyridine-type bidentate and bis(imino)pyridine type tridentate ligands have been chosen for this work. With these ligands, we therefore plan to form and study in the gas phase a series of organometallic complexes with zinc and ruthenium metal centers. Doubly charged organometallic species should be produce by electrospray ionization and subject to charge reduction using two different types of electron activated methods, ECD and ETD. InfraRed Multiple Photon Dissociation (IRMPD) action spectroscopy has emerged recently as an efficient and generally applicable technique for the analysis of isolated ions through measurement of their IR spectra,[18] these ‘‘action’’ spectra are generated through on-resonance absorption of multiple IR photons at an active vibrational mode of a mass-selected ion, and take the form of a plot of fragmentation

abundance as a function of photon wavelength. IRMPD has been used previously to study interaction of metals with redox-active ligands generated by electrospray ionization.[19] A combination of ECD and IRMPD techniques has also allowed the structure of an even-electron ECD-generated peptide fragment to be established by IR action spectroscopy.[20] The detailed experimental procedure of ECD and ETD fragmentation techniques and of IRMPD spectroscopy has been explained in the methodology chapter (Chapter II). In this chapter, we describe our work related to the reduction of dicationic organometallic species with the ECD and ETD fragmentation techniques. IRMPD spectroscopy studies of these complexes will be described in chapters V and VI.

III.2. Principles and organometallic complexes choice

Our main goal in this part is to prepare reduced organometallic complexes in the gas phase. For this, we need to form multiply-charged organometallic complexes with non-innocent ligands and to study their reduction process in the gas phase through ECD and ETD techniques. On the basis of difficulties to study and stabilize the radical species in solution, we indeed planned to form and characterize them in the gas phase. Several requirements have to be achieved in order to successfully form and characterize reduced organometallic complexes in the gas phase, which is the main goal of our work:

1. We first need to be able to form multiply charged organometallic species in the gas phase through ESI. This requires that we have at our disposal the organometallic precursor species in solution. To that end, we have developed collaboration with Duncan Carmichael, who is an experimentalist in our laboratory. Depending on our

needs, Duncan Carmichael and his student Eleonore Payen de la Garanderie have synthesized the chemical species in solution we needed.

2. These compounds should be easily useable. This means that they should not be too sensitive to air and moisture because it seems difficult, before the source, to maintain the solution under an inert atmosphere. Indeed, some experiment performed with iron(II) complexes of bipyridine have shown that these compounds are degraded within a few minutes in a water/acetonitrile solution under air atmosphere. On the opposite, Ru(II) and Zn(II) complexes are stable for months in such conditions.
3. The synthesis of compounds should not be too complex, and above all, we have sought to use quickly synthesizable compounds. This has focused our interest to zinc complexes. Indeed, mixing $[Zn(BF_4)_2]$ and *N*-donor ligands in a water/acetonitrile solution, which could be done in a mass spectrometry laboratory, allows after few minutes to observe $[Zn(N\text{-donor ligands})_n]^{2+}$ complexes through ESI. On the opposite, Ru complexes have to be synthesized in a well-equipped chemistry laboratory.
4. A difficult task was to use organometallic complexes well adapted for the experiments we have planned. This mean that, beyond the formation of the multiply charged species in the gas phase and its reduction through ECD experiments, the subsequent IRMPD experiment requires easy fragmentation under irradiation and, if possible, characteristic IR signatures. This has mainly driven the choice of ligands that we have used, which are depicted on Scheme 3.1.
5. We plan to use model compounds to develop our experiment, but we also wanted to study compounds of chemical interest, eg for catalysis.

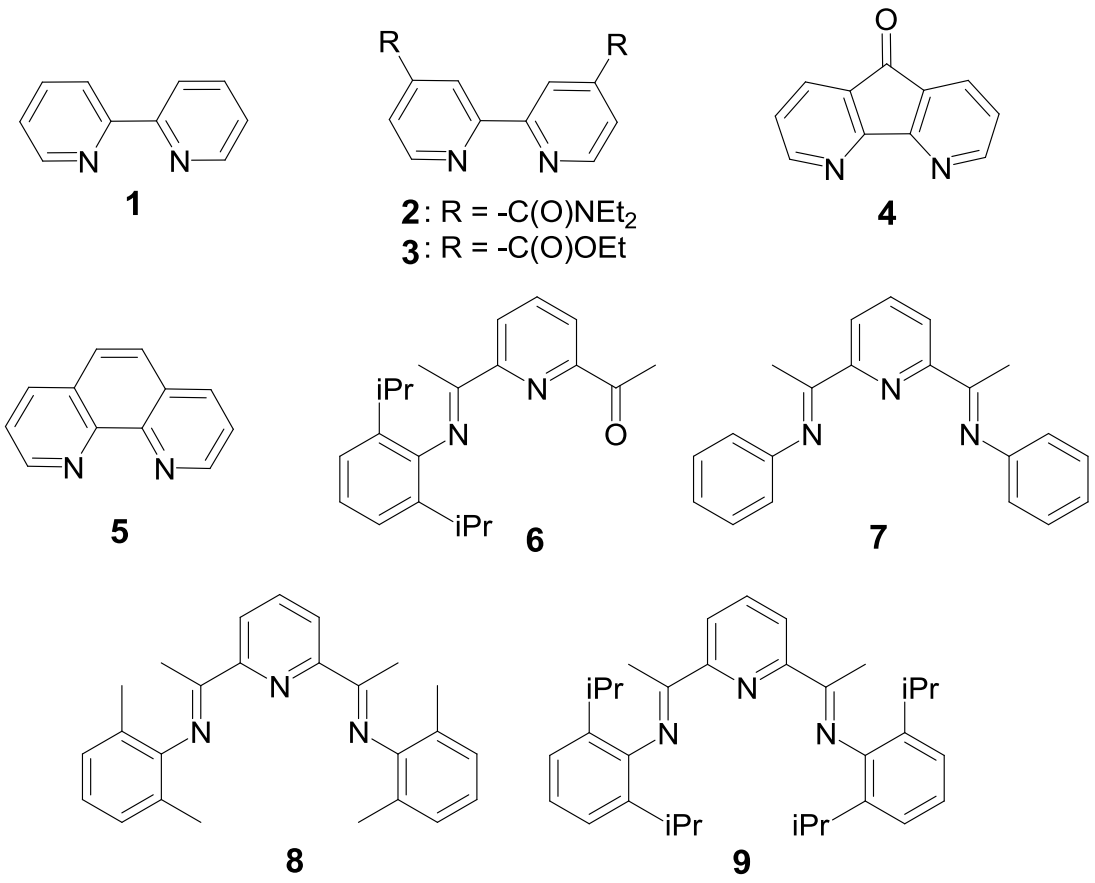

***Scheme 3.1**. ligand systems used to prepare metal complexes.*

The nature of the complexes we have studied has been driven by these various requirements. During this work, we have focused on zinc complexes, which serve as model, and on ruthenium complexes which are used in photocatalysis and belong to the same group as iron. We have selected bipyridyl (**1**-**5**) and bis(imino)pyridine-type (**6**-**9**) ligands (Scheme 3.1). The numbering of the ligands has been used throughout this thesis manuscript. **1** and **5** were selected because they are well-known bidentate ligands. We expected a characteristic IR signature for the CO stretch of **4**. **2** and **4** were synthesized because they should combine a characteristic CO stretch and they should induce more easily fragmentations under irradiation due to their amide and ester substituents. **9** is the ligand, which has been used extensively in iron catalysis by the Chirik's group (see IIA.5). **6** is a byproduct of the synthesis of **9**, whereas

the less sterically crowded aryl substituents on **7** and **8** where expected to facilitate formation of $[M(\mathbf{7})_2]^{2+}$ or $[M(\mathbf{8})_2]^{2+}$ because $[M(\mathbf{9})_2]^{2+}$ cannot be obtained.

Based on these chemicals, we explore in this chapter the influence of the structure of the complexes on the nature of radicals that we can form and isolate after ECD and ETD.

III.3. ECD and ETD on dicationic complexes

III.3.1. Reduction of homoleptic dicationic complexes

We are able to observe both $[ZnL_3]^{2+}$ and $[ZnL_2]^{2+}$ dicationic complexes when the mixture of one ligand (L) and zinc(II) metal center (Zn) was electrosprayed in FT-ICR. Only $[RuL_3]^{2+}$ can be obtained in the gas phase with bidentate L ligands, whereas $[RuL'_2]^{2+}$ complexes are obtained with tridentate L' ligands. These ions can be isolated in the quadrupole and accumulated in the collision cell of our FT-ICR apparatus. From these complexes, upon capture or transfer of one electron, we expect to obtain radical cations $[ML_n]^{\bullet+}$. A key issue when adding one electron is the potential fragmentation of the organometallic complex, and in particular the dissociation of one ligand from the metal center. To describe the typical behavior of the molecules that we studied, some examples are presented below.

III.3.1.1. ECD of $[Zn(1)_3]^{2+}$

Dicationic complex $[Zn(\mathbf{1})_3]^{2+}$ was formed in an electrospray source in FT-ICR tandem mass spectrometer. The $[Zn(\mathbf{1})_3]^{2+}$ ion with mass m/z at 266 was isolated in the quadrupole and accumulated in the collision cell. Figure 3.1 shows that electron capture dissociation (ECD) on this dication leads to the formation of $[Zn(\mathbf{1})_2]^{\bullet+}$ (peak at m/z 376) and $[Zn(\mathbf{1})]^{\bullet+}$ (peak at m/z 220) radical cations.

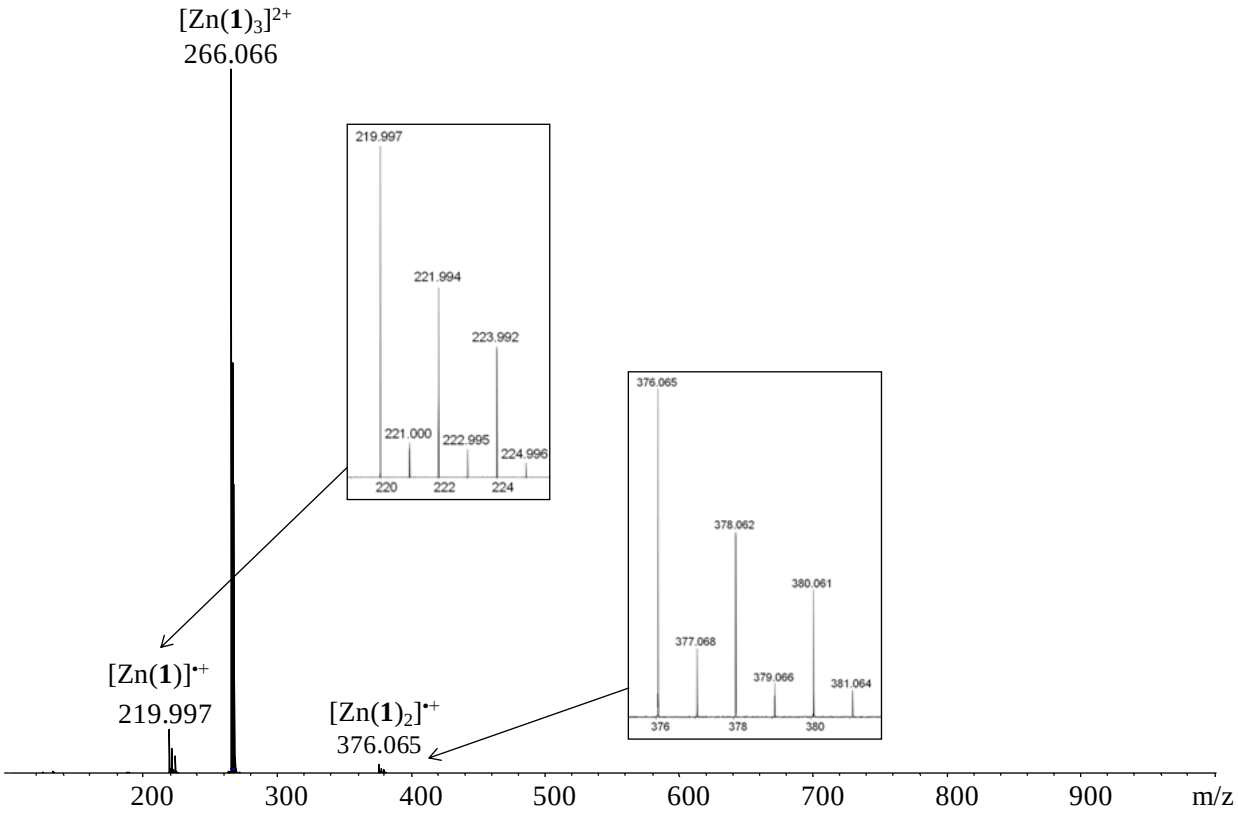

***Figure 3.1**: Electron capture dissociation FT-ICR mass spectrum of $[Zn(\mathbf{1})_3]^{2+}$ at m/z 266.*

The mass spectrum of the electron capture dissociation on $[Zn(\mathbf{1})_3]^{2+}$ shows that it is not possible to form $[Zn(\mathbf{1})_3]^{\bullet+}$ by this approach. The loss of one or two ligands observed during the reduction process of $[Zn(\mathbf{1})_3]^{2+}$ results from the high internal energy provided on the metal complex by the ECD fragmentation method. To explore in more details the effect of the reduction method and of the nature of the complex, we scrutinized various parameters of the experiment:

(i) The energy of the electron provided in the reduction step can be altered, using ETD instead of ECD. Indeed, in the electron transfer dissociation (ETD) method, an electron is transferred from a reagent anion, such as the radical anions derived from fluoranthene, to dicationic complexes whereas the ECD technique is based on the capture of near thermal energy electrons;

(ii) The nature of the metal atom (Ru versus Zn), in order to modify the metal-ligand bond strength. Indeed, DFT B3LYP/6-31+G(d,p) (LanL2DZ on Ru) calculations on $[Ru(\mathbf{1})_n]^{2+}$ and $[Zn(\mathbf{1})_n]^{2+}$ (n = 2, 3) indicate that the dissociation of the first ligand from $[Ru(\mathbf{1})_3]^{2+}$ is more difficult than from $[Zn(\mathbf{1})_3]^{2+}$. Indeed, the calculated binding energies are respectively 404 and 305 $kJ.mol^{-1}$.

(iii) The nature of the ligands, which can be either tridentate or bidentate. Expectedly, the tridentate ligands are more strongly coordinated to the metal center than bidentate ligands.

All these aspects are detailed in the following experiments. One objective of these investigations is to determine the conditions to form a gas phase radical octahedral complex, ie a complex which has retained the coordination sphere of it had before reduction.

III.3.1.2. ETD of $[Zn(1)_3]^{2+}$

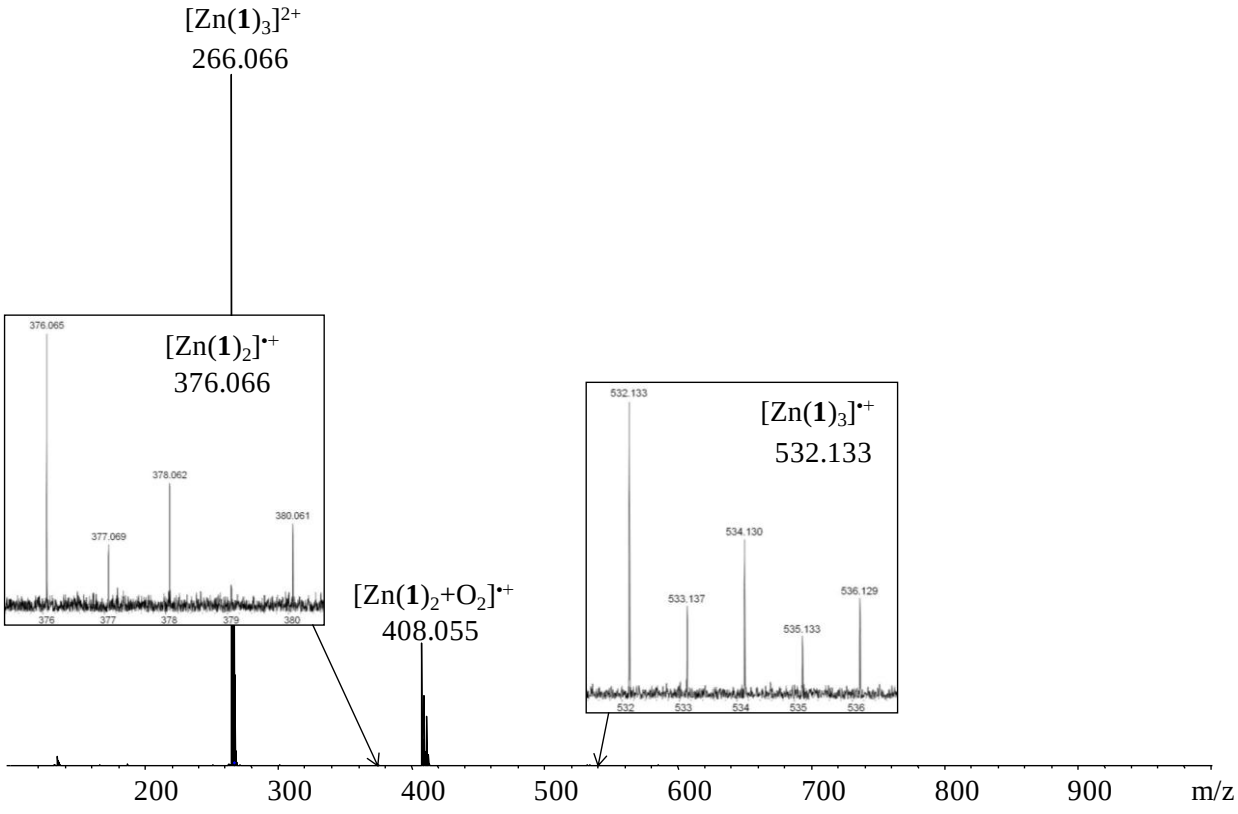

***Figure 3.2**: Electron transfer dissociation FT-ICR mass spectrum of $[Zn(\mathbf{1})_3]^{2+}$ at m/z 266.*

The electron transfer dissociation spectrum of $[Zn(\mathbf{1})_3]^{2+}$ is shown in Figure 3.2. Interestingly, we observe the formation of a radical cationic complex including a complete coordination sphere, $[Zn(\mathbf{1})_3]^{\bullet+}$, at m/z 532, but as a minor product. We also observe $[Zn(\mathbf{1})_2]^{\bullet+}$ at m/z 376 with the loss of one bipyridine ligand whereas loss of two bipyridine is not observe. Surprisingly, the major product corresponds to the adduct between $[Zn(\mathbf{1})_2]^{\bullet+}$ and O_2, $[Zn(\mathbf{1})_2+O_2]^{\bullet+}$, at m/z 408. Since the experiment was performed in normal conditions, we suspected that O_2 is present in low amount in the quadrupole were the ETD process takes place. As a biradical, O_2 reacts easily with the formed radical organometallic complex. It should however be noted that we do not observe formation of $[Zn(\mathbf{1})_3+O_2]^{\bullet+}$, which can be an indication that O_2 occupies the vacant coordination site on the radical cationic organometallic complex.

III.3.1.3. ECD of $[Ru(1)_3]^{2+}$

Application of electron capture dissociation on the dication $[Ru(\mathbf{1})_3]^{2+}$ generates the spectrum given in Figure 3.3. We observe an unique product, $[Ru(\mathbf{1})_2]^{\bullet+}$, at m/z 414. This indicates that the gas phase mono-electron capture process induces the release of one, and only one, bipyridine ligand. Comparison between the experimental results observed for the Ru and Zn complexes in the ECD process agrees with the bond strength between metal and bipyridine computed at the DFT level (Zn–bipy 305 $kJ.mol^{-1}$ and Ru–bipy 404 $kJ.mol^{-1}$). More strongly bonded ligands in the cationic species are more difficult to eliminate during the ECD process.

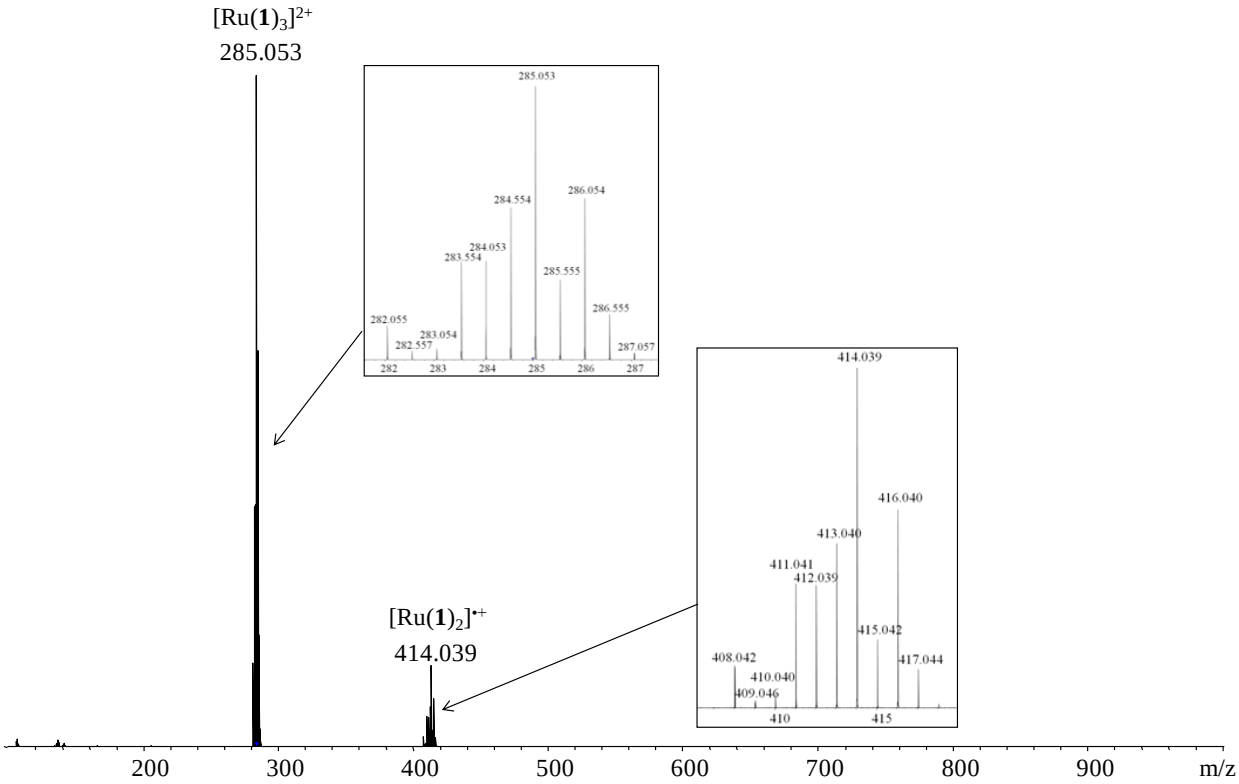

***Figure 3.3**: Electron capture dissociation FT-ICR mass spectrum of [Ru(**1**)$_3$]$^{2+}$ at m/z 285.*

III.3.1.4. ETD of [Ru(1)$_3$]$^{2+}$

Electron transfer dissociation on [Ru(**1**)$_3$]$^{2+}$ results in the formation of the radical cation [Ru(**1**)$_3$]$^{\bullet+}$ (m/z 570), which has a complete coordination sphere (Figure 3.4). In addition, we also observed the formation of another radical cation where O_2 molecule is coordinated to the ruthenium complex after loss of one ligand, [Ru(**1**)$_2$+O_2]$^{\bullet+}$, found at m/z 446.

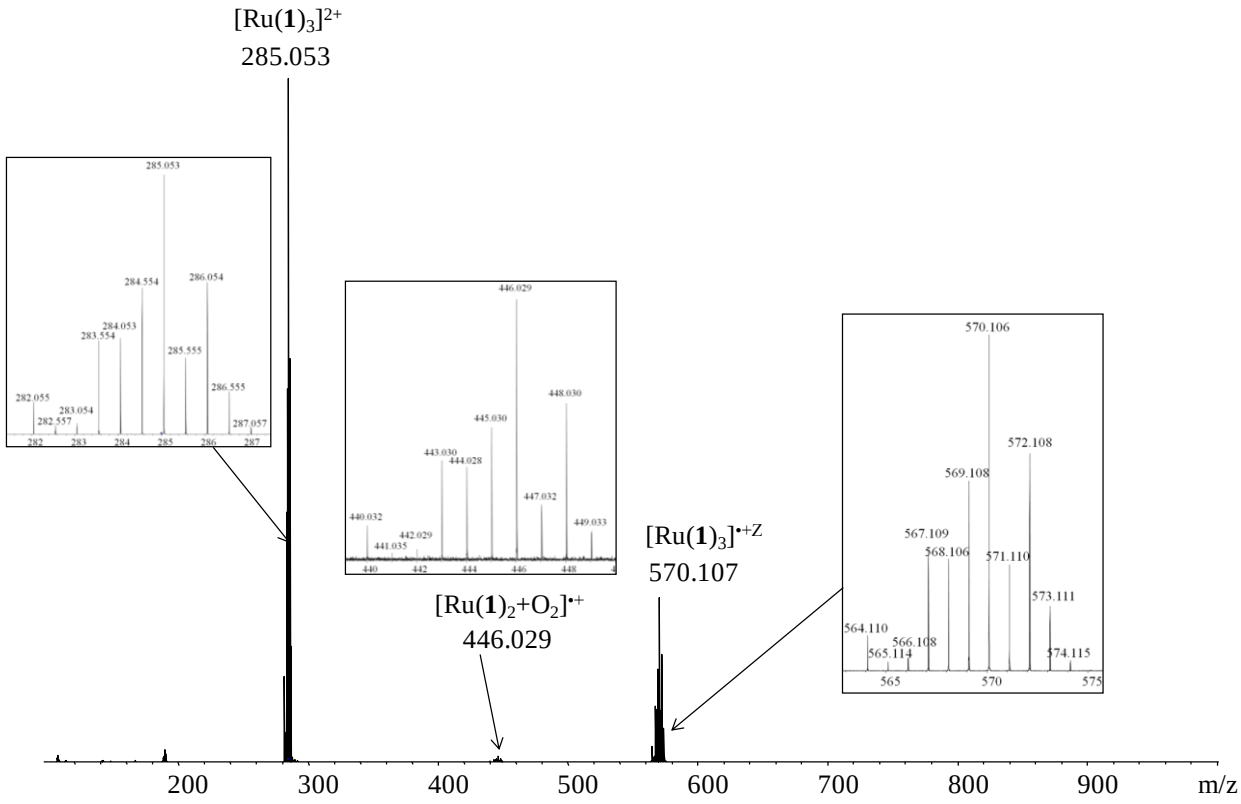

***Figure 3.4**: Electron transfer dissociation FT-ICR mass spectrum of [Ru(**1**)$_3$]$^{2+}$ at m/z 285.*

We have been able to achieve the formation of various radical organometallic complexes. ETD process allows the formation of complexes with a complete coordination sphere. ECD process provides more internal energy to the dicationic complexes, leading to the dissociation of ligands to the metal center. It should be noted however that it is not possible to coupled ETD and IRMPD experiments because the ETD fragmentation technique is not available at CLIO. So we will be able to study by IRMPD spectroscopy, for complexes with bidentate ligands, only complexes with one and two ligands. We then explore the effect of a tridentate ligand, as well as the effect of having two different ligands coordinated to a metal center.

III.3.1.5. ECD of [Ru(7)$_2$]$^{2+}$

When electron capture dissociation is applied on a ruthenium metal complex bound with two tridentate bis(imine)pyridine type ligands, we observe the formation of a radical cation, which

corresponds to the reduced dication without loss of any ligand. This can be seen in Figure 3.5. The addition of an electron by ECD on $[Ru(\mathbf{7})_2]^{2+}$ (m/z 364) generated a radical cation at $[Ru(\mathbf{7})_2]^{\bullet+}$ (m/z 728), showing that the internal energy provides by the ECD process is not sufficient to de-coordinate a tridentate ligand..

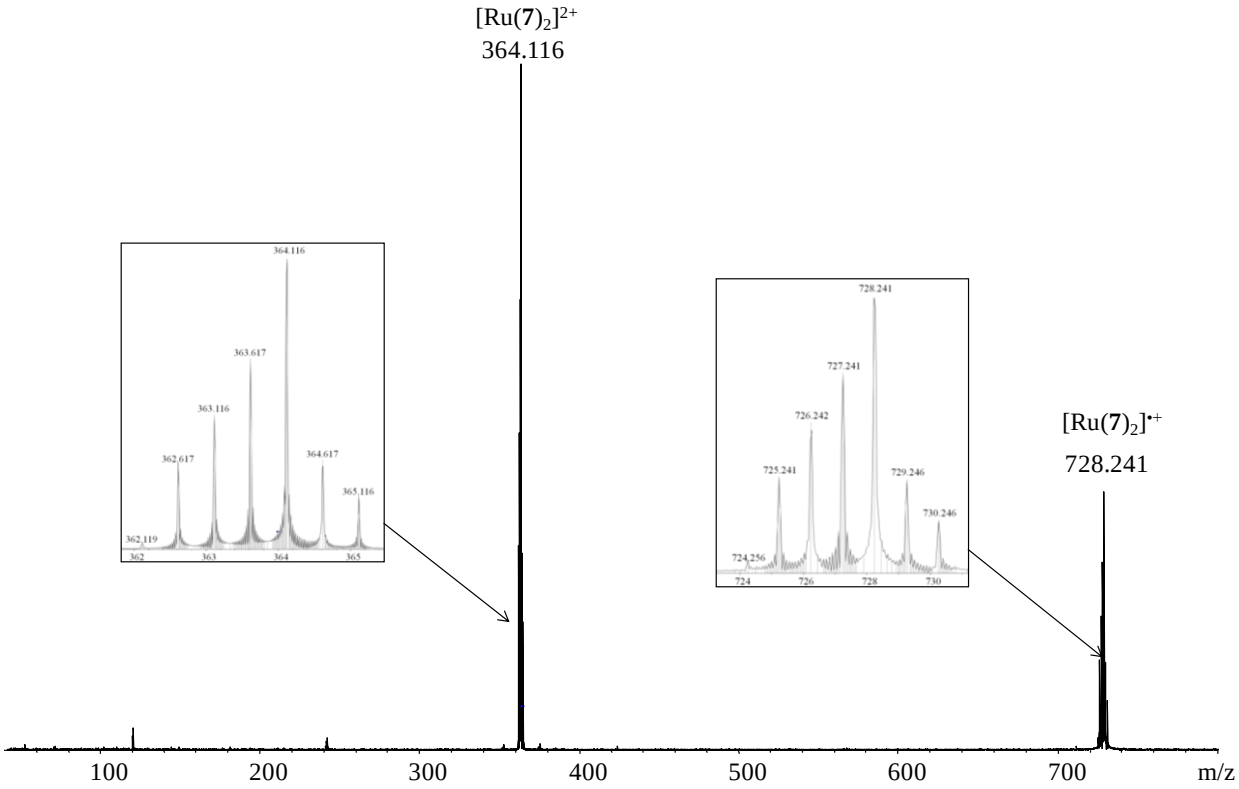

***Figure 3.5**: Electron capture dissociation FT-ICR mass spectrum of $[Ru(\mathbf{7})_3]^{2+}$ at m/z 364.*

III.3.2. Reduction of heteroleptic dicationic complexes

We were interested to form radical complexes with different ligands. To that end, we use a mixture of two different bidentate ligands (L and L') with the zinc metal cation. The formation of dicationic complexes such as $[M(L)_2(L')]^{2+}$, $[M(L)(L')_2]^{2+}$ or/and $[M(L)(L')]^{2+}$ is expected. From these species, it should be possible to form heteroleptic radical complexes, in particular $[Zn(L)(L')]^{\bullet+}$. This is shown with an example in which we use a mixture of bipyridine (**1**) and phenanthroline (**5**) ligands.

III.3.2.1. ECD of $[Zn(1)_2(5)]^{2+}$:

Mass spectrum obtained after the capture of an electron by the dicationic complex $[Zn(\mathbf{1})_2(\mathbf{5})]^{2+}$ (m/z 278) is shown in Figure 3.6. It indicates the formation of two radical cations. One radical is $[Zn(\mathbf{1})(\mathbf{5})]^{\bullet+}$ (m/z 400), which results from the loss of one bipyridine moiety, and the second radical is $[Zn(\mathbf{5})]^{\bullet+}$ (m/z 244), which is formed by the loss of two bipyridine moieties. This result agrees with our DFT calculations performed on the dissociation process of the ligands in the heteroleptic $[Zn(\mathbf{1})(\mathbf{5})]^{2+}$ complex. Indeed, B3LYP/6-31+G(d,p) calculations reveal that **5** is more strongly bonded to the zinc cation (562 $kJ.mol^{-1}$) than **1** (546 $kJ.mol^{-1}$) in $[Zn(\mathbf{1})(\mathbf{5})]^{2+}$, explaining the preferential loss of **1** upon ECD experiment.

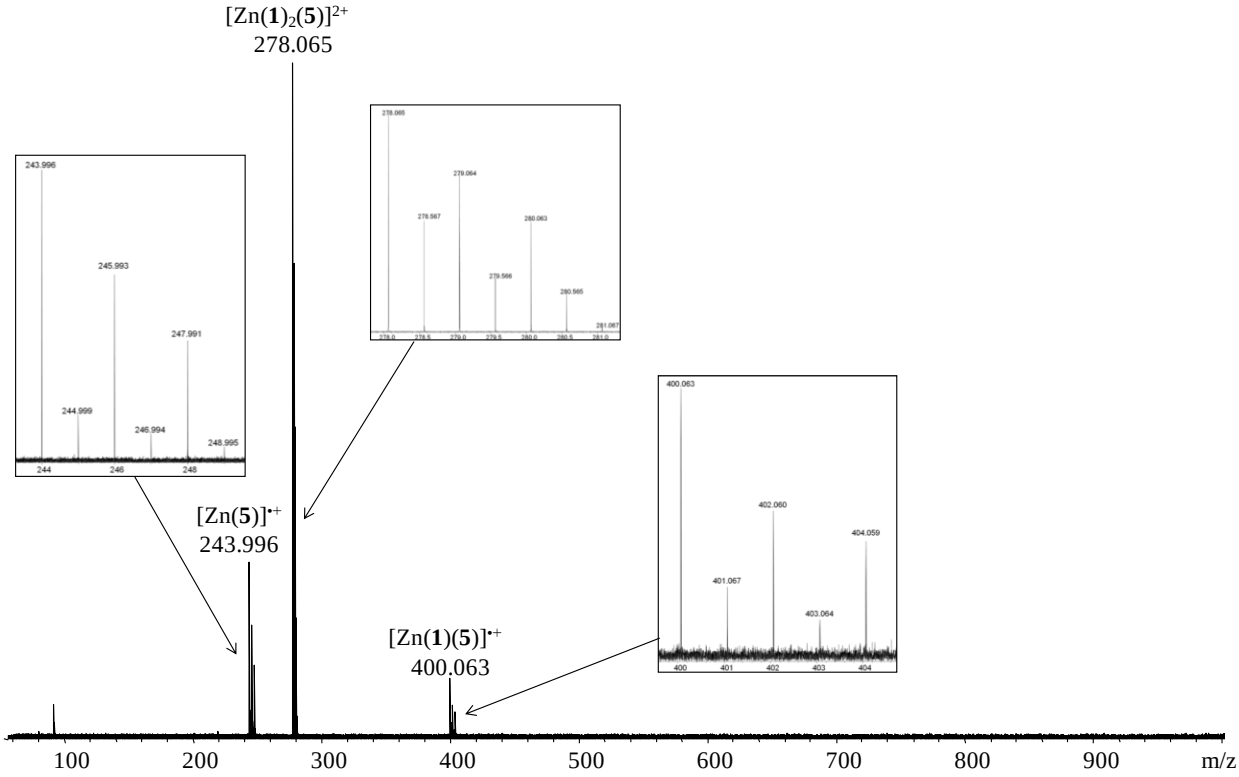

***Figure 3.6**: Electron capture dissociation FT-ICR mass spectrum of $[Zn(\mathbf{1})_2(\mathbf{5})]^{2+}$ at m/z 278.*

III.3.2.2. ETD of $[Zn(1)_2(5)]^{2+}$:

Figure 3.7 shows the ETD spectrum of $[Zn(\mathbf{1})_2(\mathbf{5})]^{2+}$ (m/z 278). We observe the dissociation of one bipyridine ligand, leading to the formation of the radical cation $[Zn(\mathbf{1})(\mathbf{5})]^{\bullet+}$ (m/z 400). The radical further react with O_2 during the ETD process, leading to the formation of a second radical at m/z 432.

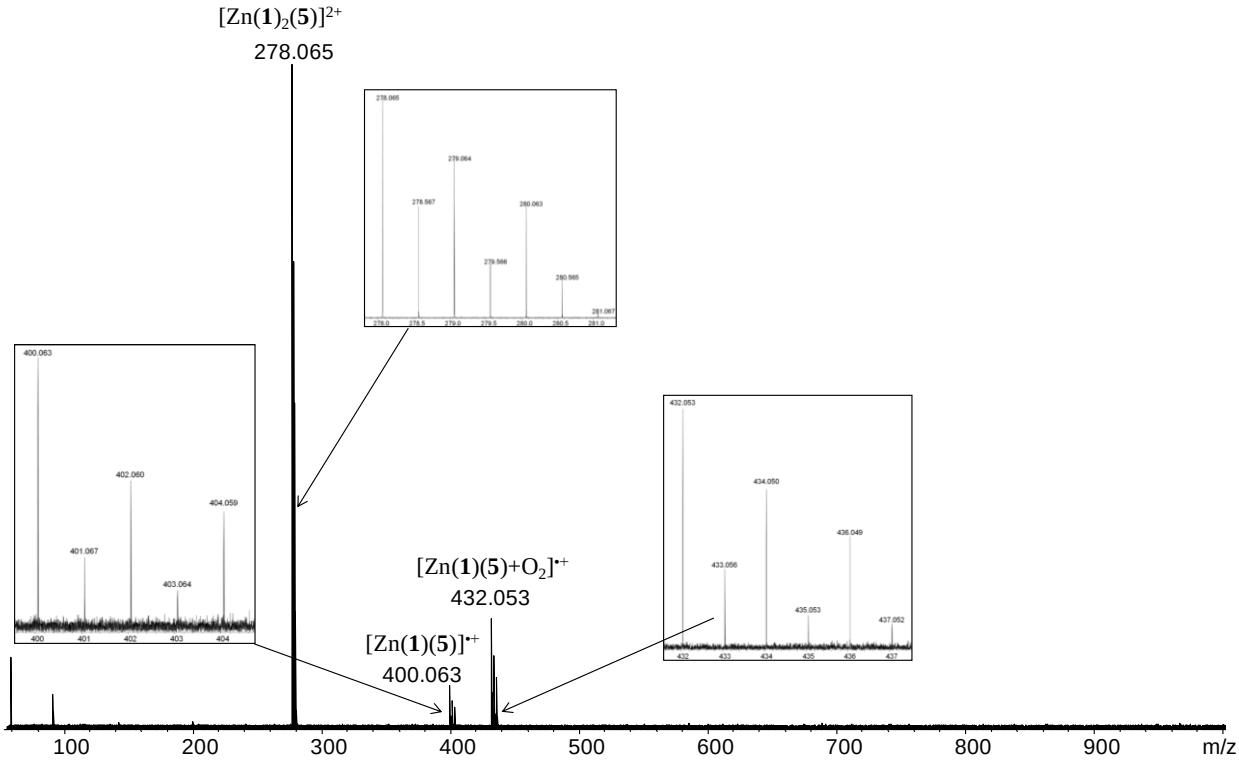

***Figure 3.7**: Electron transfer dissociation FT-ICR mass spectrum of $[Zn(\mathbf{1})_2(\mathbf{5})]^{2+}$ at m/z 278.*

III.3.2.3. ECD of $[Zn(1)(5)_2]^{2+}$:

Electron capture dissociation on Zn-dicationic complex containing one bipyridine and two phenanthroline molecule (m/z 290) generates three radical cations. The major compound is $[Zn(\mathbf{5})_2]^{\bullet+}$ (m/z 424), which corresponds to the dissociation of one bipyridine ligand, in agreement with our DFT calculations indicated above. We also observed formation of $[Zn(\mathbf{5})]^{\bullet+}$ (m/z 244), which means that the loss of one bipyridine and one phenanthroline

ligands is possible. Surprisingly, despite its larger interaction energy with zinc dication, **5** can dissociate before **1** upon ECD experiment on $[Zn(\mathbf{1})(\mathbf{5})_2]^{2+}$, leading, as a very minor product, to the formation of $[Zn(\mathbf{1})(\mathbf{5})]^{\bullet+}$ (m/z 400). The presence of two phenanthroline ligands in $[Zn(\mathbf{1})(\mathbf{5})_2]^{2+}$ probably explains why it is possible, to a low amount, to dissociate **5** before **1**.

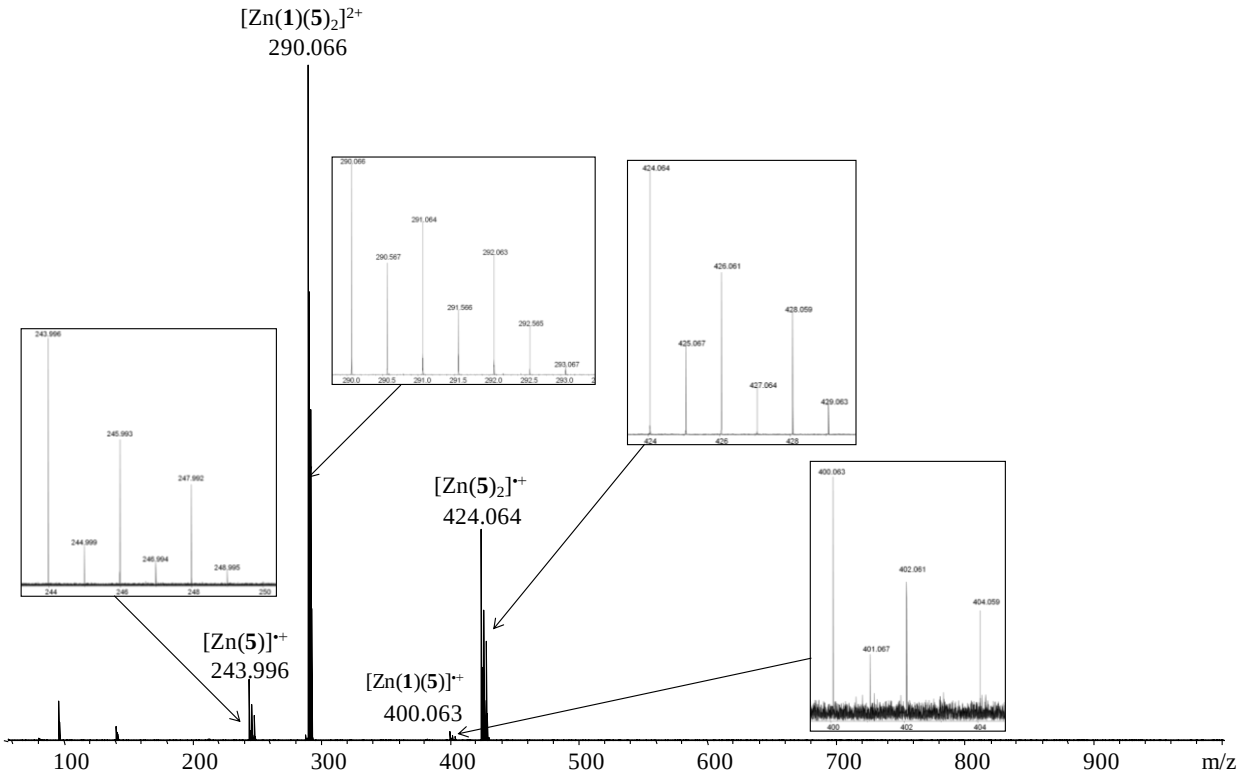

***Figure 3.8**: Electron capture dissociation FT-ICR mass spectrum of $[Zn(\mathbf{1})(\mathbf{5})_2]^{2+}$ at m/z 290.*

III.3.2.4. ETD of $[Zn(1)(5)_2]^{2+}$:

The electron transfer dissociation of dication $[Zn(\mathbf{1})(\mathbf{5})_2]^{2+}$ results in the formation of the radical cation $[Zn(\mathbf{5})_2]^{\bullet+}$ (m/z 290) with the loss of the bipyridine moiety. In addition, we also observed another radical cationic species that coordinated with oxygen molecule $[Zn(\mathbf{5})_2+O_2]^{\bullet+}$ (m/z 456), as shown in Figure 3.9.

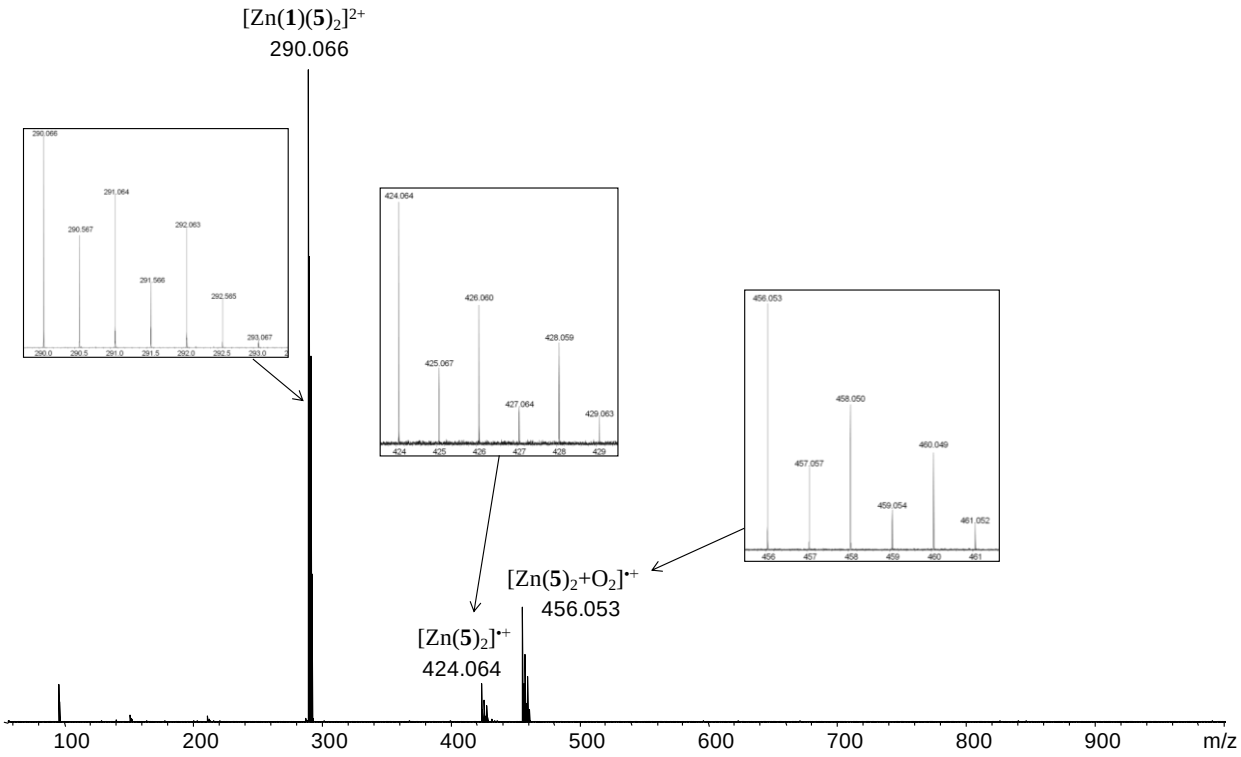

***Figure 3.9**: Electron transfer dissociation FT-ICR mass spectrum of [Zn(**1**)(**5**)$_2$]$^{2+}$ at m/z 290.*

III.3.2.5. ECD of [Zn(1)(5)]$^{2+}$:

In Figure 3.10, the dication [Zn(**1**)(**5**)]$^{2+}$ dissociates on electron capture dissociation. It leads to two radical cationic species, which are [Zn(**5**)]$^{\bullet+}$ (m/z 244) and [Zn(**1**)]$^{\bullet+}$ (m/z 220) with the loss of bipyridine and phenanthroline moieties respectively. The relative intensity of [Zn(**1**)]$^{\bullet+}$ and [Zn(**5**)]$^{\bullet+}$ agrees with the bond strength computed previously.

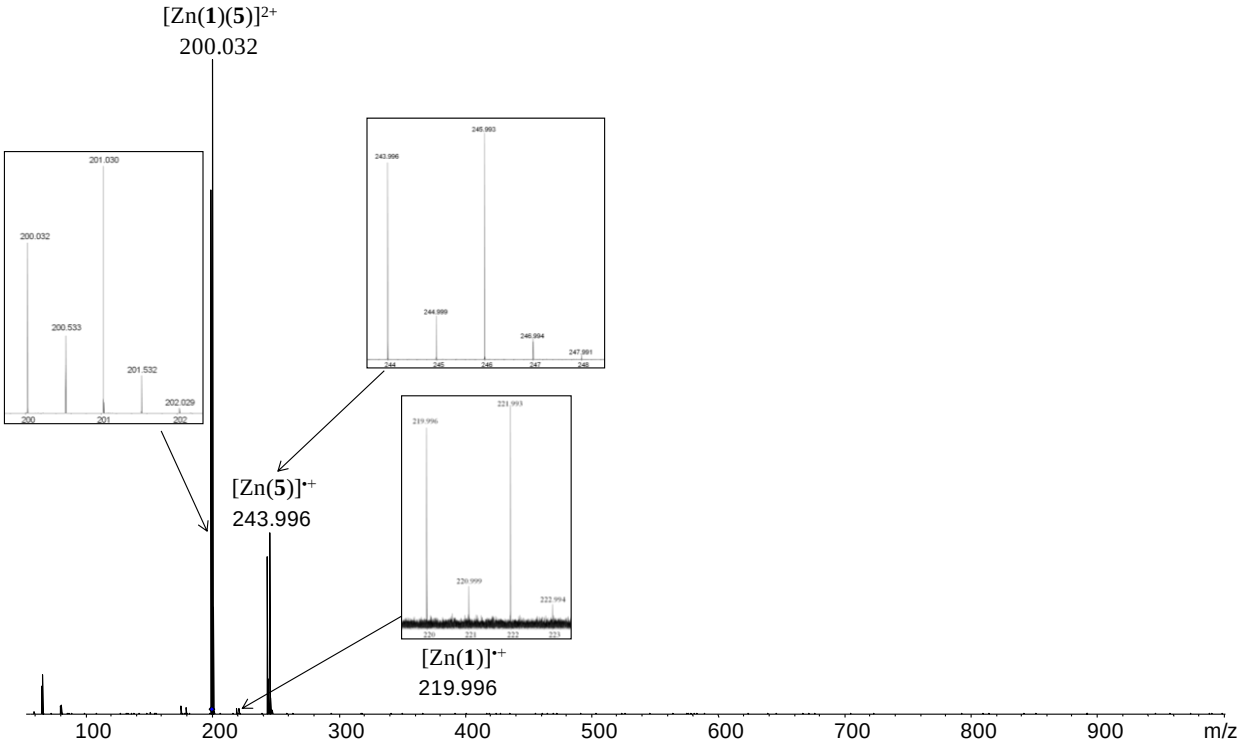

***Figure 3.10**: Electron capture dissociation FT-ICR mass spectrum of [Zn(**1**)(**5**)]$^{2+}$ at m/z 200.*

III.3.2.6. ETD of [Zn(1)(5)]$^{2+}$:

[Zn(**1**)(**5**)]$^{2+}$ dicationic complex reduced through an electron transfer dissociation process induces the formation of [Zn(**1**)(**5**)]$^{\bullet+}$ (m/z 400) and [Zn(**5**)]$^{\bullet+}$ (m/z 234) as well as their dioxygen additive products [Zn(**1**)(**5**)+O_2]$^{\bullet+}$ (m/z 432) and [Zn(**5**)+O_2]$^{\bullet+}$ (m/z 276) as shown in Figure 3.11.

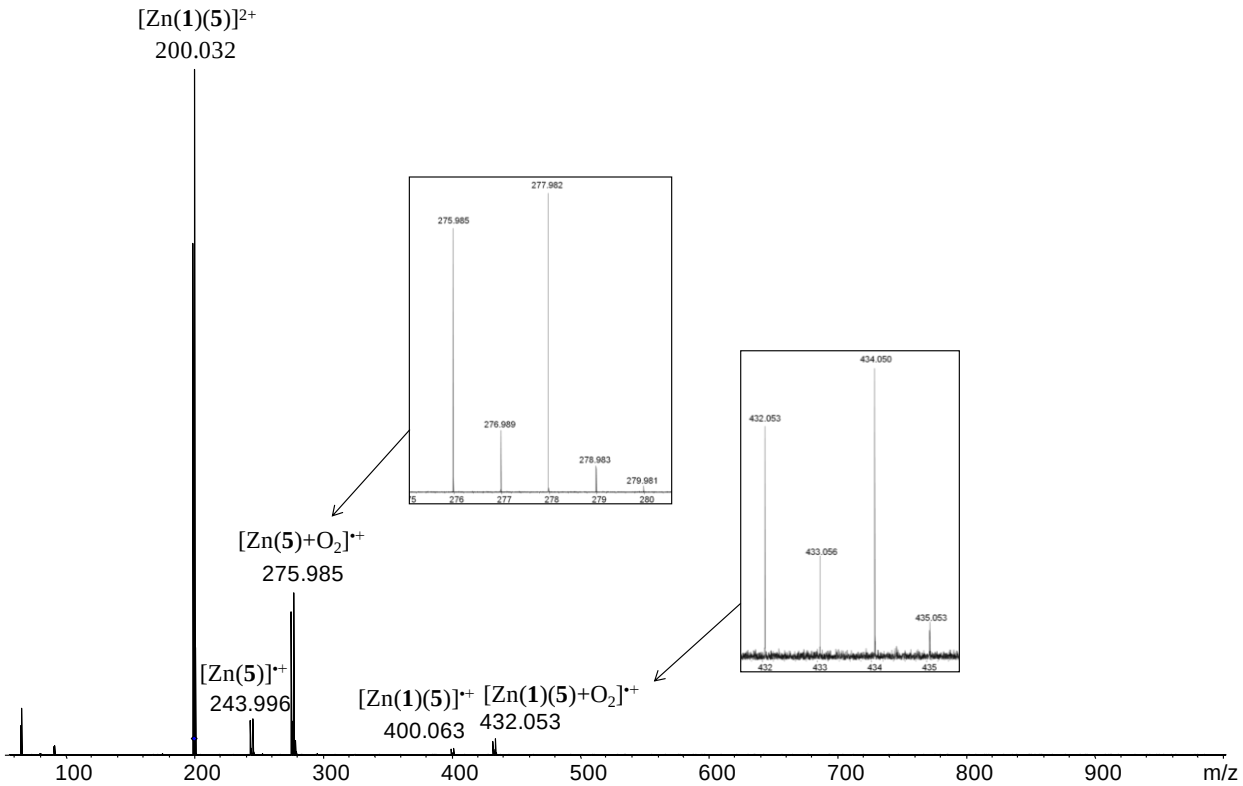

***Figure 3.11**: Electron transfer dissociation FT-ICR mass spectrum of [Zn(**1**)(**5**)]$^{2+}$ at m/z 200.*

III.4. Conclusions

The fragmentation techniques such as electron capture dissociation and electron transfer dissociation available in FT-ICR allow as expected the formation of reduced organometallic complexes in the gas phase. The nature of the parent dicationic complex, and in particular the metal-ligand bond strength, and the internal energy provided by the electron-based method induce the formation of various radical species. It is now clear that the choices of the ligands and of the metal are crucial, in particular if the goal is to form a hexacoordinated reduced organometallic complex in the gas phase. Based on these experimental findings, our objective to characterize in the gas phase reduced organometallic complex seems reachable. To that end, we will perform IRMPD spectroscopy experiments, which will described in chapters V and VI. Interpretation of IRMPD spectra requires in most case a computational support.

Therefore, before the experimental work, we have studied the ability of DFT functionals to describe the electronic structure of reduced organometallic complexes.

III.5. References

[1]. G. L. Glish, R. W. Vachet, *Nat. Rev. Drug Discovery*, **2003**, *2*, 140–150.

[2]. R. Aebersold, *J. Am. Soc. Mass Spectrom.*, **2003**, *14*, 685–695.

[3]. R. P. Rodgers, A. M. McKenna, *Anal. Chem.*, **2011**, *83*, 4665–4687.

[4]. I. J. Amster, *J. Mass Spectrom.*, **1996**, *31*, 1325–1337.

[5]. Y. Qi, P. B. O'Connor, *Mass Spectrom. Rev.*, **2014**, *33*, 333–352.

[6]. E. de Hoffmann, V. Stroobant, Mass Spectrometry : Principles and Applications, *Wiley, Chichester, John Wiley, Hoboken, N.J.*, **2007**.

[7]. D. P. Little, J. P. Speir, M. W. Senko, P. B. O'Connor, F. W. McLafferty, *Anal. Chem.*, **1994**, 66, 2809–2815.

[8]. R. Zubarev, K. Haselmann, B. Budnik, F. Kjeldsen, F. Jensen, *Eur. J. Mass Spectrom.*, **2002**, *8*, 337–349.

[9]. Y. Qi, D. A. Volmer, *Mass Spectrom. Rev.*, in press, DOI: 10.1002/mas.21482.

[10]. P. Perez-Hurtado, P. B. O'Connor, *Mass Spectrom. Rev.*, **2012**, *31*, 609–625.

[11]. H. J. Cooper, K. Håkansson, A. G. Marshall, *Mass Spectrom. Rev.*, **2005**, *24*, 201–222.

[12]. R. A. Zubarev, *Mass Spectrom. Rev.*, **2003**, *22*, 57–77.

[13]. J. J. Coon, J. Shabanowitz, D. F. Hunt, J. E. Syka, *J. Am. Soc. Mass Spectrom.*, **2005**, *16*, 880–882

[14]. B. A. budnik, K. F. Haselmann, R. A. Zubarev, *Chem. Phys. Lett.*, **2001**, *342*, 299–302

[15]. Y. O. Tsybin, J. P. Quinn, O. Y. Tsybin, C. L. Hendrickson, A. G. Marshall, *J. Am. Soc. Mass Spectrom.*, **2008**, *19*, 762–771.

[16]. H. J. Yoo, N. Wang, S. Zhuang, H. Song, K. Håkansson, *J. Am. Chem. Soc.*, **2011**, *133*, 16790–16793.

[17]. M. Huzarska, I. Ugalde, D. A. Kaplan, R. Hartmer, M. L. Easterling, N. C. Polfer, *Anal. Chem.*, **2010**, *82*, 2873–2878.

[18]. (a). T. D. Fridgen, *Mass Spectrom. Rev.*, **2009**, *28*, 586–607; (b) J. R. Eyler, *Mass Spectrom. Rev.*, **2009**, *28*, 448–467; (c). N. C. Polfer, J. Oomens, *Mass Spectrom. Rev.*, **2009**, 28, 468–494; J. Roithova, *Chem. Soc. Rev.*, **2012**, *41*, 547–559.

[19]. (a) P. Milko, J. Roithova, N. Tsierkezos, D. Schroder, *J. Am. Chem. Soc.*, **2008**, *130*, 7186–7187; (b). P. Milko, J. Roithova, D. Schroder, J. Lemaire, H. Schwarz, M. C. Holthausen, *Chem. – Eur. J.*, **2008**, *14*, 4318–4327; (c). P.Milko, J. Roithova, *Inorg. Chem.*, **2009**, *48*, 11734–11742; (d). L. Duchackova, V. Steinmetz, J. Lemaire, J. Roithova, *Inorg.*

Chem., **2010**, *49*, 8897–8903; (e). L. Duchackova, J. Roithova, P. Milko, J. Zabka, N. Tsierkezos D. Schroder, *Inorg. Chem*., **2011**, *50*, 771–782.

[20]. G. Frison, G. van der Rest, F. Turecek, T. Besson, J. Lemaire, P. Maitre, J. Chamot-Rooke, *J. Am. Chem. Soc*., **2008**, *130*, 14916–14917.

Chapter IV

Electronic structure of reduced radical species: a survey of DFT results

IV.1. Introduction

N-donor bidentate ligands (L) such as 2,2'-bipyridine (bpy) and phenanthroline form complexes with many transition metal. Their remarkable coordination behavior has been intensively utilized in organometallic and supramolecular chemistry.[1] The photophysical and photochemical properties of these metal polypyridyl structures allow the design of complexes with interesting luminescent[2,3] or nonlinear optical properties.[4] These complexes can also undergo reversible redox processes, which make them attractive system for use in artificial photosynthesis[5,6] or visible light photocatalysis.[7,8] Efforts put towards a better understanding of the structure and properties of these complexes have combined theoretical calculations[9] and condensed[10] and gas-phase experiments.[11] For examples, Nose and Rodgers have recently used a combination of DFT studies and mass spectrometry measurements in order to determine sequential binding energies of various transition metals dications with bpy,[12] and Weber and Xu have recorded absorption spectrum of a ruthenium(II)-aquo complex in vacuo, allowing to resolve several electronic bands contrary to what is obtained in condensed phase.[13]

Similar studies have been performed on singly reduced analogues. These radical species, obtained by a single-electron transfer, are strong reductants which are difficult to isolate in solution due to their high reactivity. Gas-phase mass spectrometry studies offer an attractive experimental strategy to form these species and access their properties in more details. Metal cation such as Sc^+, Ti^+, Cr^+, Mn^+, Fe^+, Co^+, Ni^+ or Zn^+ can be generated in a continuous direct-current discharge by Ar^+ sputtering of a cathode made from the metal of interest.[14] $[M(L)_n]^+$ complexes (n=1, 2 or 3, L = *N*-donor bidentate ligand) in their ground electronic state are then obtained by condensation of M^+ metal cation with one or more neutral L ligands in a flow tube ion source.[15] Alternatively, $[Ru(bpy)_3]^+$ complex has been obtained in the gas-

phase by reduction of $[Ru(bpy)_3]^{2+}$ in collisional electron transfer from cesium atoms.[16] Structural properties, such as gas-phase UV/Vis spectroscopy and sequential ligand-binding energy,[15] as well as reactivity toward O_2 and H_2O,[17] have been explored for these singly-reduced complexes.

However, the question regarding the electronic structure of $[M(L)_n]^+$ complexes remains controversial. Zinc complexes have been described as a Zn^+ metal center coordinated by neutral ligands, $Zn^+(L^0)_n$.[15c] On the contrary, it is now well established that the Ru and Fe metal center keep their d^6 configuration in $[Ru(L)_3]^+$ and $[Fe(L)_3]^+$ complexes, the additional electron being on the ligand, and most probably on a single ligand, which corresponds to the $[M^{2+}(L^0)_2(L^{-1})_1]$ formulation. It has however to be noted that DFT-B3LYP calculations leads to structures with three equivalent ligands, each carrying 1/3 of a spin, which correspond to a delocalized single electron over the three ligands, $[M^{2+}(L^{-1/3})_3]$.[9d] The reliability of DFT functionals for describing these radical species is thus questionable.

DFT methods are known to induce an overly disperse spin density after single-electronic reduction or oxidation of closed-shell systems.[18] Our group has shown recently that the description of the ground state electronic structure of singly-reduced doubly protonated peptides is a problematic case for "conventional" DFT functionals, including local spin density approximation (LSDA) functionals, generalized gradient approximation (GGA) functionals, *meta* GGA and most of the global hybrid (GH) functionals. Indeed, they show excess delocalization of the spin density, comparable to what is observed in charge-transfer excited states, due to the incorrect long-range behavior resulting from the self-interaction error (SIE).[19] An accurate description of the ground state with DFT methods is observed only if the functional included a full Hartree-Fock exchange at long-range interelectronic distance, even if this prerequisite is not always sufficient.[20] Others problematic cases have been described in the literature, such as iron nitrosyl complexes.[21] To the best of our knowledge, the influence

of the functionals on the electronic description of singly-reduced closed-shell $[M(L)_n]^{2+}$ complexes remains to be studied.

It has been shown that the variation of the intramolecular CC and CN bond lengths of bpy^n as a function of its charge n (n=-2, -1, 0) reflects the bonding and antibonding interactions of the bpy^0 π^* orbital (lowest unoccupied molecular orbital, LUMO).[22] This structural signature can thus be used to reveal the electronic population of the ligands in $[M(L)_n]^+$ complexes, and by the way the electronic structure of the complexes. This requires a high resolution X-ray crystallography structure, which unfortunately is not always available, as for example for $[Ru(bpy)_3]^+$ and $[Fe(bpy)_3]^+$. Geometrical structures can be obtained alternatively through DFT calculations, but the DFT functional accuracies regarding changes in bond lengths after electronic reduction remains to be estimated.

In the present chapter, a panel of exchange-correlation DFT functionals is used to investigate both the structural changes and the electronic structures of singly-reduced *N*-donor bidentate ligands and their complexes. Some coupled-cluster calculations have been additionally performed as an attempt to benchmark the DFT results. We have examined two heteroleptic four-coordinate zinc complexes $\mathbf{I}^{n+}$ and $\mathbf{II}^{n+}$ (n = 1, 2), which are built from three *N*-donor bidentate ligands (**1**, **2** and **4**).

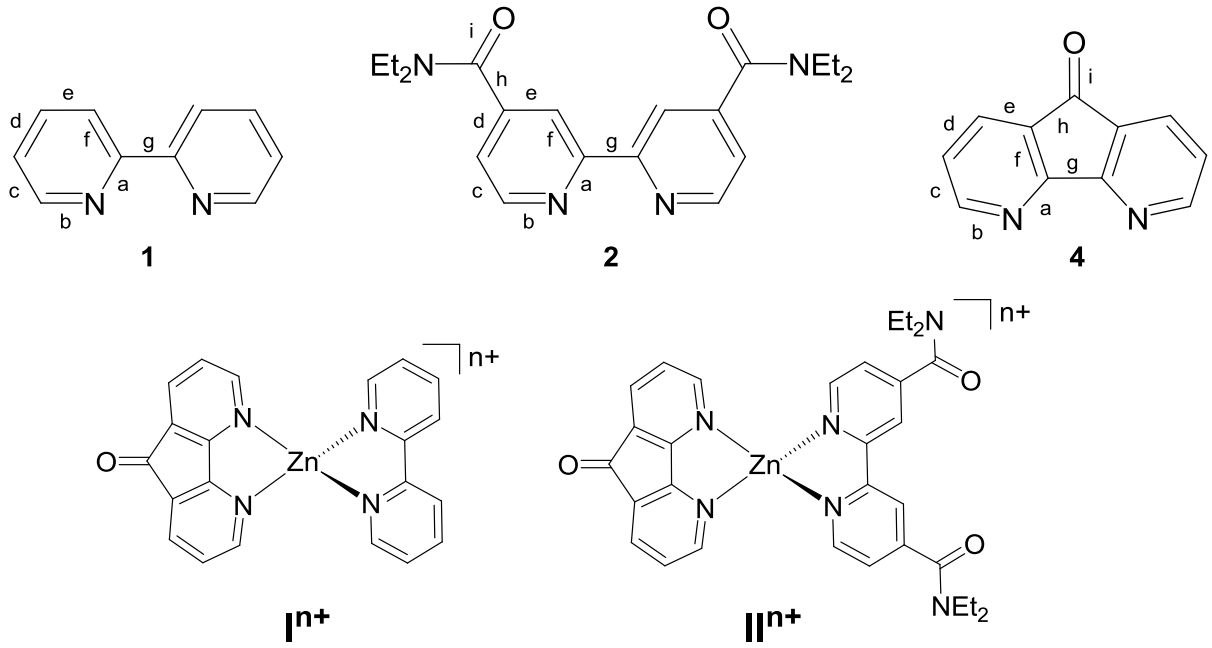

Scheme 4.1. *Zn complexes* ***I-II*** *and N-donor bidentate ligands* ***1***, ***2*** *and* ***4*** *studied in this chapter*.

IV.2. Computational methods

Calculations in chapter IV were carried out with the Gaussian09 package[23] and all structures were fully optimized without any symmetry constraints at the DFT level. Eleven different exchange-correlation functionals, which cover different categories from "conventional" to range-separated hybrid (RSH) functionals based on the amount of Hartree-Fock (HF) exchange have been applied for these calculations. This includes three different families of functionals:

(i) The "B + LYP" family is based on the Becke exchange functional published in 1988 and the Lee-Yang-Parr correlation functional. This series includes 4 functionals: one generalized gradient approximation (GGA) functional BLYP which has 0% of HF exchange;[24] the hybrid-GGA B3LYP,[25] which includes 20%

of HF exchange; and the RSHs CAM-B3LYP[26] and LC-BLYP,[27] which include 19/65 and 0/100% of HF exchange contribution at short/long-range, respectively.

(ii) The Minnesota suite developed in 2006 by the Truhlar group. Its includes also 4 functionals: one meta-GGA functional M06L (0% of HF exchange),[28] and three hybrid-meta-GGA functionals M06,[29] M06-2X[30] and M06-HF[31] which includes 27, 54 and 100% of HF exchange respectively.

(iii) The "ωB97" family developed by the Martin-Gordon group RSHs, which includes three RSHs functionals: ωB97X-D,[32] ωB97X[33] and ωB97.[34] These functionals present a growing fraction of HF exchange with increasing inter-electronic separation, with a 22.2/100, 15.77/100 and 0/100% of HF exchange contribution at short/long-range, respectively. More importantly, the speed of the transition from Kohn-Sham exchange to HF exchange is governed by the attenuation parameter ω whose value is 0.2, 0.3 and 0.4 a.u. for these three functionals, respectively. These ω values imply that ωB97X-D has somewhat higher self-interaction errors than ωB97X and especially ωB97.

The basis set def2-SVP, developed by Weigend and Ahlrichs,[35] has been used for geometry optimization for all atoms. For each stationary point, we carried out a vibrational frequency calculation at the same level to characterize their nature as minima. In order to improve the energy values, single point calculations were performed on optimized geometries of **1**, **2**, **4** and **I** with higher triple-ζ basis set def2-TZVPP.[36]

The optimized geometry of ligand **4** in its neutral and reduced forms was also computed at the CCSD coupled-cluster method.[37] In that case, $\mathbf{4^0}$ and $\mathbf{4^{-1}}$ were constrained in their C_{2v} geometries, which were obtained in all cases at the DFT level without constrain, and split valence def2-SVP and 6-31+G(d,p)[38] basis set were used to define all atoms.

In order to ascertain that the wave functions of open-shell species correspond to the minimum, their stability has been tested with the "stable" approach implemented in Gaussian09. Calculations on all open-shell species (negative ligands and monocationic complexes) used the spin-unrestricted formalism. In all DFT calculations, contamination by higher spin states was negligible to modest (the spin operator $\langle S^2 \rangle$ values are between 0.75 and 0.81), whereas it was significant for all CCSD calculation ($\langle S^2 \rangle$ values up to 1.50). The spin density populations are obtained from the difference between α-spin and β-spin natural bond orbital (NBO) atomic charges computed at the same DFT level of calculation with the NBO program implemented in Gaussian09.

IV.3. Single reduction of the ligands

We started this chapter with the study of ligands **1**, **2** and **4** and their mono-electronic reduced forms $\mathbf{1}^{-1}$, $\mathbf{2}^{-1}$ and $\mathbf{4}^{-1}$, respectively. The geometries of these neutral and anionic forms have been optimized with the eleven functionals selected in this chapter. All geometry optimizations at the DFT level have been performed with the def2-SVP basis set. As expected,[39] $\mathbf{1}^{0}$ and $\mathbf{2}^{0}$ present a twisted structure at the CC bond between the 6-membered rings, whereas their anionic forms, as well as $\mathbf{4}^{0}$ and $\mathbf{4}^{-1}$, show almost planar geometries (but the $C(O)NEt_2$ substituents for $\mathbf{2}^{-1}$).

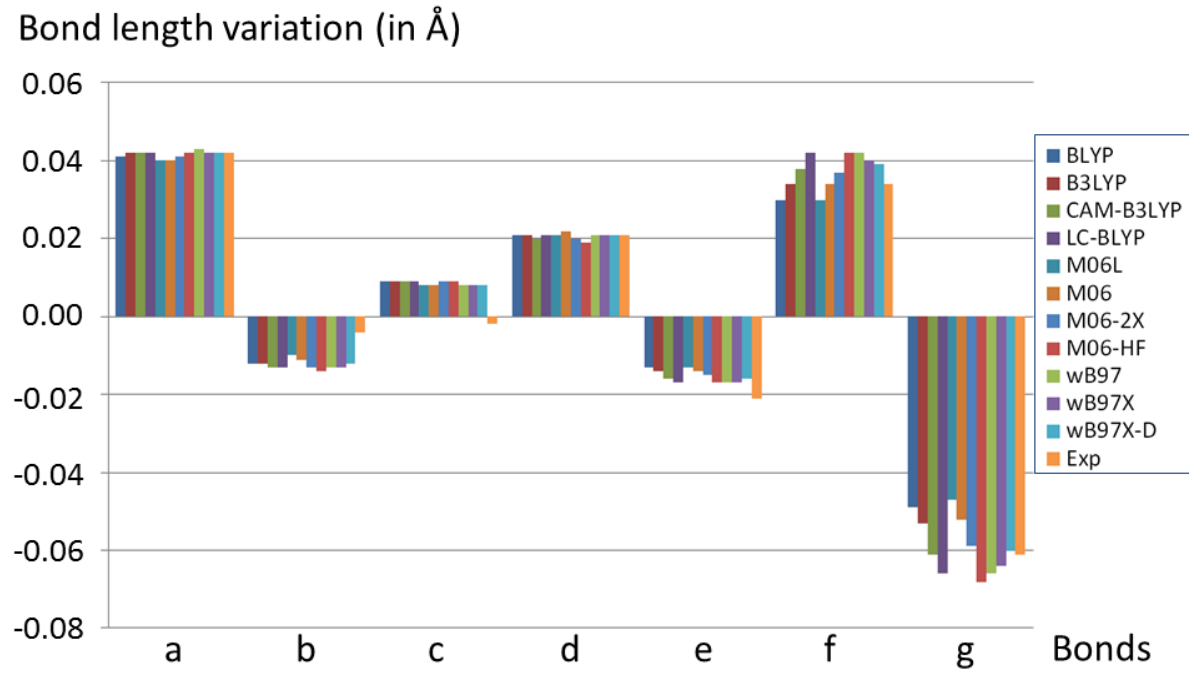

Figure 4.1. *Bond length variations between neutral* ***1*** *and singly-reduced* $\mathbf{1}^{-1}$. *Experimental values from ref [22]. See Scheme 4.1 for the definition of bonds a-g.*

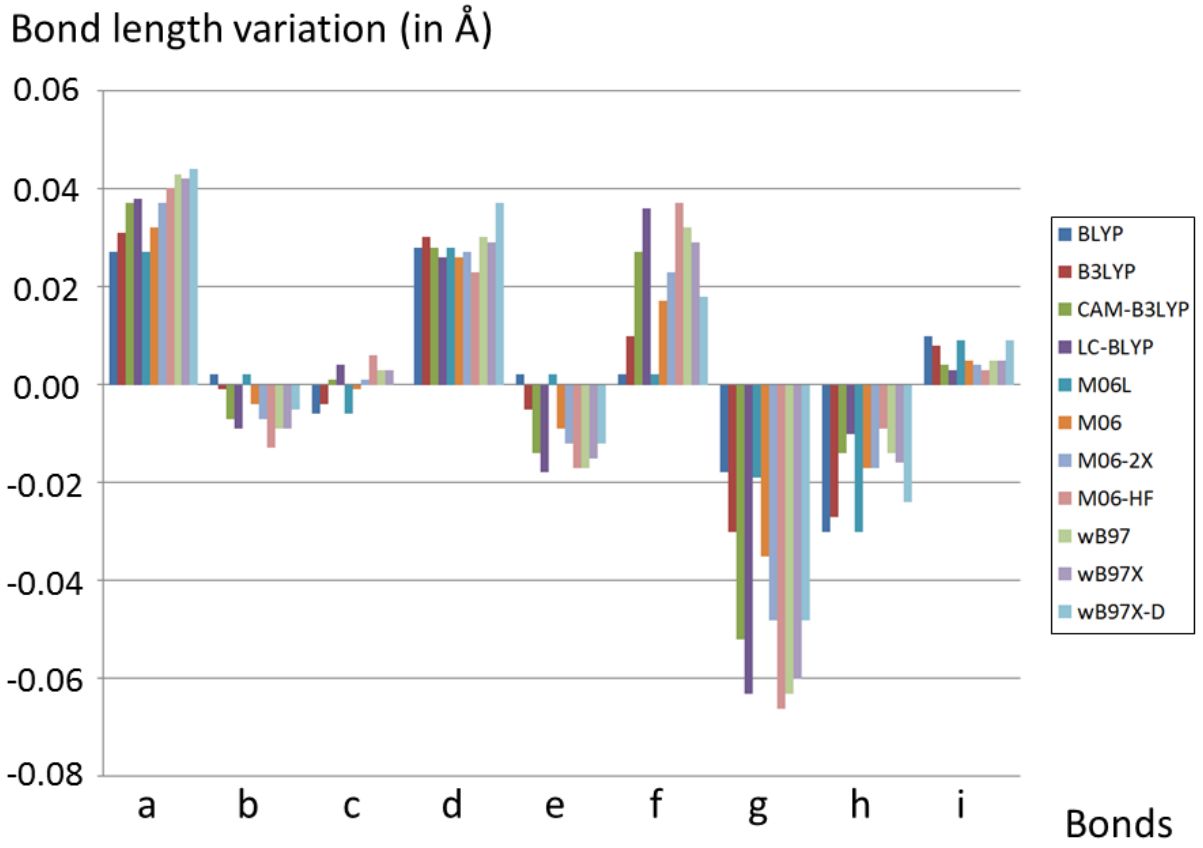

Figure 4.2. *Bond length variations between neutral* ***2*** *and singly-reduced* $\mathbf{2}^{-1}$.

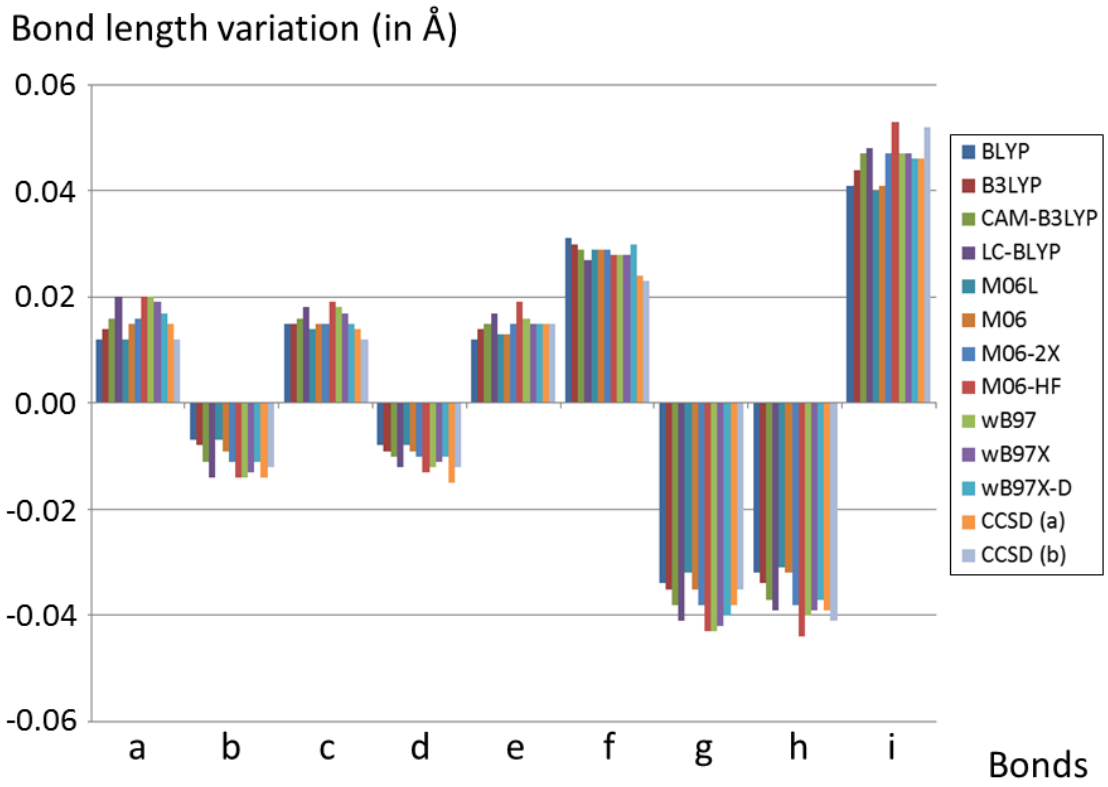

Figure 4.3. *Bond length variations between neutral* ***4*** *and singly-reduced* $\mathbf{4}^{-1}$. *(a) geometry optimization at the CCSD/def2-SVP level. (b) geometry optimization at the CCSD/6-31+G(d,p) level.*

The single reduction of neutral *N*-donor bidentate ligands **1**, **2** and **4** induces change in the CC, CN and CO bond lengths. This is illustrated in Figures 4.1-4.3 for **1**, **2** and **4**, respectively. All DFT functionals indicate that the incoming electron locates roughly in the LUMO of the neutral system of $\mathbf{1}^{0}$, $\mathbf{2}^{0}$ and $\mathbf{4}^{0}$, which therefore nearly correspond to the SOMO of the anionic form (Figure 4.4). Consequently, the CC, CN and CO bond length variations upon reduction correspond to the bonding or antibonding nature of these bonds in the LUMO of the neutral system.[22] Despite the good qualitative agreement between the results obtained using the various functionals, which agrees with the similar nature of the LUMO for all functionals (Figure 4.5), small quantitative differences can be observed in the bond length variations upon reduction. We noticed for example that the lengthening of the CC bond 'f' and the shortening of the CC bond 'g' in $\mathbf{1}^{-1}$ relative to $\mathbf{1}^{0}$ slightly depends on the functionals (Figure 4.1). Careful examination of these data indicates that the higher the amounts of

Hartree-Fock (HF) exchange in the functional, the higher the 'f' and 'g' bond lengths variations. Very similar trends are obtained for **1** and **4** (Figures 4.2-4.3).

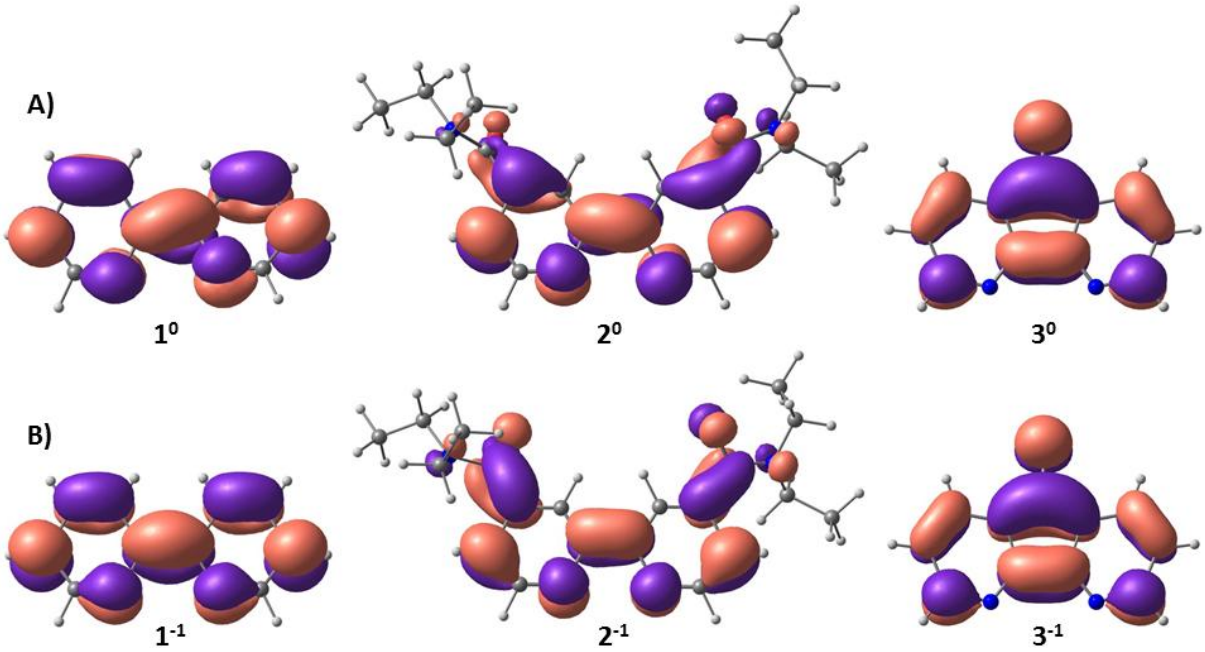

Figure 4.4. *Lowest unoccupied molecular orbital (LUMO) of **1**, **2** and **4** (A), and the singly occupied molecular orbital (SOMO) in their respective monoanionic reduced form (B) computed at the BLYP level.*

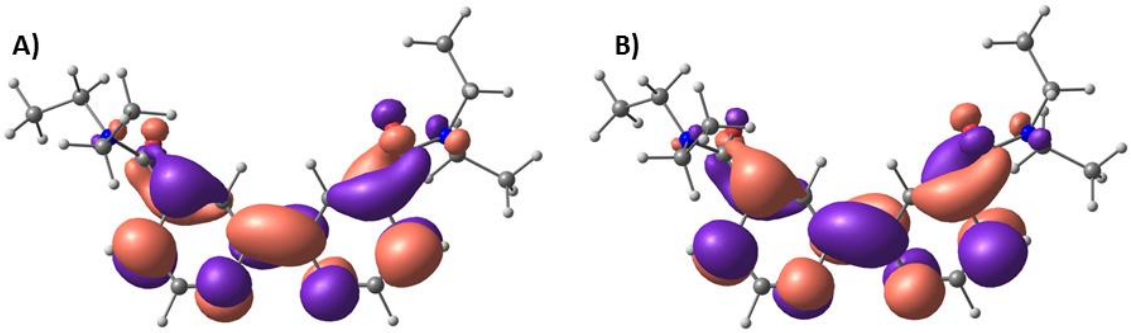

Figure 4.5. *LUMO of **2** at the BLYP (A) and LC-BLYP (B) level.*

Based on the previous studies in our group relative to the ability of DFT to describe the electronic structure of singly-reduced peptides,[19,20] we can postulated that long-range corrected DFT give the most satisfying results. However, it would be preferable to have other comparative data. Comparison with experimental values for **1** is possible as X-ray structures

of neutral $\mathbf{1}^{\mathbf{0}}$ and anionic $\mathbf{1}^{\mathbf{-1}}$ bipyridine have been published.[22] The comparison is difficult because the result depends on the bond which is considered. Therefore, differences and similarities between experimental and theoretical bond lengths are not sharp enough to conclude on the required best level of HF exchange, even if a significant high amount seems to be better. Higher level calculation methods can also be used to benchmark the DFT levels. However, to be reliable, these calculations must be performed at least at a coupled-cluster level with a large basis set. We have therefore selected the CCSD level. Due to the memory demand of this method, we could make these calculations only for the ligand **4** since it has C_{2v} symmetry for both the neutral and anionic form. We could unfortunately not use a triple zeta basis set for these calculations because our computer resources did not allow it. Therefore, we have used both the def2-SVP and 6-31+G(d,p) basis set (Figure 4.3). Again, the comparison is not easy because the result depends on the bond. For example, a higher amount of HF exchange induces DFT results which are closer to CCSD results for 'h' and 'i', whereas the opposite is observed for 'g'. The former case seems however to be more frequent, which argues for the long-range corrected DFT, even if this conclusion remains to be confirmed. It should furthermore be noticed that CCSD calculations of $\mathbf{4}^{\mathbf{-1}}$ suffer from large spin contamination, which makes these results difficult to be used as reference.

These various bond length variations reveal weak differences in the electronic structure of the singly-reduced systems depending on the functionals. Indeed, the increase of the amount of HF exchange induces a small decrease of the single electron delocalization over the whole π-system. The unrestricted nature of the wave functions leads therefore to larger amount of atomic α and β spin density on the carbon and nitrogen atoms of the six-membered ring (Figure 4.6). Similarly, the delocalization of the spin-density over the amide moiety in $\mathbf{2}^{\mathbf{-1}}$ is significantly lowered with the functionals such as CAM-B3LYP, LC-BLYP or M06-HF, which presents high amount of HF exchange (Figure 4.6). It is significant that these

differences arise only from the reduction process, as the LUMO of the neutral systems does not depend on the functional (Figure 4.5).

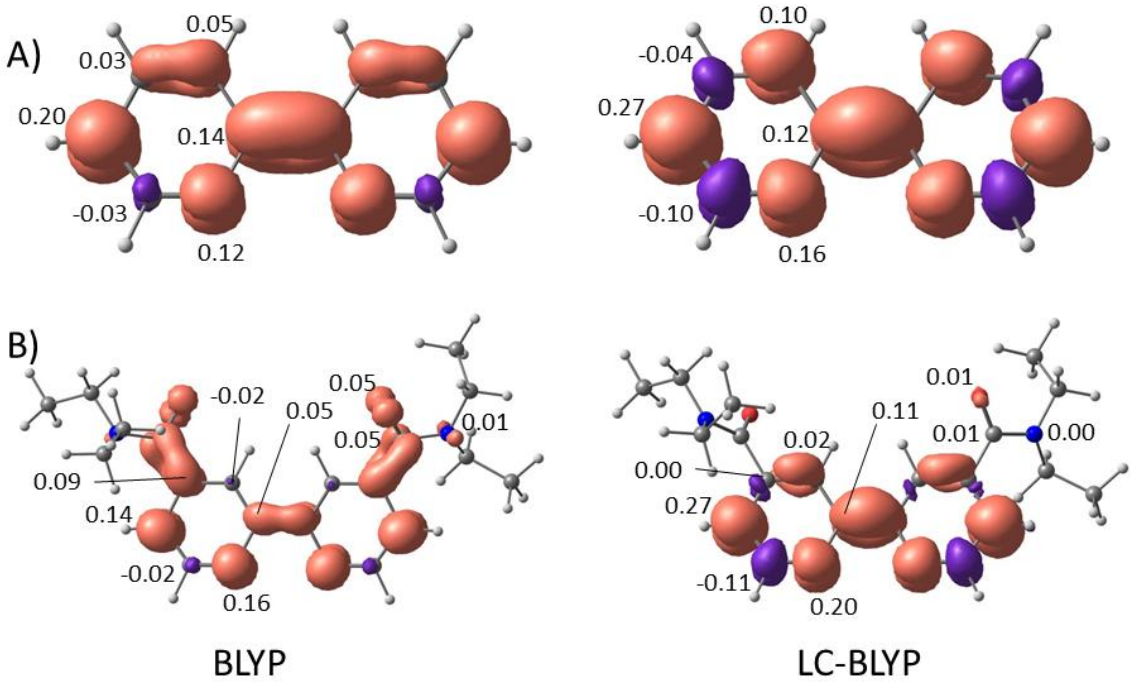

***Figure 4.6**. Spin density (isosurface at 0.0025 a.u.) and NBO spin density population (α-β) for **1**$^{-1}$ and **2**$^{-1}$ computed with the BLYP (A) and LC-BLYP (B) functionals.*

In addition to the geometric and electronic structure, we have examined the effect of the functional on the energy associated with the reduction process. To that end, we calculated the vertical (EA_v) and adiabatic (EA_a) electron affinities of the neutrals **1**, **2** and **4** and the relaxation energy (E_R) associated with the geometry variation due to the addition of one electron (Figure 4.7). Energy values were obtained first with the def2-SVP basis set at the geometries obtained at the DFT/def2-SVP level. Furthermore, single-point energy calculations were performed with the def2-TZVPP basis set at the DFT/def2-SVP geometries. The values obtained for **1**, **2** and **4** with the eleven functionals are indicated in Table 4.1 (DFT/def2-SVP levels) and Table 4.2 (DFT/def2-TZVPP//DFT/def2-SVP levels).

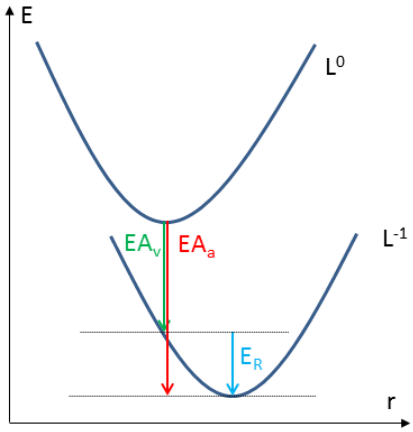

***Figure 4.7**. Definition of vertical (EA_v) and adiabatic (EA_a) electron affinities and relaxation energy (E_R).*

All functionals agree that the electron capture is an exothermic process, but for **1** with the def2-SVP basis set for most of the functionals. Nevertheless, the trends observed with def2-SVP and def2-TZVPP basis sets are similar and only the latter results will be discussed. For all functionals, the order of electron affinity is **4** > **2** > **1**. The amide electron withdrawing group induces higher adiabatic electron affinity for **2** compared to **1** by about 45 kJ.mol^{-1}, and the carbonyl bridge in **4** further improves the electron affinity by roughly 70 kJ.mol^{-1}. As expected, the planar structure of **4** in both its neutral and anionic forms induces lower recombination energy upon reduction compared to **1** and **2** for which the reduction step induces rotation around the N-C-C-N link.

Table 4.1. Computed relaxation energy and vertical and adiabatic electron affinities of **1**, **2** and **4** (in kJ.mol^{-1}) at the DFT/def2-SVP levels

	1			**2**			**4**		
	EA_v	EA_a	E_R	EA_v	EA_a	E_R	EA_v	EA_a	E_R
BLYP	-27	-2	26	24	53	29	96	110	14
B3LYP	-27	4	31	24	54	30	105	122	17
CAM-B3LYP	-46	-6	39	5	38	34	92	112	21
LC-BLYP	-58	-10	48	-7	34	41	82	106	24
M06L	-12	14	26	40	69	29	114	129	15
M06	-20	11	32	33	61	28	109	126	17

M06-2X	-39	-2	36	15	46	31	99	121	21
M06-HF	-63	-16	47	-8	32	42	90	116	27
ωB97	-54	-8	46	-5	35	40	82	106	23
ωB97X	-53	-9	44	-4	34	39	86	109	22
ωB97X-D	-48	-6	41	5	40	34	94	115	21

Table 4.2. Computed relaxation energy and vertical and adiabatic electron affinities of **1**, **2** and **4** (in $kJ.mol^{-1}$) at the DFT/def2-TZVPP//DFT/def2-SVP levels

	1			**2**			**4**		
	EA_v	EA_a	E_R	EA_v	EA_a	E_R	EA_v	EA_a	E_R
BLYP	-2	17	19	49	67	18	122	133	11
B3LYP	-5	20	25	45	66	20	125	139	14
CAM-B3LYP	-22	10	32	26	51	25	114	131	17
LC-BLYP	-32	8	40	17	49	33	107	127	20
M06L	-8	13	21	45	68	23	115	127	12
M06	-8	17	25	44	64	20	118	130	12
M06-2X	-19	12	31	33	58	24	116	134	19
M06-HF	-31	11	42	24	60	36	117	141	24
ωB97	-36	4	39	12	45	33	100	120	20
ωB97X	-34	3	37	13	44	31	103	122	19
ωB97X-D	-32	3	35	21	47	26	107	124	17

Once again, quantitative differences can be observed between the various functionals. We have seen previously that the bond length variations upon reduction depend on the DFT functionals. In particular, we observe in most cases that the higher the amounts of HF exchange, the larger the bond length variations, and then consequently the larger the computed relaxation energy. We also observe that larger amount of HF exchange induces smaller vertical electron affinities. This is related to the effect of the HF exchange on the electronic delocalization. A higher percentage of HF exchange induces that the added electron

is more localized, so that the Coulomb repulsion term is stronger, which is unfavorable to the electron capture.

The study of the DFT functional effect on the electron capture by a *N*-donor ligand reveals relatively small changes which are purely quantitative. Qualitatively, all functionals give the same trends in terms of bond length variation, spin density variation or electron affinity. We then turn our interest to the single reduction of the two heteroleptic four-coordinate zinc complexes $[Zn(\mathbf{1})(\mathbf{4})]^{2+}$ and $[Zn(\mathbf{2})(\mathbf{4})]^{2+}$, named respectively $\mathbf{I}^{2+}$ and $\mathbf{II}^{2+}$ (Scheme 4.1).

IV.4. Single reduction of the zinc complexes

As for the ligands, we first examine for complexes $\mathbf{I}^{2+}$ and $\mathbf{II}^{2+}$ the bond length variations upon reduction at the eleven DFT functionals. The results obtained for $\mathbf{I}^{2+}$ are shown in Figure 4.8. Similar results have been obtained for $\mathbf{II}^{2+}$ and they will therefore not be discussed. As previously, the bond length variations depend upon the DFT level.

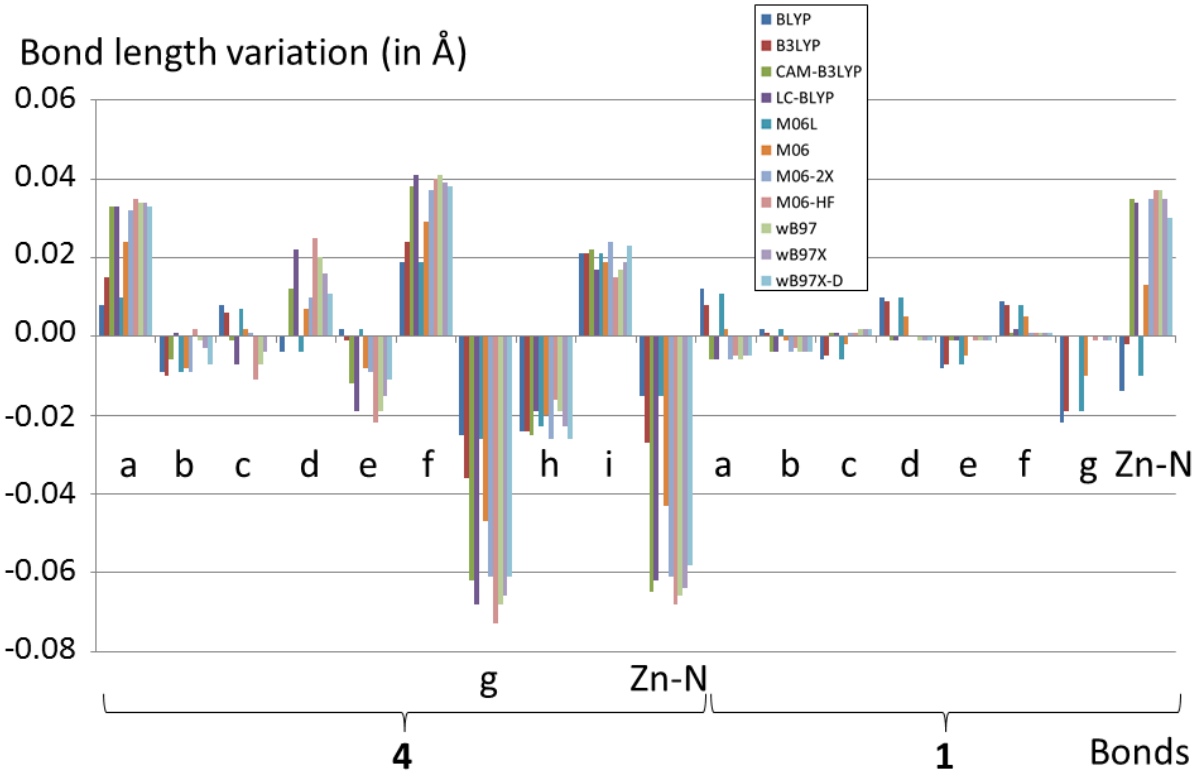

***Figure 4.8**. Bond length variations between dicationic **I**$^{2+}$ and singly-reduced **I**$^{\bullet+}$. See Scheme 4.1 for the definition of bonds.*

In most cases, only the variation intensities depend on the functional, even if the differences can be significantly larger than for the free ligands. For example, upon reduction, the bond length of 'g' for **4** decreases by -0.034 and -0.041 Å at the BLYP and LC-BLYP levels, respectively, whereas it is shortened by -0.025 and -0.068 Å in **II**. We also observe that reverse bond length variation can be obtained between "standard" DFT and long-range corrected DFT. In particular, the Zn-N bond length between ligand **1** and the metal cation is shortened upon reduction at the BLYP, B3LYP and M06L levels whereas it is lengthened with the other functionals. We also observed that the bond lengths remain almost unchanged in ligand **1** of **I** for all methods but BLYP, B3LYP, M06L and M06.

The explanation of these significant geometrical differences can be deduced from the examination of the SOMO (or the spin density) after reduction, depending on the functionals (Figure 4.9). Indeed, at the BLYP, B3LYP, M06 and M06L levels, the added electron in the

optimized geometry of $\mathbf{I}^{\bullet+}$ is delocalized on the two ligands. On the opposite, for all other methods, the added electron is only located on the ligand **4**.

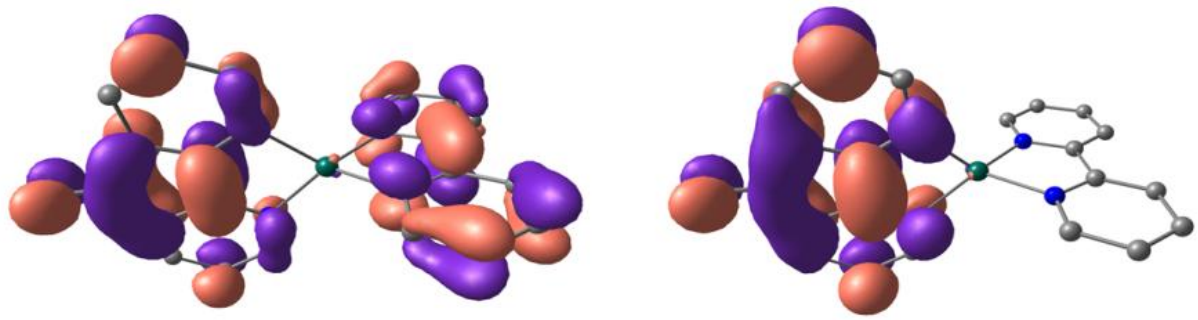

***Figure 4.9**. SOMO of $\boldsymbol{I}^{\bullet+}$ computed at the B3LYP (left) and LC-BLYP (right) level.*

Table 4.3. NBO spin density population of $\mathbf{I}^{\bullet+}$ and $\mathbf{II}^{\bullet+}$ after vertical and adiabatic reduction of $\mathbf{I}^{2+}$ and $\mathbf{II}^{2+}$. Calculations at the DFT/def2-SVP level.[a]

	I				**II**			
	Vertical reduction		Adiabatic reduction		Vertical reduction		Adiabatic reduction	
	1	**4**	**1**	**4**	**2**	**4**	**2**	**4**
BLYP	0.43	0.55	0.41	0.57	0.39	0.60	0.36	0.63
B3LYP	0.40	0.59	0.32	0.67	0.35	0.63	0.22	0.77
CAM-B3LYP	0.00	0.99	0.00	0.99	0.00	0.99	0.00	0.99
LC-BLYP	0.00	0.99	0.00	0.99	0.00	0.99	0.00	0.99
M06L	0.43	0.57	0.39	0.60	0.39	0.61	0.34	0.65
M06	0.38	0.60	0.19	0.81	0.33	0.65	0.04	0.95
M06-2X	0.12	0.87	0.00	0.99	0.00	0.99	0.00	1.00
M06-HF	0.00	0.99	0.00	0.99	0.00	0.99	0.00	0.99
ωB97	0.00	0.99	0.00	0.99	0.00	0.99	0.00	0.99
ωB97X	0.00	0.99	0.00	0.99	0.00	0.99	0.00	0.99
ωB97X-D	0.00	0.99	0.00	0.99	0.00	0.99	0.00	1.00

[a] Spin density at the zinc metal center is in all cases lowest than 0.01 electron.

Closer examination of the spin density distribution on $\mathbf{I}^{\bullet+}$ and $\mathbf{II}^{\bullet+}$ show interesting trends. Both after vertical and adiabatic reduction, the added electron is located only on ligand **4** with the CAM-B3LYP, LC-BLYP, M06-HF, ωB97, ωB97X and ωB97X-D functionals. M06-2X shows almost the same behavior, except for the vertical reduction of $\mathbf{I}^{2+}$ for which a partially delocalized electron on both ligands **1** and **4** is computed. BLYP, B3LYP, M06L and M06 show spin density on both ligands in all cases. It is noticeable that the amount of spin density on **1** (in $\mathbf{I}^{\bullet+}$) and in **2** (in $\mathbf{II}^{\bullet+}$) is related to the amount of HF exchange on the functional. Indeed, B3LYP and M06 show lower spin density on **1** and **2** compared respectively to BLYP and M06L. We also noted that the delocalization on the two ligands slightly decreases upon geometry optimization.

Data on Table 4.3 also show that ligand **4** contain in all cases the majority or the totality of the spin density. This agrees with its higher electron affinity compared to **1** and **2**. However, we observed that **2**, which has a higher electron affinity compared to **1**, has a lower spin density compared to **1**. We do not have any explanation for this observation.

These differences in the spin density distribution explain the difference in bond length variation. The $[Zn^{2+}(\mathbf{1}^{\mathbf{0}})(\mathbf{4}^{\mathbf{-1}})]$ electronic structure of $\mathbf{I}^{\bullet+}$ computed with the long-range corrected functionals explains that (*i*) the bond lengths in **1** remain almost unchanged upon reduction; (*ii*) the Zn-N bond lengths between Zn and **4** decrease, inducing lower Lewis acidity of the metal center and thus a longer Zn-N bond length between Zn and **1**. On the opposite, the $[Zn^{2+}(\mathbf{1}^{\mathbf{-1/2}})(\mathbf{4}^{\mathbf{-1/2}})]$ electronic structure given by standard DFT induces that both ligands are more tightly bounded to the metal center.

Last, we computed the vertical and adiabatic electron affinities for these dicationic complexes. The results are indicated in Table 4.4.

Table 4.4. Computed relaxation energy and vertical and adiabatic electron affinities of $\mathbf{I}^{2+}$ and $\mathbf{II}^{2+}$ (in kJ.mol^{-1}).

	I[a]			**I**[b]			**II**[a]		
	EA_v	EA_a	E_R	EA_v	EA_a	E_R	EA_v	EA_a	E_R
BLYP	739	747	8	749	755	6	704	717	12
B3LYP	731	742	11	737	746	9	706	720	14
CAM-B3LYP	701	730	29	707	735	27	684	715	31
LC-BLYP	698	733	34	706	739	32	684	719	35
M06L	757	766	9	745	752	7	727	740	12
M06	734	746	12	729	738	9	711	728	17
M06-2X	704	733	29	707	735	28	688	719	30
M06-HF	690	724	35	706	739	33	677	712	35
ωB97	694	728	33	696	728	32	679	713	34
ωB97X	697	728	32	698	728	30	681	714	33
ωB97X-D	703	731	29	702	729	27	686	717	30

[a] Computed at the DFT/def2-SVP level. [b] Computed at the DFT/def2-TZVPP//DFT/def2-SVP level.

For these cationic species, we observe that the DFT/def2-TZVPP//DFT/def2-SVP and DFT/def2-SVP levels give almost similar values for **I**. Therefore, regarding the extended size of **II**, calculations with the def2-TZVPP basis set have been performed only for **I**. The difference in electron affinity between $\mathbf{I}^{2+}$ and $\mathbf{II}^{2+}$ is about 20 kJ.mol^{-1} in all cases, which is smaller than the difference between the electron affinities between the ligands. This agrees with the observation that the added electron is only (or mostly) located on ligand **4**. The difference between the various functionals is not large for these calculations, however we noted that the relaxation energy is significantly smaller with the standard DFT compared to the long-range corrected functionals. This agrees with the fact that, with the latter, the Zn-N bond lengths show larger variations because one ligand becomes more tightly bonded whereas the other is less tightly bonded.

IV.5. Conclusion

Based on the literature survey and previous work in our group, we suspected that the electronic structure determination of radical reduced *N*-donor ligands and their organometallic complexes can be a problematic case for DFT methods. The results obtained in this chapter confirm this hypothesis. Geometrical and electronic structures of 3 bipyridyl-type ligands **1**, **2** and **4** and two of their tetracoordinated zinc complexes were studied in their close-shell and singly-reduced open-shell states by various density functionals ranging from GGA to RSHs. Depending on the functionals used for the calculations, various electronic structures have been obtained for the reduced species, inducing diverse bond length variations upon reduction and electron affinities. These observations can be explained on the basis of relationship between the amount of HF exchange involved in the applied DFT functionals, and in particular at long interelectronic range, and the localized/delocalized behavior of the added electron. Indeed, self-interaction error promotes a delocalized single electron whereas long-range corrected functionals leads to structure with a more localized spin density. In particular, for $[Zn(L)(L')]^{\bullet+}$-type structures, a $[Zn^{2+}(L^{-1})(L'^{0})]$ electronic structure is obtained with RSH functionals (CAM-B3LYP, LC-BLYP, ωB97, ωB97X, ωB97X-D) and M06-HF, whereas a delocalized $[Zn^{2+}(L^{-1/2})(L'^{-1/2})]$ electronic structure is computed with BLYP, B3LYP, M06L and M06 functionals. Results from the M06-2X functional are almost similar to those obtained with the former, even if a partly delocalized electron on both ligand is observe when $[Zn(\mathbf{1})(\mathbf{4})]^{2+}$ is vertically reduced. Comparisons of these diverse results with experimental data from X-ray studies and with high level theoretical calculations are mainly inconclusive, even if they suggest, in agreement with previous studies on others molecular systems, that a high level of HF exchange is more desirable. In view of these difficulties of DFT calculations, it would be very interesting to obtain experimental evidence of the electronic structure of these

radical organometallic species that we are able to form and isolate in the gas phase. Therefore, the measure of infrared signatures of these species would allow not only to characterize them experimentally, but also to assess the reliability of DFT functionals. This is achieved in chapters V and VI.

IV.6. References

[1]. U.S. Schubert, C. Eschbaumer, *Angew. Chem. Int. Ed.* **2002**, *41*, 2892–2926.

[2]. A. Barbieri, G. Accorsi, N. Armaroli, *Chem. Commun.* **2008**, 2185–2193.

[3]. R.D. Costa, E. Orti, H.J. Bolink, F. Monti, G. Accorsi, N. Armaroli, *Angew. Chem. Int. Ed.* **2012**, *51*, 8178–8211.

[4]. H. Le Bozec, V. Guerchais, *C. R. Chimie* **2013**, *16*, 1172–1182.

[5]. E.S. Andreiadis, M. Chavarot-Kerlidou, M. fontecave, V. Artero, *Photochem. Photobiol.* **2011**, *87*, 946–964.

[6]. M.D. Kärkäs, O. Verho, E.V. Johnston, B. Akermark, *Chem. Rev.* **2014**, *114*, 11863–12001.

[7]. T.P. Yoon, M.A. Ischay, J. Du, *Nat. Chem.* **2010**, *2*, 527–532.

[8]. C.K. Prier, D.A. Rankic, D.W.C. MacMillan, *Chem. Rev.* **2013**, *113*, 5322–5363

[9]. (a) A. Vlcek Jr., S. Zalis, *Coord. Chem. Rev.* **2007**, *251*, 258–287.;(b) C.C. Scarborough, S. Sproules, T. Weyhermuller, S. DeBeer, K. Wieghardt, *Inorg. Chem.* **2011**, *50*, 12446–12462. ;(c) A.C. Bowman, S. Sproules, K. Wieghardt, *Inorg. Chem.* **2012**, *51*, 3707–3717.; (d) J. England, C.C. Scarborough, T. Weyhermuller, S. Sproules, K. Wieghardt, *Eur. J. Inorg. Chem.* **2012**, 4605–4621.; (e) A.C. Bowman, J. England, S. Sproules, T. Weyhermuller, K. Wieghardt, *Inorg. Chem.* **2013**, *52*, 2242–2256.; (f) M. Wang, T. Weyhermuller, J. England, K. Wieghardt, *Inorg. Chem*. **2013**, *52*, 12763–12776.; (g) M. Wang, T. Weyhermuller, K. Wieghardt, *Chem. Eur. J.* **2014**, *20*, 9037–9044.; (h) M. Wang, J. England, T. Weyhermuller, K. Wieghardt, *Inorg. Chem.* **2014**, *53*, 2276–2287.; (i) C. Wolff, A. Gottschlich, J. England, K. Wieghardt, W. Saak, D. Haase, R. Beckhaus, *Inorg. Chem.* **2015**, *54*, 4811–4820.; (j) J. England, E. Bill, T. Weyhermuller, F. Neese, M. Atanasov, K. Wieghardt, *Inorg. Chem.* **2015**, *54*, 12002–12018.

[10]. (a) K. Kalyanasundaram, *Coord. Chem. Rev.* **1982**, *46*, 159–244.; (b) W. Kaim, *Coord. Chem. Rev.* **1987**, *76*, 187–235.; (c) E.C. Constable, *Adv. Inorg. Chem.* **1989**, *34*, 1–63.; (d) C. Turro, Y.C. Chung, N. Leventis, M.E. Kuchenmeister, P.J. Wagner, G.E. Leroi, *Inorg. Chem.* **1996**, *35*, 5104–5106.

[11]. (a) N.G. Tsierkezos, M. Diefenbach, J. Roithova, D. Schröder, H. Schwarz, *Inorg. Chem.* **2005**, *44*, 4969–4978.; (b) L. Duchackova, V. Steinmetz, J. Lemaire, J. Roithova, *Inorg. Chem.* **2010**, *49*, 8897–8903.; (c) M.B.S. Kirketerp, S. Brondsted Nielsen, *Int. J. Mass*

Spectrom. **2010**, *297*, 63–66. (d) M.H. Stockett, S. Brondsted Nielsen, *J. Chem. Phys.* **2015**, *142*, 171102.

[12]. H. Nose, M.T. Rodgers, *ChemPlusChem* **2013**, *78*, 1109–1123.

[13]. S. Xu, J.M. Weber, *J. Phys. Chem. A* **2015**, *119*, 11509–11513.

[14]. M.T. Rodgers, J.R. Stanley, R. Amunugama, *J. Am. Chem. Soc.* **2000**, *122*, 10969–10978.

[15]. (a) N.S. Rannulu, M.T. Rodgers, *J. Phys. Chem. A* **2007**, *111*, 3465–3479.; (b) N.S. Rannulu, M.T. Rodgers, *J. Phys. Chem. A* **2009**, *113*, 4534–4548.; (c) N.S. Rannulu, M.T. Rodgers, *J. Phys. Chem. A* **2012**, *116*, 1319–1332.

[16]. C. Skinnerup Byskov, J.M. Weber, S. Brondsted Nielsen, *Phys. Chem. Chem. Phys.* **2015**, *17*, 5561–5564.

[17]. H. Cox, C. Norris, G. Wu, J. Guan, S. Hessey, A.J. Stace, *Dalton Trans.* **2011**, *40*, 11200–11210.

[18]. A.J. cohen, P. Mori-Sanchez, W. Yang, *Science* **2008**, *321*, 792–794.

[19]. A.I. Gilson, G. van der Rest, J. Chamot-Rooke, W. Kurlancheek, M. Head-Gordon, D. Jacquemin, G. Frison, *J. Phys. Chem. Lett.* **2011**, *2*, 1426–1431.

[20]. (a) V. Riffet, D. Jacquemin, E. Cauët, G. Frison, *J. Chem. Theory Comput.* **2014**, *10*, 3308–3318.; (b) V. Riffet, D. Jacquemin, G. Frison, *Int. J. Mass Spectrom.* **2015**, *390*, 28–38.

[21]. (a) J. Conradie, A. Ghosh, *J. Phys. Chem. B* **2007**, *111*, 12621–12624.; (b) K. Boguslawski, C.R. Jacob, M. Reiher, *J. Chem. Theory Comput.* **2011**, *7*, 2740–2752.

[22]. E. Gore-Randall, M. Irwin, M.S. Denning, J.M. Goicoechea, *Inorg. Chem.* **2009**, *48*, 8304–8316.

[23]. M. J. Frisch, G. W. Trucks, H. B. Schlegel, G. E. Scuseria, M. A. Robb, J. R. Cheeseman, G. Scalmani, V. Barone, B. Mennucci, G. A. Petersson, H. Nakatsuji, M. Caricato, X. Li, H. P. Hratchian, A. F. Izmaylov, J. Bloino, G. Zheng, J. L. Sonnenberg, M. Hada, M. Ehara, K. Toyota, R. Fukuda, J. Hasegawa, M. Ishida, T. Nakajima, Y. Honda, O. Kitao, H. Nakai, T. Vreven, J. A. Montgomery, Jr., J. E. Peralta, F. Ogliaro, M. Bearpark, J. J. Heyd, E. Brothers, K. N. Kudin, V. N. Staroverov, T. Keith, R. Kobayashi, J. Normand, K. Raghavachari, A. Rendell, J. C. Burant, S. S. Iyengar, J. Tomasi, M. Cossi, N. Rega, J. M. Millam, M. Klene, J. E. Knox, J. B. Cross, V. Bakken, C. Adamo, J. Jaramillo, R. Gomperts, R. E. Stratmann, O. Yazyev, A. J. Austin, R. Cammi, C. Pomelli, J. W. Ochterski, R. L. Martin, K. Morokuma, V. G. Zakrzewski, G. A. Voth, P. Salvador, J. J. Dannenberg, S.

Dapprich, A. D. Daniels, Ö. Farkas, J. B. Foresman, J. V. Ortiz, J. Cioslowski, D. J. Fox, Gaussian, Inc., Wallingford CT, **2013:q**, Gaussian 09 (Revision D.01).

[24]. A. D. Becke, *Phys. Rev. A*, **1988**, *38*, 3098.

[25]. (a) A. D. Becke, *J. Chem. Phys*. **1993**, *98*, 5648-5652.; (b) A. D. Becke, *Phys. Rev. A* **1988**, *38*, 3098-3100.; (c) C. Lee, W. Yang, R. G. Parr, *Phys. Rev. B* **1988**, *37*, 785–789.

[26]. T. Yanai, D. Tew, N. Handy, *Chem. Phys. Lett.* **2004**, *393*, 51–57.

[27]. H. Likura, T. Tsuneda, T. Yanai, K. Hirao, *J. Chem. Phys.* **2001**, *115*, 3540–3544.

[28]. Y. Zhao, D. G. Truhlar, *J. Chem. Phys.*, **2006**, *125*, 1–18.

[29]. Y. Zhao, D. G. Truhlar, *Theor. Chem. Acc.*, **2008**, *120*, 215–241.

[30]. Y. Zhao, D. G. Truhlar, *Theor. Chem. Acc.*, **2008**, *120*, 215–241.

[31]. (a) Y. Zhao, D. G. Truhlar, *J. Phys. Chem.*, **2006**, *110*, 5121–5129.

[32]. J. D. Chai, M. Head-Gordon, *Phys. Chem. Chem. Phys.*, **2008**, *10*, 6615–6620.

[33]. J.-D. Chai, M. Head-Gordon, *J. Chem. Phys.*, **2008**, *128*, 084106.

[34]. (a) A. D. Becke, *J. Chem. Phys.*, **1997**, *107*, 8554-60; (b) H. L. Schmider, A. D. Becke, *J. Chem. Phys.*, **1998**, *108*, 9624–9631.

[35]. F. Weigend, R. Ahlrichs, *Phys. Chem. Chem. Phys.* **2005**, *7*, 3297–3305.

[36]. F. Weigend, *Phys. Chem. Chem. Phys.*, **2006**, *8*, 1057–1065.

[37]. G. D. Purvis, R. J. Bartlett, *J. Chem. Phys.*, **1982**, *76*, 1910–1918.

[38]. (a) W. J. Hehre, R. Ditchfield, J. A. Pople, *J. Chem. Phys.* **1972**, *56*, 2257–2261.; (b) M. M. Francl, W. J. Pietro, W. J. Hehre, J. S. Binkley, D. J. DeFrees, J. A. Pople, M. S. Gordon, *J. Chem. Phys.* **1982**, *77*, 3654–3665.

[39]. G. Chung, D. Lee, *Bull. Korean, Chem. Soc.* **2008**, *29*, 2419–2422.

Chapter V

Characterization of dicationic metal complexes

V.1. Introduction

InfraRed Multiple Photon Dissociation (IRMPD) spectroscopy produces the infrared signature of gaseous molecular ions trapped in the high vacuum cells of mass spectrometers.[1] The technique emerged at the beginning of this century[2,3] and is recognized as a powerful tool for distinguishing between isomers and conformers of organic, inorganic and biological species.[4] In most cases, the IRMPD band assignments that allow structural characterization are made through comparison with model spectra that are predicted by modern electronic structure calculations such as density functional theory (DFT). The accuracy of these calculations is essential to use of the technique.

Agreement between experimental IRMPD and calculated spectra is generally satisfying, in particular for band positions, but some small differences are often observed. When IR spectra are calculated by DFT methods that include harmonic approximations, discrepancies can arise from anharmonic and finite temperature effects. Methods to model IR spectra that inherently include these effects have therefore been devised for both classical[5,6] and quantum[7] molecular dynamic simulations. Anharmonic effects can also be included for high level calculations with methods such as VSCF[8] or GVPT2.[9] However, static DFT calculations remain the fastest and most convenient and common way to model IR spectra, their main drawback being that they require the use of a scaling factor to obtain the correct vibrational frequencies. Numerous studies in the literature report vibrational scaling factors that are appropriate for a given combination of DFT functionals and basis sets.[10] The numerical values of these scaling factors can vary slightly as a function of the database used to establish the scaling factor; for example the values of 0.9614,[10a] 0.9664[11] and 0.9800[12] have been recommended in different studies at the B3LYP/6-31G(d) calculational level. consequently, these empirical scaling factors introduce a degree of uncertainty, which is expressed in the predicted vibrational

frequencies.[13,14] For example, for a band computed at υ = 1800 cm^{-1} at the B3LYP/6-31G(d) level, the values obtained after scaling by 0.9614 (1731 cm^{-1}) or 0.9800 (1764 cm^{-1}) differ by 33 cm^{-1}, which is highly significant figure in terms of interpretation. Beyond the standard approach of applying a uniform scaling factor over the whole infrared spectral region, different strategies have also been developed to improve the accuracy of the predicted vibrational frequencies.[15,16] Two different scaling factors can be used for low-energy (< 1800 cm^{-1}) and high-energy (> 1800 cm^{-1}) vibrational modes.[17] Scaling equations or specific (or local) scaling factors have also been determined for specific family of compounds or vibrational modes.[18]

These scaling factors are based on experimental infrared absorption spectra, and it is known that IRMPD spectra, which are gas-phase "action" (or "consequence") spectra, show a slight red-shift relative to classical absorption spectra. Nonetheless, classical scaling factors are commonly used to assign IRMPD bands and to distinguish between different isomers and/or conformers. Specific scaling factors have been determined for gas phase spectroscopic studies of biomolecules,[19] and the relative performance of different DFT functionals has been evaluated in several studies.[20,21,22] A mean error of around 10 cm^{-1} is obtained for the best functionals, which include B3LYP. However, these calibrations have generally been made upon small libraries of compounds and are only available for a restricted range of functionals. An improved understanding of the nature of the difference between experimental and calculated IRMPD spectra would obviously be of significant interest: in cases where a computed spectrum does not fit exactly with an experiment, it would clarify whether the discrepancy arises from inaccuracies of computation or from the fact that the calculated structure does not correspond to the experimentally observed one.

For some years, our group and others have been interested in the measurement and modeling of IRMPD spectra of fragments that result from electron capture or transfer dissociation

(ECD/ETD) processes.[23,24,25] ECD and ETD are mass spectrometry fragmentation methods that rely on the adjunction of one electron to a multiply-charged gas phase cation.[26] The fragmentation mechanism of ECD and ETD is still a matter of conjecture,[27,28] and considerable debate surrounds where the incoming electron is first attached to the parent polycation. It has been demonstrated that self-interaction error prevents conventional exchange-correlation functionals such as B3LYP from properly describing the intermediate radical protonated peptides that are generated by ECD and ETD.[29] However, range-separated hybrid (RSH) functionals improve the description of these peptides significantly. Our work described in the previous chapter (chapter IV) shows also the influence of the functionals on the description of reduced organometallic complexes. It is therefore important to understand the accuracy of RSH when they are used to model infrared spectra, because these spectra will allow the site of electron attachment to be defined adequately.

The following section (section V.2) presents our initial attempts to record IR vibrations of metal complexes through IRMPD action spectroscopy experiments. In view of the poor agreement between the experimental and theoretical spectra obtained for the reduced species with two different functionals, as well as with a RSH functional for all complexes, we then decide to perform an evaluation of the functional accuracy on our molecules of interest. These benchmark calculations are describe in section V.3

V.2. IRMPD spectra-First attempts

Infrared multiple photon dissociation is a unique spectroscopy technique allowing to record IR vibrations of ions in the gas phase. Our work described in Chapter III allows us to perform IRMPD studies on two different families of complexes: (i) dicationic organometallic

complexes directly formed through ESI and selected in the quadrupole of the FT-ICR; (ii) singly-reduced monocationic organometallic complexes, obtained after electron capture by the former (through ECD method) and isolation in the FT-ICR cell. One example of such studies in presented for each family of complexes in sections V.2.1 and V.2.2, as well as the comparison of the experimental IR spectra with calculated IR spectra obtained with a standard (B3LYP) and a RSH (LC-BLYP) functionals.

V.2.1. **Dicationic complex**

A 3:1 mixture of phenanthroline (ligand **5**) and $Zn(BF_4)_2$ in a 1:2 water/acetonitrile solution has been prepared and transferred in the gas phase through ESI. Among the numerous ions which are obtained, we observe the ion at m/z = 302, which correspond to the dicationic complex $[Zn(\mathbf{5})_3]^{2+}$. This ion is then mass-selected in the quadrupole, transferred in the FT-ICR cell and irradiated with monochromated IR photons in the 1000-2000 cm^{-1} range. The ion can absorb multiple photons if its vibration is resonant with the laser frequency. In that case, multiple photon absorption induces fragmentation of the ion. For the dicationic complex $[Zn(\mathbf{5})_3]^{2+}$, the fragmentation corresponds to the loss of a neutral phenanthroline ligand to yield product $[Zn(\mathbf{5})_2]^{2+}$ ion at m/z = 212 as shown in Figure 5.1.

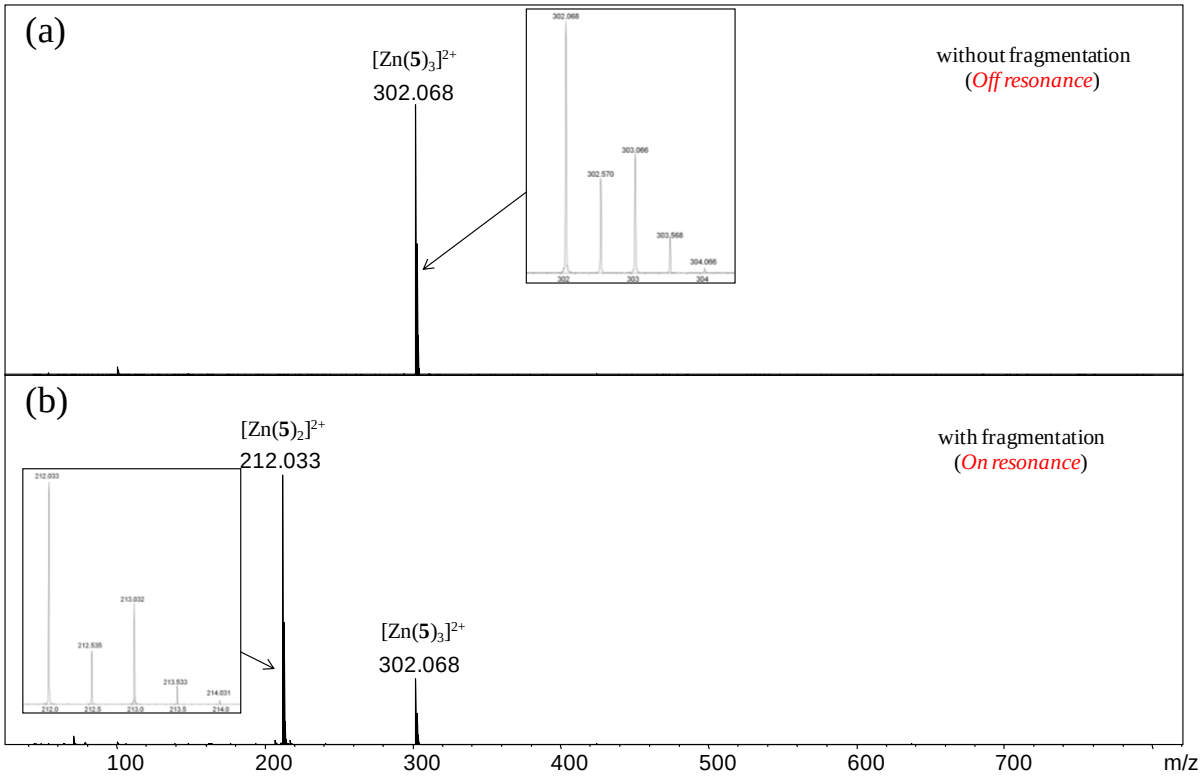

Figure 5.1. *IRMPD mass spectrum (Ion intensity in arbitrary units) obtained after mass selection of* $[Zn(\mathbf{5})_3]^{2+}$ *(m/z 302) in the quadruple (a); after irradiation by the free electron laser at 1427* cm^{-1} *in the FT-ICR cell (b).*

Gas-phase IR action spectroscopy of $[Zn(\mathbf{5})_3]^{2+}$ was performed several times in the 1000–2000 cm^{-1} region, as shown in Figure 5.2, which allows to identified 5 IR bands. The average values of the IR experimental bands are 1113, 1162, 1427, 1515 and 1575 cm^{-1}. More about these vibrations will be discussed in section V.3.

As a preliminary study, we have computed the IR spectra of $[Zn(\mathbf{5})_3]^{2+}$ at two DFT levels of calculations with the 6-31+G(d,p) basis set. We used a hybrid (B3LYP) and a RSH (LC-BLYP) functionals in order to evaluate their ability to reproduce the experimental spectra. Figure 5.2 shows that B3LYP reproduces nicely the experimental spectra, whereas LC-BLYP has a much more significant discrepancy.

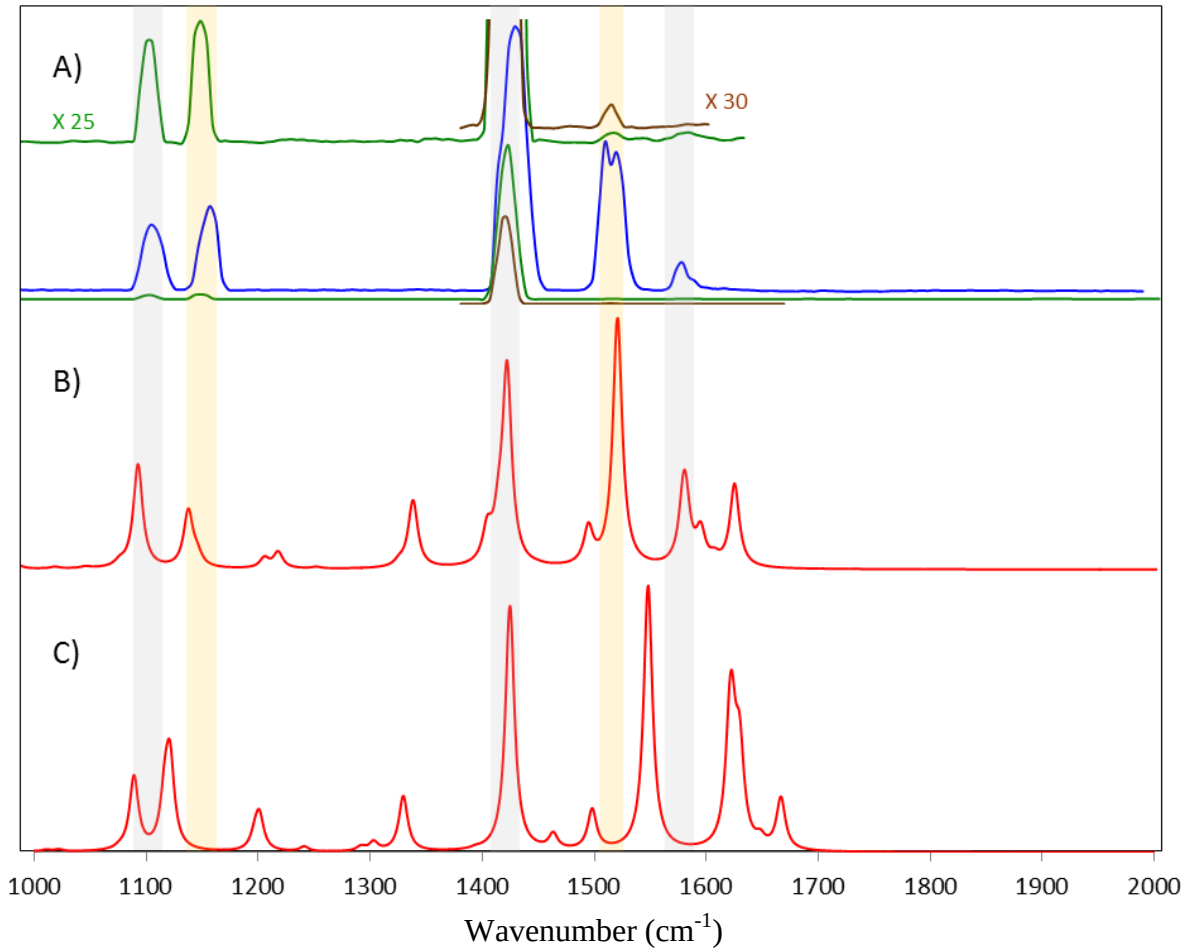

***Figure 5.2**: Experimental IR action spectra (A) and DFT computed IR spectra of $[Zn(\mathbf{5})_3]^{2+}$ at the B3LYP/6-31+G(d,p) (scaling factor 0.978) (B) and LC-BLYP/6-31+G(d,p) (scaling factor 0.94) (C) levels.*

V.2.2. **Reduced metal complex**

Following our IRMPD experiments performed on a dicationic complex mass-selected in the quadrupole to record its IR spectra, we explore the possibility to obtain IR action spectra of a radical cation. This requires coupling two successive processes in the FT-ICR cell, i.e. an electronic reduction through ECD followed by mass selection of the radical cation and then its irradiation by the tunable laser. The principle is simple. Its achievement is complicated by the need to have sufficient intensity of the radical allowing to observe its fragments after

irradiation by the laser. This requires having sufficient intensity of the parent dicationic complex and to finely adjust the ECD parameters.

In this strategy, we have obtained the reduced metal species $[Zn(\mathbf{2})_2]^{\bullet+}$ by the one electron reduction through ECD on the dicationic metal complex $[Zn(\mathbf{2})_3]^{2+}$. This radical is then isolated in the FT-ICR cell. Subsequently, IRMPD experiments performed on this isolated species reveal four intense bands at 1301, 1428, 1481 and 1670 cm^{-1} (average values of the two experimental data), as shown in Figure 5.3.

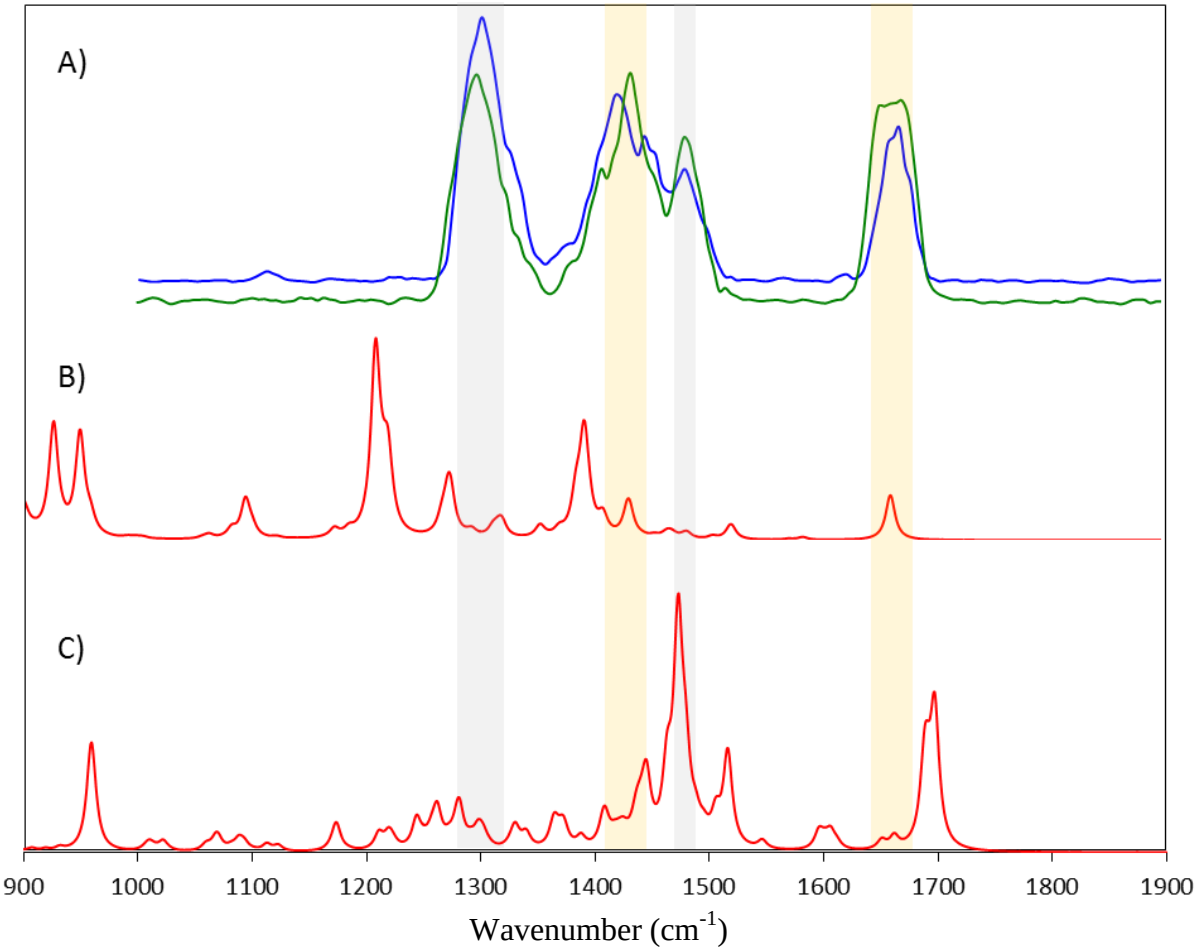

***Figure 5.2**: Experimental IR action spectra (A) and DFT computed IR spectra of $[Zn(\mathbf{2})_2]^{\bullet+}$ at the B3LYP/6-31+G(d,p) (scaling factor 0.978) (B) and LC-BLYP/6-31+G(d,p) (scaling factor 0.94) (C) levels.*

Contrary to what is observed for the dicationic complex $[Zn(\mathbf{5})_3]^{2+}$, comparison between experimental and theoretical IR spectra show very poor agreement, which in principle does

not allow to explain the experimental spectrum and furthermore does not permit to determine which electronic structure (localized or delocalized) is the correct one. On that basis, we decide to evaluate more deeply the ability of functionals to reproduce experimental spectra of organometallic complexes.

V.3. Benchmark DFT calculations for IRMPD spectra

Estimating the precision with which DFT methods can model infrared spectra requires a solid body of experimental IRMPD reference spectra that, under ideal circumstances, would be associated unequivocally with one specific conformation of a chemical compound. This is a difficult constraint to meet with peptides, but it is normally nicely satisfied by metal complexes whose geometries are usually well-characterized and clearly defined. In this section, we have therefore measured IRMPD spectra of ten organometallic complexes that contain bipyridyl-type ligands, and computed their infrared spectra using standard and RSH functionals. The comparison between the theoretical and experimental results is used to define scaling procedures that can be used to provide satisfactory interpretations of IRMPD gas-phase studies involving cations, as well as to evaluate the degree of confidence it is possible to expect when these functionals, basis set and scaling procedures are used to model infrared spectra.

V.3.1. Computational details

V.3.1.1. DFT calculations-Analysis tools

Calculations were carried out with the Gaussian09 package[30] and all structures were fully optimized without any symmetry constraints at the DFT level. Five different exchange-correlation functionals, which cover different categories from “conventional” to range-

separated hybrid (RSH) functionals , have been applied for these calculations: (i) the hybrid GGA functional B3LYP,[31] which includes 20% of Hartree-Fock exchange (X^{HF}); (ii) the hybrid meta-GGA functional M06-2X,[32] which includes 54% of X^{HF}; (iii) the RSHs CAM-B3LYP,[33] LC-BLYP,[34] and ωB97X-D,[35] which present a growing fraction of X^{HF} with increasing interelectronic separation in the 19-65, 0-100 and 22.2-100 range, respectively. The speed of the transition from Kohn-Sham exchange to X^{HF} is governed by the attenuation parameter ω whose value is 0.33, 0.47 and 0.20 a.u. for these three functionals, respectively. Three valence double-ζ basis set have been used. The first one, noted def2-SVP, used the def2-SVP split-valence basis set developed by Weigend and Ahlrichs for all atoms.[36] The second and third basis set, noted respectively 6-31G(d,p) and 6-31+G(d,p), used valence double-ζ Pople basis set,[37] without or with diffuse function on heavy atoms,[38] for all atoms but Ru for which the LanL2DZ pseudopotential and associated basis set[39] has been employed. For each stationary point, we carried out a vibrational frequency calculation at the same level to characterize their nature as minima. Stick spectra, as well as Lorentzian line shapes, with a full width at half maximum (fwhm) of 5 or 10 cm^{-1}, were used to generate the calculated IR spectra.

V.3.1.2. Analysis tools

For each level of theory and each protocol used to obtained unscaled theoretical vibrational frequencies, the predicted frequency values are obtained following two various strategies. First, we used the traditional approach which consists to determine (or select in the literature) a scaling factor and to multiply the unscaled theoretical vibrational frequencies by this scaling factor (*vide infra*). In a second strategy, the unscaled theoretical vibrational frequencies are plotted against the determined experimental vibrational frequencies for the 68 vibrational modes ν. A linear correlation is then used to determine a linear relationship (y = ax + b)

between experimental and theoretical values. The equation (1) produces the predicted frequency values $\upsilon^{\nu}_{predict}$ from the unscaled theoretical vibrational frequencies υ^{ν}_{calc}.

$$\upsilon^{\nu}_{predict} = \frac{\upsilon^{\nu}_{calc} - b}{a} \qquad (1)$$

The accuracy of the predicted frequency values is analyzed by two numerical tests. First we use the mean absolute error (MAE) given by equation (2).

$$MAE = \frac{\sum |\upsilon^{\nu}_{predict} - \upsilon^{\nu}_{exp}|}{68} \qquad (2)$$

Second, the root-mean-square error (RMSE, equation (3)) between the experimental and predicted frequency values has been calculated to evaluate the prediction capabilities.

$$RMSE = \sqrt{\frac{\sum (\upsilon^{\nu}_{predict} - \upsilon^{\nu}_{exp})^2}{68}} \qquad (3)$$

Since the errors are squared before they are averaged, the RMSE gives a relatively high weight to large errors compared to MAE.

Three different scaling factors have been estimated for each level of theory and each protocol used to obtained unscaled theoretical vibrational frequencies. First, Individual scaling factors sf^{ν} have been obtained for each of the 68 vibrational modes ν by dividing the experimental value υ^{ν}_{exp} by the corresponding calculated value υ^{ν}_{calc}. The arithmetic averaging of the individual scaling factors is used to determine the "average" scaling factor $sf_{ave} = (\Sigma\ sf^{\nu})/68$. Scaling factors which minimize the MAE (sf_{MAE}) or the RMSE (sf_{RMSE}) have also being obtained.

V.3.2. Studied complexes

The ten complexes **I**-**X** that are depicted in Figure 5.5 have been studied in this benchmark. They are mainly dicationic zinc (**I**-**VIII**) and ruthenium (**IX**) complexes, but one monocationic ruthenium complex (**X**) is also included. All are hexacoordinated, and each complex includes at least one of the bipyridyl-type ligands **1**-**5** describe previously in Chapter III (for clarity, they are drawn again in Figure 5.5). They therefore comprise a series of geometrically related homoleptic (**I**-**V**) or heteroleptic (**VI**-**X**) complexes.

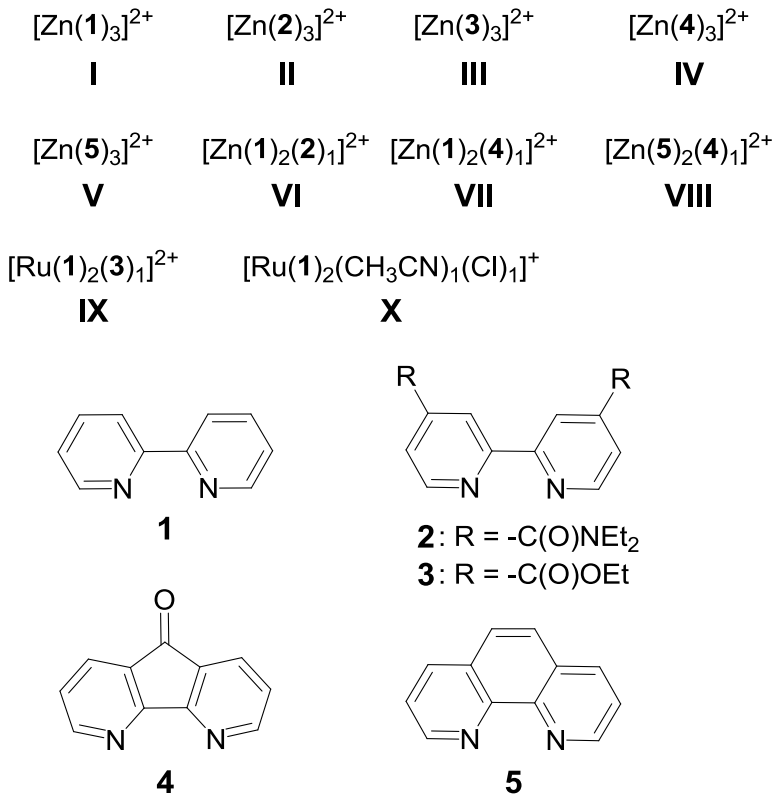

Figure 5.5*. Complexes **I-X** studied in this benchmark study.*

V.3.3. Experimental details

$Ru(bipy)_2Cl_2$ (1 eq.) and $AgBF_4$ (2 eq.) were mixed in acetonitrile and heated at 60°C overnight, the mixture was filtrated and then **3** was added to the filtrated solution and stirred for 2h. **IX** is observed in the full mass spectra obtained from the diluted crude solution.

$Ru(bipy)_2Cl_2$ complex was stirred for 2h in acetonitrile solution. **X** is observed in the full mass spectra obtained from the diluted crude solution.

Solutions for zinc complexes **I-VIII** and **XI** were prepared in a 1:2 water/acetonitrile solution by mixing one or two ligands and zinc(II) tetrafluoroborate.

Zinc and ruthenium complexes were formed in an electrospray source in positive mode and observed by high resolution mass spectrometry with a 7T Fourier Transform Ion Cyclotron Resonance (FT-ICR) tandem mass spectrometer (Bruker Apex Qe). The ion of interest was

isolated in the quadrupole with an isolation window of *m*/*z* 0.5-10.0 and accumulated in the collision cell for between 0.5 to 2.0 seconds. This ion is then transferred to the ICR Cell and irradiated for between 0.15 to 2.0 seconds with an IR laser. Vibrational spectra were obtained in the 900-2000 cm^{-1} region by IRMPD using the FT-ICR spectrometer coupled to a tunable free electron laser at the Centre Laser Infrarouge d'Orsay (CLIO).[40] In IRMPD action spectroscopy, when the laser wavelength becomes resonant with a vibrational transition of the mass-selected species, a sequential absorption of multiple photons that is coupled to fast intramolecular vibrational redistribution can deposit internal energy within the species up to threshold energy for fragmentation. The intensity of parent and fragment ions after laser irradiation are monitored as a function of the excitation wavelength, with the photofragmentation yield being calculated for each wavelength according to $-\ln[I_{parent}/(I_{parent} + \Sigma I_{fragments})]$. At each wavelength step, 4 to 6 mass spectra were averaged.

V.3.4. Experimental spectra database

The IRMPD spectra of **I**-**X** have been recorded over a 900-2000 cm^{-1} range. To ensure the accuracy of the measurements, at least two spectra have been obtained for each complex on different days, so as to eliminate calibration errors. These representative spectra recorded for **I-X** are given in Figures 5.6-5.15. The largest bands are observed in every spectrum of a given compound, but lower intensity bands may be absent in some spectra. These variations of detail reflect how variables such as laser alignment, intensity of the parent ion, irradiation time or laser attenuation affect the precise nature of the fragmentation process that occurs within the parent ion and gives rise to the IRMPD.

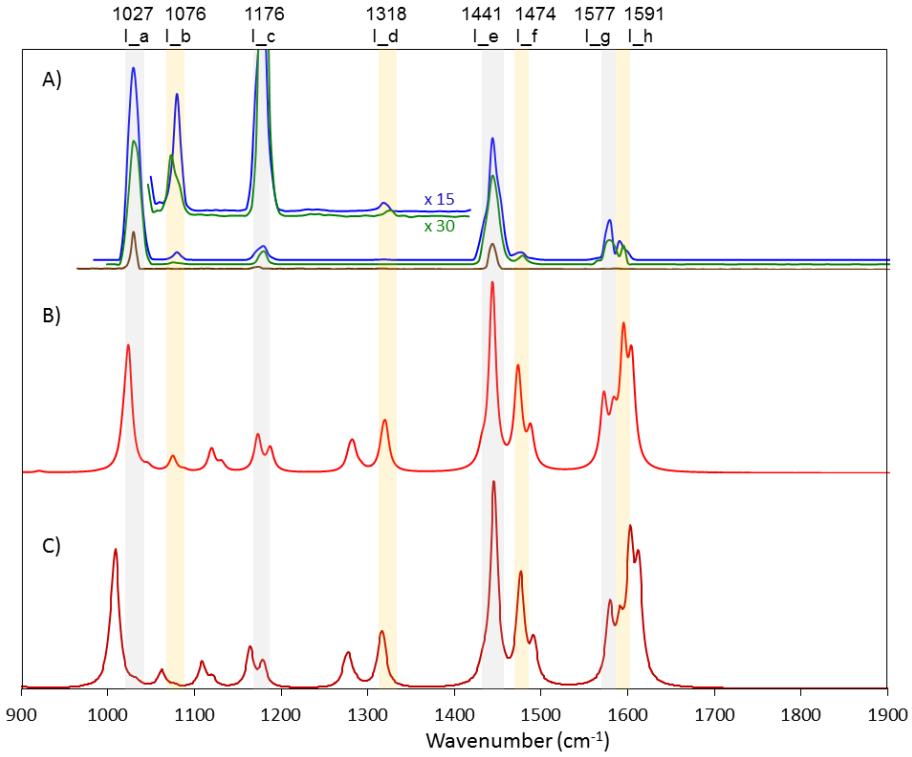

***Figure 5.6**. Experimental IRMPD spectra (A) and B3LYP/6-31+G(d,p) computed IR spectra of compound **I** scaled using the linear correlation method (B) and by a factor of 0.9786 (C) after convolution with a 5 cm^{-1} (fwhm) Lorentzian linewidth function.*

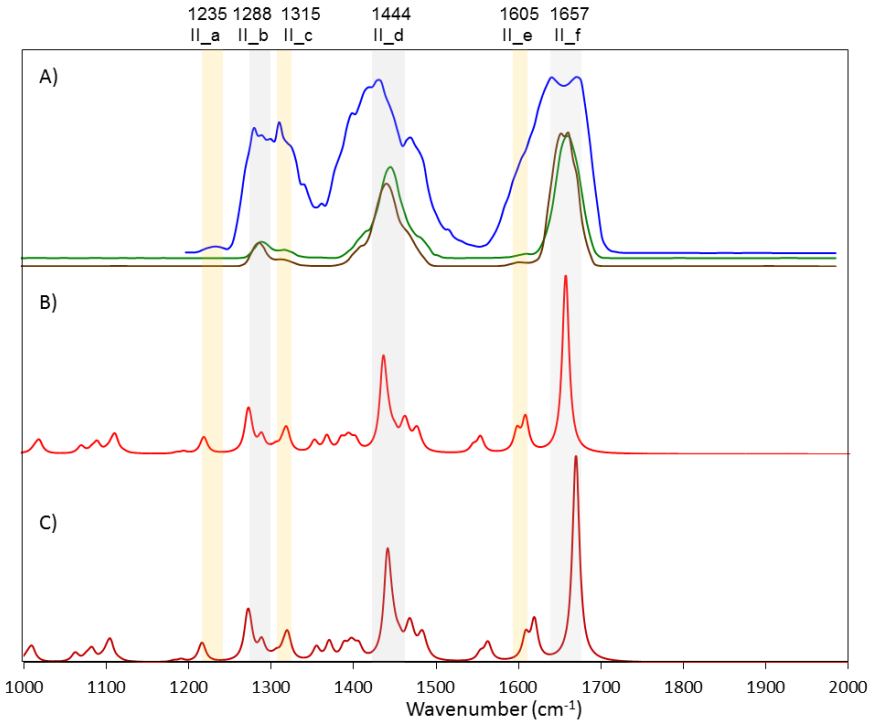

***Figure 5.7**. Experimental IRMPD spectra (A) and B3LYP/6-31+G(d,p) computed IR spectra of compound **II** scaled using the linear correlation method (B) and by a factor of 0.9786 (C) after convolution with a 5 cm^{-1} (fwhm) Lorentzian linewidth function.*

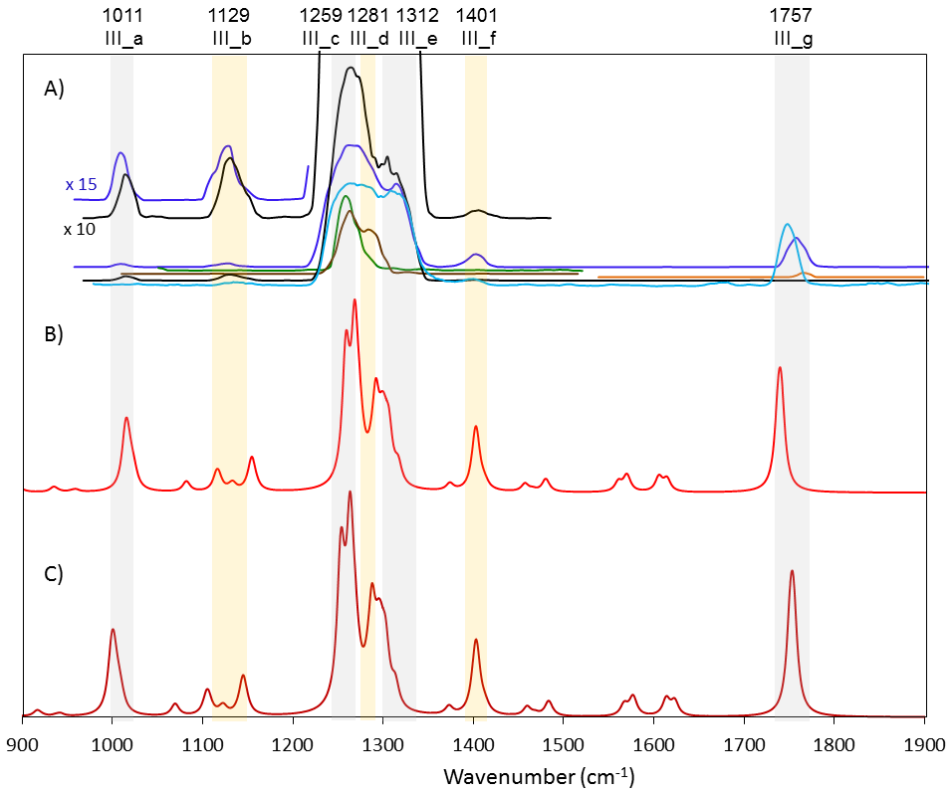

***Figure 5.8**. Experimental IRMPD spectra (A) and B3LYP/6-31+G(d,p) computed IR spectra of compound **III** scaled using the linear correlation method (B) and by a factor of 0.9786 (C) after convolution with a 5 cm^{-1} (fwhm) Lorentzian linewidth function.*

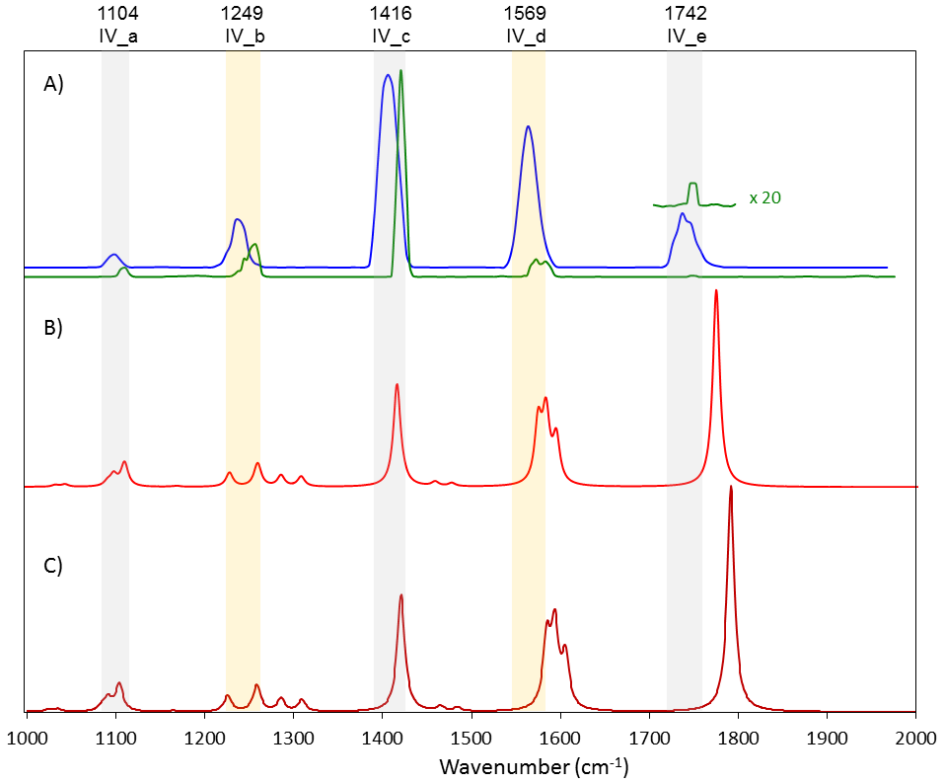

***Figure 5.9**. Experimental IRMPD spectra (A) and B3LYP/6-31+G(d,p) computed IR spectra of compound **IV** scaled using the linear correlation method (B) and by a factor of 0.9786 (C) after convolution with a 5 cm^{-1} (fwhm) Lorentzian linewidth function.*

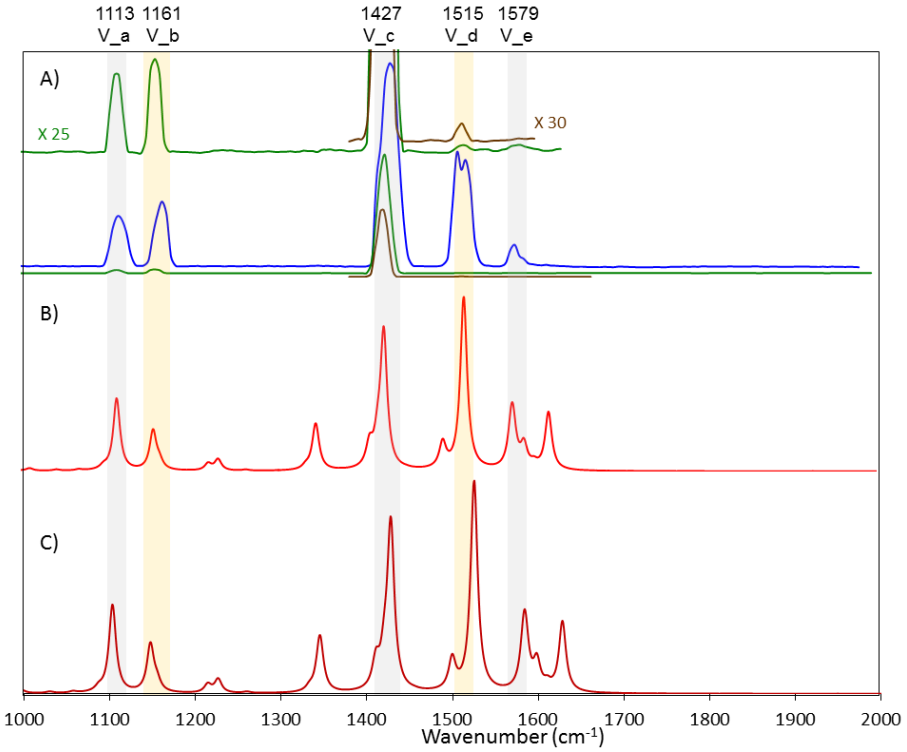

Figure 5.10. *Experimental IRMPD spectra (A) and B3LYP/6-31+G(d,p) computed IR spectra of compound* ***V*** *scaled using the linear correlation method (B) and by a factor of 0.9786 (C) after convolution with a 5 cm^{-1} (fwhm) Lorentzian linewidth function.*

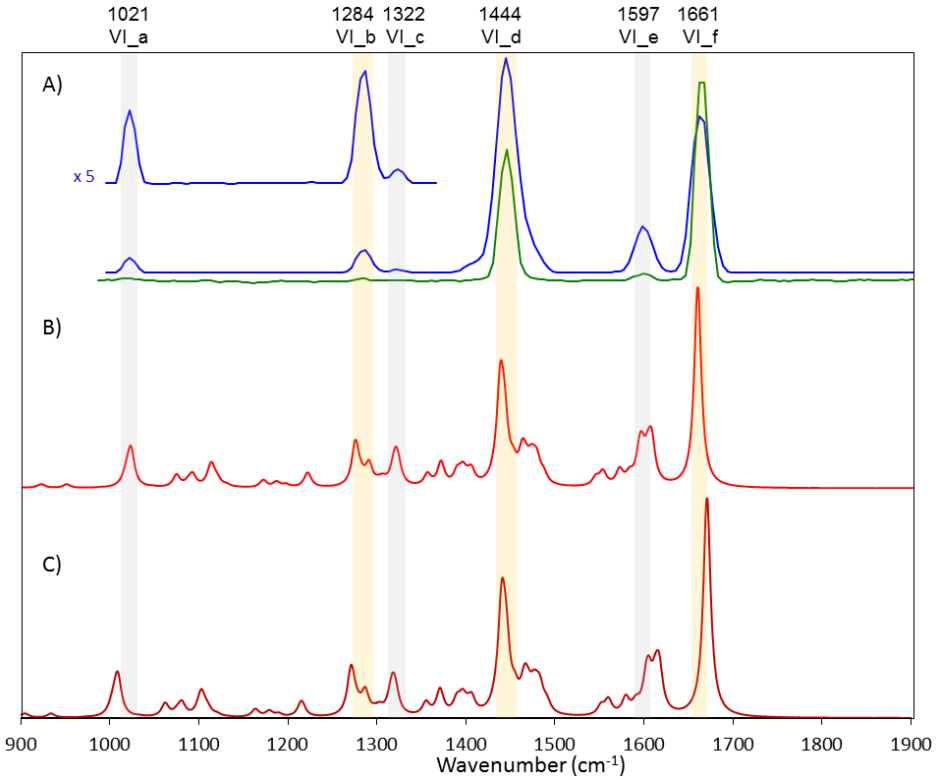

Figure 5.11. *Experimental IRMPD spectra (A) and B3LYP/6-31+G(d,p) computed IR spectra of compound* ***VI*** *scaled using the linear correlation method (B) and by a factor of 0.9786 (C) after convolution with a 5cm^{-1} (fwhm) Lorentzian linewidth function.*

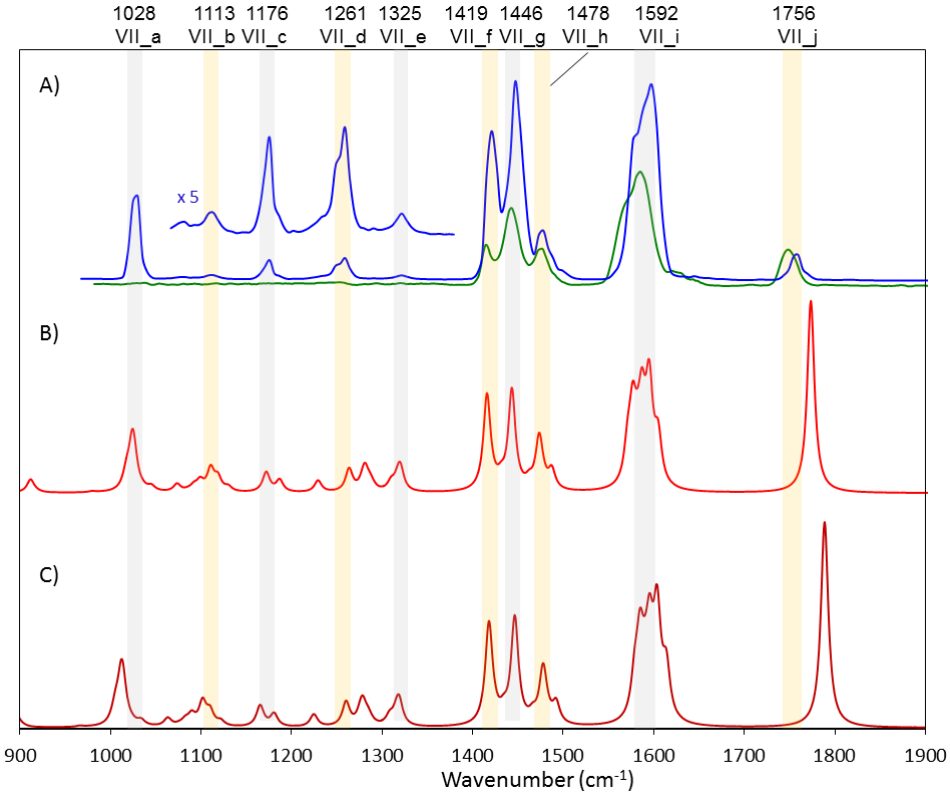

***Figure 5.12**. Experimental IRMPD spectra (A) and B3LYP/6-31+G(d,p) computed IR spectra of compound **VII** scaled using the linear correlation method (B) and by a factor of 0.9786 (C) after convolution with a 5 cm^{-1} (fwhm) Lorentzian linewidth function.*

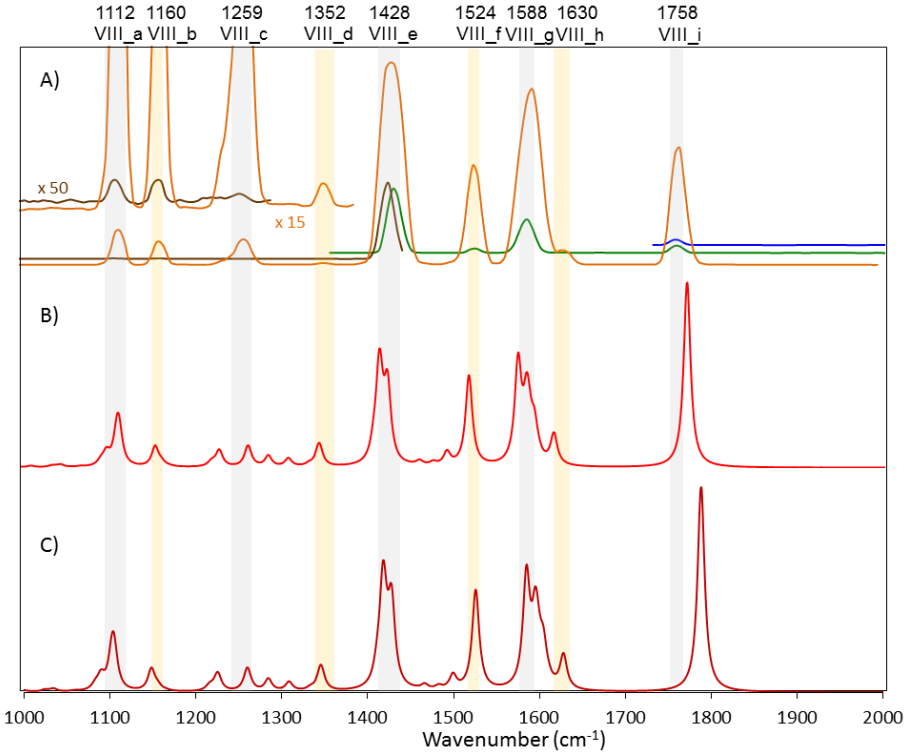

***Figure 5.13**. Experimental IRMPD spectra (A) and B3LYP/6-31+G(d,p) computed IR spectra of compound **VIII** scaled using the linear correlation method (B) and by a factor of 0.9786 (C) after convolution with a 5cm^{-1} (fwhm) Lorentzian linewidth function.*

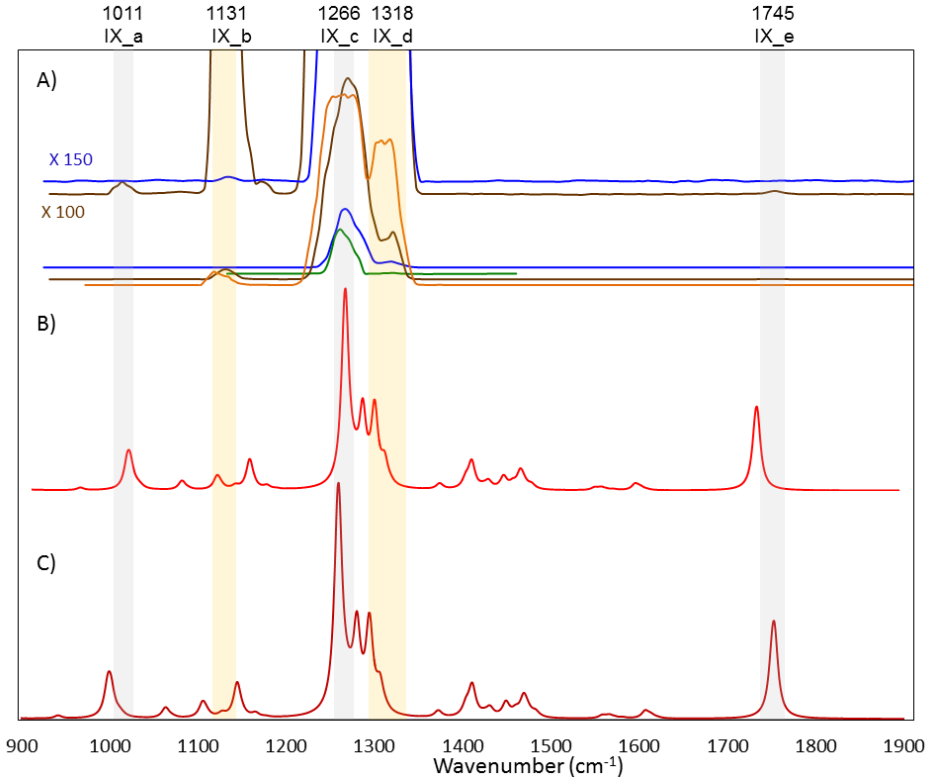

Figure 5.14. *Experimental IRMPD spectra (A) and B3LYP/6-31+G(d,p) computed IR spectra of compound **IX** scaled using the linear correlation method (B) and by a factor of 0.9786 (C) after convolution with a 5 cm^{-1} (fwhm) Lorentzian linewidth function.*

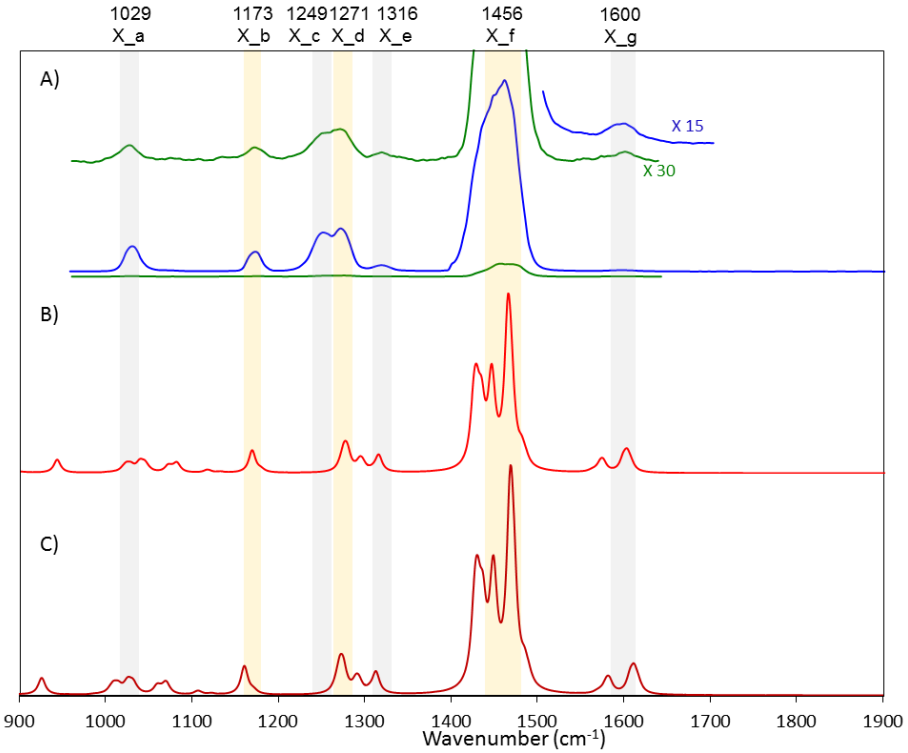

Figure 5.15. *Experimental IRMPD spectra (A) and B3LYP/6-31+G(d,p) computed IR spectra of compound **X** scaled using the linear correlation method (B) and by a factor of 0.9786 (C) after convolution with a 5 cm^{-1} (fwhm) Lorentzian linewidth function.*

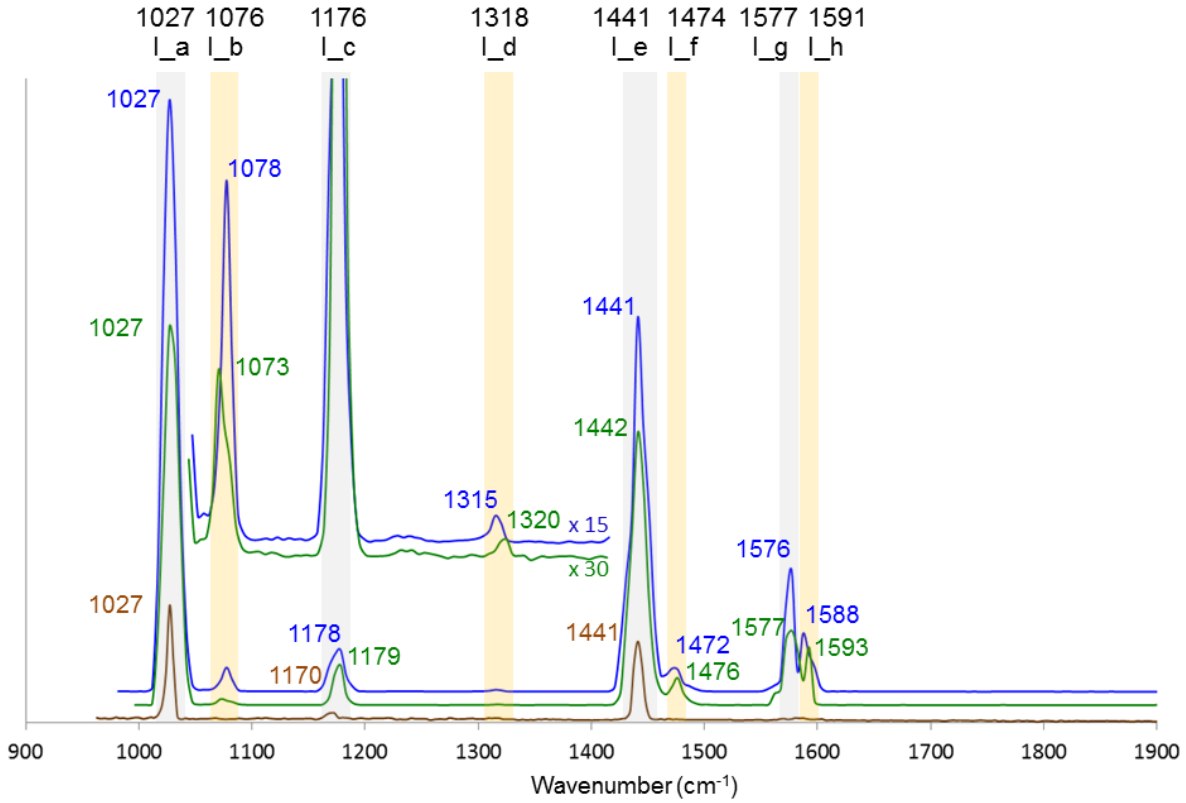

***Figure 5.16**. Experimental IRMPD spectra of **I**. Irradiation time: 500 ms (blue and green lines) or 250 ms (brown line).*

Eight bands, noted I_a to I_h, have been clearly identified for compound **I** (Figure 5.16) and a total of 68 bands have been obtained from compounds **I-X**. Comparing different spectra from a given compound shows that slightly different wavenumbers can be obtained for any given band, and this serves to illustrate the degree of uncertainty that is associated with the IRMPD experiment. For example, the band I_b is observed at 1073 and 1078 cm^{-1} in two different measurements of **I**. Differences are normally smaller than 10 cm^{-1}, but quite large variations (of up to 29 cm^{-1} for band III_g) are occasionally observed. The mean of the different values is taken here to be the experimental wavenumber of each band.

V.3.5. Vibrational modes assignment

Assignments of the vibrational modes, which have been made through comparison with B3LYP/6-31+G(d,p) computed IR spectra (Table 5.1), are in agreement with the solution-phase spectra obtained for similar zinc and ruthenium complexes including bipyridyl- and related ligands.[41,42]

Table 5.1. Observed IRMPD resonances for **I-X** and their assignments.

Band name	Wavenumber (cm^{-1})	Vibrational mode[a]
I_a	1027	ring breathing, βCH out-of-plane (**1**)
I_b	1076	ring breathing (**1**)
I_c	1176	βCH in plan (**1**)
I_d	1318	υCC_{ring}, υCN_{ring}, βCH in plan (**1**)
I_e	1441	υCC_{ring}, υCN_{ring}, βCH in plan (**1**)
I_f	1474	υCC_{ring}, υCN_{ring}, βCH in plan (**1**)
I_g	1577	υCC_{ring}, υCN_{ring} (**1**)
I_h	1591	υCC_{ring} (**1**)
II_a	1235	$\upsilon N\text{-}CH_2$ + βCH_3 antisymmetric
II_b	1288	υCC_{ring}, υCN_{ring} (**2**)
II_c	1315	Twist CH_2
II_d	1444	υCN_{amide}, βCH_2 (scissors)
II_e	1605	υCC_{ring} (**2**)
II_f	1657	$\upsilon C{=}O_{amide}$
III_a	1011	$\upsilon C\text{-}O_{ester}$, $\upsilon C\text{-}C_{ester}$
III_b	1129	$\upsilon C\text{-}O_{ester}$, ring breathing (**3**)
III_c	1259	$\upsilon C\text{-}O_{ester}$, υCC_{ring}, υCN_{ring}, βCH in plan (**3**)
III_d	1281	$\upsilon C\text{-}O_{ester}$, υCC_{ring}, υCN_{ring}, βCH in plan (**3**)
III_e	1312	$\upsilon C\text{-}O_{ester}$, υCC_{ring}, υCN_{ring}, βCH in plan (**3**)
III_f	1401	βCH_3 symmetric (umbrella), wag CH_2
III_g	1757	$\upsilon C{=}O_{ester}$
IV_a	1104	ring breathing, βCH in plan (**4**)
IV_b	1249	υCC_{ring}, υCN_{ring}, βCH in plan (**4**)
IV_c	1416	υCC_{ring}, βCH in plan (**4**)
IV_d	1569	υCC_{ring}, υCN_{ring} (**4**)
IV_e	1742	υC=O (**4**)
V_a	1113	ring breathing, βCH in plan (**5**)
V_b	1161	βCH in plan (**5**)
V_c	1427	υCC_{ring}, υCN_{ring}, βCH in plan (**5**)
V_d	1515	υCC_{ring}, υCN_{ring} (**5**)

V_e	1579	υCC_{ring}, υCN_{ring} (**5**)
VI_a	1021	ring breathing, βCH out-of-plan (**1**)
VI_b	1284	υCC_{ring}, υCN_{ring} (**2**)
VI_c	1322	Twist CH_2
VI_d	1444	υCN_{amide}, βCH_2 (scissors)
VI_e	1597	υCC_{ring} (**2**)
VI_f	1661	$\upsilon C{=}O_{amide}$
VII_a	1028	ring breathing (**1**)
VII_b	1113	ring breathing + βCH in plan (**4**)
VII_c	1176	βCH in plan (**1**)
VII_d	1261	υCC_{ring}, υCN_{ring}, βCH in plan (**4**)
VII_e	1325	υCC_{ring}, υCN_{ring}, βCH in plan (**1**)
VII_f	1419	υCC_{ring}, βCH in plan (**4**)
VII_g	1446	υCC_{ring}, υCN_{ring}, βCH in plan (**1**)
VII_h	1478	υCC_{ring}, υCN_{ring}, βCH in plan (**1**)
VII_i	1592	υCC_{ring}, υCN_{ring} (**1** and **4**)
VII_j	1756	υC=O (**4**)
VIII_a	1112	ring breathing + βCH in plan (**4** and **5**)
VIII_b	1160	βCH in plan (**5**)
VIII_c	1259	υCC_{ring}, υCN_{ring}, βCH in plan (**4** and **5**)
VIII_d	1352	υCC_{ring}, υCN_{ring}, βCH in plan (**5**)
VIII_e	1428	υCC_{ring}, βCH in plan (**4** and **5**)
VIII_f	1524	υCC_{ring}, υCN_{ring} (**5**)
VIII_g	1588	υCC_{ring}, υCN_{ring} (**4** and **5**)
VIII_h	1630	υCC_{ring} (**5**)
VIII_i	1758	υC=O (**4**)
IX_a	1011	$\upsilon C\text{-}O_{ester}$, $\upsilon C\text{-}C_{ester}$
IX_b	1131	$\upsilon C\text{-}O_{ester}$, ring breathing (**3**)
IX_c	1266	$\upsilon C\text{-}O_{ester}$, υCC_{ring}, υCN_{ring}, βCH in plan (**3**)
IX_d	1318	υCC_{ring}, υCN_{ring}, βCH in plan (**3**)
IX_e	1745	υC=O (**3**)
X_a	1029	ring breathing (**1**)
X_b	1173	βCH in plan (**1**)
X_c	1249	υCC_{ring}, υCN_{ring} (**1**)
X_d	1271	υCC_{ring}, υCN_{ring} (**1**)
X_e	1316	υCC_{ring}, υCN_{ring}, βCH in plan (**1**)
X_f	1456	υCC_{ring}, υCN_{ring}, βCH in plan (**1**)
X_g	1600	υCC_{ring} (**1**)

[a] υ = stretching; β = bending; wag = wagging; number in parentheses indicates the bidentate ligand on which the vibrational mode operates.

In depth comparison of the various complexes indicates that the vibrational modes of each ligand are largely independent of the nature of the complex, so that they can be assigned quite easily for each ligand **1-5** (Figure 5.17).

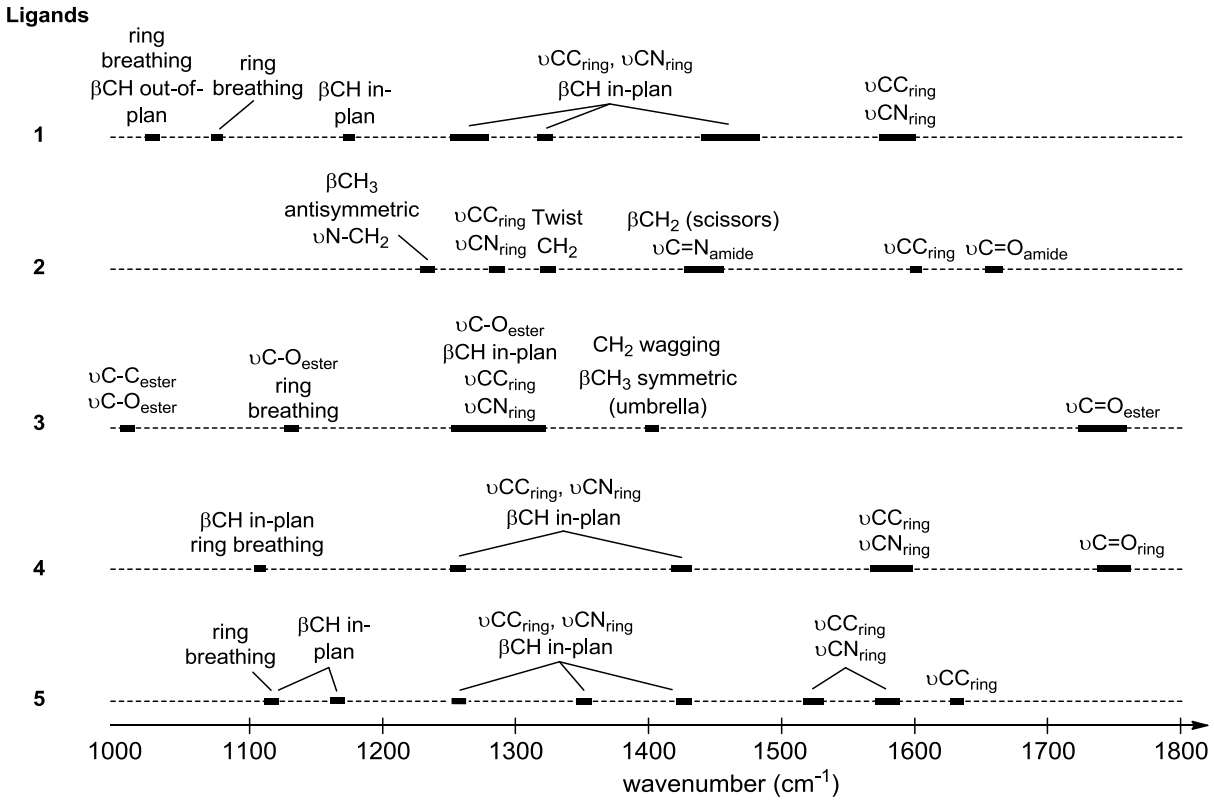

Figure 5.17*. Assignment of vibrational mode wavenumbers for neutral ligands **1-5** in organometallic complexes.*

V.3.6. Post-treatment of calculated spectra

In an initial study, IR spectra of **I-X** were modeled at the B3LYP/6-31+G(d,p) level. Comparison between experimental and theoretical spectra (see Figures 5.6-5.15) reveals a satisfying qualitative agreement. As expected, because IRMPD spectra are traced as a function of molecular fragmentation rather than dipole changes, line intensities are not well reproduced. This is nicely illustrated by the I_a band which has the largest intensity in the

experimental spectrum, but not in the theoretical one, whose line intensity is plotted as a function of IR absorption. We also note that a few of the bands that should be theoretically present at low intensity are not observed in the experimental spectra. In the subsequent discussion, we will restrict our comparison to those peaks that are observed in the experimental spectra.

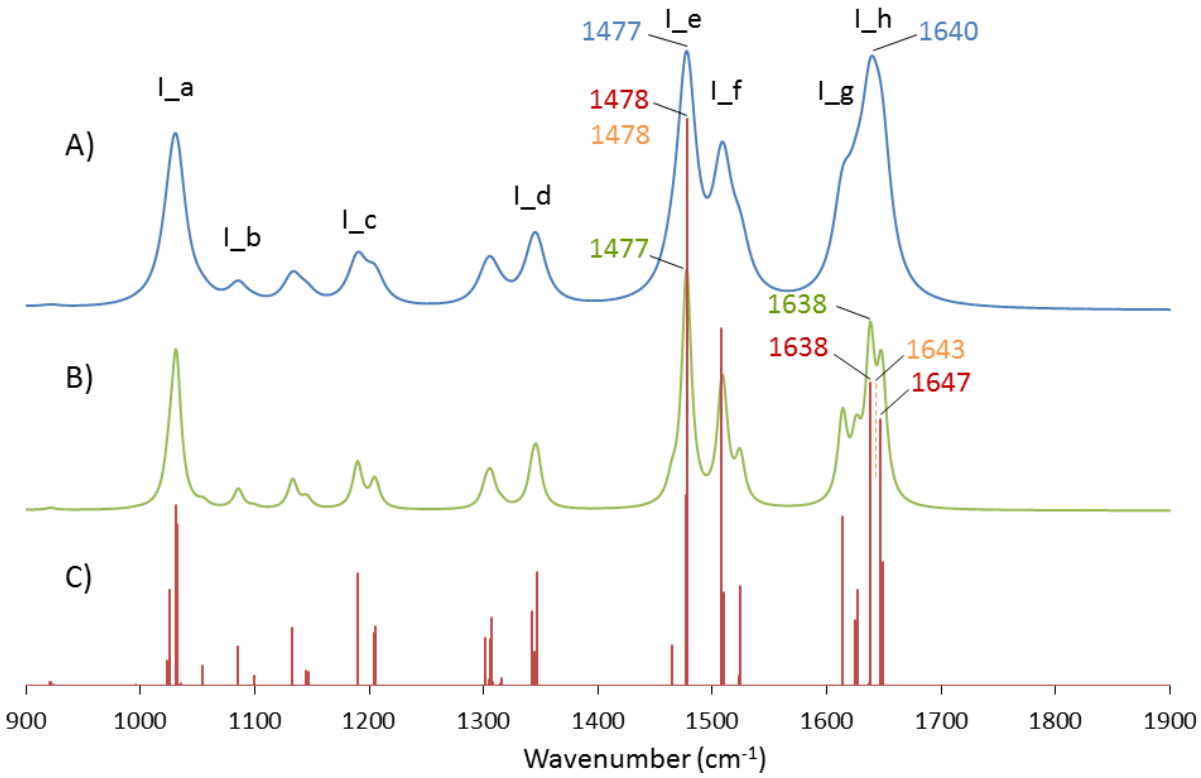

***Figure 5.18**. Unscaled calculated IR spectra of **I** at the B3LYP/6-31+G(d,p) level. Convoluted spectra obtained using a 10 (A) or 5 (B) cm^{-1} (fwhm) Lorentzian linewidth function, and stick bars spectra (C).*

Different strategies have been used to compare the experimental and theoretical vibrational frequencies quantitatively. Whilst the experiments produce broad bands having a linewidth of c.a. 10-15 cm^{-1}, the DFT calculations furnish stick spectra that can be convoluted using Gaussian or Lorentzian profiles. We have explored four different protocols for treating these theoretical data in ways that transform them into single vibrational frequencies that are suitable for comparison with the experimentally observed bands. Initially, we identify the

wavenumber range in the computed spectra that correspond to each experimental band. For example, bands I_e and I_h are associated with all of the unscaled theoretical vibrational frequencies in the 1464-1478 and 1637-1649 cm^{-1} ranges, respectively (Figure 5.18). In the first treatment protocol (P1), the largest peak of each range in the theoretical spectrum is considered to determine the unscaled theoretical vibrational frequency corresponding to the associated experimental band (Figure 5.18C, in red), and this attributes values of 1478 and 1638 cm^{-1} to I_e and I_h, respectively. The second protocol (P2) differs from the first one when several peaks are computed in the same region, and these have an intensity that is at least equal to half of the most intense local peak, a situation that occurs in the 1637-1649 cm^{-1} range of **I**. In this case, the mean of the different values of these computed peak frequencies is taken (Figure 5.18C, in orange). The third (P3) and fourth (P4) protocols involve convoluting the theoretical spectra with a 5 (Figure 5.18B, in green) or 10 cm^{-1} (Figure 5.18A, in blue) (fwhm) Lorentzian linewidth function, respectively. If several peaks still appear in the convoluted spectra (see I_h in Figure 5.18B), the most intense is then used to determine the unscaled theoretical vibrational frequency, and if a band is convoluted with a neighboring band, then the same unscaled theoretical vibrational frequency is attributed to both bands (see I_g and I_h in Figure 5.18A).

The ability of these different data management protocol to generate satisfactory band frequencies was evaluated using unscaled B3LYP/6-31+G(d,p) theoretical vibrational data (Table 5.2). Firstly, we observe that changing the protocol (P1 to P4) that is used to transform the theoretical vibrational frequencies into single band frequencies for quantitative comparison with the experimental spectra has a negligible influence on the scaling factor that is required for subsequent correction to the experimental values. The associated mean absolute error (MAE) and root-mean-square error (RMSE) also show a minimal dependence upon the protocol employed, except in the case of protocol P4 which generates slightly greater values

of both RMSE and MAE. Equally, the mathematical treatment employed to obtain the scaling factor (which involved either averaging the individual values or the minimization of MAE or RMSE), also has a minimal effect on the scaling factor, which ranges from 0.9766 to 0.9786 when using P2. The variation of MAE and RMSE values when used with these scaling factors are small, with their values being 10.2 ± 0.2 cm^{-1} for MAE and 13.3 ± 0.3 cm^{-1} for RMSE. However, it should be noted that the use of imprecise scaling factors can lead to significant deviations, as shown in Figure 5.19. For example, increasing or decreasing the scaling factor by 0.01 increases the errors by roughly 50 %.

Table 5.2. Scaling factors, linear correlation values and associated MAE and RMSE obtained at the B3LYP/6-31+G(d,p) level of calculation for different data management.

		P1[a]	P2[a]	P3[a]	P4[a]
Average[b]	sf_{ave}	0.9786	0.9786	0.9787	0.9786
	MAE	10.08	10.07	10.07	10.28
	RMSE	13.47	13.40	13.32	13.58
MAE[c]	sf_{MAE}	0.9777	0.9776	0.9782	0.9782
	MAE	9.99	9.98	10.04	10.24
	RMSE	13.26	13.17	13.19	13.47
RMSE[d]	sf_{RMSE}	0.9767	0.9766	0.9767	0.9765
	MAE	10.14	10.18	10.21	10.43
	RMSE	13.17	13.09	13.03	13.26
Linear correction[e]	a [e]	1.0621	1.0635	1.0625	1.0641
	b [e]	-53.4	-55.1	-54.0	-56.0
	R^2 [f]	0.9977	0.9979	0.9979	0.9978
	MAE	7.53	7.28	7.18	7.32
	RSME	10.08	9.77	9.82	9.88

[a] Protocol used to associate calculated peak with experimental bands (see text); [b] scaling factor obtained as the arithmetic averaging of the individual scaling factors; [c] scaling factor selected to minimize the MAE; [d] scaling factor selected to minimize the RMSE; [e] predicted frequencies values obtained from the linear correlation analysis, with $\upsilon_{predict} = (\upsilon_{calc} - b)/a$; [f] linear correlation coefficient.

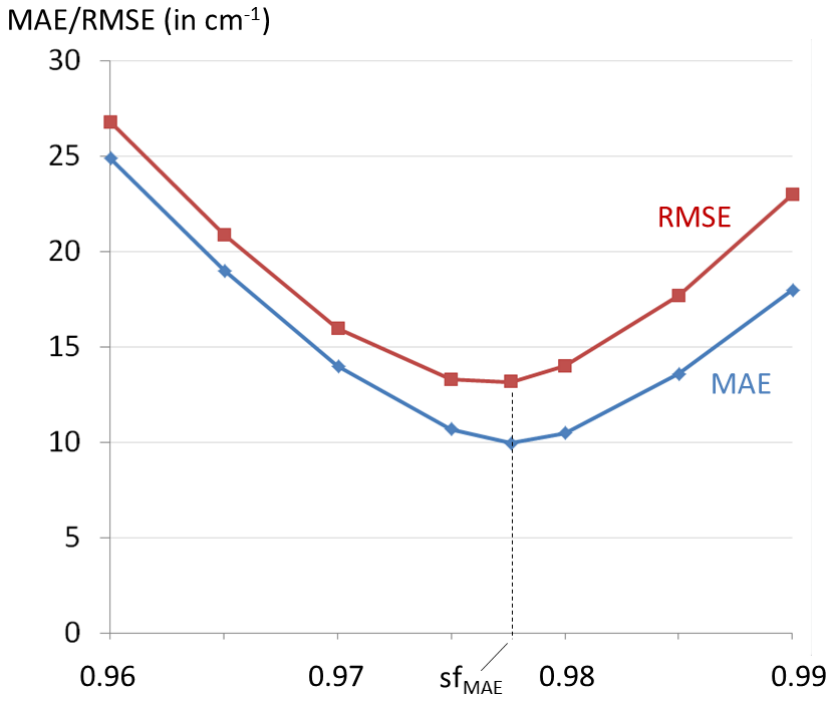

***Figure 5.19**. Variation of MAE and RMSE depending on the scaling factor, at the B3LYP/6-31+G(d,p) level with protocol P2.*

V.3.7. Scaling factors vs linear correction

Figure 5.20 shows the unscaled theoretical vibrational frequencies that are generated by protocol P2 at the B3LYP/6-31+G(d,p) level and their relation to the experimental vibrational frequencies. A clear, and very convincing, linear correlation (coefficient of determination R^2 = 0.9979) is observed, as would be expected given the widespread use of scaling factors to fit experimental data of this kind. However, the linear correlation equation takes the general form: $y = ax + b$ where $b \neq 0$, and this indicates that the use of the scaling factor alone is not optimal for the prediction of experimental values from the theoretical vibrational frequencies. Indeed, Figure 5.20 suggests that a simple linear correction is likely to be a better option than a multiplicative scaling factor. Calculations of MAE and RMSE using the linear correction confirm this (Table 5.2), in that the errors are then reduced significantly, by about 25%, when compared to the best values obtained using the scaling factor. Comparing the results from the

various protocols used to transform the theoretical vibrational frequencies from the calculated spectra into single bands shows slightly larger errors for P1. Large individual errors are particularly undesirable when comparing experimental and theoretical spectra. Consequently, RMSE appears to give a better accuracy diagnosis compared to MAE. Protocol P2, which shows the lowest RMSE (9.77 cm^{-1}), is therefore employed to define theoretical band positions in the remainder of this work.

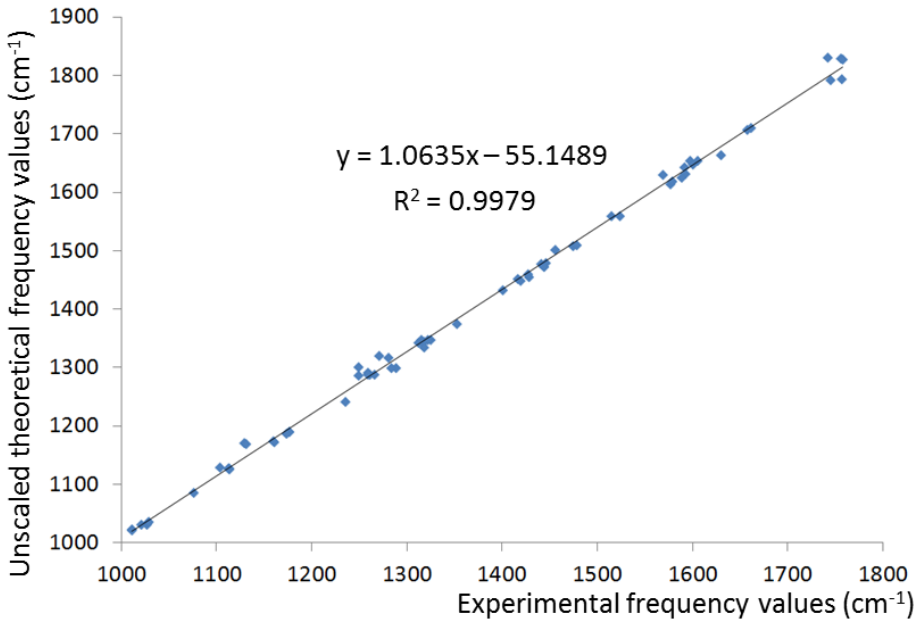

***Figure 5.20**. Experimental vs unscaled theoretical vibrational frequencies computed at the B3LYP/6-31+G(d,p) level with protocol P2.*

V.3.8. Evaluation of the DFT functionals

Calculated MAE and RMSE for a variety of basis sets and DFT functionals are provided in Figure 5.21 and scaling factors and linear correlations that best correct the output from each method to the reference experimental spectra of **I-X** are provided in Table 5.3. In all cases, using the linear correlation instead of a scaling factor decreases the errors in the predicted frequencies significantly, which implies that the traditional procedure is not the optimal one. This can be visualized at the B3LYP level for compounds **I-X** in Figures 5.6-5.15. Three

double ζ basis sets have been evaluated with the B3LYP functional. The def2-SVP basis set shows larger errors than the Pople basis set, with the best predicted frequency values being displayed when diffuse functions are included on the heavy atoms (6-31+G(d,p)). B3LYP outperforms the other functionals M06-2X, CAM-B3LYP, LC-BLYP and ωB97X-D, with LC-BLYP showing the lowest accuracy. Within the RSH class, ωB97X-D gives the smallest errors, even if they are 70% larger than those for B3LYP (with a RMSE for the linear correlation of 16.5 vs 9.8 cm^{-1}). It should be noted that the linear correlation coefficient (Table 5.3) can also be used as a measure of accuracy, in that it varies in the same ways as MAE and RMSE.

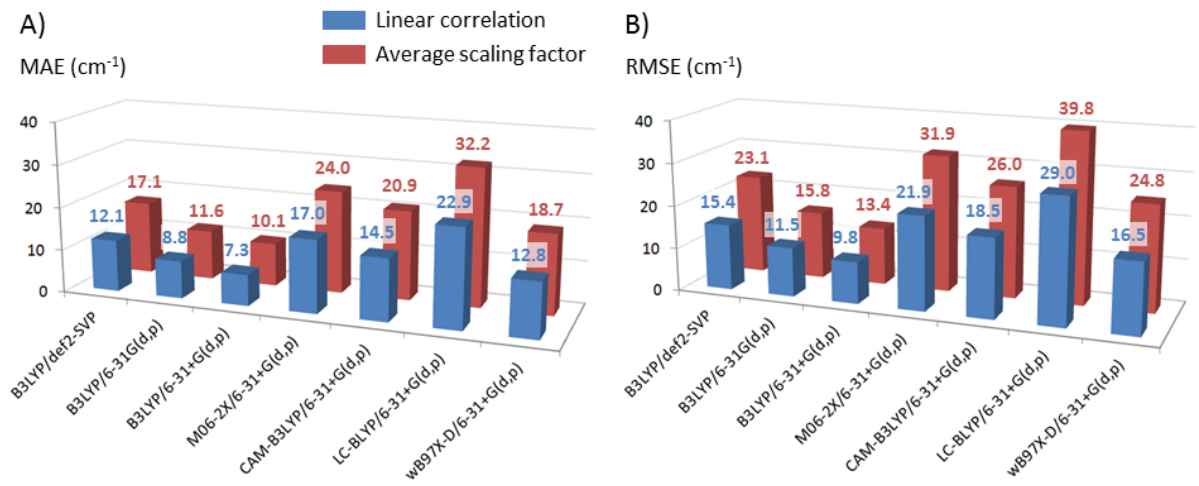

Figure 5.21. *MAE (A) and RMSE (B) calculations between experimental and predicted vibrational frequencies at various DFT levels.*

Table 5.3. A comparison of determined parameters to be used to computed predicted frequency values from unscaled theoretical values.

Functional	Basis set	a[a]	b[a]	R^{2} [b]	sf_{ave}
B3LYP	def2-SVP	1.1010	-102.6	0.9948	0.9769
B3LYP	6-31G(d,p)	1.0743	-65.1	0.9971	0.9754
B3LYP	6-31+G(d,p)	1.0635	-55.1	0.9979	0.9786
M06-2X	6-31+G(d,p)	1.1399	-134.5	0.9894	0.9629
CAM-B3LYP	6-31+G(d,p)	1.1208	-107.3	0.9924	0.9617

LC-BLYP	6-31+G(d,p)	1.1776	-152.1	0.9815	0.9412
ωB97X-D	6-31+G(d,p)	1.1227	-110.8	0.9940	0.9624

[a] predicted frequencies values are obtained from the linear correlation analysis, with $\upsilon_{predict} = (\upsilon_{calc} - b)/a$; [b] linear correlation coefficient.

V.3.9. Confidence interval

The calculated MAE and RMSE with respect to the experimental data for complexes **I-X**, called hereafter global MAE and RMSE, can be taken to be an "accuracy index" for the vibrational frequencies predicted by the respective functionals. We then wonder whether these error values could be used as an indication of the reliability of a calculated structure. In other words, as to whether, when a difference is observed between the experimental and theoretically predicted spectra of other molecules, if this discrepancy results from an intrinsic error of the functional or is due to the fact that an incorrect structure is calculated. To that end, we first compute the individual RMSE, i.e. the RMSE for each individual complex **I-X** at all DFT levels, using the linear relationship parameters (Figure 5.22). The lowest individual RMSE are obtained at all DFT levels for **V** whereas the largest individual RMSE are found for **III** (CAM-B3LYP), **IV** (B3LYP), **IX** (LC-BLYP) or **X** (M06-2X and ωB97X-D). The deviation relative to the global RMSE reaches a maximum of 75% for all DFT levels, i.e. all individual RMSE of **I-X** are in the [global RMSE*(1-3/4); global RMSE*(1+3/4)] range. It means that if the RMSE between the experimental and theoretical spectra are within this range for any studied molecule, then the deviation agrees with the accuracy of the used DFT level and the computed structure could corresponds to the experimental one. On the opposite, it suggests that if an individual RMSE is outside of this range, then the computed structure should probably be checked. This range can therefore be seen as a confidence interval.

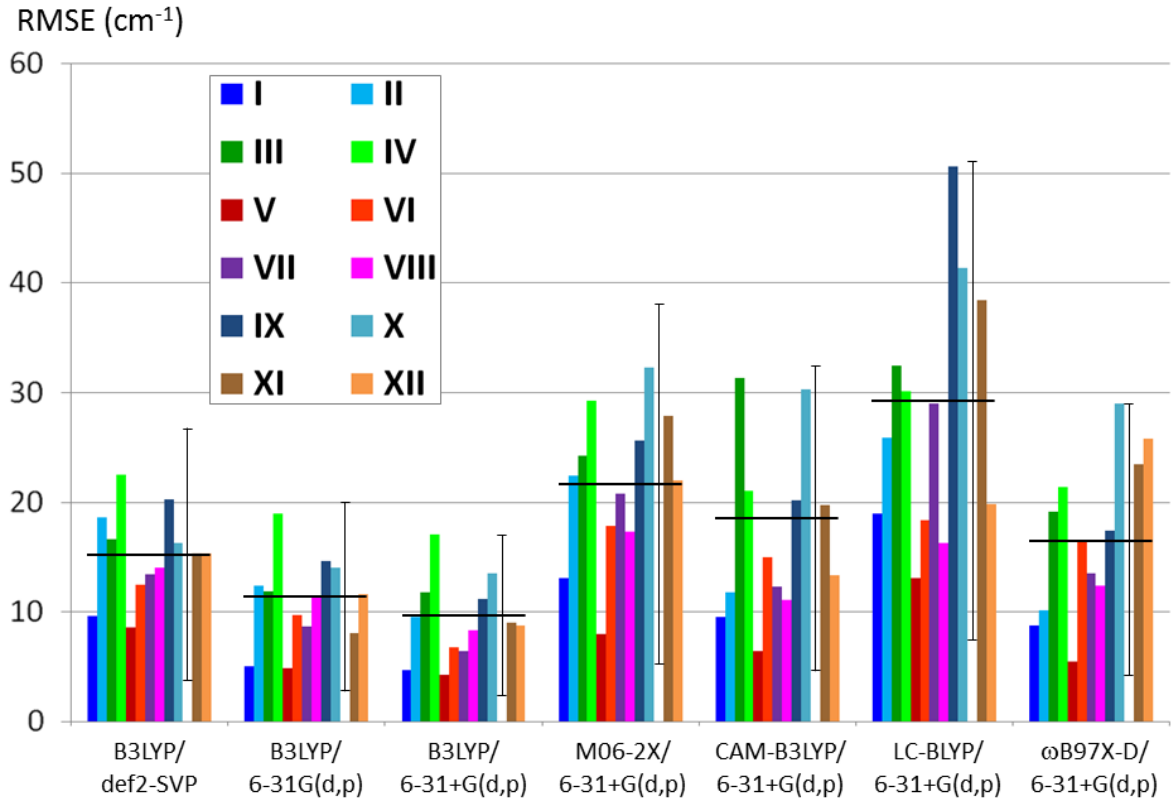

Figure 5.22. *Computed individual RMSE based on the linear correlation analysis for each individual complex **I-XII** at various DFT levels. The global RMSE values for the 68 vibrational modes whole dataset (complexes **I-X**) are indicated by the horizontal black line. The error bar indicates the [global RMSE*(1-3/4); global RMSE*(1+3/4)] range*

To finish, we have studied two other compounds, namely $[Zn(\mathbf{2})_2]^{2+}$ (**XI**) and $[Zn(\mathbf{4})]^{\bullet+}$ (**XII**), in order to compare the results obtained on our database **I-X** to other compounds studied independently. The experimental IRMPD spectrum of **XI** has been recorded following the same experimental process used for **I-X** and is given is Figure 5.23.

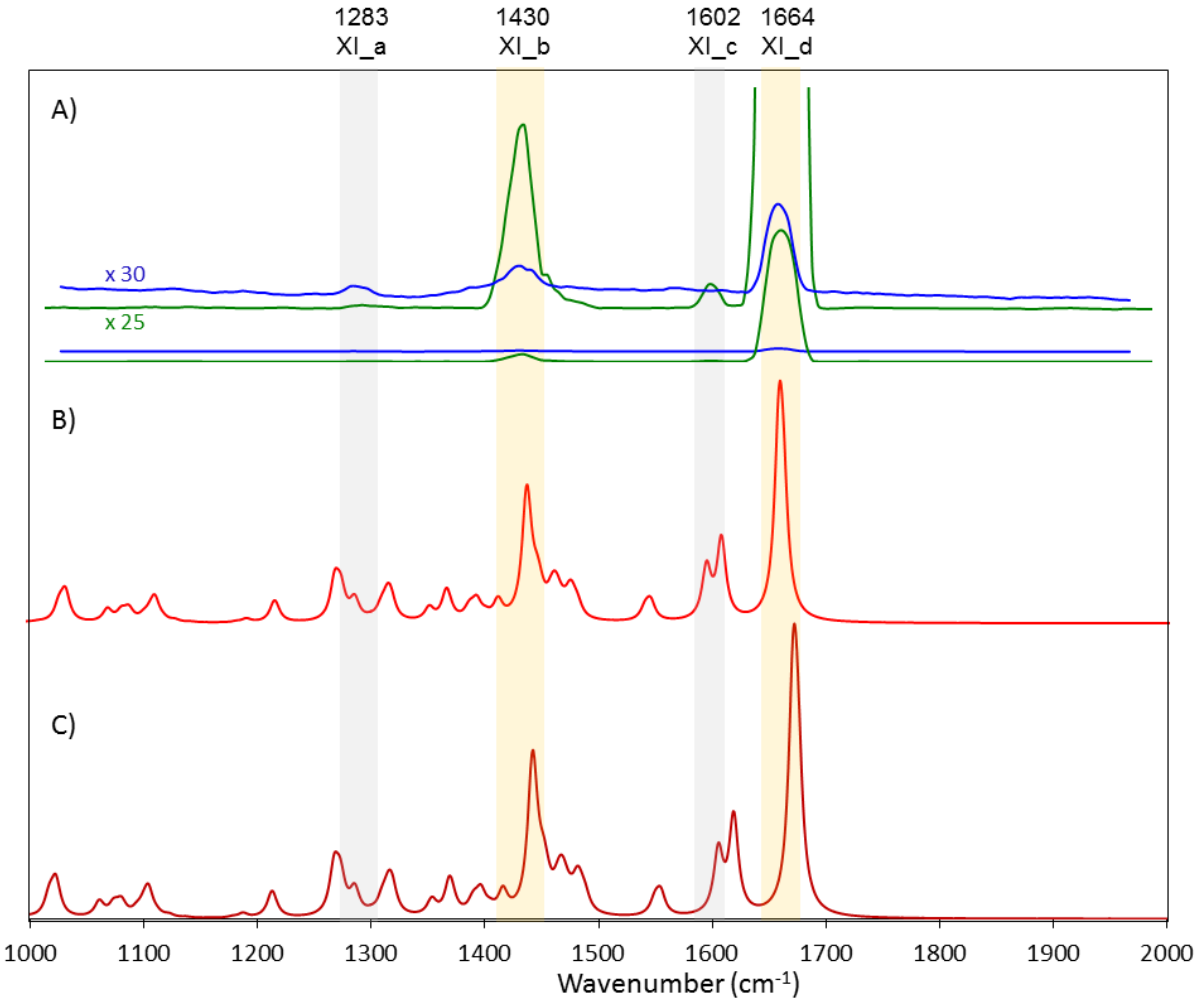

Figure 5.23. *Experimental IRMPD spectra (A) and B3LYP/6-31+G(d,p) computed IR spectra of compound **XI** scaled using the linear correlation method (B) and by a factor of 0.9786 (C) after convolution with a 5 cm^{-1} (fwhm) Lorentzian linewidth function.*

The experimental IRMPD spectrum of **XII** has been included in this comparison because it has been published recently.[43] Theoretical spectra of **XI** and **XII** have been computed with the different DFT levels used previously. The comparison between the experimental IRMPD spectra and the predicted theoretical spectra leads to individual RMSE values which are indicated in Figure 5.22. For both **XI** and **XII**, all individual RMSE are within the confidence interval (i.e. within the [global RMSE*(1-3/4); global RMSE*(1+3/4)] range), suggesting that the computed structure correspond to the experimental one. In other word, it means that even if the ωB97X-D calculated IR spectra of **XII** shows significant deviation compared to the experimental one, with an individual RMSE value equal to 25.8 cm^{-1}, the computed structure

should be considered as the correct one because this error value is lower than the global RMSE for this method (16.5 cm^{-1}) increased by 75% (16.5*(1+3/4) = 28.9 > 25.8). This agrees with the fact that for all DFT levels, the computed structure of **XI** and **XII** corresponds respectively to a tetrahedral zinc(II) complex and to a planar di-coordinated Zn(I) complex.

V.4. Conclusion

In this Chapter, we have presented primary experiments of IRMPD and we have explored the ability of various DFT functionals to reproduce IRMPD spectra of organometallic complexes presenting a well-defined structure. For this purpose, we have recorded a set of experimental benchmark data for gas-phase IR frequencies containing 68 vibrational modes for 10 molecules. These spectra were used as reference for comparison with the calculated spectra obtained with three basis set and five different DFT functionals. Standard B3LYP and M06-2X functionals have been tested, as well as the CAM-B3LYP, LC-BLYP and ωB97X-D RSH functionals, which are of interest if the electronic structure of a molecule, in particular radicals, is imperfectly described due to the self-interaction error. The comparison between experimental and theoretical spectra allows to define scaling factors for these level of calculations well adapted for gas-phase studies. Moreover, we showed that the universal procedure of scaling factors is not the most efficient for comparing experimental and theoretical spectra. Indeed, a linear correlation analysis allows obtaining predicted spectra which, compared with the experimental spectra, have both MAE and RMSE errors lowered by about 30% relative to spectra predicted with a scaling factors. With the 6-31+G(d,p) basis set, the order of accuracy of the functionals to predict IRMPD spectra are B3LYP > ωB97X-D > CAM-B3LYP > M06-2X > LC-BLYP with RMSE computed for the whole dataset equal

respectively to 9.8, 16.5, 18.5, 21.9 and 29.0 cm^{-1}. Calculation of individual RMSE for **I**-**X** indicates relatively dispersed results with an error margin of ±75% relative to the global RMSE. The study of two other complexes confirms that as ±75% range from the global RMSE may be considered as a confidence interval for a calculated structure. If the deviation of the individual RMSE relative to the global RMSE is less than 75% of the latter, the studied structure can be considered relevant, while for a larger difference, the structure should probably be rejected.

Based on this work, we are now equipped to study reduced organometallic complexes for which the electronic structure is questionable.

V.5. References

[1]. J. R. Eyler, *Mass Spectrom. Rev.* **2009**, *28*, 448–467.

[2]. J. Oomens, A. J. A. van Roij, G. Meijer, G. von Helden, *Astrophys. J.* **2000**, *542*, 404–410.

[3]. R. C. Dunbar, *Int. J. Mass Spectrom.* **2015**, *377*, 159–171.

[4]. (a) N. R. Walker, R. S. Walters, M. A. Duncan, *New J. Chem.* **2005**, *29*, 1495–1503.: (b) L. Macaleese, P. Maître, *Mass Spectrom. Rev.* **2007**, *26*, 583–605.; (c) N. C. Polfer, J. Oomens, *Mass Spectrom. Rev.* **2009**, *28*, 468–494.; (d) T. D. Fridgen, *Mass Spectrom. Rev.* **2009**, *28*, 586–607. (e) N. C. Polfer, *Chem. Soc. Rev.* **2011**, *40*, 2211–2221. (f) J. Roithova, *Chem. Soc. Rev.* **2012**, *41*, 547–559.

(g) K. R. Asmis, D. M. Neumark, *Acc. Chem. Res.* **2012**, *45*, 43–52. (h) A. L. Patrick, N. C. Polfer, *Top. Curr. Chem.* **2015**, *364*, 153–182.

[5]. D. Semrouni, A. Sharma, J.-P. Dognon, G. Ohanessian, C. Clavaguéra, *J. Chem. Theory Comput.* **2014**, *10*, 3190–3199.

[6]. F. Thaunay, J.-P. Dognon, G. Ohanessian, C. Clavaguéra, *Phys. Chem. Chem. Phys.* **2015**, *17*, 25968–25977.

[7]. M. P. Gaigeot, M. Martinez, R. Vuilleumier, *Mol. Phys.* **2007**, *105*, 2857–2878.

[8]. K. Yagi, T. Taketsugu, K. Hirao, M. S. Gordon, *J. Chem. Phys.* **2000**, *113*, 1005–1017.

[9]. V. Barone, *J. Chem. Phys.* **2005**, *122*, 014108: 1–10.

[10]. (a) A. P. Scott, L. Radom, J. Phys. Chem. 1996, 100, 16502-16513.; (b) M. W. Wong, Chem. Phys. Lett. 1996, 256, 391-399.; (b) L. A. Curtiss, P. C. Redfern, K. Raghavachari, J. A. Pople, *J. Chem. Phys.* **2001**, *114*, 108–117.; (c) P. Sinha, S. E. Boesch, C. M. Gu, R. A. Wheeler, A. K. Wilson, *J. Phys. Chem. A* **2004**, *108*, 9213–9217.; (d) M. P. Andersson, P. Uvdal, *J. Phys. Chem. A* **2005**, *109*, 2937–2941.; (e) Y. Tantirungrotechai, K. Phanasant, S. Roddecha, P. Surawatanawong, V. Sutthikhum, J. Limtrakul, *J. Mol. Struct-Theochem.*, **2006**, *760*, 189–192.; (f) J. P. Merrick, D. Moran, L. Radom, *J. Phys. Chem. A* **2007**, *111*, 11683–11700.; (g) I. M. Alecu, J. Zheng, Y. Zhao, D. G. Truhlar, *J. Chem. Theory Comput.* **2010**, *6*, 2872–2887.; (h) M. L. Laury, M. J. Carlson, A. K. Wilson, *J. Comput. Chem.* **2012**, *33*, 2380–2387.

[11]. J. Jaramillo, G. E. Scuseria, *Chem. Phys. Lett.* **1999**, *312*, 269–276.

[12]. C. W. Bauschlicher Fr, H. Partridge, *J. Chem. Phys.* **1995**, *103*, 1788–1791.

[13]. K. K. Irikura, R. D. Johnson III, R. N. Kacker, *J. Phys. Chem. A* **2005**, *109*, 8430–8437.

[14]. R. D. Johnson III, K. K. Irikura, R. N. Kacker, R. Kessel, *J. Chem. Theory Comput.* **2010**, *6*, 2822–2828.

[15]. G. Maes, J. Smets, L. Adamowicz, W. McCarthy, M. K. Van Bael, L. Houben, K. Schoone, *J. Mol. Struct.* **1997**, *410-411*, 315–322.

[16]. P. Borowski, M. Fernandez-Gomez, M. P. Fernandez-Liencres, T. P. Ruiz, *Chem. Phys. Lett.* **2007**, *446*, 191–198.

[17]. M. D. Halls, J. Velkovski, H. B. Schlegel, *Theor. Chem. Acc.* **2001**, *105*, 413–421.

[18]. (a) M. A. Palafox, *Int. J. Quantum Chem.* **2000**, *77*, 661–684.; (b) M. A. Palafox, N. Iza, M. Gil, *J. Mol. Struct : THEOCHEM* **2002**, *585*, 69–92.; (c) M. A. Palafox, V. K. Rastogi, L. Mittal, *Int. J. Quantum Chem.* **2003**, *94*, 189–204.; (d) M. A. Palafox, M. Gill, N. J. Nunez, V. K. Rastogi, L. Mittal, R. Sharma, *Int. J. Quantum Chem.* **2005**, *103*, 394–421.

[19]. Y. bouteiller, J. C. Gillet, G. Grégoire, J. P. Schermann, *J. Phys. Chem. A* **2008**, *112*, 11656–11660.

[20]. Y. Bouteiller, J. C. Poully, C. Desfrançois, G. Grégoire, *J. Phys. Chem. A* **2009**, *113*, 6301–6307.

[21]. D. Semrouni, C. Clavaguéra, J. P. Dognon, G. Ohanesian, *Int. J. Mass Spectrom.* **2010**, *297*, 152–161.

[22]. A. Sharma, G. Ohanessian, C. Clavaguéra, *J. Mol. Model.* **2014**, *20*, 2426.

[23]. G. Frison, G. van der Rest, F. Turecek, T. Besson, J. Lemaire, P. Maitre, J. Chamot-Rooke, *J. Am. Chem. Soc.* **2008**, *130*, 14916–14917.

[24]. J. Martens, J. Grzetic, G. Berden, J. Oomens, *Nat. Commun.* **2016**, DOI: 10.1038/ncomms11754.

[25]. C. J. Shaffer, J. Martens, A. Marek, J. Oomens, F. Turecek, *J. Am. Soc. Mass Spectrom.* **2016**, *27*, 1176–1185.

[26]. (a) R. A. Zubarev, *Mass Spectrom. Rev.* **2003**, *22*, 57–77.; (b) H. J. Cooper, K. Hakansson, A. G. Marshall, *Mass Spectrom. Rev.* **2005**, *24*, 201–222.; (c) L. M. Mikesh, B. Ueberheide, A. Chi, J. J. Coon, J. E. P. Syka, J. Shabanowitz, D. F. Hunt, *Biochim. Biophys. Acta* **2006**, *1764*, 1811–1822.; (d) K. O. Zhurov, L. Fornelli, M. D. Wodrich, Ü. A. Laskay, Y. O. Tsybin, *Chem. Soc. Rev.* **2013**, *42*, 5014–5030.

[27]. J. Simons, *Chem. Phys. Lett.* **2010**, *484*, 81–95.

[28]. F. Turecek, R. R. Julian, *Chem. Rev.* **2013**, *113*, 6691–6733.

[29]. (a) A. I. Gilson, G. van der Rest, J. Chamot-Rooke, W. Kurlancheek, M. Head-Gordon, D. Jacquemin, G. Frison, *J. Phys. Chem. Lett.* **2011**, *2*, 1426–1431.; (b) V. Riffet, D.

Jacquemin, E. Cauët, G. Frison, *J. Chem. Theory Comput.* **2014**, *10*, 3308–3318.; (c) V. Riffet, D. Jacquemin, G. Frison, *Int. J. Mass Spectrom.* **2015**, *390*, 28–38.

[30]. M. J. Frisch, G. W. Trucks, H. B. Schlegel, G. E. Scuseria, M. A. Robb, J. R. Cheeseman, G. Scalmani, V. Barone, B. Mennucci, G. A. Petersson, H. Nakatsuji, M. Caricato, X. Li, H. P. Hratchian, A. F. Izmaylov, J. Bloino, G. Zheng, J. L. Sonnenberg, M. Hada, M. Ehara, K. Toyota, R. Fukuda, J. Hasegawa, M. Ishida, T. Nakajima, Y. Honda, O. Kitao, H. Nakai, T. Vreven, J. A. Montgomery, Jr., J. E. Peralta, F. Ogliaro, M. Bearpark, J. J. Heyd, E. Brothers, K. N. Kudin, V. N. Staroverov, T. Keith, R. Kobayashi, J. Normand, K. Raghavachari, A. Rendell, J. C. Burant, S. S. Iyengar, J. Tomasi, M. Cossi, N. Rega, J. M. Millam, M. Klene, J. E. Knox, J. B. Cross, V. Bakken, C. Adamo, J. Jaramillo, R. Gomperts, R. E. Stratmann, O. Yazyev, A. J. Austin, R. Cammi, C. Pomelli, J. W. Ochterski, R. L. Martin, K. Morokuma, V. G. Zakrzewski, G. A. Voth, P. Salvador, J. J. Dannenberg, S. Dapprich, A. D. Daniels, Ö. Farkas, J. B. Foresman, J. V. Ortiz, J. Cioslowski, D. J. Fox, Gaussian, Inc., Wallingford CT, **2013:q**, Gaussian 09 (Revision D.01).

[31]. (a) A. D. Becke, *J. Chem. Phys*. **1993**, *98*, 5648–5652.; (b) A. D. Becke, *Phys. Rev. A* **1988**, *38*, 3098–3100.; (c) C. Lee, W. Yang, R. G. Parr, *Phys. Rev. B* **1988**, *37*, 785–789.

[32]. Y. Zhao, D. G. Truhlar, *Theor. Chem. Acc.* **2008**, *120*, 215–241.

[33]. T. Yanai, D. Tew, N. Handy, *Chem. Phys. Lett.* **2004**, *393*, 51–57.

[34]. H. Likura, T. Tsuneda, T. Yanai, K. Hirao, *J. Chem. Phys.* **2001**, *115*, 3540–3544.

[35]. J. D. Chai, M. Head-Gordon, *Phys. Chem. Chem. Phys.* **2008**, *10*, 6615–6620.

[36]. F. Weigend, R. Ahlrichs, *Phys. Chem. Chem. Phys.* **2005**, *7*, 3297–3305.

[37]. (a) W. J. Hehre, R. Ditchfield, J. A. Pople, *J. Chem. Phys.* **1972**, *56*, 2257–2261.; (b) M. M. Francl, W. J. Pietro, W. J. Hehre, J. S. Binkley, D. J. DeFrees, J. A. Pople, M. S. Gordon, *J. Chem. Phys.* **1982**, *77*, 3654–3665.; (c) V. A. Rassolov, J. A. Pople, M. A. Ratner, T. L. Windus, *J. Chem. Phys.* **1998**, *109*, 1223–1229.

[38]. T. Clark, J. Chandrasekhar, G. W. Spitznagel, P. v. R. Schleyer, *J. Comp. Chem.* **1983**, *4*, 294–301.

[39]. P. J. Hay, W. R. Wadt, *J. Chem. Phys.* **1985**, 82, 270–283.

[40]. R. Prazeres, F. Glotin, C. Insa, D. A. Jaroszynski, J. M. Ortega, *Eur. Phys. J. D* **1998**, *3*, 87–93.

[41]. R. G. Inskeep, *J. Inorg. Nucl. Chem.* **1962**, *24*, 763–776.

[42]. A. A. Schilt, R. C. Taylor, *J. Inorg. Nucl. Chem.* **1959**, *9*, 211–221.

[43]. M. Katari, E. Payen de la Garanderie, E. Nicol, V. Steinmetz, G. van der Rest, D. Carmichael, G. Frison, *Phys. Chem. Chem. Phys.* **2015**, *17*, 25689–25692.

Chapter VI

Characterization of reduced metal complexes

VI.1. Introduction

In the previous chapter of this thesis manuscript, with have shown that:

i. Electrospray ionization (ESI) can be used to form in the gas phase dicationic zinc and ruthenium complexes containing non-innocent ligands (Chapter III).

ii. Electron capture dissociation (ECD) and electron transfer dissociation (ETD) methods applied on these ligands induces the formation of singly-reduced metal complexes containing non-innocent ligands. In most cases, the formation of these radical compounds is accompanied by the dissociation of one or two ligands from the parent dication, preventing to obtain some complexes (Chapter III).

iii. Infrared multiple photon dissociation (IRMPD) action spectroscopy method can be applied both on dicationic and on reduced monocationic complexes, providing IR signature of these compounds. The fragmentation upon irradiation, mostly one ligand dissociation, is often more difficult for the latter because their formation already go along with a ligand loss. Furthermore, the intensity of the reduced compounds is always low, which induces that the IRMPD spectra of the reduced monocationic complexes are noisy. (Chapter V)

iv. Range-separated hybrid (RSH) functionals, such as ωB97X-D, LC-BLYP and CAM-B3LYP, as well as the M06-2X functional, provide IR spectra that are in modest agreement with experimental IR spectra, compared to the B3LYP functional. A confidence interval for these methods has been established for the calculation of IR spectra, based on the study of closed-shell organometallic complexes (Chapter V).

v. The electronic structure of reduced radical organometallic species are, at least for systems such as $[Zn(L)(L')]^{\bullet+}$ (L, L' = bidentate ligands), problematic cases for

DFT methods. Indeed, depending on the amount of Hartree-Fock (HF) exchange, in particular at long interelectronic distance, a localized ($[Zn^{2+}(L^{-1})(L'^{0})]$) or delocalized ($[Zn^{2+}(L^{-1/2})(L'^{-1/2})]$) electronic structure can be obtained. We hypothesize that RSH functionals give the correct electronic structure, unlike more "standard" functionals.

On the basis of these results, we describe in this chapter the characterization of open-shell reduced organometallic complexes by combining IRMPD experiments and DFT calculations. In section VI.2, we reproduce the manuscript we have published recently in the Physical Chemistry Chemical Physics journal, which demonstrates the capability of our approach to characterize a reduced zinc complex coordinated by a single bidentate ligand. In the following sections, we extend this study to other organometallic complexes.

VI.2. Proof of Concept

Following our work in Chapter IV in which we have shown that the electronic structure of $[Zn(L)(L')]^{\bullet+}$ is a problematic case for DFT methods, we have looked for a simpler radical system for a first experimental characterization. This was found for $[Zn(L)]^{\bullet+}$ complexes for which all DFT methods give the same electronic structure with the single electron located on the zinc atom. We therefore decide to start our study of radical species by one of these radical for which there is no computational problem. For this first proof of our approach, we select the zinc complex with ligand **4** because it's C=O stretch is characteristic. The publication which has resulted from this study is reproduced in the following pages, as well as the most important data which were put in the supporting information.

VI.2.1. Manuscript

PCCP

COMMUNICATION

Combining gas phase electron capture and IRMPD action spectroscopy to probe the electronic structure of a metastable reduced organometallic complex containing a non-innocent ligand†

Cite this: *Phys. Chem. Chem. Phys.*, 2015, **17**, 25689

Received 13th March 2015,
Accepted 29th May 2015

DOI: 10.1039/c5cp01501d

www.rsc.org/pccp

Madanakrishna Katari,[a] Eleonore Payen de la Garanderie,[a] Edith Nicol,[a] Vincent Steinmetz,[b] Guillaume van der Rest,[b] Duncan Carmichael[a] and Gilles Frison*[a]

Combining electron capture dissociation mass spectrometry and infrared multiple photon dissociation action spectroscopy allows the formation, selection and characterisation of reduced metal complexes containing non-innocent ligands. Zinc complexes containing diazafluorenone ligands have been studied and the localisation of the single electron on the metal atom in the mono-ligated complex has been demonstrated.

Despite the ubiquitous nature of electronic reduction processes, the question of where the reducing electron becomes localized on the recipient molecule often remains unanswered. Addressing this fundamental question is crucial to the understanding of many chemical processes, such as the site(s) of the electron attachment to biological molecules after exposure to ionizing radiation, which leads to cell damage,[1] or the implication of innocent *vs.* non-innocent ligands in coordination chemistry,[2] and organometallic[2,3] or enzymatic catalysis.[4] Several experimental methods including NMR, EPR, cyclic voltammetry and UV/Vis spectroscopy are available for addressing this issue in solution, but most of them are poorly adapted to the analysis of trace components in complex mixtures, such as catalytic intermediates in ongoing reactions, and often provide only partial information.

Electron-based methods in mass spectrometry (MS) are fragmentation techniques which have shown profound potential for the analysis of peptides and proteins.[5] They are also used to

bring important information on native protein structure.[6] Among them, electron capture and transfer dissociation (ECD/ETD) attaches an electron to multiply-charged electrosprayedcations and treats the subsequent fragmentation of the reduced radicalcation products.[7] Obtaining a good experimental electronic description of the product radicals remains an open and challenging issue,[8] but, recently, coupling ETD to near-UV photodissociationtechniques has allowed the nature of some cation-peptide radical chromophores to be resolved.[9] The application of ECD/ETD to transition metal organometallic cations has mostly focused on metal-peptide complexes,[10,11] although some studies have shown their use for cationizedoligosaccharide[12] and phosphocholine[13] fragmentation, as well as for the generation of reduced cation species in water clusters.[14] Metal complexes of polyamidoamine dendrimers[15] and oligonuclearmetallo-supramolecular complexes[16,17] have also been subjected to ECD studies, providing some evidence of electron capture on a bipyridyl ligand.[17] The capacity of ECD/ETD techniquesto generate specifically reduced organometallic radical ions was not explored in these studies.However, a method employing gas phase electron transfer from cesium atoms has been used recently to reduce a dicationic Ru complex, and the structure of the reduction product was studied by UV-photodissociation.[18]

InfraRed Multiple Photon Dissociation (IRMPD) action spectroscopy has emerged recently as an efficient and generally applicable technique for the analysis of isolated ions through measurement of their IR spectra;[19] these "action" spectra are generated through on-resonance absorption of multiple IR photons at an active vibrational mode of a mass-selected ion, and take the form of a plot of fragmentation abundance as a function of photon wavelength. Whilst the nature of the multiple photon excitation mechanism can cause the IR action spectra to differ from the calculated linear IR absorption spectra, particularly with respect to relative line intensities,[20] the resulting experimental spectra are ideally adapted for comparison with

DFT-derived computational data, which represent isolated gas phase ions well. They therefore allow the nature of the product species to be verified with precision. IRMPD has been used previously to study interaction of metals with redox-active ligands generated by electrospray ionization.[21] Acombination of ECD and IRMPD techniques has also allowed the structure of an even-electron ECD-generated peptide fragment to be established by IR action spectroscopy.[22]

Herein, we demonstrate the possibility to combine sequentiallyECD and IRMPD processes to select organometallic species from mixtures and characterize the electronic structures of their reduction products in the gas phase. Zn complexes of 4,5-diazafluoren-9-one (abbreviated here as dafo), a ligand which incorporates two typical functionalities that are widespread in coordination and organometallic chemistry (2,2'-bipyridine and CO), were chosen for the study.

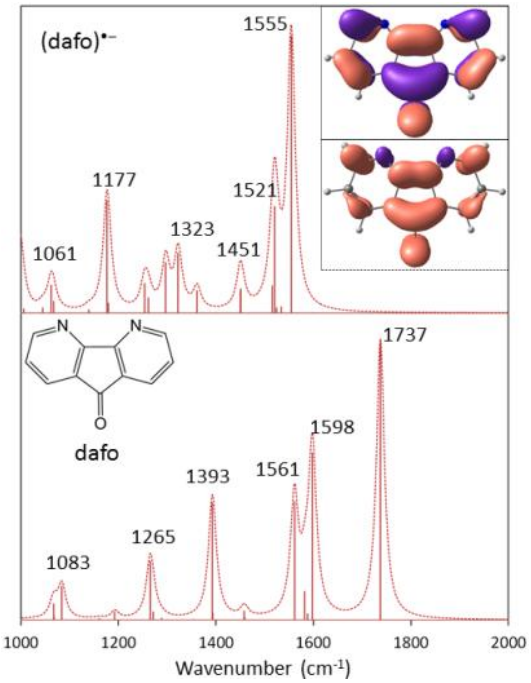

Figure M1. *B3LYP/6-31+G(d,p) calculated IR spectra (scaling factor 0.97) of 4,5-diazafluoren-9-one (bottom) and its reduced form (top). Inset: the SOMO (top) and spin density (bottom) of* $(dafo)^{\bullet-}$.

B3LYP/6-31+G(d,p) calculations on both free neutral (dafo), which at this level of calculation has an adiabatic electron affinity of 149 $kJ.mol^{-1}$,and its anion radical reduced form $(dafo)^{\bullet-}$

show that the C=O stretching vibration shifts from 1737 to 1555 cm^{-1} upon accepting an electron (Figure M1) and confirm that the π-antibonding nature of the singly occupied molecular orbital (SOMO) delocalizes the unpaired electron well over the whole π-system. Whilst the bipyridyl unit in the neutral dafo molecule features four well-separated bands around 1580 (mainly CC and CN stretches), 1393 (CH bending), 1265 (CC stretches and CH bending) and 1083 (CH bending) cm^{-1}, a more complex signature including many different bands (mixed CC and CN stretches, and CH bending) between 1000 and 1521 cm^{-1} appears for the reduced radical anion $(dafo)^{\bullet-}$ (see the Supporting Information for a complete description of the calculated bands).

Subjecting a simple 3:1 mixture of dafo and $Zn(BF_4)_2$ in a 1:2 water/acetonitrile solution to electrospray ionization generates, *inter alia*, the gas-phase $[Zn(dafo)_3]^{2+}$ complex (*m*/*z* 305). This ion was mass-selected and irradiated with monochromated IR photons. When these were on resonance, multiple photon absorption induced dissociation of the ion, with the loss of a neutral dafo ligand to yield a product ion at *m*/*z* 214 (see MS spectrum in the SI). IR action spectroscopy of $[Zn(dafo)_3]^{2+}$ was performed in the 1000-2000 cm^{-1} region (Figure M2) and five bands, centered at 1090, 1229, 1407, 1559 and 1740 cm^{-1} are revealed in the experimental spectrum. These lie close those calculated at the DFT level for the octahedral $[Zn(dafo)_3]^{2+}$ complex wherein all three ligands are equivalent; the C=O stretching frequency of 1740 cm^{-1} (DFT: 1776 cm^{-1}) is close to the calculated value for the free ligand dafo (1737 cm^{-1}), whilst the other bands (CC and CN stretchingand CH bending) also overlap nicelywith those of the freeligand. Coordination to the zinc(II) center therefore has minimal influenceon theligand spectroscopicsignature.

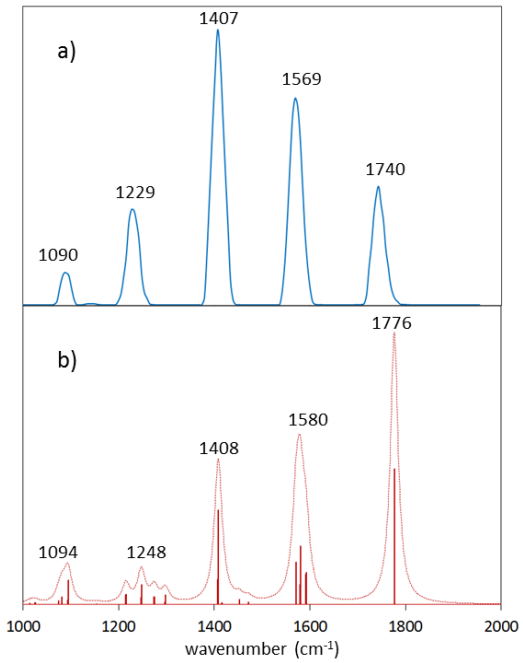

Figure M2. *Experimental IR action spectrum (a) and calculated IR absorption spectrum at the B3LYP/6-31+G(d,p) level (scaling factor 0.97) (b) of* $[Zn(dafo)_3]^{2+}$

Application of ECD to effect reduction of the $[Zn(dafo)_3]^{2+}$dication generated the spectrum given in Figure M3. One unique product having an *m/z* of 246 is observed, so that gas phase monoelectron capture is associated with the release of two neutral dafo ligands, and the product is $[Zn(dafo)]^{\bullet+}$. This fragmentation is consistent with B3LYP/6-31+G(d,p) calculations that predict *a)* a vertical electron affinity for $[Zn(dafo)_3]^{2+}$ of 717 kJ.mol^{-1} and *b)* that the dissociation of the two neutral ligands is endothermic by 641 kJ.mol^{-1}.

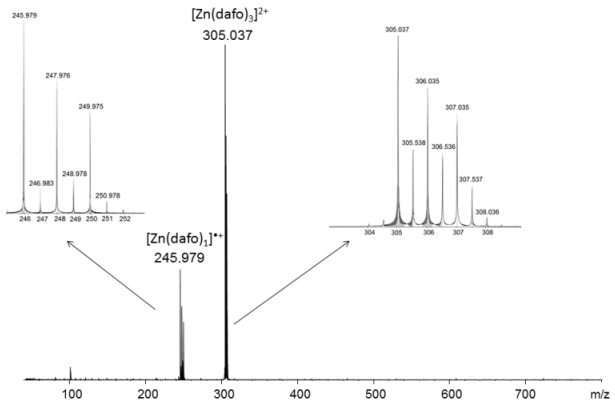

Figure M3. *ECD mass spectrum of* $[Zn(dafo)_3]^{2+}$*. The peak at m/z 101.679 is the third harmonic of the parent ion.*

N-donor chelating ligands of the bipy family are important because of their ability to accept an electron to form bipyridyl radical anions, in $[Ru(bipy)_3]^{\bullet+}$ and related complexes.[23] This is well known in solution, where the solvent can stabilize the ligand as a radical anion, but has also been evidenced recently for gas phase metal complexes.[17,18] Equally, Zn^{2+} is apt for the capture of an incoming electron in Zn-peptide systems.[10] The generation of the $[Zn(dafo)]^{\bullet+}$ radical above allows its electronic structure and the electron localization on the two potential (Zn and dafo) sites to be probed experimentally through IR action spectroscopy.

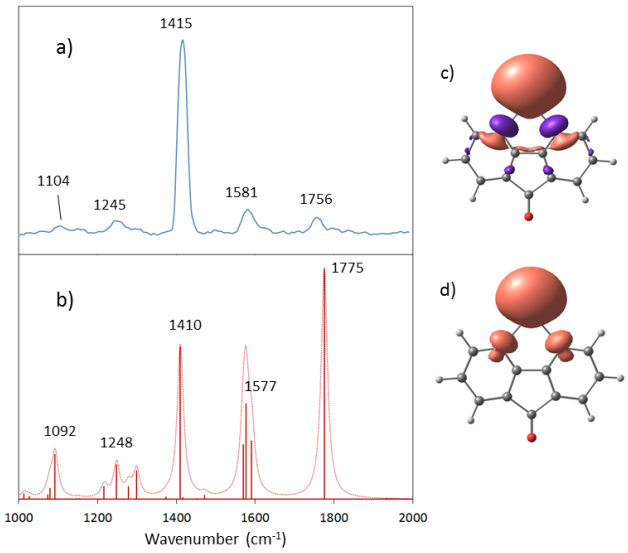

Figure M4. *Experimental IR action spectrum of* $[Zn(dafo)]^{\bullet+}$ *(a) and its calculated IR absorption spectrum (b), SOMO (c) and spin density (d) in the ground state at the B3LYP/6-31+G(d,p) level (scaling factor 0.97). Note the intensity differences between the DFT-predicted classical IR spectrum and the IRMPD generated experimental spectrum.*

The observation of one intense band at 1415 cm^{-1} and four low intensity bands at 1104, 1245, 1581 and 1756 cm^{-1} in the IR action spectrum of $[Zn(dafo)]^{\bullet+}$ (Figure 4), along with their similarity to the IR action spectrum of $[Zn(dafo)_3]^{2+}$, indicate that the dafo ligand in $[Zn(dafo)]^{\bullet+}$ does not take the electron: both the C=O stretching mode and the delocalized CC and CN stretching and CH bending modes remain unperturbed, so it is the zinc center that is reduced. This is confirmed by DFT calculations, which give an electronic ground state having

the single electron located on the metal center and provide a calculated IR spectrum for [($Zn^{\bullet+}$)(dafo)] that matches the experimental IR action spectrum well (Figure M4).

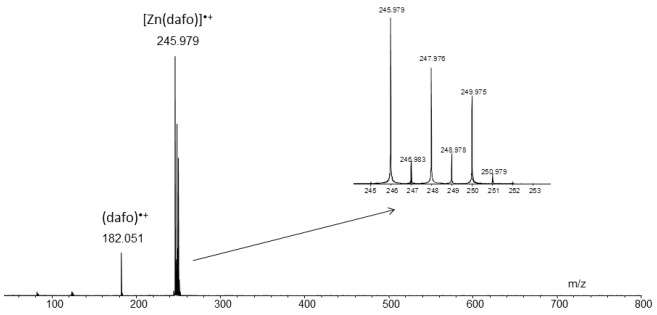

Figure M5. *IRMPD mass spectrum obtained after mass selection of* $[Zn(dafo)]^{\bullet+}$ *(m/z 246) and irradiation on resonance at 1415* cm^{-1}.

The fragment that is observed at *m*/*z* 182 when $[Zn(dafo)]^{\bullet+}$ (*m*/*z* 246) is photon irradiated at appropriate resonance frequencies (Figure M5) results from the collapse of $[Zn(dafo)]^{\bullet+}$ through loss of neutral Zn(0) to form the free ligand radical cation $(dafo)^{\bullet+}$; a similar fragmentation process has been observed recently in collision-induced dissociation of $[Zn(bipy)]^{\bullet+}$complex.[24] B3LYP/6-31+G(d,p) calculations indicate that this fragmentation channel (i) is more favorable by 80 $kJ.mol^{-1}$than the formation of $Zn^{\bullet+}$ and neutral dafo; and (ii) is significantly more endothermic (237 $kJ.mol^{-1}$) than the loss of one dafo ligand from $[Zn(dafo)_3]^{2+}$ that was observed above (157 $kJ.mol^{-1}$), and this explains the relatively noisy IR action spectrum, despite prolonged IR irradiation (2 seconds) compared to that used for $[Zn(dafo)_3]^{2+}$ (0.45 s). Both the localization of the incoming electron in the $[Zn(dafo)]^{\bullet+}$ radical cation and its fragmentation pathway are therefore established.

The experiments demonstrate that a desired organometallic complex can be selected by electrospray MS from a mixture and then mono-reduced in the gas phase, where its vibrational spectra can be obtained. This provides an IR spectroscopic signature of a reduced metal-ligand ensemble which can then be compared either *a)* with spectra observed in non-reduced systems or *b)* with DFT computational results. Further, coupling ECD and IR action

spectroscopy constitutes an approach that is likely to be particularly advantageous when studies of highly reactive radical complexes that are unstable in solution are required. Likewise, the means to generate simple monoligated metal centers for study, that this methodology provides, obviously constitutes a particularly desirable simplification for interpreting any M-L interactions that may be essential to catalytic processes. Finally, the gas phase signature of these species has been shown to reveal intimate details of the localization of the single electron within the complex. Comparison with solvated ions should allow the influence of solvent molecules or counter ions in the electronic structure of reduced species to be identified and optimised.[25]

VI.2.2. Supporting Information

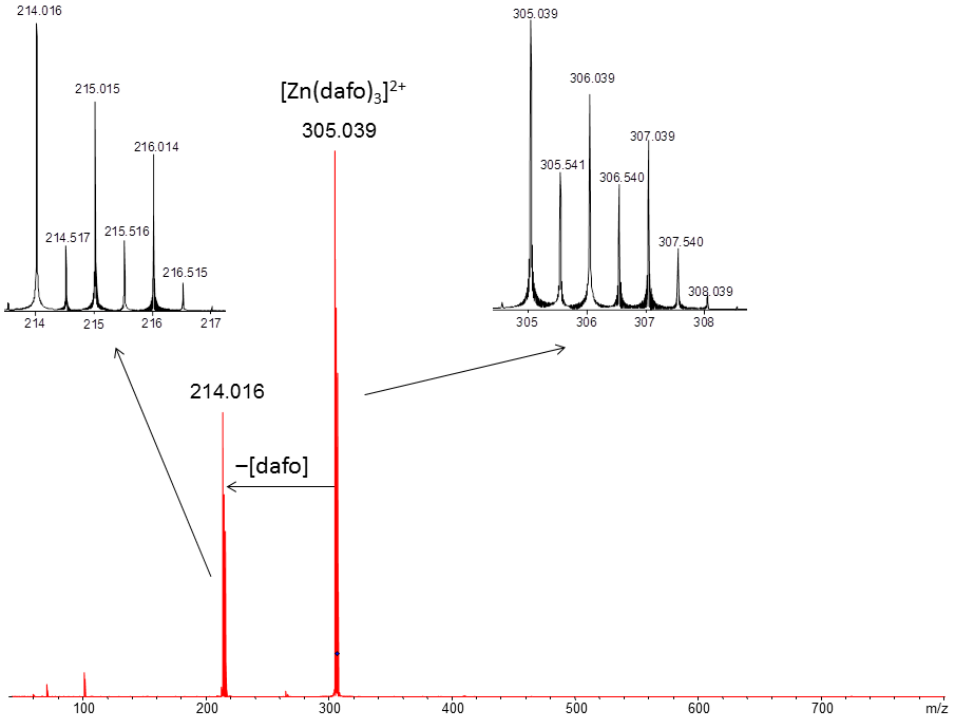

***Figure S5**. IRMPD mass spectrum (Ion intensity in arbitrary units) obtained after mass selection of $[Zn(dafo)_3]^{2+}$ (m/z 305) in a 7T Fourier transform ion cyclotron resonance (FT-ICR) tandem mass spectrometer (Bruker Apex Qe) followed by irradiation with tunable free electron laser IR radiation on resonance at 1408 cm^{-1}.*

Methods

Experimental methods

The solution was prepared in a 1:2 water/acetonitrile solution by mixing 4,5-diazafluorenone-9 and zinc(II) tetrafluoroborate. Dicationic complex $[Zn(dafo)_3]^{2+}$ was formed in an electrospray source in positive mode and observed by high resolution mass spectrometry with a 7T Fourier Transform Ion Cyclotron Resonance (FT-ICR) tandem mass spectrometer (Bruker Apex Qe). The $[Zn(dafo)_3]^{2+}$ ion was isolated in the quadrupole with an isolation window of *m*/*z* 5 and accumulated in the collision cell for 2 seconds. The radical cation $[Zn(dafo)]^{\bullet+}$ was obtained by Electron Capture Dissociation (ECD) experiments performed on the mass-selected $[Zn(dafo)_3]^{2+}$ ion with an indirectly heated cathode at 1.6 A. The ECD pulse length was set at 0.1 second, the ECD Bias at 6 V and the ECD Lens at 10 V. The radical cation $[Zn(dafo)]^{\bullet+}$ was mass-selected in the ICR Cell. The ion of interest is then irradiated for either 0.45 ($[Zn(dafo)_3]^{2+}$) or 2 seconds ($[Zn(dafo)]^{\bullet+}$) with an IR laser. Vibrational spectra were obtained in the 1000-2000 cm^{-1} region by IRMPD using the FT-ICR spectrometer coupled to a tunable free electron laser at the Centre Laser Infrarouge d'Orsay (CLIO).[26] In IRMPD action spectroscopy, when the laser wavelength becomes resonant with a vibrational transition of the mass-selected species, a sequential absorption of multiple photons that is coupled to fast intramolecular vibrational redistribution can deposit internal energy within the species up to threshold energy for fragmentation. The intensity of parent and fragment ions after laser irradiation are monitored as a function of the excitation wavelength, with the photofragmentation yield being calculated for each wavelength according to $-\ln[I_{parent}/(I_{parent} + \Sigma I_{fragments})]$. At each wavelength step, 4 mass spectra were averaged.

Computational Methods

Calculations were carried out with the Gaussian09 package[27] and all structures were fully optimized without any symmetry constraints at the DFT level by means of the B3LYP functional.[28] The 6-31+G(d,p) basis set was applied for all atoms. This level of calculation was shown previously to provide reliable structure and IR spectra.[29] For each stationary point, we carried out vibrational frequency calculation at the same level to characterize their nature as minima. To get accurate geometries and energies, the SCF convergence criterion was systematically tightened to 10^{-8} au, and the force minimizations were carried out until the rms force became smaller that (at least) 1 x 10^{-5} au ("tight" optimization keyword in Gaussian 09). The "UltraFine" grid (99 radial shells and 590 angular points per shell) was used throughout the calculations, as recommended when using Gaussian 09. It should be noted that almost identical results (in terms of geometries, relative energies and IR frequencies and intensities) have been obtained using the default "FineGrid" (75 radial shells and 302 angular points per shell). Lorentzian line shapes, with a full width at half maximum (FWHM) of 10 cm^{-1}, was used to generate the calculated IR spectra. A scaling factor of 0.9729 was applied to the calculated IR frequencies.

Vertical electron affinity of $[Zn(dafo)_3]^{2+}$ has been computed as the difference between the energy of $[Zn(dafo)_3]^{2+}$ in its optimized geometry and the energy of $[Zn(dafo)_3]^{\bullet+}$ in the optimized geometry of the dication.

VI.3. Extension of the study to other complexes

This first successful characterization leads us to extend our study to other complexes, i.e to complexes with different ligands with similar or different denticity, with different number of ligands, and with different metal centers. All these characterization are described in the following.

VI.3.1. $[ZnL]^{\bullet+}$ type complexes (L= bidentate ligand)

We have shown that the electronic structure of $[Zn(\mathbf{4})]^{\bullet+}$ is $[Zn^{+}(\mathbf{4}^{0})]$. So we wondered if the same electronic structure is observed for other bidentate ligands. To answer this question, we studied complex $[Zn(\mathbf{2})]^{\bullet+}$. This radical cationic species was prepared from $[Zn(\mathbf{2})_2]^{2+}$ dication, after reduction by ECD which induces loss of one ligand.

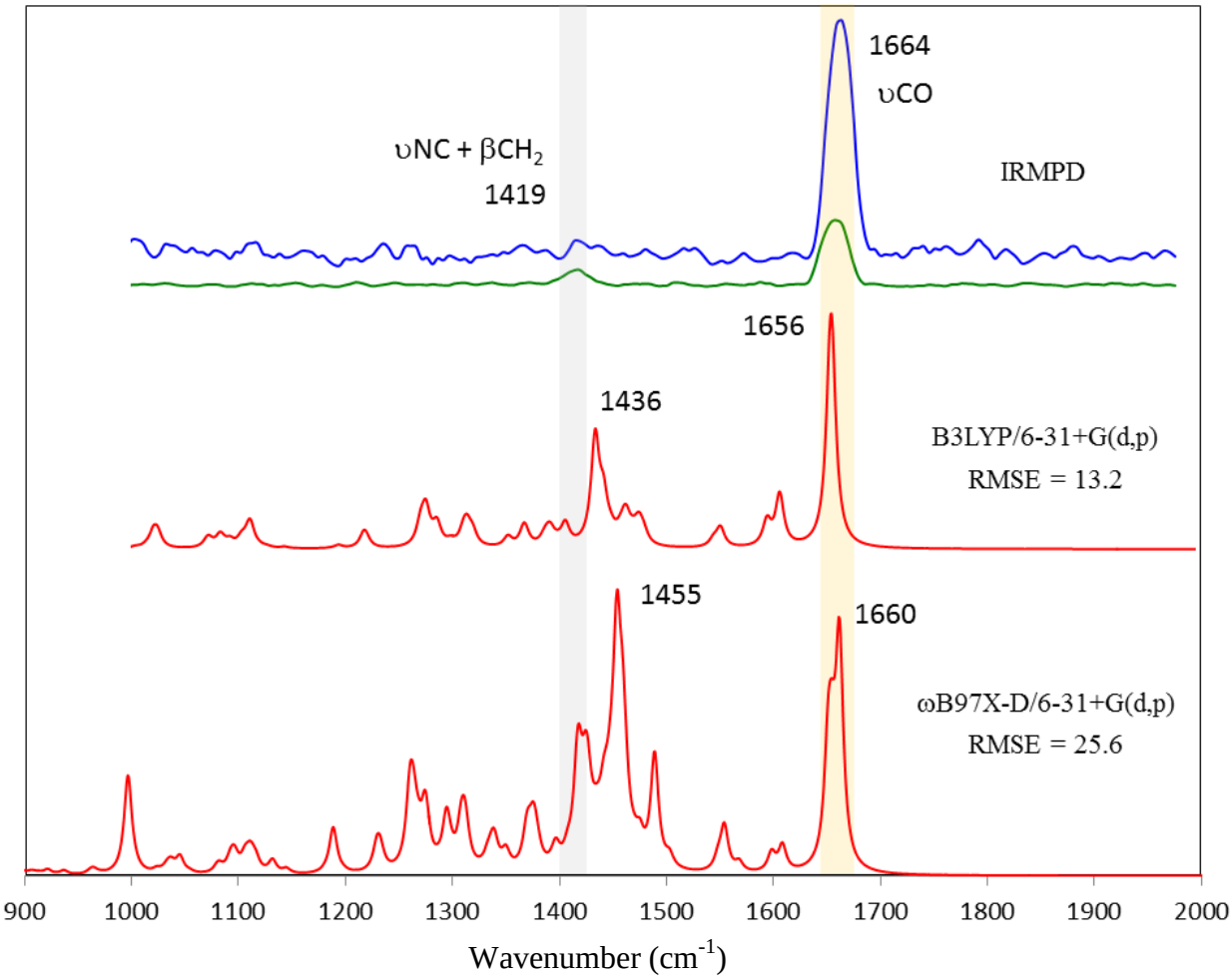

Figure 6.1: *Experimental and computed (B3LYP/6-31+G(d,p) and ωB97X-D/6-31+G(d,p) levels) IR spectrum of [Zn(**2**)]$^{\bullet+}$. Linear correction as indicated in Table 5.3 is used for the computed spectra.*

Figure 6.1 shows the gas-phase IR spectra of [Zn(**2**)]$^{\bullet+}$. It indicates only two peaks at 1419 and 1664 cm^{-1}, due to low fragmentation (Figure 6.2). Two fragments are observed upon irradiation on resonance, at *m*/*z* 319 and 255. The former and more intense fragment comes from the C_{aryl}-C(O)NEt_2 bond breaking and subsequent capture of a hydrogen. The latter is obtained from the loss of neutral Zn(0) from the m/z 319 fragment. This shows that, contrary to what was observed for [Zn(**4**)]$^{\bullet+}$, fragmentation of [Zn(**2**)]$^{\bullet+}$ benefits from the presence of substituents on the bipyridyl ligand, even if it remains weak.

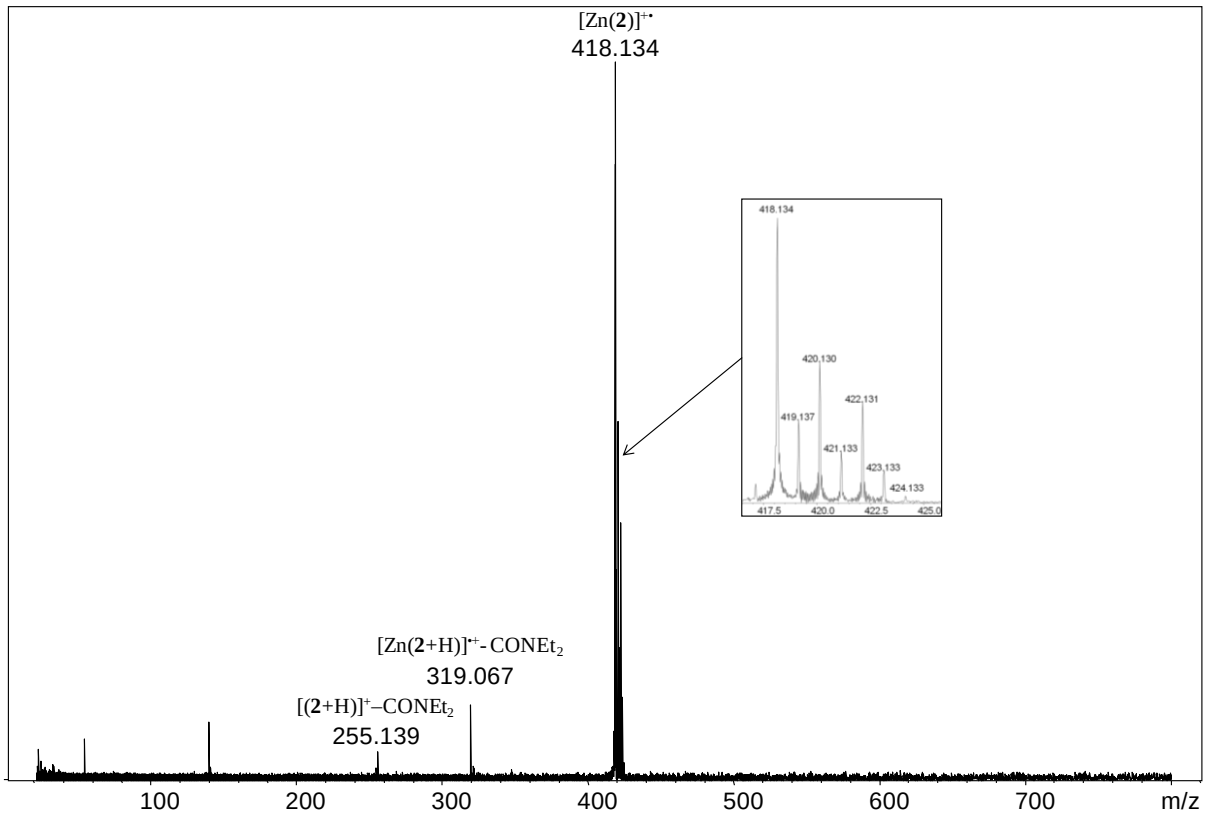

***Figure 6.2**: IRMPD mass spectrum obtained after mass selection of [Zn(**2**)]$^{\bullet+}$ (m/z 418) and irradiation on resonance at 1664 cm^{-1}.*

The experimental bands correspond approximately to the two most intense bands computed at both the B3LYP and ωB97X-D levels. Therefore, these computational methods give deviation from the experimental spectra which are inside the confidence interval defined in Chapter V (Table 6.1). Similar agreement between experimental and theoretical results is obtained at the CAM-B3LYP, LC-BLYP and M06-2X levels. The fact that the calculated electronic structure is the same for all DFT methods, with a [Zn^{+}(**2**^{0})] description (Figure 6.3), explained their agreement.

Table 6.1. Computed individual RMSE for each individual radical complex at various DFT levels after linear correction of the computed frequency values.[a]

Reduced Complex	RMSE (cm^{-1})				
	B3LYP/ 6-31+G(d,p)	CAM-B3LYP/ 6-31+G(d,p)	LC-BLYP/ 6-31+G(d,p)	M06-2X/ 6-31+G(d,p)	ωB97X-D/ 6-31+G(d,p)
$[Zn(\mathbf{2})]^{\bullet+}$	13.1	18.5	21.3	18.1	17.0
$[Zn(\mathbf{4})]^{\bullet+}$	9.2	11.2	21.4	25.7	23.1
$[Zn(\mathbf{8})]^{\bullet+}$	28.6	44.0	28.3	36.4	38.7
$[Zn(\mathbf{9})]^{\bullet+}$	13.5	25.2	42.7	19.7	25.8
$[Zn((\mathbf{2})_2]^{\bullet+}$	49.1	26.8	20.8	20.6	20.6
$[Zn(\mathbf{3})_2]^{\bullet+}$	48.8	30.9	35.2	20.9	26.1
$[Zn(\mathbf{1})(\mathbf{3})]^{\bullet+}$	32.5	21.4	36.6	13.6	13.2
$[Zn(\mathbf{2})(\mathbf{3})]^{\bullet+}$	51.7	5.3	9.2	11.8	9.2
$[Zn(\mathbf{3})(\mathbf{5})]^{\bullet+}$	25.9	8.6	14.3	12.8	10.5
$[Ru(\mathbf{1})(\mathbf{3})]^{\bullet+}$	16.4	23.3	55.5	30.7	24.7
$[Ru(\mathbf{3})(\mathbf{4})]^{\bullet+}$	14.5	19.6	53.1	44.4	20.7
Confidence interval[b]	2.4 – 17.1	4.6 – 32.4	7.3 – 50.8	5.5 – 38.3	4.1 – 28.8

[a] The values in red correspond to the one outside the confidence interval. [b] as determined in Chapter V.

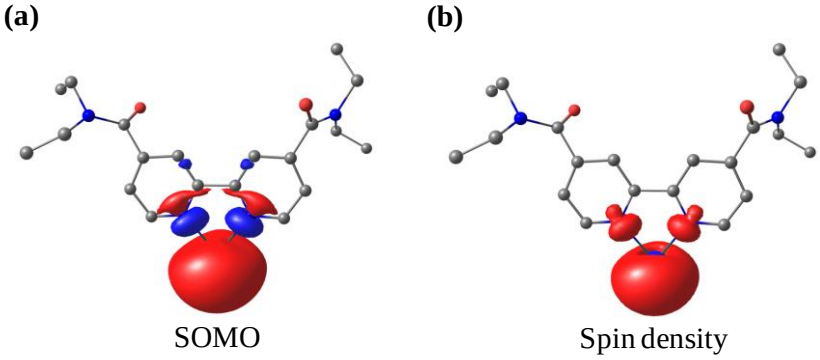

***Figure 6.3**: SOMO (a) and spin density (b) of $[Zn(\mathbf{2})]^{\bullet+}$ in the ground state at the B3LYP/6-31+G(d,p) level.*

From this result and the previous one observed for $[Zn(\mathbf{4})]^{\bullet+}$, we conclude that the added electron is located on the metal in $[Zn(L)]^{\bullet+}$ complexes with L being a bipyridyl-type bidentate ligand. We then wondered if similar results are obtained for tridentate ligands, as

their greater electron-donation to zinc will probably reduce the electron affinity of the metal center.

VI.3.2. $[ZnL']^{\bullet+}$ type complexes (L'= tridentate ligand)

Our collaborator in the lab have synthesized for us 4 tridentate ligands L' **6**-**9**. For all of them, we have tried to obtain IRMPD signature of $[Zn(L')]^{\bullet+}$; we were successful only for L' = **8** and **9**. For L' = **6** and **7**, we form the radical compound $[Zn(L')]^{\bullet+}$, but we were unable to observe any fragmentation upon irradiation by the tunable laser in the 1000-2000 cm^{-1} range. The IRMPD spectra of $[Zn(\mathbf{8})]^{\bullet+}$ and $[Zn(\mathbf{9})]^{\bullet+}$ are depicted in Figures 6.4 and 6.5, respectively. These ions were obtained after isolation of $[Zn(\mathbf{8})_2]^{2+}$ and $[Zn(\mathbf{6})(\mathbf{9})]^{2+}$, respectively, and their reduction by ECD which induce loss of one ligand.

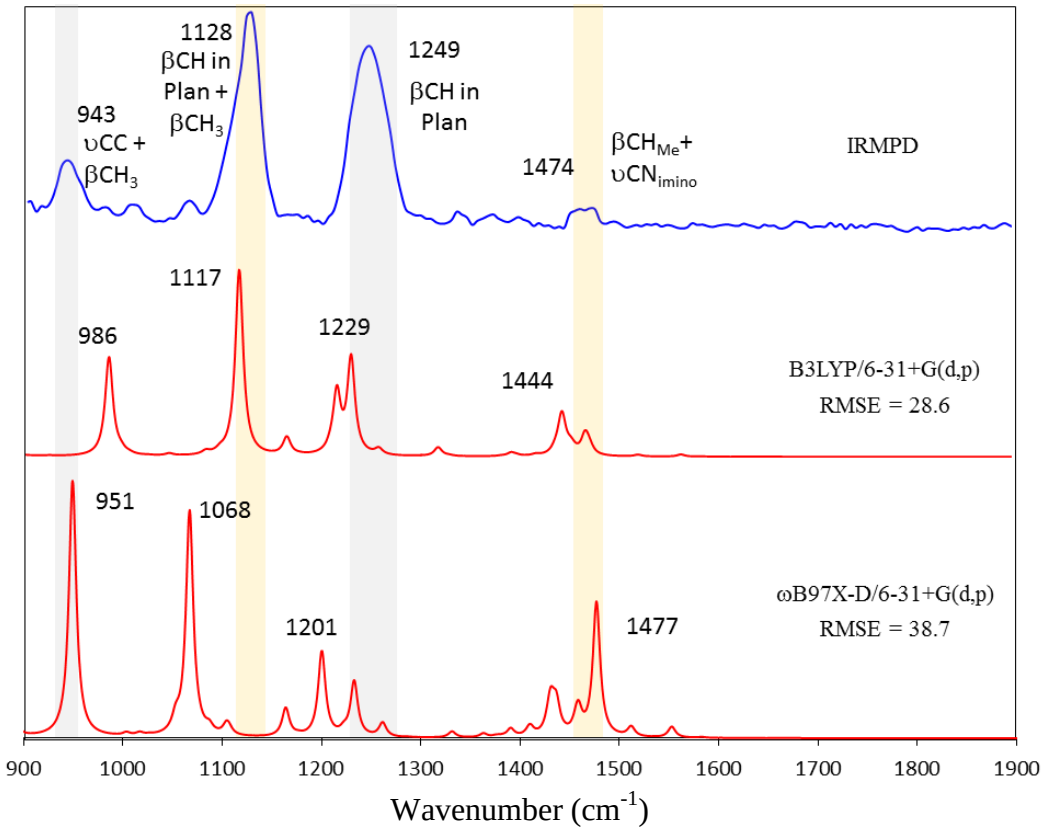

Figure 6.4: *Experimental and computed (B3LYP/6-31+G(d,p) and ωB97X-D/6-31+G(d,p) levels) IR spectrum of* $[Zn(\mathbf{8})]^{\bullet+}$*. Linear correction as indicated in Table 5.3 is used for the computed spectra.*

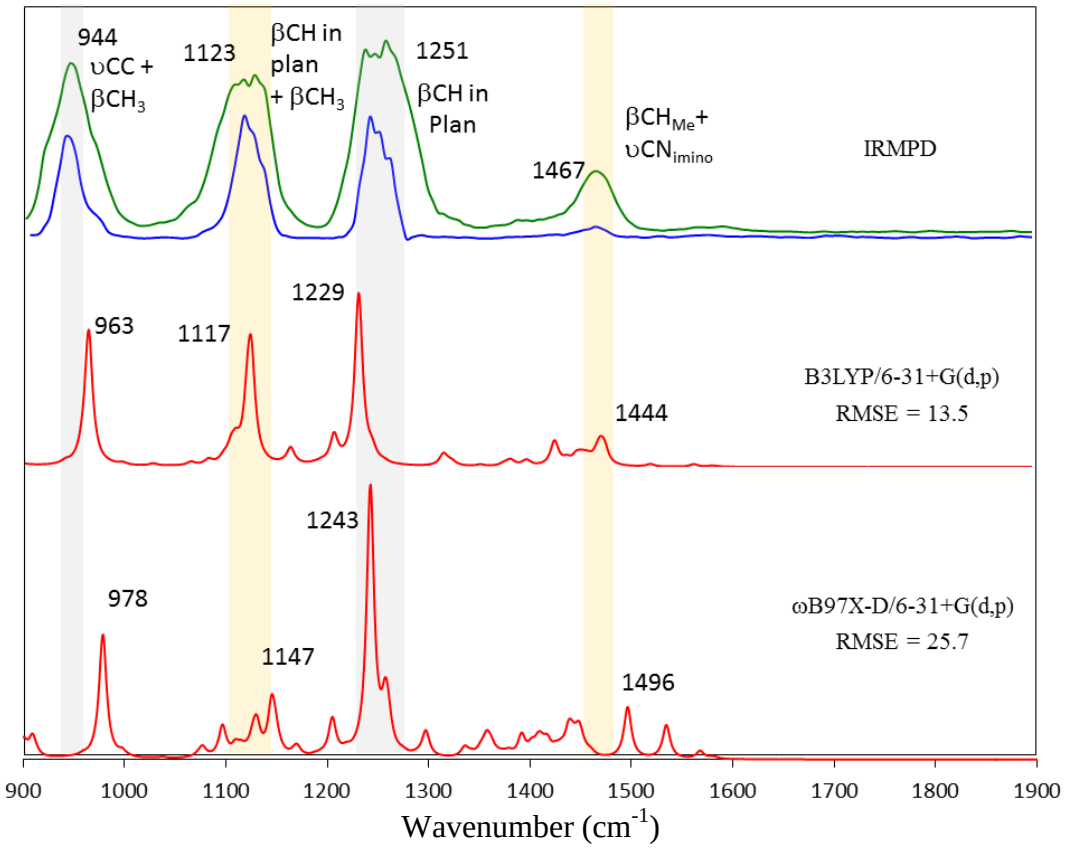

Figure 6.5: *Experimental and computed (B3LYP/6-31+G(d,p) and ωB97X-D/6-31+G(d,p) levels) IR spectrum of [Zn(**9**)]$^{\bullet+}$. Linear correction as indicated in Table 5.3 is used for the computed spectra.*

IRMPD spectra of [Zn(**8**)]$^{\bullet+}$ and [Zn(**9**)]$^{\bullet+}$ are very similar, with 4 bands at about 943-944, 1125, 1250 and 1470 cm^{-1}. The spectra of [Zn(**9**)]$^{\bullet+}$ is significantly less noisy, due to an higher intensity of the radical ion relative to the baseline and an easier fragmentation. Both ion (m/z 433 for [Zn(**8**)]$^{\bullet+}$ and 545 for [Zn(**9**)]$^{\bullet+}$) losses a CH_3 moiety upon photon irradiation (Figure 6.5 and 6.6), with fragments at m/z 418 and 530, respectively. Contrary to the former, the latter undergoes further fragmentation with loss of an aryl (2,6-i$Pr_2C_6H_3$) group and formation of a fragment at m/z 370.

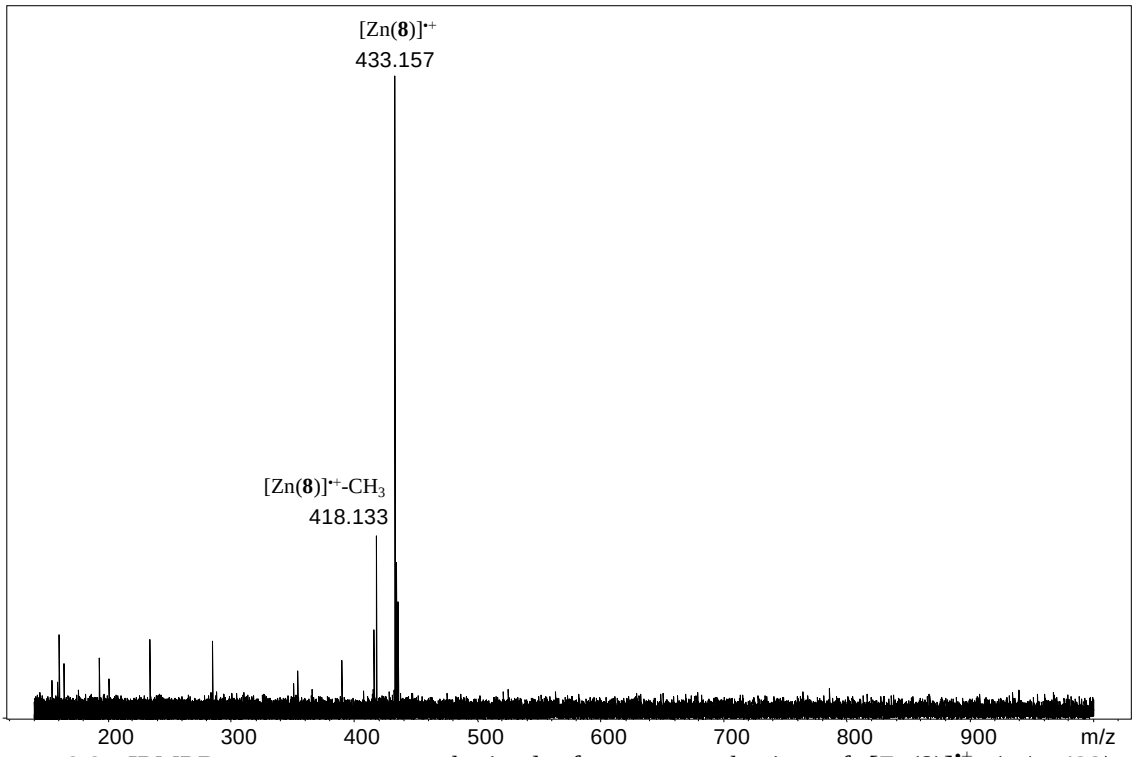

***Figure 6.6**: IRMPD mass spectrum obtained after mass selection of [Zn(**8**)]•+ (m/z 433) and irradiation on resonance at 1249 cm^{-1}.*

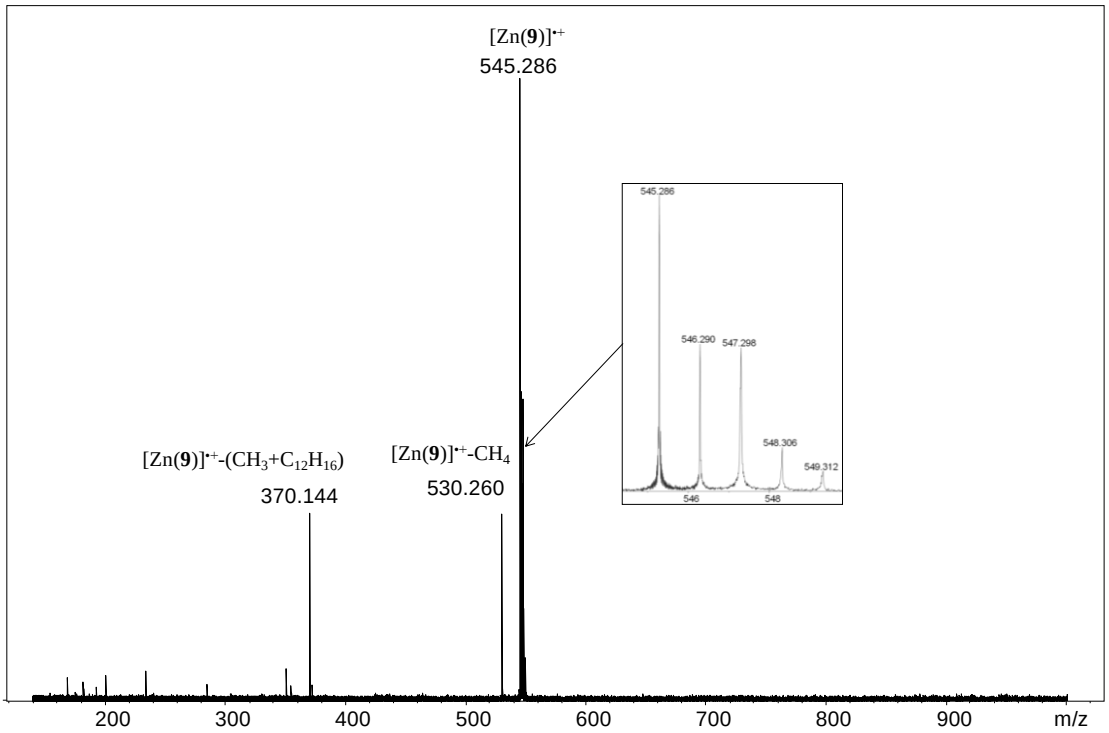

***Figure 6.7**: IRMPD mass spectrum obtained after mass selection of [Zn(**9**)]•+ (m/z 545) and irradiation on resonance at 1123 cm^{-1}.*

A good agreement is obtained between the experimental and the B3LYP/6-31+G(d,p) computed spectra for [Zn(**9**)]$^{\bullet+}$, with a RMSE equal to 13.5 cm^{-1}. Surprisingly, this is not the case for [Zn(**8**)]$^{\bullet+}$ with a RMSE equal to 28.6 cm^{-1}, mainly due to the large discrepancy for the band with the lowest frequency (943 vs 986 cm^{-1}). Similar results are obtained with the ωB97X-D method, with good agreement with the experimental spectra only for [Zn(**9**)]$^{\bullet+}$.

We do not find any explanation for the poor agreement for [Zn(**8**)]$^{\bullet+}$ and the good agreement for [Zn(**9**)]$^{\bullet+}$. Indeed, these molecules present similar geometrical and electronic structures, at both the B3LYP and ωB97X-D levels. The added electron is located in the bis(imino)pyridine ligands **8** or **9** (Figures 6.8 and 6.9).

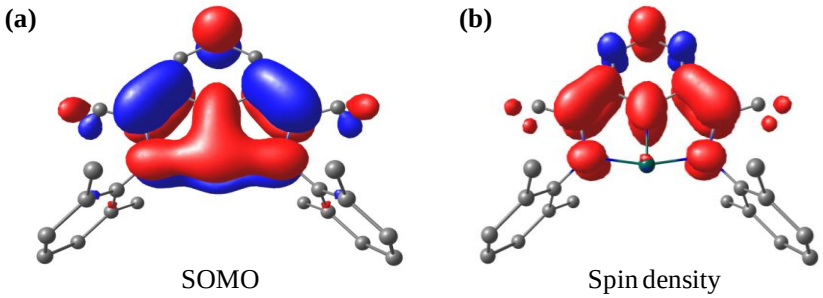

***Figure 6.8**: SOMO (a) and spin density (b) of [Zn(**8**)]$^{\bullet+}$ in the ground state at the B3LYP/6-31+G(d,p) level.*

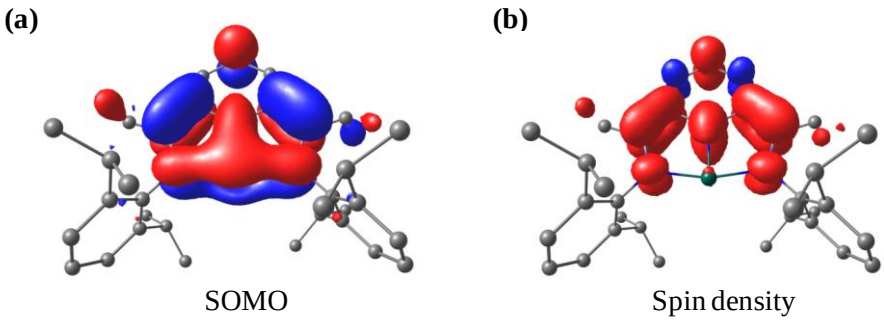

***Figure 6.9**: SOMO (a) and spin density (b) of [Zn(**9**)]$^{\bullet+}$ in the ground state at the B3LYP/6-31+G(d,p) level.*

This electronic structure obtained for [Zn(**8**)]$^{\bullet+}$ and [Zn(**9**)]$^{\bullet+}$ indicates a significant difference between complexes with bidentate and complexes with tridentate ligands, the former being

Zn(I) complexes whereas the latter are Zn(II) complexes. We also noted that the SOMO of both $[Zn(\mathbf{8})]^{\bullet+}$ and $[Zn(\mathbf{9})]^{\bullet+}$ has a strong component on the metal center, whereas the zinc atom does not possess any spin density, which is explained by the unrestricted nature of the wavefunction.

After these studies on zinc complexes with a single bidentate or tridentate ligand, which show that the ligand denticity has an important role on the oxidation number of the metal, we now focus on zinc and ruthenium complexes bearing two bidentate ligands.

VI.3.3. $[Zn(L^1)(L^2)]^{\bullet+}$ type complexes (L^1, L^2 = bidentate ligands)

We first start our study on zinc complexes. These systems are particularly interesting, as shown previously, because we know that for such complexes, the various DFT methods give different electronic structures. We have therefore studied five different complexes, namely $[Zn(\mathbf{2})_2]^{\bullet+}$, $[Zn(\mathbf{3})_2]^{\bullet+}$, $[Zn(\mathbf{1})(\mathbf{3})]^{\bullet+}$, $[Zn(\mathbf{2})(\mathbf{3})]^{\bullet+}$ and $[Zn(\mathbf{3})(\mathbf{5})]^{\bullet+}$. These radical complexes have been obtained from $[Zn(\mathbf{2})_3]^{2+}$, $[Zn(\mathbf{3})_3]^{2+}$, $[Zn(\mathbf{1})(\mathbf{3})_2]^{2+}$, $[Zn(\mathbf{2})(\mathbf{3})_2]^{2+}$ and $[Zn(\mathbf{3})_2(\mathbf{5})]^{2+}$ dications after ECD process, respectively. Their IRMPD spectra are depicted in Figures 6.10-6.14.

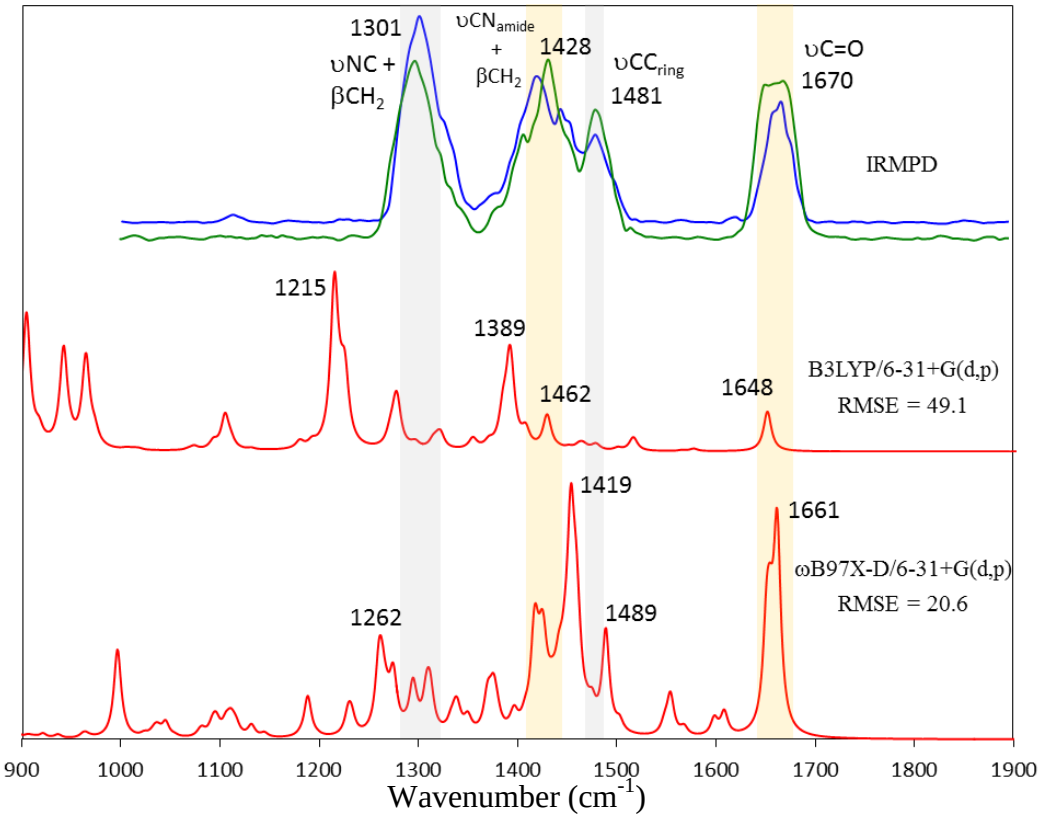

Figure 6.10: *Experimental and computed (B3LYP/6-31+G(d,p) and ωB97X-D/6-31+G(d,p) levels) IR spectrum of $[Zn(\mathbf{2})_2]^{\bullet+}$. Linear correction as indicated in Table 5.3 is used for the computed spectra.*

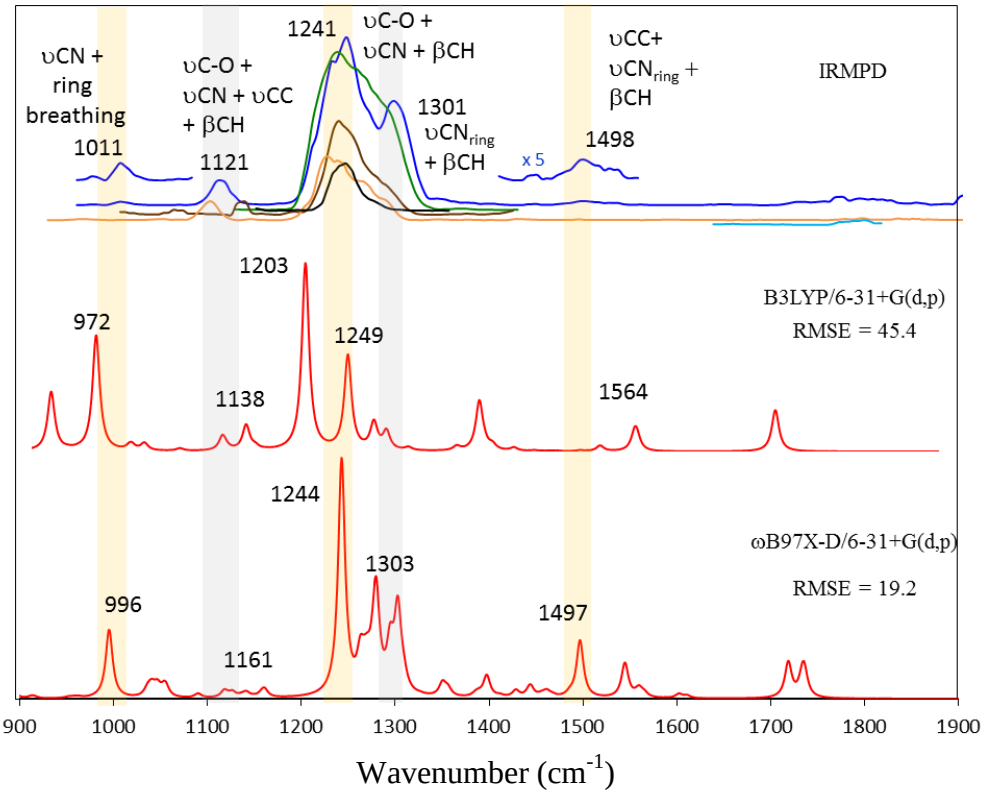

Figure 6.11: *Experimental and computed (B3LYP/6-31+G(d,p) and ωB97X-D/6-31+G(d,p) levels) IR spectrum of $[Zn(\mathbf{3})_2]^{\bullet+}$. Linear correction as indicated in Table 5.3 is used for the computed spectra.*

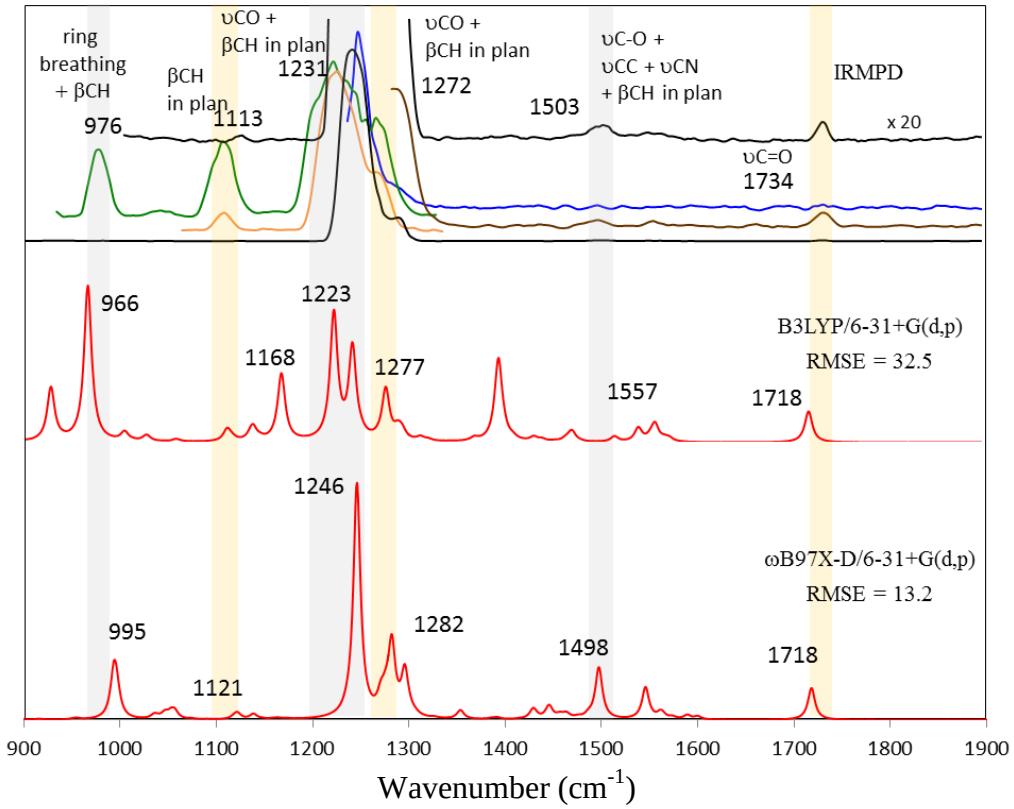

Figure 6.12: *Experimental and computed (B3LYP/6-31+G(d,p) and ωB97X-D/6-31+G(d,p) levels) IR spectrum of [Zn(**1**)(**3**)]$^{\bullet+}$. Linear correction as indicated in Table 5.3 is used for the computed spectra.*

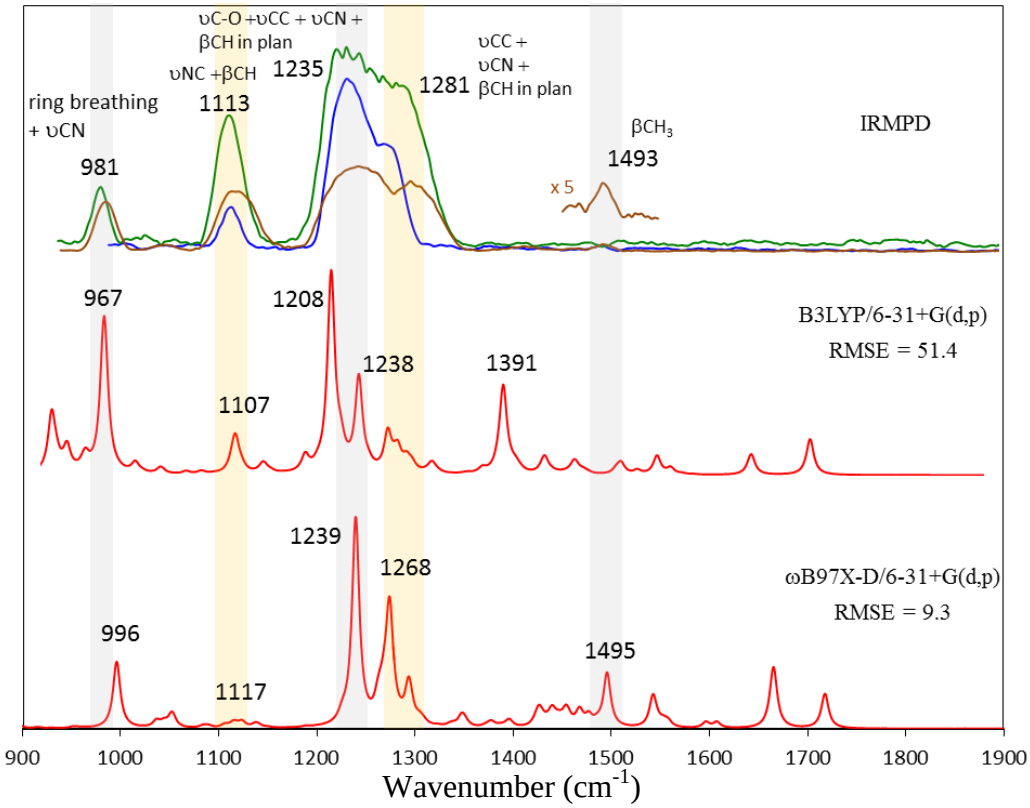

Figure 6.13: *Experimental and computed (B3LYP/6-31+G(d,p) and ωB97X-D/6-31+G(d,p) levels) IR spectrum of [Zn(**2**)(**3**)]$^{\bullet+}$. Linear correction as indicated in Table 5.3 is used for the computed spectra.*

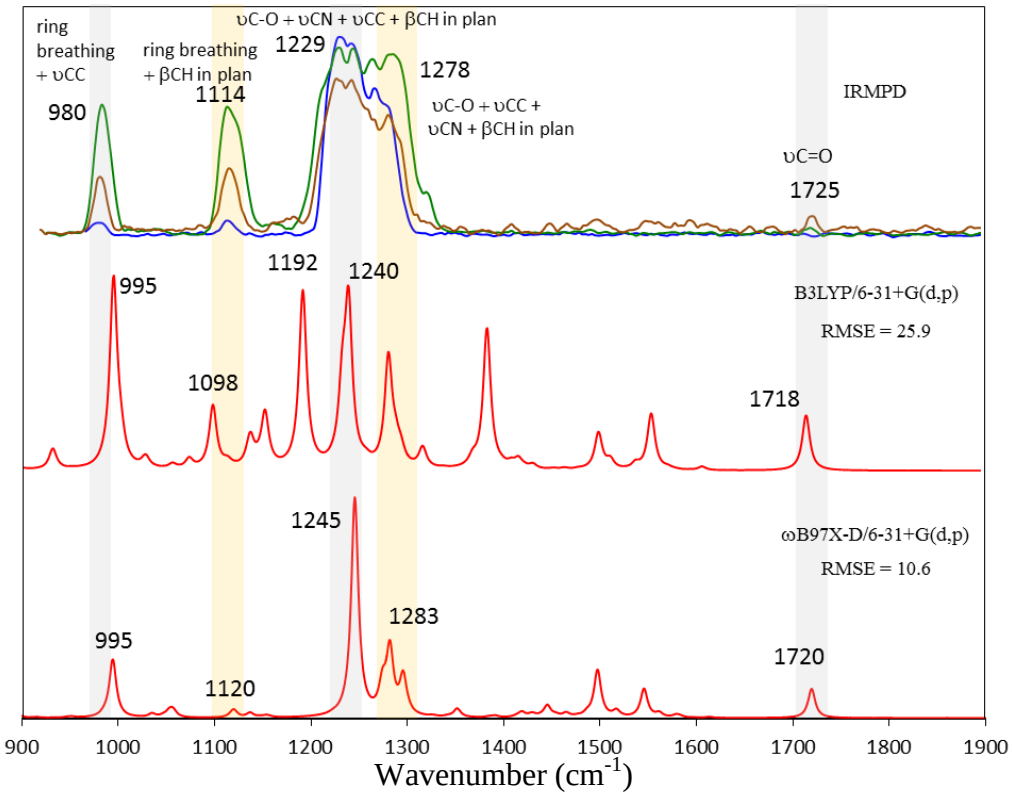

Figure 6.14: *Experimental and computed (B3LYP/6-31+G(d,p) and ωB97X-D/6-31+G(d,p) levels) IR spectrum of [Zn(**3**)(**5**)]$^{\bullet+}$. Linear correction as indicated in Table 5.3 is used for the computed spectra.*

It can be noticed that these spectra show in most case a noisy baseline, mainly resulting from the low intensity of the parent radical in the IRMPD fragmentation process, as well as, in most cases, from the difficulty to fragment these radical species. We also observe that some expected band could not be observed. For example, the C=O stretch of the ester group of ligand **3** has been seen without doubt only for [Zn(**1**)(**3**)]$^{\bullet+}$ and [Zn(**3**)(**5**)]$^{\bullet+}$, even if the ligand **3** is present in two other complexes.

The fragmentation observe upon IRMPD indicates mainly loss of one ligand, as shown in Figure 6.15-6.19.

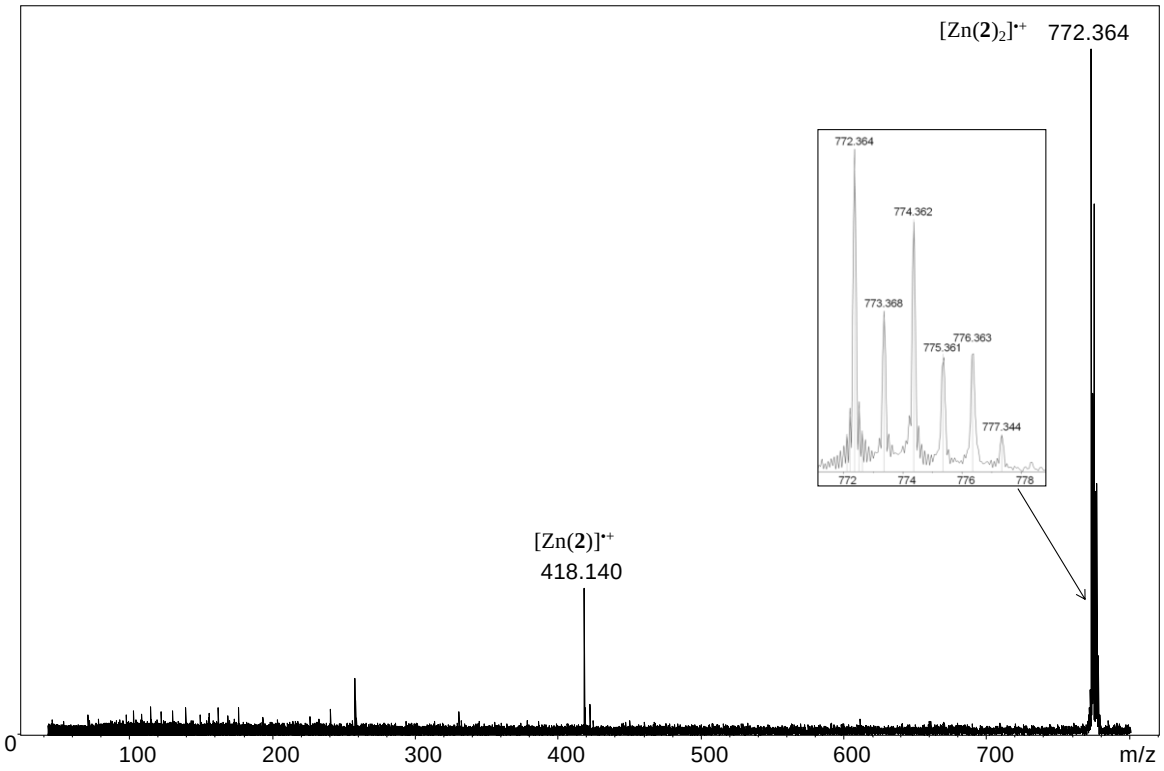

***Figure 6.15**: IRMPD mass spectrum obtained after mass selection of [Zn(**2**)$_2$]$^{\bullet+}$ (m/z772) and irradiation on resonance at 1301 cm^{-1}.*

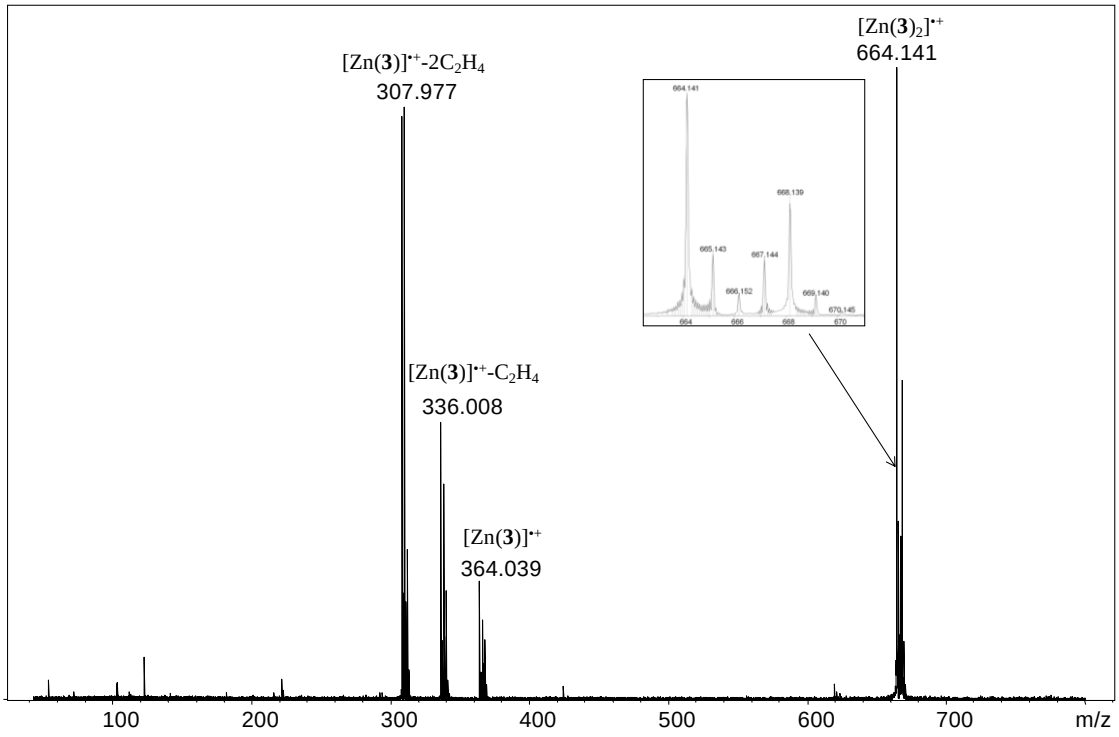

***Figure 6.16**: IRMPD mass spectrum obtained after mass selection of [Zn(**3**)$_2$]$^{\bullet+}$ (m/z 664) and irradiation on resonance at 1241 cm^{-1}.*

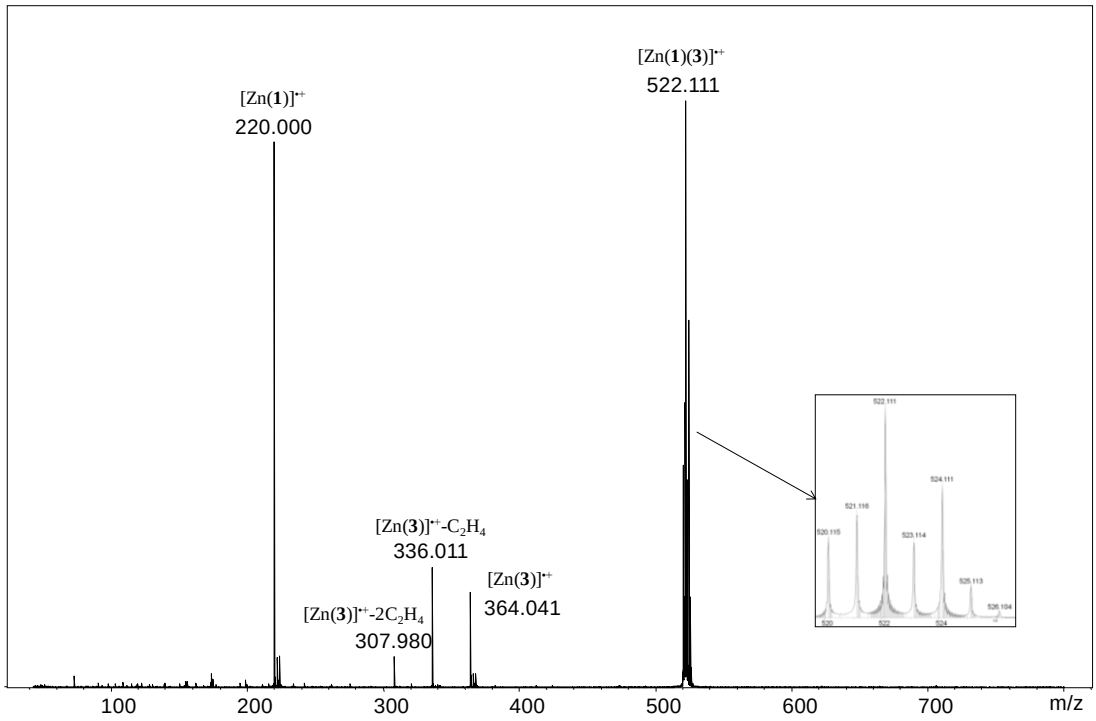

***Figure 6.17**: IRMPD mass spectrum obtained after mass selection of [Zn(**1**)(**3**)]$^{\bullet+}$ (m/z 522) and irradiation on resonance at 1231 cm^{-1}.*

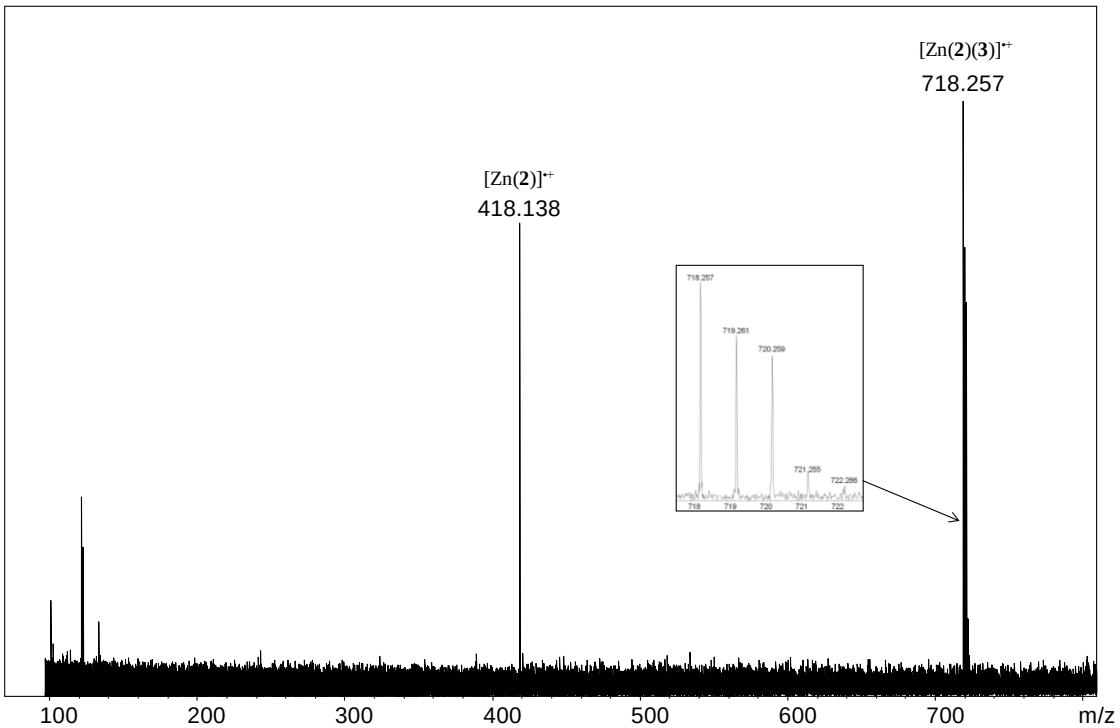

***Figure 6.18**: IRMPD mass spectrum obtained after mass selection of [Zn(**2**)(**3**)]$^{\bullet+}$ (m/z 718) and irradiation on resonance at 1235 cm^{-1}.*

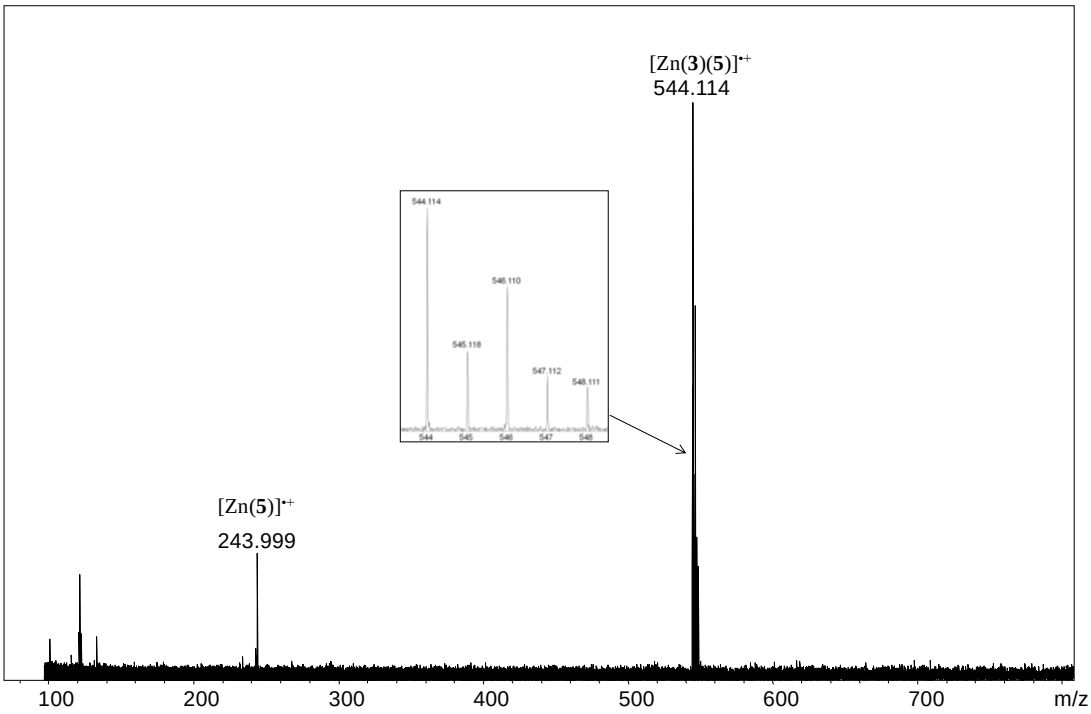

***Figure 6.19**: IRMPD mass spectrum obtained after mass selection of [Zn(**3**)(**5**)]$^{\bullet+}$ (m/z 544) and irradiation on resonance at 1229 cm^{-1}.*

The largest fragmentation is observed for [Zn(**3**)$_2$]$^{\bullet+}$ (m/z 664) which shows the loss of one ligand ([Zn(**3**)]$^{\bullet+}$ at m/z 364), as well as its further fragmentation by loss of one (m/z 336) or two (m/z 308) C_2H_4 moiety from the ester substituents. This good fragmentation of ligand **3** by the loss of C_2H_4 moiety has prompted us to use it for most of the complexes (as well as for the Ru complexes, see the next section). However, this fragmentation was observed only for [Zn(**1**)(**3**)]$^{\bullet+}$ as for the other two cases, ligand **3** dissociates from the zinc center. Similar dissociation of one ligand (**2**) is observed for [Zn(**2**)$_2$]$^{\bullet+}$.

Comparison between the experimental and theoretical spectra (Figures 6.10-6.14) is not straightforward, as a large discrepancy exists between the experimental and the computed data. Significantly fewer bands are observed in the experimental spectra, compared to the calculated ones. In particular, intense bands observed in spectra computed at the B3LYP level are absent in the experimental spectra (see the band at ~1400 cm^{-1} for [Zn(**1**)(**3**)]$^{\bullet+}$ and [Zn(**3**)(**5**)]$^{\bullet+}$), a situation which has not been observed previously in close-shell systems at this

level of calculation. Furthermore, B3LYP spectra show intense band which are significantly shifted compared to the experimental bands. This is for example observed for the band at 1215 cm^{-1} in the computed spectra of $[Zn(\mathbf{2})_2]^{\bullet+}$, whereas the experimental band has a 1301 cm^{-1} frequency value. Significant discrepancy is also observed for $[Zn(\mathbf{2})_2]^{\bullet+}$ (1203 vs 1241 cm^{-1}), $[Zn(\mathbf{1})(\mathbf{3})]^{\bullet+}$ (1113 vs 1168 cm^{-1}) or $[Zn(\mathbf{2})(\mathbf{3})]^{\bullet+}$ (1391 vs 1493 cm^{-1}). As a consequence, the RMSE computed between the experimental and the B3LYP theoretical spectra are large for all these radical species (> 25.9 cm^{-1}) and is outside the confidence interval defined for this level of calculation. On the opposite, spectra obtained at the ωB97X-D show smaller discrepancy with the experiments, even if the agreement is far from perfect. The RMSE is between 9 and 21 cm^{-1}, i.e. inside the confidence interval for the ωB97X-D/6-31+G(d,p) level. Calculations have also been achieved at the M06-2X, CAM-B3LYP and LC-BLYP for most compounds, and in all cases, the RMSE is inside their confidence interval (Table 6.1). This clearly indicates that the B3LYP functional has a problem for these tetrahedral radical zinc complexes, whereas this is apparently not the case for the other functionals.

An explanation of this difference in the ability of these functionals to reproduce experimental IR spectra can be found in the electronic structure observed for these systems at the various DFT levels. Indeed, has observed previously in Chapter IV, B3LYP leads to a delocalized single electron ($[Zn^{2+}(L^{-1/2})(L'^{-1/2})]$ structure), whereas the other functionals indicates that the single electron is localized only on one ligand ($[Zn^{2+}(L^{-1})(L'^{0})]$ structure). This is illustrated in Figures 6.20 and 6.21 for complexes $[Zn(\mathbf{3})_2]^{\bullet+}$ and $[Zn(\mathbf{1})(\mathbf{3})]^{\bullet+}$. Similarly, the single electron is located on one of the two ligands **2** in $[Zn(\mathbf{2})_2]^{\bullet+}$ and in ligand **3** in $[Zn(\mathbf{2})(\mathbf{3})]^{\bullet+}$ and $[Zn(\mathbf{3})(\mathbf{5})]^{\bullet+}$ with the M06 and RSH functionals, whereas it is delocalized at the B3LYP level.

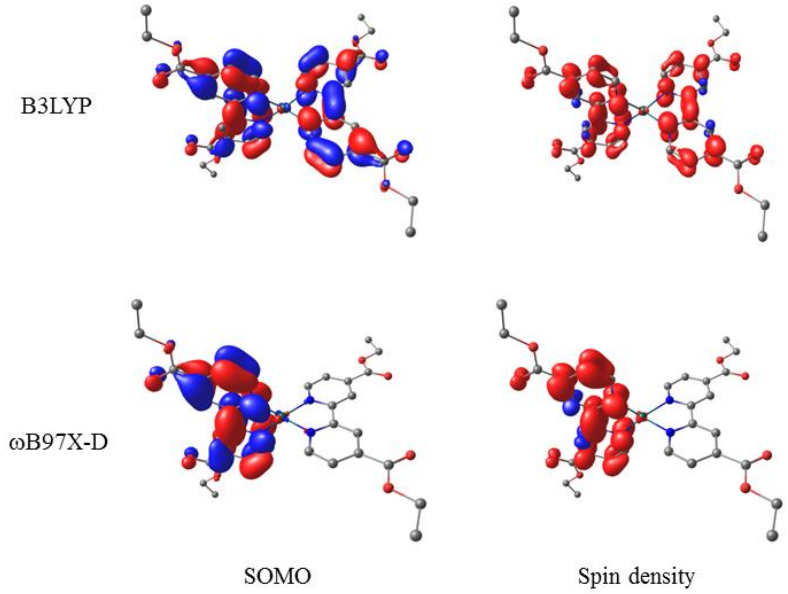

Figure 6.20. *SOMO and spin density of* $[Zn(\mathbf{3})_2]^{\bullet+}$ *in the ground state at the B3LYP/6-31+G(d,p) and ωB97X-D/6-31+G(d,p) levels.*

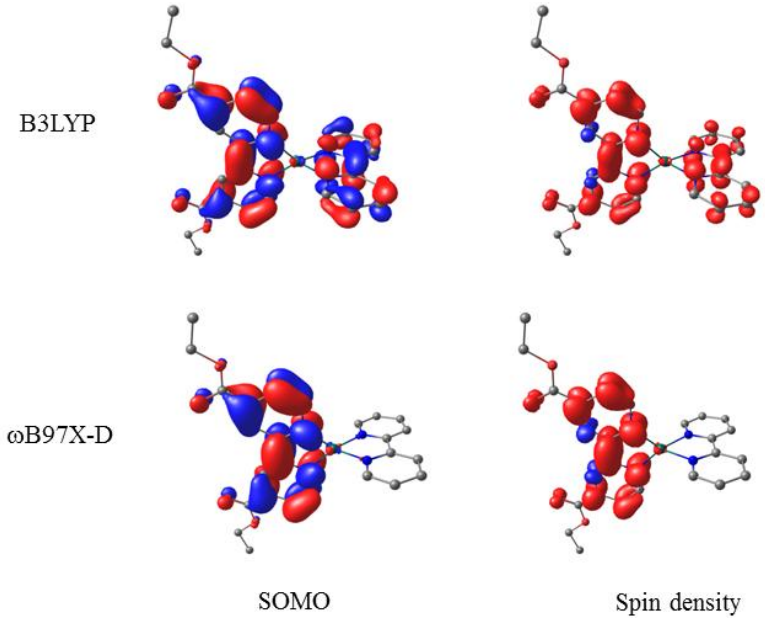

Figure 6.21. *SOMO and spin density of* $[Zn(\mathbf{1})(\mathbf{3})]^{\bullet+}$ *in the ground state at the B3LYP/6-31+G(d,p) and ωB97X-D/6-31+G(d,p) levels.*

Therefore, our IRMPD spectroscopy data and their comparison with the calculated data are proof of the correct electronic structure of these complexes, with the single electron located only on one ligand. This work also demonstrates that B3LYP fail to describe the electronic structure of these molecular systems, contrary to M06-2X or RSH functionals.

One last point deserves our attention before closing this section. Our calculations indicate that the single electron is located on the ligand **3** in $[Zn(\mathbf{1})(\mathbf{3})]^{\bullet+}$, $[Zn(\mathbf{2})(\mathbf{3})]^{\bullet+}$and $[Zn(\mathbf{3})(\mathbf{5})]^{\bullet+}$. This suggests that, in these radical complexes, the ligand **3**, which has a negative charge, should be more tightly bound to the metal center than the other ligand (**1**, **2** or **5**) which is neutral. However, the IRMPD fragmentation indicates only (for $[Zn(\mathbf{2})(\mathbf{3})]^{\bullet+}$and $[Zn(\mathbf{3})(\mathbf{5})]^{\bullet+}$) or mostly (for $[Zn(\mathbf{1})(\mathbf{3})]^{\bullet+}$) a dissociation of this ligand, furthermore as a neutral moiety. We do not have satisfactory explanation for this apparent discrepancy between the observed fragmentation and the calculated electronic structure. Our calculations show that vacant low lying π^* orbitals are available on these radical species. One hypothesis, which remains to be studied, is that the energy required to achieve fragmentation of the ion, which is reached through the intramolecular vibrational relaxation (IVR), is greater than the energy necessary to electronically excite the radical cation, inducing fragmentation which is not related to the ground state electronic structure.

VI.3.4. $[Ru(L^1)(L^2)]^{\bullet+}$ type complexes (L^1, L^2 = bidentate ligands)

To complete this study of the reduced complexes, we have examined ruthenium compounds, namely $[Ru(\mathbf{1})(\mathbf{3})]^{\bullet+}$, which was prepared from dication$[Ru(\mathbf{1})_2(\mathbf{3})]^{2+}$, and $[Ru(\mathbf{3})(\mathbf{4})]^{\bullet+}$, which was obtained from $[Ru(\mathbf{3})(\mathbf{4})_2]^{2+}$. The fragmentation of these ions upon photon irradiation are similar, with first the loss of one C_2H_4 moiety (Figures 6.22 and 6.23). Further fragmentation induces the loss of a second C_2H_4 group or the loss of CO + H_2O, as well as loss of both of them. Here again we find that the Ru-ligand bond is stronger than the Zn-ligand binding, since, unlike the previous case, we do not see the loss of a neutral ligand.

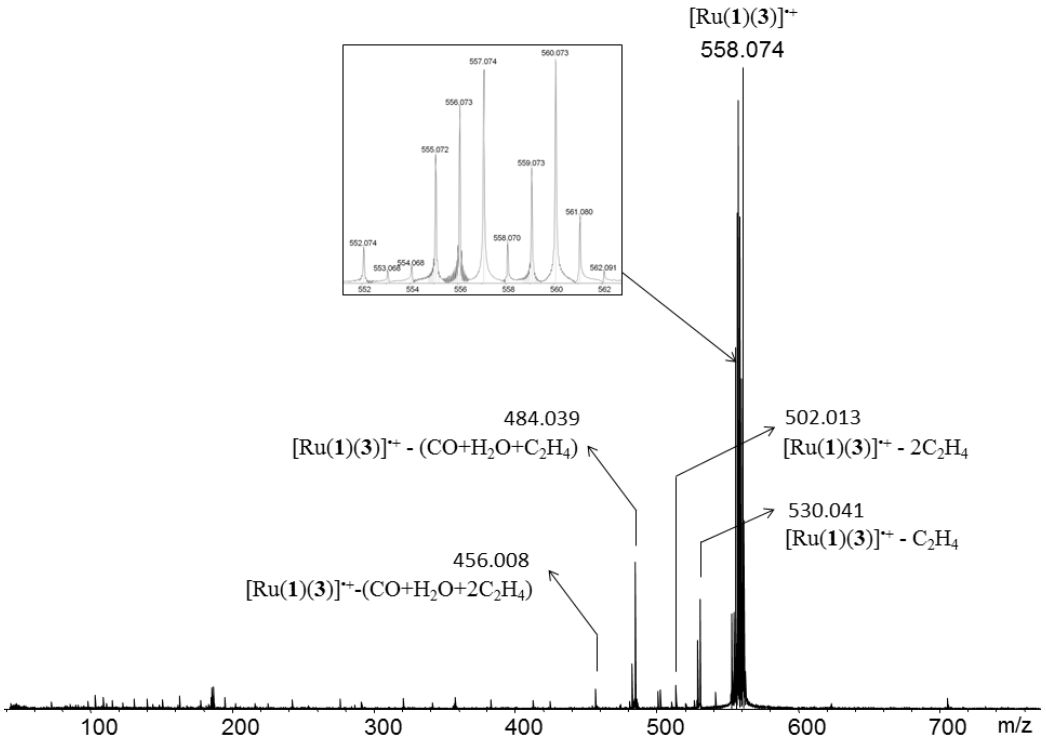

Figure 6.22. *IRMPD mass spectrum obtained after mass selection of [Ru(**1**)(**3**)]$^{\bullet+}$ (m/z 560) and irradiation on resonance at 1304 cm^{-1}.*

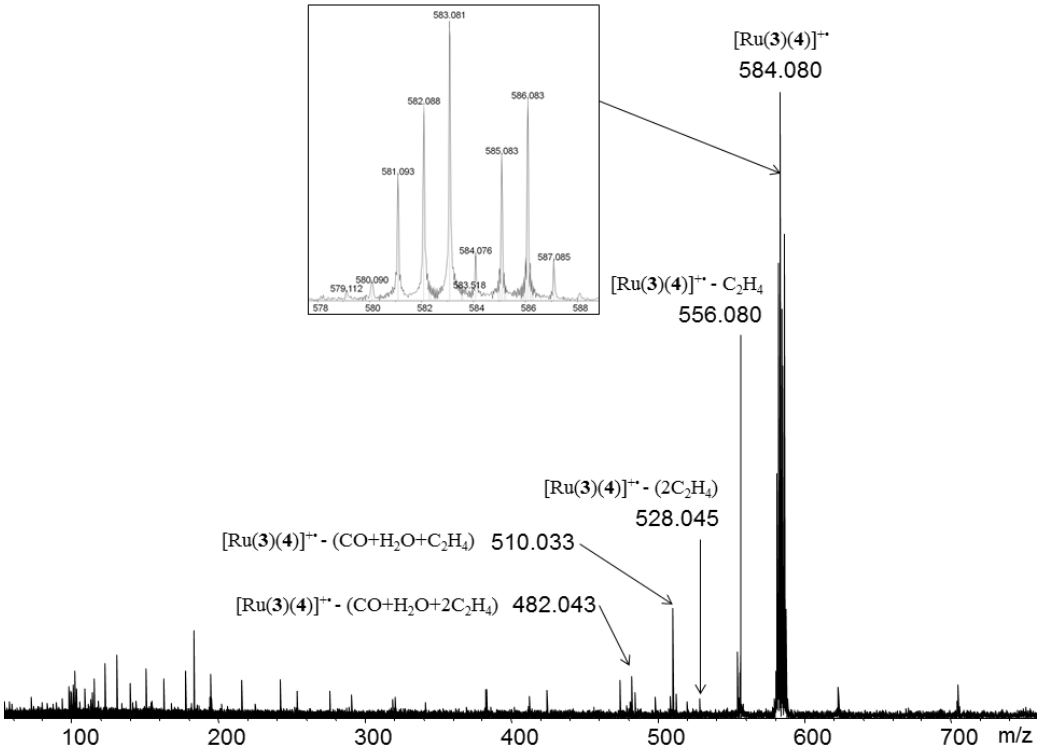

Figure 6.23. *IRMPD mass spectrum obtained after mass selection of [Ru(**3**)(**4**)]$^{\bullet+}$ (m/z 584) and irradiation on resonance at 1263 cm^{-1}.*

Based on the intensity of these fragments, we have obtained the IRMPD spectra of [Ru(**1**)(**3**)]$^{\bullet+}$ (Figure 6.24) and [Ru(**3**)(**4**)]$^{\bullet+}$ (Figure 6.25). Following our work on zinc complexes, it was surprising to observe good agreement between these experimental spectra and the calculated IR spectra at both the ωB97X-D and B3LYP levels.

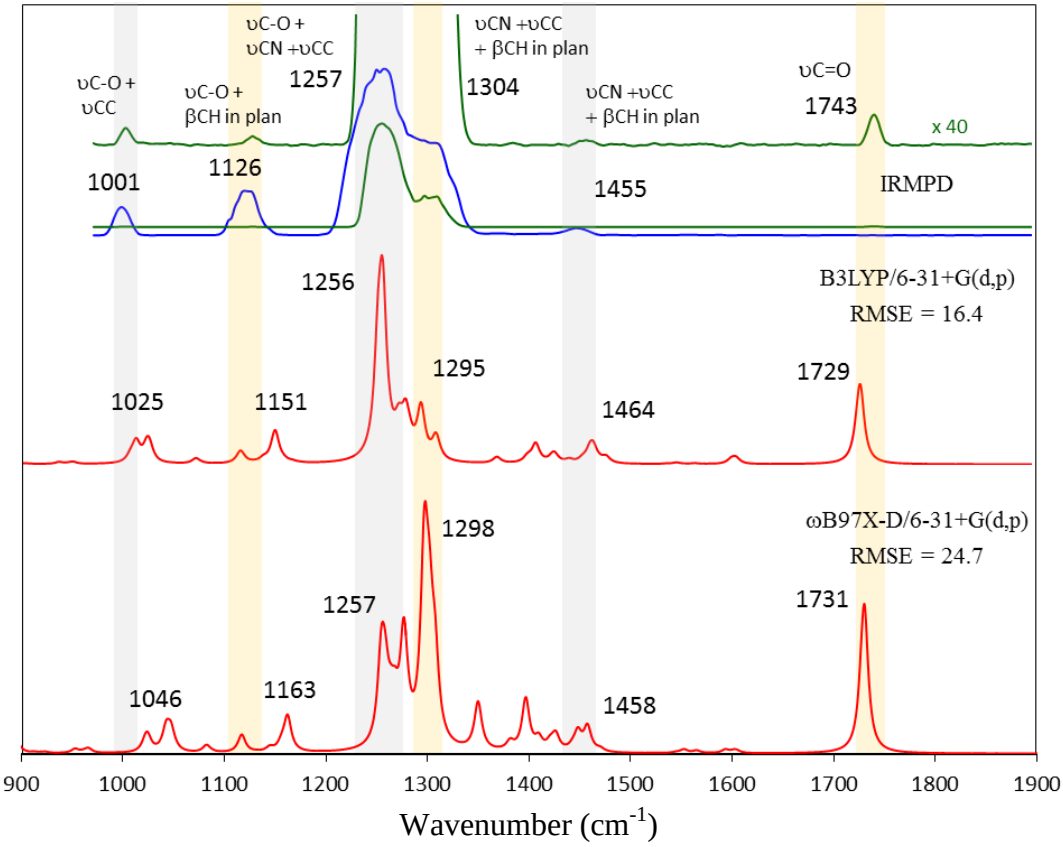

Figure 6.24: *Experimental and computed (B3LYP/6-31+G(d,p) and ωB97X-D/6-31+G(d,p) levels with LanL2DZ ECP and basis set for Ru) IR spectrum of [Ru(**1**)(**3**)]$^{\bullet+}$. Linear correction as indicated in Table 5.3 is used for the computed spectra.*

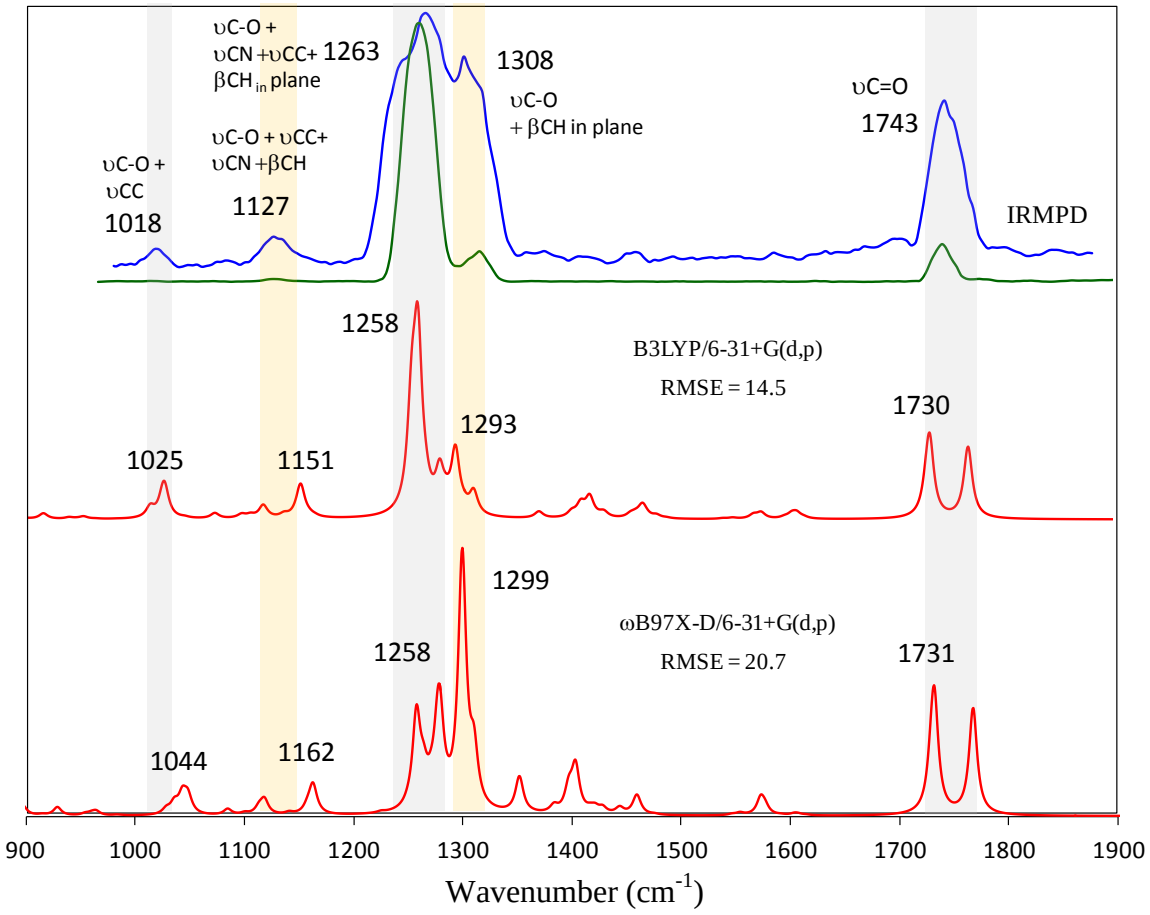

Figure 6.25: *Experimental and computed (B3LYP/6-31+G(d,p) and ωB97X-D/6-31+G(d,p) levels with LanL2DZ ECP and basis set for Ru) IR spectrum of [Ru(**3**)(**4**)]$^{\bullet+}$. Linear correction as indicated in Table 5.3 is used for the computed spectra.*

This agreement can be understood when viewing the electronic structure of these radical cations (Figures 6.26 and 6.27). It seems that for these Ru complexes, the DFT methods do not suffer defects previously observed for similar zinc complexes. Indeed, all methods give the same electronic structure which corresponds to a distorted square planar Ru(I) complex with by two neutral bipyridyl-type ligands. Singly occupied molecular orbital and spin density for the radical cations indicate that the added electron is located at the metal center.

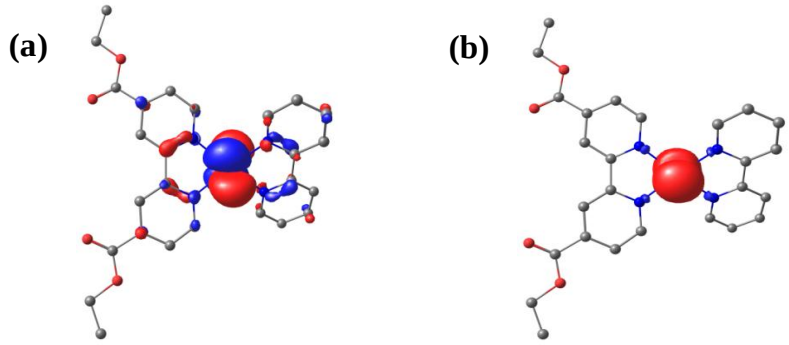

***Figure 6.26**. SOMO (a) and spin density (b) of [Ru(**1**)(**3**)]$^{\bullet+}$ in the ground state at the B3LYP/6-31+G(d,p) (LANL2DZ for Ru) level.*

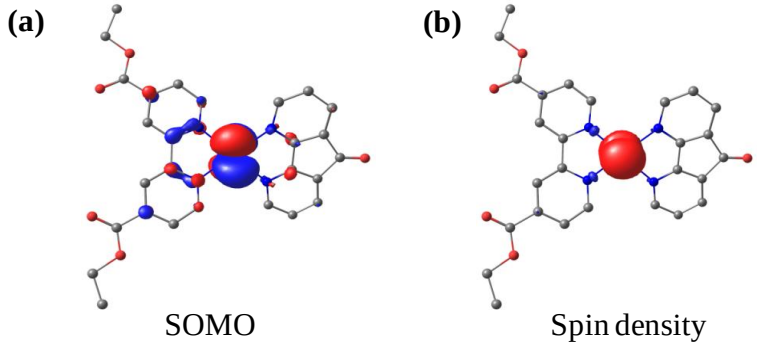

***Figure 6.27**. SOMO (a) and spin density (b) of [Ru(**3**)(**4**)]$^{\bullet+}$ in the ground state at the B3LYP/6-31+G(d,p) (LANL2DZ for Ru) level.*

VI.4. Conclusion

This chapter is a culmination of the research project developed during the thesis. It uses the information acquired in the previous chapter to address the most difficult and interesting cases: the characterization of reduced metal complexes.

Eleven different radical cationic complexes, divided into 4 distinct families were studied: (A) two zinc complexes with one bidentate ligand; (B) two zinc complexes with one tridentate ligand; (C) five zinc complexes with two bidentate ligands; and (D) two ruthenium complexes with two bidentate ligands. For all these complexes, we record the IRMPD spectra and

computed its IR spectra at various DFT levels. The comparison between the experimental and theoretical data allows to show that the added electron is located on the metal center in types (A) and (D) complexes, whereas types (B) and (C) complexes are characterized by a bidentate ligand which bears a charge of -1. This shows that the electronic structure of reduced Zn and Ru complexes with non-innocent ligands depends on the nature of the metal center and of the number of bonds to the metal. The electron affinity of the metal center is large enough to capture the added electron when it has a small number of bonds (two for zinc, four for Ru). A larger number of ligands around the metal induces decrease of its Lewis acidity and therefore its capability to trap the added electron which is consequently located on a ligand. Finally, we have shown that when several ligands are present, the electron is localized on only one of them. This is in agreement with the electronic structure given by self-interaction error (SIE)–corrected functionals, whereas functionals with a low amount of Hartree-Fock exchange, such as B3LYP, fails to describe such systems.

VI.5. Reference

[1]. E. Alizadeh, L. Sanche, *Chem. Rev.***2012**, *112*, 5578-5602.

[2]. (a) A. I. O. Suarez, V. Lyaskovskyy, J. N. H. Reek, J. I. van der Vlugt, B. de Bruin, *Angew. Chem. Int. Ed.* **2013**, *52*, 12510-12529; (b) T. Büttner, J. Geier, G. Frison, J. Harmer, C. Calle, A. Schweiger, H. Schönberg, H. Grützmacher,*Science*, **2005**, *307*, 235-238.

[3]. (a) P. J. Chirik, K. Wieghardt,*Science*, **2010**, *327*, 794-795; (b) S. Blanchard, E. Derat, M. Desage-El Murr, L. Fensterbank, M. Malacria, V. Mouriès-Mansuy,*Eur. J. Inorg. Chem.* **2012**, 376-389; (c) O. R. Luca, R. H. Crabtree,*Chem. Soc. Rev.* **2013**, *42*, 1440-1459.

[4]. (a) J. Stubbe, W. A. van der Donk, *Chem. Rev.* **1998**, *98*, 705-762; (b) J. W. Whittaker, *Chem. Rev.* 2003, **103**, 2347-2363.

[5]. R. A. Zubarev, *Mass Spectrom. Rev.* **2003**, *22*, 57-77; (b) H. J. Cooper, K. Hakansson, A. G. Marshall, *Mass Spectrom. Rev.* **2005**, *24*, 201-222; (c) L. M. Mikesh, B. Ueberheide, A. Chi, J. J. Coon, J. E. P. Syka, J. Shabanowitz, D. F. Hunt, *Biochim. Biophys.Acta* **2006**, *1764*, 1811-1822; (d) K. O. Zhurov, L. Fornelli, M. D. Wodrich, Ü. A. Laskay, Y. O. Tsybin, *Chem. Soc. Rev.* **2013**, *42*, 5014-5030.

[6]. (a) K. Breuker, F. W. McLafferty, *Angew. Chem. Int. Ed.* **2003**, *42*, 4900-4904; (b) S. R. Harvey, M. Porrini, A. Konijnenberg, D. J. Clarke, R. C. Tyler, P. R. R. Langridge-Smith, C. E. MacPhee, B. F. Volkman, P. E. Barran, *J. Phys. Chem. B* **2014**, *118*, 12348-12359.

[7]. (a) J. Simons, *Chem. Phys. Lett.* **2010**, *484*, 81-95; F. Turecek, R. R. Julian, *Chem. Rev.* **2013**, *113*, 6691-6733.

[8]. (a) A. I. Gilson, G. van der Rest, J. Chamot-Rooke, W. Kurlancheek, M. Head-Gordon, D. Jacquemin, G. Frison, *J. Phys. Chem. Lett.* **2011**, *2*, 1426-1431; (b) V. Riffet, D. Jacquemin, E. Cauët, G. Frison, *J. Chem. Theory Comput.* **2014**, *10*, 3308-3318.

[9]. (a) C. J. Shaffer, A. Marek, R. Pepin, K. Slovakova, F. Turecek, *J. Mass Spectrom.* **2015**, *50*, 470-475; (b) H. T. H. Nguyen, C. J. Shaffer, F. Turecek, *J. Phys. Chem. B* **2015**, *119*, 3948-3961.

[10]. (a) X. Chen, W. Y. K. Chan, P. S. Wong, H. S. Yeung, T. W. D. Chan, *J. Am. Soc. Mass Spectrom.* **2011**, *22*, 233-244.

[11]. T. G. Flick, W. A. Donald, E. R. Williams, *J. Am. Soc. Mass Spectrom.* **2013**, *24*, 193-201.

[12]. (a) J. T. Adamson, K. Hakansson, *Anal. Chem.* **2007**, *79*, 2901-2910; (b) L. Han, C. E. Costello, *J. Am. Soc. Mass Spectrom.***2011**, *22*, 997-1013.

[13]. P. F. James, M. A. Perugini, R. A. J. O'Hair, *J. Am. Soc. Mass Spectrom.* **2008**, *19*, 978-986.

[14]. (a) W. A. Donald, R. D. Leib, J. T. O'Brien, A. I. S. Holm, E. R. Williams, *Proc. Natl. Acad. Sci. U.S.A.* **2008**, *105*, 18102-18107; (b) W. A. Donald, R. D. Leib, J. T. O'Brien, E. R. Williams, *Chem. Eur. J.* **2009**, *15*, 5926-5934; (c) W. A. Donald, M. Demireva, R. D. Leib, M. J. Aiken, E. R. Williams, *J. Am. Chem. Soc.* **2010**, *132*, 4633-4640.

[15]. M. A. Kaczorowska, H. J. Cooper, *J. Am. Soc. Mass Spectrom.* **2009**, *20*, 674-681.

[16]. (a) M. A. Kaczorowska, A. C. G. Hotze, M. J. Hannon, H. J. Cooper, *J. Am. Soc. Mass Spectrom.* **2010**, *21*, 300-309; (b) C. Gütz, R. Hovorka, N. Struch, J. Bunzen, G. Meyer-Eppler, Z. W. Qu, S. Grimme, F. Topic, K. Rissanen, M. Cetina, M. Engeser, A. Lützen, *J. Am. Chem. Soc.* **2014**, *136*, 11830-11838.

[17]. R. Hovorka, M. Engeser, A. Lützen, *Int. J. Mass Spectrom.***2013**, *354-355*, 152-158.

[18]. C. S. Byskov, J. M. Weberc, S. Brondsted Nielsen, *Phys. Chem. Chem. Phys.* **2015**, *17*, 5561-5564.

[19]. (a) T. D. Fridgen, *Mass Spectrom. Rev.* **2009**, *28*, 586-607; (b) J. R. Eyler, *Mass Spectrom.Rev.* **2009**, *28*, 448-467; (c) N. C. Polfer, J. Oomens, *Mass Spectrom. Rev.* **2009**, *28*, 468-494; (d) J. Roithova, *Chem. Soc. Rev.* **2012**, *41*, 547-559.

[20]. N. C. Polfer, *Chem. Soc. Rev.* **2011**, *40*, 2211-2221.

[21]. (a) P. Milko, J. Roithova, N. Tsierkezos, D. Schröder, *J. Am. Chem. Soc.* **2008**, *130*, 7186-7187; (b) P. Milko, J. Roithova, D. Schröder, J. Lemaire, H. Schwarz, M. C. Holthausen, *Chem. Eur. J.* **2008**, *14*, 4318-4327; (c) P. Milko, J. Roithova, *Inorg. Chem.* **2009**, *48*, 11734-11742; (d) L. Duchackova, V. Steinmetz, J. Lemaire, J. Roithova, *Inorg. Chem.* **2010**, *49*, 8897-8903; (e) L. Duchackova, J. Roithova, P. Milko, J. Zabka, N. Tsierkezos, D. Schröder, *Inorg. Chem.* **2011**, *50*, 771-782.

[22]. G. Frison, G. van der Rest, F. Turecek, T. Besson, J. Lemaire, P. Maitre, J. Chamot-Rooke, *J. Am. Chem. Soc*. **2008**, *130*, 14916-14917.

[23]. B. Noble, R. D. Peacock, *Inorg. Chem.* **1996**, *35*, 1616-1620.

[24]. N. S. Rannulu, M. T. Rodgers, *J. Phys. Chem. A* **2012**, *116*, 1319-1332.

[25]. J. Gu, J. Leszczynskic, H. F. Schaefer III, *Chem. Rev.* **2012**, *112*, 5603-5640.

[26]. R. Prazeres, F. Glotin, C. Insa, D. A. Jaroszynski, J. M. Ortega, *Eur. Phys. J. D*, **1998**, *3*, 87–93.

[27]. M. J. Frisch, G. W. Trucks, H. B. Schlegel, G. E. Scuseria, M. A. Robb, J. R. Cheeseman, G. Scalmani, V. Barone, B. Mennucci, G. A. Petersson, H. Nakatsuji, M.

Caricato, X. Li, H. P. Hratchian, A. F. Izmaylov, J. Bloino, G. Zheng, J. L. Sonnenberg, M. Hada, M. Ehara, K. Toyota, R. Fukuda, J. Hasegawa, M. Ishida, T. Nakajima, Y. Honda, O. Kitao, H. Nakai, T. Vreven, J. A. Montgomery, Jr., J. E. Peralta, F. Ogliaro, M. Bearpark, J. J. Heyd, E. Brothers, K. N. Kudin, V. N. Staroverov, R. Kobayashi, J. Normand, K. Raghavachari, A. Rendell, J. C. Burant, S. S. Iyengar, J. Tomasi, M. Cossi, N. Rega, J. M. Millam, M. Klene, J. E. Knox, J. B. Cross, V. Bakken, C. Adamo, J. Jaramillo, R. Gomperts, R. E. Stratmann, O. Yazyev, A. J. Austin, R. Cammi, C. Pomelli, J. W. Ochterski, R. L. Martin, K. Morokuma, V. G. Zakrzewski, G. A. Voth, P. Salvador, J. J. Dannenberg, S. Dapprich, A. D. Daniels, Ö. Farkas, J. B. Foresman, J. V. Ortiz, J. Cioslowski, D. J. Fox, Gaussian, Inc., Wallingford CT, 2010. Gaussian 09 (Revision B.01).

[28]. (a) A. D. Becke, *J. Chem. Phys*. **1993**, *98* , 5648–5652; (b) A. D. Becke, *Phys. Rev. A* **1988**, *38*, 3098-3100; (c) C. Lee, W. Yang, R. G. Parr, *Phys. Rev. B* **1988**, *37*, 785–789.

[29]. A. M. Rijs, G. Ohanessian, J. Oomens, G. Meijer, G. von Helden, I. Compagnon, *Angew. Chem. Int. Ed.*, **2010**, *49*, 2332–2335.

General Conclusions and Prospectives

The objective of the thesis was to gain more insights into the electronic structure of open-shell reduced organometallic complexes with non-innocent ligands. Currently; these one electron reduced species have been keen importance in the field of organometallic complexes. For example, such ruthenium complexes are chemical intermediates in recently developed visible-light photocatalysis processes, and such complexes of base metals like Fe, Cu, Zn are used in organometallic catalysis to replace organometallic catalysts containing noble metal. Due to enormous difficulties to study the very unstable organometallic complexes in the solution phase as well as difficulties with separation of these complexes in mixture, we developed an analytical method to study the formation and characterization of reduced metal complexes in the gas-phase.

Different state of art techniques such as mass spectrometry and electron activated dissociation techniques were played vital role to prepare the desired organometallic complexes. In addition, we have used the coupling of these techniques with action IR-spectroscopy in order to characterize isolated reduced ions in the gas-phase.

Multi charged organometallic complexes with selected chemical components, i.e zinc and ruthenium dicationic metal centers with bipyridine and bis(imino)pyridine type ligands, have been prepared. These cations are obtained in the gas phase through electrospray ionization in a Fourier transform ion cyclotron resonance (FT-ICR) mass spectrometer. Two fragmentation techniques, the electron capture dissociation and the electron transfer dissociation, available in FT-ICR have allowed us to induce mono-electronic reduction of these dicationic metal species. We showed that electron capture dissociation method induce loss of at least one bidentate ligand for zinc complexes. On the contrary, using electron transfer dissociation method, which provide less internal energy to the ion, and ruthenium complexes which have

stronger metal-ligand bond, permits reduction without loss of ligands. These different possibilities have been observed for various complexes, depending on the nature of the metal, the structure of the ligand as well as its denticity. Anyway, in all cases, mono-cationic open-shell complexes in the gas phase can be isolated in the FT-ICR cell and further study by IRMPD spectroscopy.

Density functional theory methods have been used to characterize the organometallic species under study along with the experimental findings. The use of these modeling methods has faced a major issue. On one hand, we have shown that the nature of the ground state of open-shell reduced ligands and zinc complexes in function of the amount of Hartree-Fock exchange, which parallels known failure of DFT methods due to the self-interaction error. This has suggested that range-separated hybrid functionals should be use to study the reduced complexes, even if, at this stage, it remains to be demonstrated. On the other hand, range-separated hybrid functionals showed great inaccuracy to predict IR spectra. Therefore, no functional seems able to provide us both the correct electronic structure and the IR spectra of reduced organometallic complexes.

To overcome the problem, we made benchmark calculations to find the suitable range separated hybrid density functional in order to corroborate with the experimental data. For this purpose, we generated a set of experimental data as a reference for the theoretical calculated IR spectra. These studies gave us new prospect for analyzing the experimental data with computed evidences. Indeed, we showed that ωB97X-D is the best SIE-corrected functional, among those we tested, for prediction of frequency values and we determined a confidence interval for this functional and others on their ability to model IR spectra. Furthermore, we showed that the universal procedure of scaling factors is not the most efficient for comparing experimental and theoretical spectra. Indeed, a linear correlation analysis allows obtaining

predicted spectra which on comparison with the experimental spectra, have errors lowered by about 30% relative to spectra predicted with a scaling factors.

Last, we combine our ability to form radical open-shell organometallic complexes in the gas phase, the possibility to obtain IRMPD spectra of these species, and our knowledge on the accuracy of the functional to characterize eleven singly-reduced complexes. The agreement, or disagreement, between experimental and theoretical spectra allows demonstrating that, depending on the complex, the added electron can be located either on the metal center or on the ligand. In case of low coordination, i.e. high Lewis acidity, the single-electron is located on the metal center. On the opposite, higher coordination induces that the electron goes to one ligand. Last, we demonstrate, for complexes with a tetracoordinated zinc center by two bidentate ligands, that B3LYP fails to describe its ground state. Indeed, our results clearly establish that the self-interaction error in standard DFT makes them totally ineffective to describe the electronic structure of open-shell singly-reduced organometallic species studied in this thesis.

The overall results enriched our knowledge on the redox properties of ligated metal cations through an appropriate experimental and theoretical framework. This work opens various prospective, among which:

- The formation and characterization of other organometallic complexes with different metal center (Fe^{2+}, Al^{3+},…) and ligands
- The extension of our spectroscopic study to UV/Vis spectroscopy thanks to the tunable laser which should be coupled soon to the FT-ICR in or lab.
- The determination of the best functional to describe excited states of gas phase reduced organometallic complexes through TD-DFT calculations

Formation et caractérisation de complexes métalliques réduits en phase gazeuse

Mots clés : methodes DFT, spectrométrie de masse, chimie computationnelle, structure electronique, spectroscopie IR, ligands non-innocents

Résumé : La caractérisation complète d'intermédiaires réactionnels intervenants dans des procédés de catalyse homogène est une tâche ardue en raison de leur réactivité et de leur faible concentration. Ceci est particulièrement vrai pour les espèces radicalaires telles que les complexes organométalliques réduits, qui sont des intermédiaires en photocatalyse ou lorsque ces complexes possèdent des ligands non-innocents. Par conséquent, leur structure électronique est encore mal comprise, sachant que l'électron ajouté peut être situé sur différents sites de la molécule.

Dans ce contexte, nous avons développé une méthode d'analyse pour étudier en phase gazeuse des complexes organométalliques radicalaires. Des complexes organométalliques multichargés du zinc et du ruthénium avec des ligands bidentes de type bipyridine ou tridente de type bis(imino)pyridine ont d'abord été obtenus et isolés en phase gazeuse. Ils sont ensuite réduits avec les méthodes d'activation par un électron spécifiques à la spectrométrie de masse, la dissociation par capture ou transfert d'électron (ECD/ETD), permettant de former des espèces métalliques radicalaires monochargées. Celles-ci sont enfin isolés et leur spectre infrarouge est obtenu à l'aide de la spectroscopie d'action basée sur la dissociation induite par l'absorption de plusieurs photons dans l'infrarouge (IRMPD). Les méthodes DFT fournissent un complément pour modéliser la structure électronique et le spectre IR de ces espèces. Les challenges à relever pour développer ce nouvel outil d'analyse étaient de deux ordres. Tout d'abord, nous devions être en mesure d'obtenir les complexes souhaités en phase gazeuse. Ceci nous a conduit à examiner de multiples paramètres, tels que la nature des ligands ou l'énergie interne déposée lors de l'étape de réduction. Le deuxième défi portait sur l'utilisation des méthodes de modélisation. Nous avons montré l'absence de fiabilité des méthodes standards de modélisation pour décrire à la fois la structure électronique et le spectre infrarouge des complexes réduits. Les données expérimentales obtenues durant ce travail ont donc été utilisées comme références pour identifier les fonctionnelles DFT les plus appropriées pour l'étude de ces complexes radicalaires.

Formation and Characterization of Reduced Metal Complexes in the Gas Phase

Keywords : DFT methods, Mass spectrometry, Computational chemistry, Electronic Structure, IR spectroscopy, Non-innocent ligands

Abstract : The complete characterization of reaction intermediates in homogeneous catalytic processes is often a difficult task owing to their reactivity and low concentration. This is particularly true for radical species such as reduced organometallic complexes, which are intermediates in photocatalysis, or when these complexes included non-innocent ligands. Consequently, their electronic structure in the ground state is still poorly understood, knowing that the added electron can be located on different sites of the molecule.

In this context, we developed an analytical method to study radical organometallic complexes in the gas phase. We started with formation of suitable multi-charged zinc and ruthenium organometallic complexes in the gas phase from mixture of zinc metal cation and bipyridine-type bidentate or bis(imino)pyridine tridentate ligands. Under ideal circumstances these complexes were isolated and reduced in the gas phase to form monocationic metal species. Electron activated methods such as electron capture dissociation (ECD) and electron transferred dissociation (ETD) techniques, available in FT-ICR mass spectrometers, have been used to that end. The resulting Zn and Ru radical cation complexes are then isolated in the gas phase and probed via infrared multi photon dissociation (IRMPD) action spectroscopy. In support, DFT theoretical calculations were performed to model their electronic structure and IR spectra

Two main issues were faced during the development of this new analytical tool. First, we had to be able to obtain the desired complexes in the gas phase. This has lead to monitor various parameters, such as the nature of the ligands or the internal energy provided by the reduction step. The second challenge dealt with the use of modeling methods. We have shown that standard modelling tools lack the accuracy to predict both electronic structure and spectral signatures of reduced complexes. The experimental data gathered in this work have therefore been used as benchmarks for the identification of DFT functionals that are most appropriate for the study of these radical complexes.